Doctoral theses at NTNU, 2021:242

Siri Marie Skaftun

Manganese Oxide in Zinc Electrowinning

Deposition and removal at platinum, gold and IrO_2-Ta_2O_5/Ti anodes in sulphuric acid

Doctoral thesis

NTNU
Norwegian University of Science and Technology
Thesis for the Degree of
Philosophiae Doctor
Faculty of Natural Sciences
Department of Materials Science and Engineering

NTNU
Norwegian University of
Science and Technology

Siri Marie Skaftun

Manganese Oxide in Zinc Electrowinning

Deposition and removal at platinum, gold and IrO_2-Ta_2O_5/Ti anodes in sulphuric acid

Thesis for the Degree of Philosophiae Doctor

Trondheim, July 2021

Norwegian University of Science and Technology
Faculty of Natural Sciences
Department of Materials Science and Engineering

NTNU
Norwegian University of
Science and Technology

NTNU
Norwegian University of Science and Technology

Thesis for the Degree of Philosophiae Doctor

Faculty of Natural Sciences
Department of Materials Science and Engineering

ISBN 978-82-326-6032-2 (printed ver.)
ISBN 978-82-326-6849-6 (electronic ver.)
ISSN 1503-8181 (printed ver.)
ISSN 2703-8084 (online ver.)

Doctoral theses at NTNU, 2021:242

Printed by NTNU Grafisk senter

Preface

This work was funded by the Department of Materials Science and Engineering at the Norwegian University of Science and Technology (NTNU). The experimental work was conducted in the laboratories at the Department of Materials Science and Engineering, NTNU, except for the synthesis of dimensionally stable anodes that was performed in the laboratory at Permascand AB, Ljungaverk, Sverige. All experiments were conducted by me, except acquisition of STEM-images that was performed by Dr. Amin H. Zavieh.

While this work was not officially a part of the research project ”Sustainable and Energy Efficient Electrochemical Production and Refining of Metals” (SUPREME), I have participated in project meetings. The SUPREME project (no. 228296) was a knowledge-building project for industry funded by the Research Council of Norway and the following industrial partners: BOLIDEN Odda, Glencore Nikkelverk, Permascand and Hydro Aluminium.

The thesis is written as a monograph. After the introduction, literature review is presented in a separate chapter (Chapter 2). A brief description of the theory behind less conventional techniques is presented in Chapter 3. Then follows the experimental and results chapters (Chapters 4 and 5, respectively). These chapters are organized mainly by set-ups and techniques. In the results chapter, images from scanning electron microscopy (SEM) are presented first (sections 5.1 and 5.2, including results from energy dispersive X-Ray spectroscopy (EDS)). Then, results from the most employed set-ups are presented; conventional cell in section 5.3 and electrochemical quartz crystal microbalance (EQCM) in section 5.4. These two sections are organized first by type of experiment (i.e. cyclic voltammetry, chronoamperometry, etc.), then by working electrode material, and finally by electrolyte. Subsequently, results are presented from a rotating disc electrode set-up (secs. 5.5 and 5.6) and in situ Raman spectroscopy (sec. 5.7) before a brief comparison between electrode materials used in the different set-ups is presented in section 5.8. The discussion is presented in Chapter 6 starting with mechanisms for deposition of manganese oxide, divided into short deposition times (sec. 6.1) and longer deposition times (sec. 6.2). Then, the mechanism for reduction of manganese oxide is discussed in section 6.3 before discussing a procedure for removal of manganese oxide in section 6.4. Finally, conclusions are presented in Chapter 7 and outlook and suggestions for future work in Chapter 8.

Acknowledgements

First of all I would like to thank my supervisor, Professor Frode Seland, for all his time, support, and guidance. Thank you very much for the many great discussions and for many great laughs too. I would also like to thank my co-supervisors, Professors Svein Sunde and Geir Martin Haarberg for their valuable input and interesting discussions.

I am very grateful that I got to participate in the project meetings in the SUPREME project although I was not officially a part of the project, and I would like to thank all the participants in those meetings. A lot of interesting discussions took place during those meetings and they served as a great motivation throughout my PhD. Particularly, I would like to thank Steinar Jørstad at Boliden Odda for many interesting discussions about zinc electrowinning. I am also very grateful for being allowed to come to the lab at Permascand in Ljungaverk to synthesise electrodes and I am very thankful for the guidance from Dr. John Gustavsson and Dr. Susanne Holmin.

The financial support from the Department of Materials Science and Engineering, NTNU is appreciated, giving me this opportunity.

I would like to thank the technical and administrative staff at the department, particularly Magnus Bentzen Følstad, Agnes Digranes, Anita Storsve and Solveig Jonassen, for their ability to find and fix things, and for fun hallway conversations.

Many thanks to Professor Andreas Erbe for discussions about Raman spectroscopy, and to Dr. Alaa Faid and Johannes Ofstad for teaching me how to perform Raman spectroscopy. I would also like to thank Dr. Julian Tolchard for teaching me how to operate the SEM and EDS. The help of Dr. Amin H. Zavieh in acquiring STEM images is appreciated.

I would like to thank all my friends and colleagues throughout my years in K2 for many fruitful conversations, mostly non-scientific. Thank you for all the nice chats, walks and lunch- and coffee-breaks! :)

To my parents and sisters – thank you for both moral and practical support. My sisters Ingvild and Eirin are also acknowledged for their guidance in Matlab and how to cheat with style, respectively. To my kids, Alve and Idun, thank you for providing some perspective and for giving me other things to think about when returning from work. Finally, I would like to thank Øystein for his support and patience with me being at work all the time and also for cleaning yellow paint and such. Completing this PhD would not have been possible without you.

Abstract

An environmentally friendly and energy efficient replacement for lead anodes in zinc electrowinning is highly desired. Oxygen evolution reaction (OER) is the desired anode reaction in acidic sulphate electrolytes. However, manganese oxide forms in large quantities at the anode during zinc electrowinning due to the presence of dissolved manganese in the electrolyte. Manganese oxide formation causes increased cell resistance, increases the risk of short circuits and prevents implementation of catalytic anode materials. To succeed, a method is required for removing deposited manganese oxide from these anodes without destroying the catalytic coating.

A deeper understanding of the mechanism of manganese oxide formation and reduction can lead to better control over the deposit formed in the zinc electrowinning process and make it possible to suggest an electrochemical procedure for removing it. In this thesis, the mechanism of manganese oxide formation and reduction at platinum, gold, titanium and IrO_2-Ta_2O_5/Ti electrodes is studied using conventional electrochemical methods, such as cyclic voltammetry, linear sweep voltammetry and chronoamperometry, as well as electrochemical quartz crystal microbalance (EQCM) and in-situ Raman spectroscopy. The morphology of deposited manganese oxide is also examined. The mechanism for manganese oxide deposition and reduction is found to depend on many factors; most importantly pH, electrode potential and thickness of the deposit, i.e. with deposition time. An electrochemical procedure for removal of deposited manganese oxide is developed, and is further validated in synthetic electrolyte. The sequence involves applying several electrode potentials, including forming a prelayer of manganese oxide at a low electrode potential (1.45 V), which is shown to reduce easier. Only a short reduction step, i.e. seconds, is necessary as this reduction diminishes the adhesion of remaining manganese oxide, which can then easily be removed mechanically.

This thesis reveals that it is possible to remove deposited manganese oxide by a procedure involving a sequence of electrode potentials. Implementing such a procedure can make it possible to replace the lead anodes used in zinc electrowinning today with more energy efficient and environmentally friendly anodes.

Contents

Notations and symbols

List of abbrevations

AFM	Atomic Force Microscopy
CA	Chronoamperometry
CE	Counter Electrode
CV	Cyclic Voltammetry
DSA	Dimensionally Stable Anode
ECE	Electrochemical Chemical Electrochemical
EDS	Energy Dispersive X-Ray Spectroscopy
EIS	Electrochemical Impedance Spectroscopy
EQCM	Electrochemical Quartz Crystal Microbalance
GC	Glassy Carbon
LSV	Linear Sweep Voltammetry
MSE	Mercury Mercurous Sulphate Electrode
NHE	Normal Hydrogen Electrode
OCP	Open Circuit Potential
OER	Oxygen Evolution Reaction
PEEK	Polyetheretherketone
PTFE	Polytetrafluoroethylene
RDE	Rotating Disc Electrode
RHE	Reversible Hydrogen Electrode
RRDE	Rotating Ring Disc Electrode
RT	Room temperature
RVC	Reticulated vitreous carbon
SCE	Saturated Calomel Electrode
SEM	Scanning Electron Microscopy

STEM	Scanning Transmission Electron Microscopy
TEM	Transmission Electron Microscopy
TGA	Thermogravimetric Analysis
WE	Working Electrode
XAS	X-Ray Absorption Spectroscopy
XRD	X-Ray Diffraction
XRF	X-Ray Fluorescence

List of symbols

A	Area
A	First order nucleation rate constant
c	Concentration
C_f	Sensitivity factor (Sauerbrey coefficient)
D	Diffusion coefficient
E	Potential
E^0	Standard potential
f	Frequency
F	Faraday constant
i	Current density
i_m	Current density at the maximum in a current transient
I	Current
m	Mass
M	Molar mass
μ_q	Shear modulus of quartz
n	Number of electrons
N	Number density of active sites
ν	Sweep rate
q^*	Voltammetric charge
q_i^*	Inner charge
q_s^*	Surface charge (outer charge)
q_{tot}^*	Total charge
R	Resistance
ρ	Density
ρ_q	Density of quartz
t	Time

t_m	Time at the maximum in a current transient
ω	Rotation speed

Chapter 1

Introduction

Climate change is the most important issue of our time. Consumption of energy is a key factor in this regard and increasing the share of renewable energy in the global energy mix as well as improving energy efficiency are among the United Nations sustainable development goals.

Production of high-purity non-ferrous metals (aluminium, copper, zinc, nickel and cobalt) and water electrolysis consumes large amounts of electric energy. The production of metals from their ores by electrolysis is referred to as electrowinning. During electrowinning, the product is formed at the cathode, while a reaction passing the same amount of current takes place at the anode. In aqueous electrowinning the main reaction at the anode is either evolution of oxygen gas or chlorine gas, depending on the electrolyte used. While chlorine evolution is a rather fast reaction, oxygen evolution is slow and often represents the primary source of energy loss in related electrochemical processes.

In zinc and copper electrowinning the main anodic reaction is oxygen evolution from acidic sulphur electrolytes. The anode materials in these processes are commonly lead based alloys due to their adequate electrical conductivity, low contact resistance, high durability and good corrosion resistance in the very corrosive conditions under which they operate. On the other hand, lead is a poor electrocatalyst towards the oxygen evolution reaction, tend to creep due to its high ductility and density and is toxic, representing a potential hazard both in terms of working environment and discharge of polluting material to aquatic environments. Furthermore, dissolved lead will co-deposit with the metal product at the cathode, reducing the quality of the product and depreciate values of potential by-products.

Based on the disadvantages, it is highly desirable to replace the lead anodes with more active, environmentally friendly and stable anodes such as dimensionally stable anodes (DSA). Dimensionally stable anodes consist of a base metal (i.e. titanium) coated with metal oxides, typically comprising of a variety of noble metal oxides with the aim of increasing the activity and maintaining a satisfying lifetime of the layer [1]. In some copper refineries DSAs have already been implemented, but in zinc electrowinning the situation is more complex particularly due to the high concentrations of Mn^{2+} in the electrolyte and higher current densities [2]. At the anode, Mn^{2+} is oxidized to MnO_2 that deposits at the electrode. At lead electrodes there are both benefits and drawbacks of the resulting layer of MnO_2. However, at DSA electrodes the deposited MnO_2 poses one essential problem as it blocks the surface of the more active DSA-coating, reducing the energy efficiency gained when converting from lead to DSA anodes. The DSA-coating typically contains oxides of expensive platinum group metal, such as iridium and ruthenium, and a certain gain in energy efficiency is required for DSA electrodes to be an economically viable option. Furthermore, a method is required for removing the deposited manganese oxide without damaging the DSA-coating and deteriorate the electrode performance.

1.1 Zinc Electrowinning

Zinc is mainly used for corrosion protection and as an alloying element. It can be produced both through a pyrometallurgical process and through electrowinning. Electrowinning produces purer zinc and the global annual production is appoximately 7 million tons (about 60 % of the overall production) [3]. Zinc is produced from ores consisting mainly of sulphides (e.g. sphalerite). The ore is concentrated and subsequently roasted to obtain zinc oxide. In the electrowinning process, the zinc oxide is leached in sulphuric acid to obtain a solution containing Zn^{2+}-ions. The solution also contains several detrimental impurities and a number of purification and processing steps are performed before it enters the electrolysis tank house. The electrolyte contains a wide variety of constituents ranging from zinc ions and sulphuric acid to inorganic and organic impurities and additives. Table 1.1 provides a short list of relevant electrolyte constituents, and typical oper-

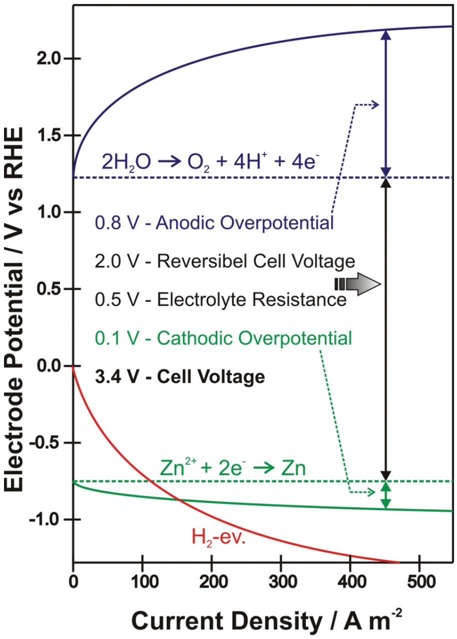

Figure 1.1: Illustration of the various contribution to the total cell voltage at different current densities. Adapted from [4].

ational parameters are provided in Table 1.2. An overview of the various contributions to the cell voltage is presented in Figure 1.1.

1.1.1 Cathode processes

During electrolysis, zinc is deposited at the cathode according to Eq. (1.1). Deposition of zinc is accompanied by hydrogen evolution (Eq. (1.2)) as a side reaction. Fortunately, zinc is a poor electrocatalyst for the hydrogen

Table 1.1: Typical concentration of relevant electrolyte constituents.

Species	Concentration			
Zn^{2+}	55	$g\,L^{-1}$	0.84	$mol\,L^{-1}$
H_2SO_4	180	$g\,L^{-1}$	1.8	$mol\,L^{-1}$
Mn^{2+}	8	$g\,L^{-1}$	0.15	$mol\,L^{-1}$
Cl^-	300	$mg\,L^{-1}$	8.5	$mmol\,L^{-1}$

Table 1.2: Typical operating parameters during zinc electrowinning.

Anode material	Lead alloyed with silver (<1 wt% Ag)	
Cathode material	Aluminium alloy	
Current density	600	$\mathrm{A\,m^{-2}}$
Cell voltage	3.5	V
Current efficiency (cathode)	90	%
Specific energy consumption	3.2	kWh/kg Zn
Temperature	37	°C

evolution reaction and hence reasonable current efficiency for the zinc deposition reaction can be achieved, particularly at high current densities (cf. Figure 1.1).

$$\mathrm{Zn^{2+} + 2\,e^- \longrightarrow Zn(s)} \qquad E^\circ = -0.76\,\mathrm{V} \tag{1.1}$$

$$\mathrm{2\,H^+ + 2\,e^- \longrightarrow H_2(g)} \qquad E^\circ = 0.00\,\mathrm{V} \tag{1.2}$$

1.1.2 Anode processes

The main reaction at the anode is oxygen evolution (Eq. (1.3)) accompanied by manganese oxide deposition (Eq. (1.4)). Chlorine evolution (Eq. (1.5)) is also a possible side reaction at the anode. The chlorine evolution reaction has a higher standard electrode potential than the oxygen evolution reaction, but since the overpotential of the latter tends to be higher, chlorine evolution can occur in chloride containing aqueous electrolytes [5]. In an energetic perspective chlorine evolution might be favourable, but in the context of a working environment chlorine evolution is undesirable because of its toxicity and increased degradation of tank house equipment. In this context, manganese oxide deposition at the anode is beneficial as it is known to favour oxygen rather than chlorine evolution in chloride containing electrolytes [6].

$$2\,H_2O \longrightarrow O_2(g) + 4\,H^+ + 4\,e^- \qquad E^\circ = 1.229\,V \qquad (1.3)$$

$$Mn^{2+} + 2\,H_2O \longrightarrow MnO_2(s) + 4\,H^+ + 2\,e^- \qquad E^\circ = 1.23\,V \qquad (1.4)$$

$$2\,Cl^- \longrightarrow Cl_2 + 2\,e^- \qquad E^\circ = 1.36\,V \qquad (1.5)$$

Manganese oxide forms in substantial amounts at the anode during zinc electrowinning. Deposition of some manganese oxide is desirable when using lead anodes as it hinders corrosion of the underlying lead surface, resulting in less contamination of the produced zinc and lower chlorine gas evolution. However, corrosion of the anode and lead impurities are not as relevant when DSA electrodes are used. For all electrode materials, the growing layer of manganese oxide leads to an increase in resistance over time. Furthermore, when using an active anode (DSA) the overpotential will increase as manganese oxide blocks active sites and diminishes the catalytic activity of the anode resulting in a decrease in energy efficiency. During long-term use of anodes without manganese oxide removal, scales of manganese oxide may detach from the anode surface and potentially cause short circuits. Short circuits cause the produced zinc to dissolve and may cause irrevocable damage to the anode. Consequently, deposition of manganese oxide must be controlled and needs to be removed at regular intervals.

Removal of manganese oxide represent a significant cost factor in zinc electrowinning. The lead anodes are removed from the cell and the manganese oxide is removed mechanically. However, when using DSA electrodes it is important that the catalytic coating is not damaged during manganese oxide removal as this may later cause the substrate to passivate, thus deactivating the electrode. Chemical and/or electrochemical dissolution of manganese oxide might be possible methods to successfully remove manganese oxide without damaging the catalytic coating. Electrochemical reduction of manganese oxide is described in more detail in section 2.3.3. Chemical dissolution can be performed by heating in concentrated sulphuric or hydrochloric acid [7], or by addition of for instance ferrous ions (Fe^{2+}) [8], H_2O_2 [9], $SO_2(aq)$ [10] or oxalic acid [11]. Many of these methods are not directly compatible with the zinc electrowinning process, and must be performed in a separate container, potentially with ventilation ($Cl_2(g)$, $SO_2(g)$). Obviously, it is important to make sure that the DSA coating does not dissolve simultaneously. The cost of the chemicals is also an important factor. Other mitigation strategies include using increased stirring causing manganese oxide to precipitate away from the anode [12] or using DSA electrodes with amorphous coatings. Amorphous IrO_2-Ta_2O_5/Ti electrodes have shown increased nucleation overpotential towards lead oxide and manganese oxide deposition [13, 14]. Formation of manganese oxide is suppressed at such electrodes. However, amorphous electrodes have short lifetime compared to crystalline electrodes [15], and in combination with the high price of Ir they are considered to be less suitable candidates for industrial application.

1.2 Aim of the thesis

This work attempts to facilitate the necessary transition away from lead-based anodes to more energy efficient and environmentally friendly anodes in acidic sulphate-based electrowinning processes. This is particularly challenging in zinc electrowinning where manganese oxide deposits at the anode, and a better control of oxide formation and removal is needed.

The manganese oxide deposition and reduction in acidic electrolytes is not fully understood and involves a number of chemical and electrochemical steps. The aim of this thesis work is to investigate the formation and reduction of manganese oxide in acidic sulphate electrolytes, and to study the impact of potential (current), pH and substrate material using electrochemical and surface sensitive techniques. Strategies for electrochemical removal of manganese oxide will be investigated based on the obtained understanding, and ultimately a procedure for manganese oxide removal will be suggested for industrially relevant pH and manganese concentration.

Chapter 2

Literature Review

2.1 The Oxygen Evolution Reaction

The oxygen evolution reaction (OER) is an important reaction in aqueous electrolytes as it is the anode reaction involved in splitting of the solvent (water). Apart from being the main anodic reaction in electrowinning of several metals, OER is important in other electrochemical processes such as water electrolysis, electrosynthesis processes [16] and electrochemical treatment of wastewater [17], among others. Unfortunately, the OER in aqueous electrolytes has a relatively large overpotential and consequently has a negative impact on the energy efficiency of the processes where it is involved. Hence, numerous studies have been conducted both to better understand the mechanism of oxygen evolution and to find optimized electrocatalysts for the reaction.

2.1.1 Mechanism

The mechanism of the oxygen evolution reaction has been studied extensively over the past decades, mostly in relation to electrocatalysts development for water electrolysis. The total reaction involves transfer of four electrons according to Eq. (2.1):

$$2\,H_2O \longrightarrow O_2 + 4\,H^+ + 4\,e^- \qquad E^\circ = 1.229\,V \tag{2.1}$$

A number of different reaction mechanisms have been proposed and evaluated both in terms of experimental data (Tafel slopes and reaction orders) [18] and density functional theory (DFT) calculations [19]. In broad terms, the proposed mechanisms involving only adsorbed species can be divided into two groups depending on how the oxygen-oxygen bond is created, as illustrated in Figure 2.1. Both mechanisms involve formation of an M−OH species that is subsequently oxidized to M−O. Then, the oxygen-oxygen bond is formed either when two neighbouring M−O species come together (named direct coupling mechanism in Fig. 2.1) or from a nucleophilic attack of water on a single M−O species creating an M−OOH species (named acid-base mechanism in Fig. 2.1). An additional oxidation step follows the oxygen-oxygen bond formation before O_2 is released.

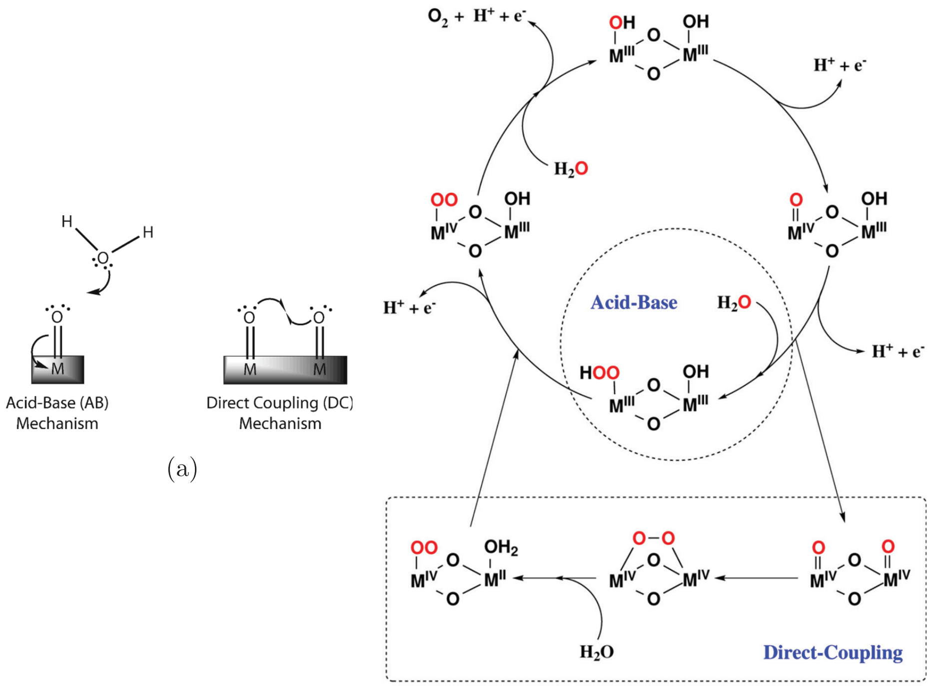

(a)

(b)

Figure 2.1: Schematic representation of the oxygen-oxygen bond formation (a) and illustration of the various steps involved (b) for the acid-base and direct coupling mechanisms for the OER. Reprinted with permission from (a) [20] and (b) [21]. Copyright 2010 and 2014 American Chemical Society, respectively.

An example of a mechanism where two neighbouring M−O species combine to form the oxygen-oxygen bond (direct coupling) is the oxide path suggested by Bockris [18]:

$$H_2O + M \rightleftharpoons M{-}OH + H^+ + e^- \tag{2.2}$$
$$2\,M{-}OH \rightleftharpoons M{-}O + M + H_2O \tag{2.3}$$
$$2\,M{-}O \rightleftharpoons 2\,M + O_2 \tag{2.4}$$

An example of a mononuclear (acid-base) mechanism is the following mechanism suggested by Rossmeisl et al. [19]:

$$H_2O + M \rightleftharpoons M{-}OH + H^+ + e^- \tag{2.5}$$
$$M{-}OH \rightleftharpoons M{-}O + H^+ + e^- \tag{2.6}$$
$$M{-}O + H_2O \rightleftharpoons M{-}OOH + H^+ + e^- \tag{2.7}$$
$$M{-}OOH \rightleftharpoons M + O_2 + H^+ + e^- \tag{2.8}$$

In both mechanisms outlined above (direct coupling and acid-base), oxygen originates from water adsorbed at the catalyst surface. However, oxygen originating from the catalyst lattice has been detected in the oxygen gas evolved at certain metal oxides [22, 23]. The mechanism involving lattice oxygen is illustrated in Fig. 2.2b, whereas Fig. 2.2a illustrates the mechanisms involving adsorbed water and is equivalent to those presented in Fig. 2.1.

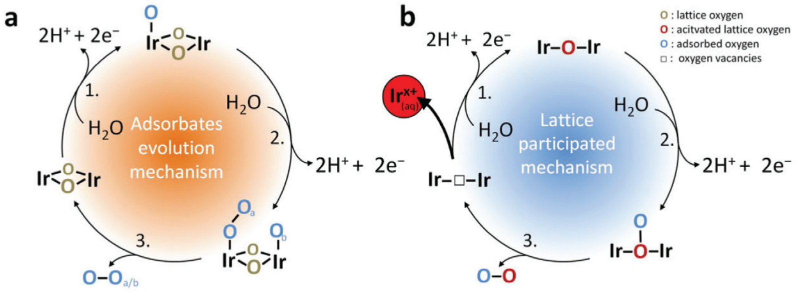

Figure 2.2: Schematic representation of OER reaction mechanisms on (a) crystalline IrO_2 involving only adsorbed species and (b) amorphous IrO_2 involving lattice oxygen. Reprinted with permission from [23]. Copyright 2018 Springer Nature.

The mechanism involving lattice oxygen is intrinsically linked to decreased stability of the catalyst [23, 24]. This is because when lattice oxygen leaves the structure, oxygen vacancies are created. In turn, this leads to decreased stability of the neighbouring metal atoms resulting in an increased dissolution rate. The lattice oxygen evolution reaction occurs at amorphous IrO_2, but not at crystalline IrO_2, and is thought to be responsible both for the increased activity and decreased stability of amorphous compared to crystalline IrO_2 [23].

2.1.2 Electrocatalysis

Oxygen evolution is slow on many materials requiring large overpotentials to proceed at a significant rate. Hence, suitable electrocatalyst are sought to decrease the energy consumption. The purpose of the electrocatalyst is to decrease the activation energy for OER. This can be achieved either by a change in the reaction mechanism or by a change in adsorption bonds [25]. The adsorption bond between the electrocatalyst and the reactant, product and any intermediate(s) should not be too strong nor too weak. This is known as the Sabatier principle. If the adsorption bond is too weak the reaction will not be able to proceed at a reasonable rate because of the lack of reactants. On the other hand, if the adsorption is too strong the product will not be able to desorb and ends up poisoning the electrocatalyst surface, which in turn also leads to a decreased reaction rate. The Sabatier principle is often presented graphically in volcano plots where the activity or overpotential is plotted against a descriptor of the adsorption energy, see Figure 2.3.

The optimal catalysts in terms of adsorption bond strength are those located at or near the apex of the volcano, such as RuO_2 and IrO_2. However, several additional factors other than the activity have to be considered when selecting an electrocatalyst. Most notably, the electrocatalyst has to be stable at the operating conditions and not be too costly to produce. Other important factors include electrical conductivity, surface area, selectivity, gas release and toxicity. Similar considerations will be discussed for the coating of DSA electrodes in section 2.4.

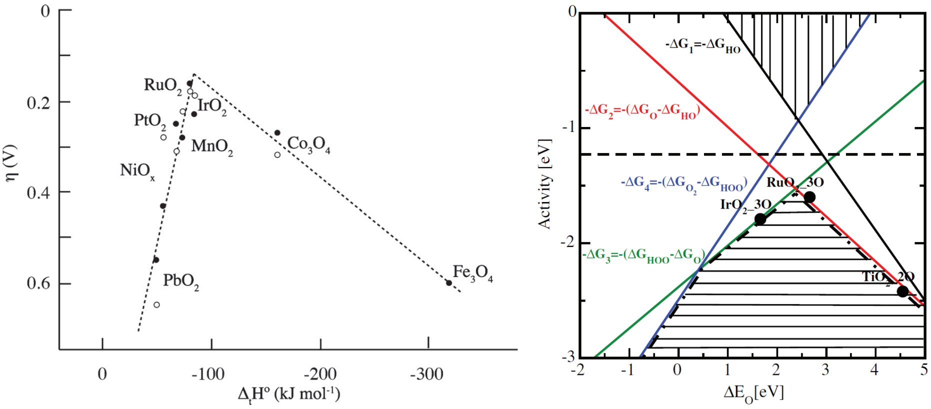

(a) (b)

Figure 2.3: Volcano plots for the oxygen evolution reaction based on (a) experimental data from acid solution (filled circles) and alkaline solution (open circles) and (b) DFT calculations. (a) Reprinted with permission from [20]. Copyright 2010 American Chemical Society. Based on data in [26]. (b) Reprinted with permission from [19]. Copyright 2007 Elsevier.

2.2 Electrodeposition of oxides onto oxide substrates

The deposition and growth of one material (deposit) on another material (substrate) in aqueous electrodeposition depends on a number of factors, including temperature, bath composition, agitation, deposition time, current density and additives, as well as substrate material and its pretreatment. In general, electrodeposition and growth depends on the interaction between the substrate and the electrolyte constituents at the applied conditions. Properties such as lattice parameters, elasticity, hardness, surface tension and wetting may affect the growth of the electrodeposit. However, these parameters may be considered to be of less importance with oxide electrodeposition onto an oxide substrate. Owe et al. [27] synthesized a range of IrO_2/RuO_2 solid solution electrocatalysts and compared their oxygen evolution reaction (OER) performance with similar compositions of physically mixed oxides. Their work showed no difference in OER catalytic performance between the solid solution and physically mixed oxides. While the performance depends on the relative composition (i.e. OER activity is different on RuO_2 than IrO_2), it is an indication that a distinct metal ion in

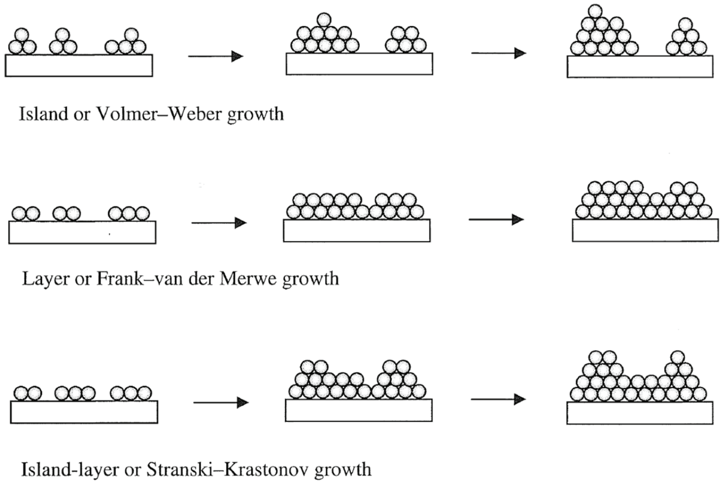

Figure 2.4: Growth modes for epitaxial growth. Reprinted from [28].

the oxide lattice is not influenced by any of its neighbouring lattice metal ions. We can therefore assume that the mechanical properties are equally independent as the electrocatalytic properties. Epitaxial growth (i.e. lattice of the deposit matches the orientation of the substrate lattice) may therefore be expected even in cases where there is a quite large mismatch between the deposit and substrate lattice. Three basic epitaxial growth modes are revealed experimentally [28] (see Fig. 2.4): 1) layered growth (Frank-van der Merwe) occurring when there is a strong interaction between the substrate and deposit (stronger than between deposited entities themselves), 2) island-growth (Volmer-Weber) ocurring when the substrate-deposit interaction is weak, and 3) layer then island growth (Stranski-Krastanov) where few nm of deposited layers form due to strong substrate-deposit interaction, which turns into island growth due to opposing forces from increasing strain with deposit thickness. The growth mode, islands sizes (commonly oblated structures in the 4-5 to 100 nm range) and distribution are typically depending significantly on temperature, deposition time and current density.

2.3 Manganese Oxide

Manganese is a quite abundant element in the earth's crust. It has a concentration of almost 1000 ppm making it the 12th most abundant element in the earth's crust [29]. It occurs in a wide range of minerals, mainly as oxides, carbonates and silicates [30]. Only among the manganese oxides/hydroxides more than 30 different minerals exist, such as pyrolusite, ramsdellite, nsutite, hausmannite, bixbyite, manganite and birnessite [31]. The primary use of manganese is for production of stainless steels.

MnO is used as a fertilizer and feed additive, in welding rod fluxes, in ceramics and glass manufacturing as well as to produce other manganese chemicals [32]. Mn_2O_3 and Mn_3O_4 are produced in smaller amounts and used in semiconductors and ceramic magnets [32].

MnO_2 has long been used as the active cathode material in batteries: first in the Leclanché cell and later in primary alkaline batteries. In more recent years, MnO_2 has also been used in other batteries such as rechargeable lithium, sodium and magnesium-ion batteries as well as in supercapacitors [33]. Furthermore, MnO_2 has been investigated as an electrocatalyst for OER in both acidic [34], neutral [35, 36] and alkaline electrolytes [37]. As shown in Figure 2.3a, MnO_2 can be suitable as an electrocatalyst for OER, especially when considering that manganese is much more abundant and hence cheaper than iridium and ruthenium. However, like most metal oxides, MnO_2 is not very stable under the conditions required for OER. This is especially true in acidic solutions [38].

MnO_2 used in batteries is usually categorized into three groups: natural manganese dioxide (NMD), chemical manganese dioxide (CMD) and electrochemical manganese dioxide (EMD) [39]. There are a number of different synthesis routes to produce CMD, resulting in different MnO_2 structures [40]. Previously, EMD was only used for high quality batteries since it was considered relatively expensive [40], but today EMD is preferred also for commercial alkaline cells because of its greater purity [33]. This is because the production method gives better control over the properties of the deposit [33]. EMD is generally electrodeposited at titanium anodes at a current density of $0.5-10\,\mathrm{mA\,cm^{-2}}$ from an electrolyte at $90-95\,^{\circ}\mathrm{C}$ that contains $0.4-0.7\,\mathrm{mol\,L^{-1}}$ H_2SO_4 and $0.3-0.5\,\mathrm{mol\,L^{-1}}$ Mn^{2+} [39]. It should be pointed out that these conditions are similar to those in the zinc electrowinning process, although the latter proceeds at higher current density, lower temperature, lower pH and lower Mn^{2+} concentration (cf. Tabs. 1.1 and 1.2).

Manganese oxide formation in electrowinning

As described in the introduction, manganese dioxide deposits at the anode during zinc electrowinning. Furthermore, MnO_2 may deposit at the anode in other electrowinning processes such as copper and manganese electrowinning.

The copper electrowinning process is closely related to the zinc electrowinning process in the sense that both take place in a sulphuric acid solution with oxygen evolution as the main anodic reaction. The anode material is commonly a lead alloy in both processes. However, the concentration of manganese in the electrolyte is significantly lower in the electrolyte used for copper electrowinning [2]. Furthermore, copper electrowinning proceeds at a lower current density and hence has a lower overpotential at the anode. Therefore, the extent of MnO_2 deposition at the anode is much lower in copper electrowinning than in zinc electrowinning.

Mangenese electrowinning usually occurs in an electrolyte containing manganese sulphate and ammonium sulphate, and hence at a higher pH than zinc electrowinning. The main reaction at the anode is oxygen evolution and lead based anodes are frequently used. However, OER is accompanied by substantial manganese oxide formation. Consequently, issues related to manganese oxide formation requires much resources in the manganese electrowinning process.

2.3.1 Thermodynamics

Manganese can exist in several oxidation states and as a result there are a wide range of manganese oxide compounds, such as MnO_2, Mn_2O_3, Mn_3O_4, and MnO. When Mn^{2+} is oxidized in an acidic solution, MnO_2 is the manganese oxide expected to form as seen in the Pourbaix diagram (Figure 2.5). Thus, MnO_2 will be mainly considered in the following.

The overall reaction for the deposition of MnO_2 is given by equation (2.9):

$$\mathrm{Mn^{2+}} + 2\,\mathrm{H_2O} \longrightarrow \mathrm{MnO_2} + 4\,\mathrm{H^+} + 2\,\mathrm{e^-} \qquad E^\circ = 1.23\,\mathrm{V} \tag{2.9}$$

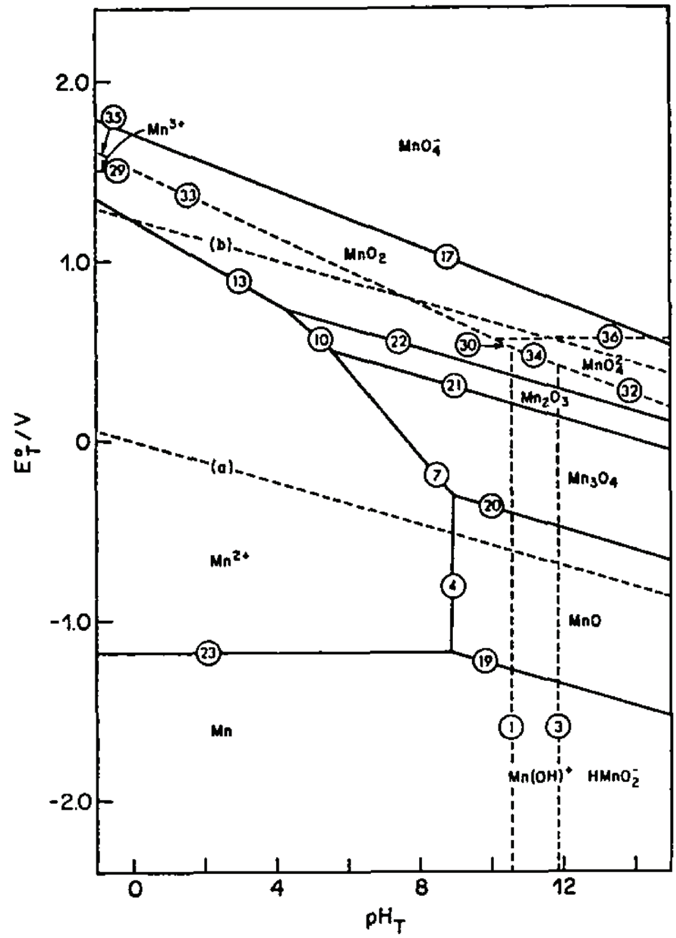

Figure 2.5: "Potential-pH diagram for the manganese/water system at 25 °C." Reproduced from [41] with permission from Elsevier.

Note that the standard potential (at 25 °C) for manganese dioxide deposition is similar to that of OER (Eq. (2.1)). Hence, it is not very surprising that manganese oxide deposition occurs as a side reaction in electrowinning processes such as zinc, copper and manganese, where OER is the main anodic reaction and Mn^{2+} is present in the electrolyte.

At more anodic potentials, Mn^{2+} can also be oxidized to the permanganate ion (MnO_4^-), which was for example found in the case of manganese electrowinning [42]:

$$\mathrm{Mn^{2+} + 4\,H_2O \longrightarrow MnO_4^- + 8\,H^+ + 5\,e^-} \qquad E^\circ = 1.51\,\mathrm{V} \tag{2.10}$$

Metal cations in the electrolyte are surrounded with a solvation sheath of water and approach the anode by means of diffusion during electrodeposition of metal oxide. Water is the source of oxygen in oxide electrodeposition, where the metal ion undergoes hydrolysis to an hydroxide before dehydrating to form the corresponding oxide. Dissolved Mn^{2+}-ions exist as manganese hexaaqua-ions ($[Mn(H_2O)_6]^{2+}$) in an octahedral coordination. The stability of manganese ions in solution depends on the pH (cf. Fig. 2.5). The $[Mn(H_2O)_6]^{2+}$ ion is relatively stable in acidic solutions, with a high pK_a value [43]:

$$\mathrm{[Mn(H_2O)_6]^{2+} \rightleftharpoons [Mn(H_2O)_5(OH)]^{+} + H^+} \qquad \mathrm{p}K_\mathrm{a} = 10.59 \tag{2.11}$$

The $[Mn(H_2O)_6]^{3+}$ ion is only stable in highly acidic solutions, with a correspondingly low pK_a value [44]:

$$\mathrm{[Mn(H_2O)_6]^{3+} \rightleftharpoons [Mn(H_2O)_5(OH)]^{2+} + H^+} \qquad \mathrm{p}K_\mathrm{a} = 0.03 \tag{2.12}$$

No data was found for the pK_a value of the $[Mn(H_2O)_6]^{4+}$ ion, and there is no evidence that it is stable in any solution. Rather, it is expected to undergo sequential hydrolysis and subsequent dehydration to form MnO_2.

2.3.2 MnO_2 structures

Crystal structures. MnO_2 exists in several polymorphs, some of which are illustrated in Figure 2.6. The MnO_2 polymorhps consist of a more or less close-packed structure of anions that differ by the arrangement of Mn^{4+} in octahedral holes [45]. They are often described as chains of $[MnO_6]$ octahedra arranged in various corner- and edge-sharing structures, such as

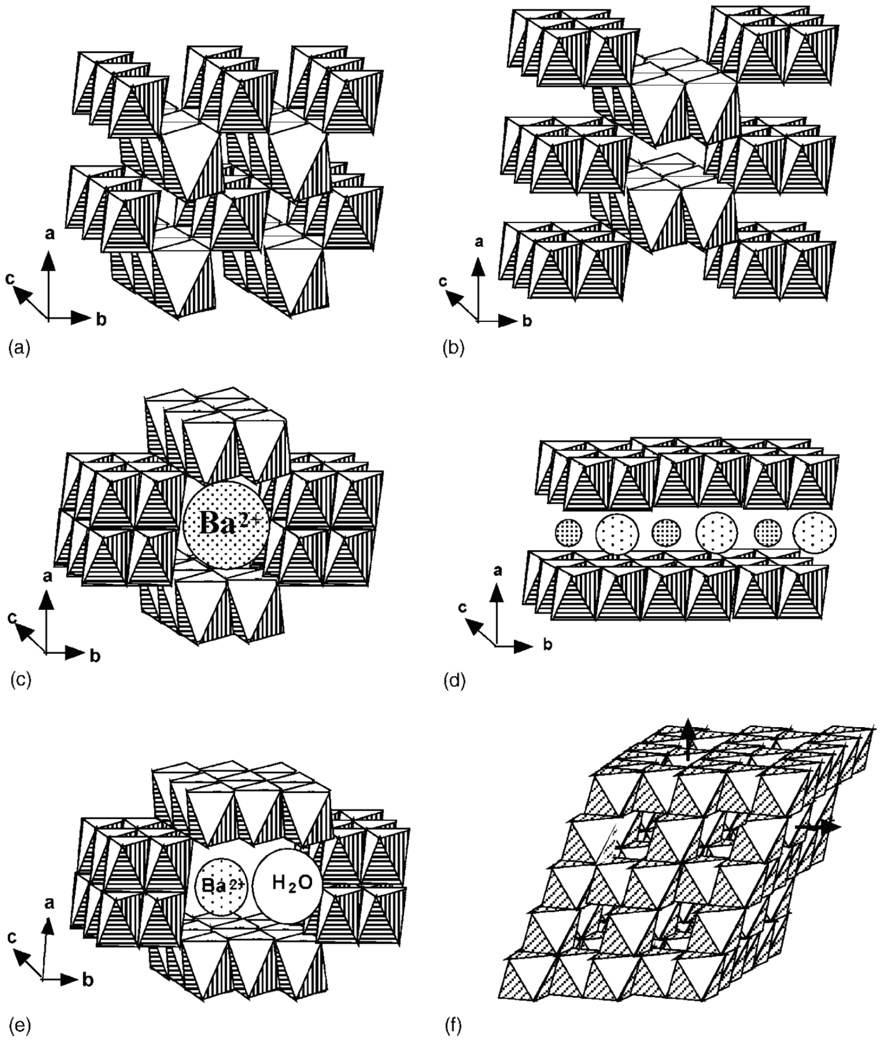

Figure 2.6: "Schematic representation of the various manganese dioxide frameworks showing the variation in the chain and tunnel ($m \times n$) structures: (a) pyrolusite (1 x 1), (b) ramsdellite (1 x 2), (c) hollandite (2 x 2), (d) birnessite (1 x 8), (e) romanechite (2 x 3), and (f) spinel (1 x 1)." Reproduced from [46] with permission from Elsevier.

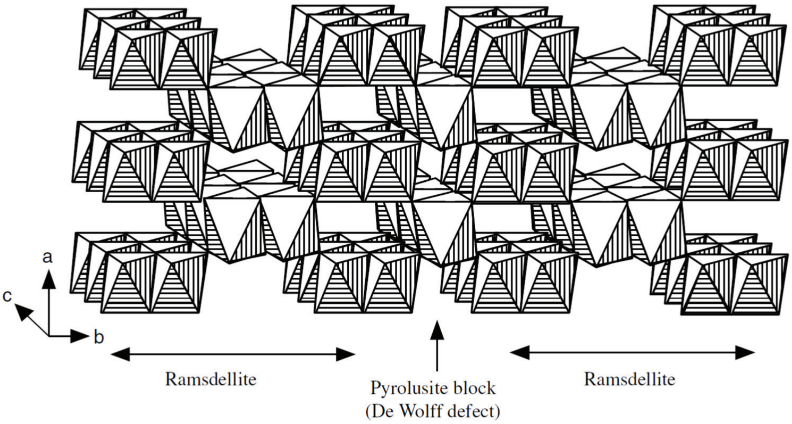

Figure 2.7: "Schematic representation of the nsutite γ-MnO_2 structure showing an intergrowth of pyrolusite and ramsdellite manganese dioxides (de Wolff defect)." Reproduced from [48] with permission from Wiley.

in Figure 2.6. These are often denoted by the size of the tunnel (m x n) formed between the [MnO_6] chains.

When manganese dioxide is formed by electrodeposition from an acidic electrolyte (production of EMD) it is commonly accepted that it forms the γ-MnO_2 (nsutite) crystal structure [45]. γ-MnO_2 is a relatively complex crystal structure which is considered as a ramsdellite matrix with a varying degree of pyrolusite intergrowth, which are also termed de Wolff defects [47]. An illustration of the crystal structure is shown in Figure 2.7 [48]. In addition to the varying degree of pyrolusite intergrowth, Chabre and Pannetier found that microtwinning occurs in γ-MnO_2 in the [021] and [061] planes [45]. Microtwinning was found to be the reason most γ-MnO_2 have poor XRD patterns. For EMDs the degree of pyrolusite intergrowth was found to be relatively constant (around 45 %), whereas the degree of microtwinning was found to be very dependent on the reaction conditions (especially current density and temperature) [45]. However, the γ-MnO_2 structure of EMD has been debated and was rejected by Heuer et al. [49], cited in [50], who found that EMD is multiphase containing ramsdellite, ε-MnO_2 and pyrolusite.

Defect structure. A cation vacancy model for γ-MnO_2 was proposed by Ruetschi [51]. The model explains how the structural water present in γ-MnO_2 (typically 4 %) must be present as OH^- replacing O^{2-} in the lattice (and not as interstitial water). As a consequence, cation vacancies has to be present for charge balance. This leads to the following formula for γ-MnO_2:

$$\mathrm{Mn}^{4+}_{1-x-y} \cdot \mathrm{Mn}^{3+}_{y} \cdot \mathrm{O}^{2-}_{2-4x-y} \cdot (\mathrm{OH})^{-}_{4x+y} \tag{2.13}$$

where x and y denotes the fraction of cation vacancies and Mn^{3+}-ions, respectively. Since the ionic radii of O^{2-} and OH^- are similar the lattice structure does not change noticeably with structural water content. In contrast, reduction (i.e substitution of Mn^{4+} by Mn^{3+}) causes lattice expansion since the ionic radii of Mn^{3+} is larger than that of Mn^{4+}.

The electrical conductivity was also considered in the cation vacancy model. It is expected to involve tunneling to a Mn^{4+} orbital and depends on the average tunneling distance. The average tunneling distance increases both with increasing fractions of vacancies (structural water content) and with an increasing fraction of Mn^{3+} (degree of reduction) in the lattice. Hence, the electrical conductivity is expected to decrease during reduction.

2.3.3 Mechanism of electrochemical deposition and reduction in acidic electrolytes

Oxidation mechanism

The mechanism of manganese dioxide deposition and dissolution in acid electrolytes has been discussed by several authors, and a number of different (and parallel) routes have been suggested [39]. Paul and Cartwright [52–54] demonstrated that during the formation of MnO_2, a relatively stable and poorly conducting intermediate is formed on the outer surface of the growing deposit. They argued that the rate of deposition is limited by the diffusion of manganese ions through this intermediate to oxidize it to MnO_2. Similarly, an ECE mechanism involving the formation of MnOOH was suggested by Petitpierre et al. [55]:

$$\mathrm{Mn}^{2+} \longrightarrow \mathrm{Mn}^{3+} + e^- \tag{2.14}$$

$$\mathrm{Mn}^{3+} + 2\,\mathrm{H_2O} \longrightarrow \mathrm{MnOOH} + 3\,\mathrm{H}^+ \tag{2.15}$$

$$\mathrm{MnOOH} \longrightarrow \mathrm{MnO_2} + \mathrm{H}^+ + e^- \tag{2.16}$$

The same authors also suggested that at high temperatures the Mn^{3+} could disproportionate and form MnO_2 in the bulk of the electrolyte according to reactions (2.17) and (2.18), as observed by Welsh [12].

$$2\,Mn^{3+} \longrightarrow Mn^{2+} + Mn^{4+} \tag{2.17}$$

$$Mn^{4+} + 2\,H_2O \longrightarrow MnO_2 + 4\,H^+ \tag{2.18}$$

The mechanisms of formation and reduction is dependent on the pH, the concentration of manganese in the solution and the temperature [56]. The Mn^{3+}-ion has an enhanced stability at low pH [57]. The oxidation mechanism of Mn^{2+} has thus been suggested to involve a competition between the two pathways presented above [58]: the hydrolysis mechanism involving a Mn(III) intermediate such as MnOOH given by Eqs. (2.14) - (2.16) which is favored at high pH, and the disproportionation mechanism given by Eqs. (2.14), (2.17) and (2.18) at low pH. While many authors have suggested MnOOH as the Mn(III) intermediate [55, 56, 59–61], its exact chemical nature has yet to be determined.

Dupont and Donne [61] used EQCM and found that the increase in mass when oxidizing Mn^{2+} in an acidic electrolyte was an intermediate between those expected from MnOOH and MnO_2 formation (based on the charge). This demonstrates that a Mn(III) intermediate is formed during deposition. However, in their work only one deposition potential (1.3 V vs. SCE) was applied.

In general, comparing literature results is difficult as manganese oxide is used or found in various contexts such as battery material, anode scale in electrowinning and oxygen evolution catalyst in water electrolysis. An overview of selected relevant literature using various deposition conditions and techniques for studying manganese oxide formation and/or reduction is provided in Table 2.1.

Nucleation and growth. A brief introduction to nucleation and growth mechanisms in general is presented in section 3.3, while this section focuses only on nucleation mechanisms of MnO_2 in acidic environments presented in existing literature.

The nucleation and growth of MnO_2 on Pt bulk electrodes at low anode overpotentials was first studied by Fleischmann et al. [66] and more recently by Gibson et al. [79] and Zhang et al. [80] Independent of Mn^{2+} ion

Table 2.1: Conditions and techniques used to study manganese oxide deposition and reduction in selected literature.

Authors	**Year**	**WE**	**Electrolyte concentrations**				**Temp.**	**Main techniques**	**Ref.**
			H_2SO_4		$MnSO_4$		°C		
Bodoardo	1994	Pt	0.5 ++	$\mathrm{mol\,L^{-1}}$	0 & 0.5	$\mathrm{mol\,L^{-1}}$	RT & 90	CV, LSV	[62]
Chotkowski	2011	RVC	0.5 - 2	$\mathrm{mol\,L^{-1}}$	0.5	$\mathrm{mol\,L^{-1}}$	25	CV, SEM, FT-IR	[63]
Clark	2006	Pt	0.1 - 5	$\mathrm{mol\,L^{-1}}$	0.1 - 1	$\mathrm{mol\,L^{-1}}$	RT - 98	RDE, RRDE, SV	[58]
Cross	2013	Pt	0.001-0.1	$\mathrm{mol\,L^{-1}}$	0.001-0.1	$\mathrm{mol\,L^{-1}}$	RT	EQCM, RRDE, ICP-OES	[64]
Devaraj	2009	Au	0 & 0.1	$\mathrm{mol\,L^{-1}}$	0.005	$\mathrm{mol\,L^{-1}}$	20	EQCM, CV	[65]
Dupont	2014	Pt	0.1	$\mathrm{mol\,L^{-1}}$	0.01	$\mathrm{mol\,L^{-1}}$	22	LSV, CA, EQCM, TEM, AFM	[61]
Fleischmann	1962	Pt	0.0025-0.25	$\mathrm{mol\,L^{-1}}$	0.001 - 0.1	$\mathrm{mol\,L^{-1}}$		CA	[66]
Gibson	2016	Pt	0 & 0.1	$\mathrm{mol\,L^{-1}}$	0.1	$\mathrm{mol\,L^{-1}}$	22	LSV, CA, RRDE, XAS	[67]
Kao	1992	Pt	0.5	$\mathrm{mol\,L^{-1}}$	0.01, 0.1	$\mathrm{mol\,L^{-1}}$	80 - 95	CV, CV-Hold, RRDE, CA	[60]
Lee, Maskell and Tye	1977-1986	Pt, Au, GC	0.0125-7.5	$\mathrm{mol\,L^{-1}}$	0	$\mathrm{mol\,L^{-1}}$	25 (90)	LSV, SEM, XRD	[68–70]
Moats	2010	DSA	150 - 200	$\mathrm{g\,L^{-1}}$	10 -150	$\mathrm{mg\,L^{-1}}$	40	SEM/EDS, XRF	[71]
Nijjer	2000	Pt, DSA	0.5 - 6	$\mathrm{mol\,L^{-1}}$	1 -40	$\mathrm{g\,L^{-1}}$	35 (21)	CV, LSV, SEM	[72]
Owen	2007	Au	0 - 1	$\mathrm{mol\,L^{-1}}$	0.1 & 1	$\mathrm{mol\,L^{-1}}$	22	Chronopot, EQCM	[73]
Pajunen	2003	Pb, DSA	160	$\mathrm{g\,L^{-1}}$	0 - 10	$\mathrm{g\,L^{-1}}$		LSV, Galvanostatic	[74]
Paul and Cartwright	1980-1986	GC	0.1	$\mathrm{mol\,L^{-1}}$	0.1 & 1	$\mathrm{mol\,L^{-1}}$	40, 70	EIS, CA, RRDE	[52–54]
Petitpierre	1990	Pt	10 - 88	%	0.02 - 0.5	$\mathrm{mol\,L^{-1}}$	10 - 85	CV	[55]
Pilla	2004	GC	0.5	$\mathrm{mol\,L^{-1}}$	0.1	$\mathrm{mol\,L^{-1}}$	RT	CV, RDE	[75]
Rodrigues	1998	Pt	0.1 - 2	$\mathrm{mol\,L^{-1}}$	0.01 - 1.5	$\mathrm{mol\,L^{-1}}$	80	CV	[76]
Rogulski	2003	Au	0.5 - 4	$\mathrm{mol\,L^{-1}}$	0.05 - 5	$\mathrm{mol\,L^{-1}}$	25	CV (RDE), SEM	[59]
Zhang	2016	DSA, Pb	180	$\mathrm{g\,L^{-1}}$	8	$\mathrm{g\,L^{-1}}$	38	OCP, CV, SEM	[77]
Yu	2002	Pb (alloyed)	180	$\mathrm{g\,L^{-1}}$	0 - 20	$\mathrm{g\,L^{-1}}$	35	CV, EIS, SEM	[78]

concentration, they all describe MnO_2 deposition on Pt via a progressive nucleation and growth mechanism at low anodic overpotentials, based on the shape of current transients from potential step measurements. Furthermore, Dupont and Donne [61] and Fleischmann et al. [66] found MnO_2 nuclei of different sizes on Pt in AFM-images and SEM-images of the surface, respectively. Interestingly, Fleischmann also found that the nucleation process required some time at a higher potential before the current transient for growth at a lower potential was affected (more than 10 ms at 1.38 V vs. NHE in $0.1\,\mathrm{mol\,L^{-1}}$ $MnSO_4$ + $0.25\,\mathrm{mol\,L^{-1}}$ H_2SO_4 + $0.9\,\mathrm{mol\,L^{-1}}$ Na_2SO_4). Correspondingly, Dupont and Donne found with EQCM that no mass was deposited during the initial stages of Mn^{2+} oxidation indicating that only reaction (2.14) is occurring initially (i.e. initial delay).

Zhang et al. [80] also evaluated the nucleation mechanism at a lead alloy in $0.1\,\mathrm{mol\,L^{-1}}$ H_2SO_4 + $30\,\mathrm{g\,L^{-1}}$ Mn^{2+} at 1.28 and 1.30 V vs. MSE, but did not reach any solid conclusion regarding the nucleation mechanism in these experiments, though they argued for a progressive nucleation mechanism. The nucleation mechanism of MnO_2 has also been investigated on a titanium electrode [81]. Several different nucleation mechanisms were found (progressive or instantaneous nucleation, 2D or 3D growth, diffusion control or kinetic control) depending on the concentration of H_2SO_4, temperature and electrode potential. Hence, it is clear that the nucleation mechanism depends very much on the deposition conditions.

Reduction mechanism

The reduction of electrodeposited MnO_2 was studied by Lee et al. and Maskell [68–70] in sulphuric acid on various substrates. They found that the reduction proceeds in two reduction peaks at all substrates. In addition, a third reduction peak appeared on glassy carbon electrodes at high acid concentrations. The first peak was found to be independent on electrode material, whereas the second peak depended very much on the electrode material. A mechanism was proposed for the first reduction peak:

$$\mathrm{MnO_2 + H^+ + e^- \longrightarrow MnOOH} \tag{2.19}$$

$$\mathrm{2\,MnOOH + 2\,H^+ \longrightarrow MnO_2 + Mn^{2+} + 2\,H_2O} \tag{2.20}$$

After the first peak, the crystal structure was found to be unaltered, whereas the conductivity had decreased. The decrease in conductivity was explained by an increase in contact resistance resulting from a volume reduction caused by the reaction. They also suggested that a blocking Schottky-type barrier was formed at the interface between the semiconducting MnO_2 and the substrate. Hence, a larger overpotential is required for the continued reduction resulting in the second peak. The Schottky barrier could also account for the difference in the position of the second peak on different substrates, since the barrier height depends on the work function of the substrate.

Moreover, Ruetschi [82] proposed a mechanism for reduction of MnO_2 in strongly acidic solutions based on his cation vacancy model (sec. 2.3.2). This mechanism is essentially the same as the mechanism proposed by Lee et al. [68] (Eqs. (2.19) and (2.20)), but written in terms of the cation vacancy model. Hence, the reduction involves insertion of protons according to Eq. (2.21), followed by disproportionation (Eq. (2.22)):

$$[\mathrm{Mn}^{4+}_{1-x} \cdot \mathrm{O}^{2-}_{2-4x} \cdot (\mathrm{OH})^{-}_{4x}](\mathrm{c}) + \mathrm{yH}^{+}(\mathrm{aq}) + \mathrm{ye}^{-} \longrightarrow [\mathrm{Mn}^{4+}_{1-x-y} \cdot \mathrm{Mn}^{3+}_{y} \cdot \mathrm{O}^{2-}_{2-4x-y} \cdot (\mathrm{OH})^{-}_{4x+y}](\mathrm{c}) \tag{2.21}$$

$$2\,\mathrm{Mn}^{3+}(\mathrm{c}) + 2\,\mathrm{OH}^{-}(\mathrm{c}) + 2\,\mathrm{H}^{+}(\mathrm{aq}) \longrightarrow \mathrm{Mn}^{4+}(\mathrm{c}) + \mathrm{Mn}^{2+}(\mathrm{aq}) + 2\,\mathrm{H_2O}(\mathrm{aq}) \tag{2.22}$$

where (c) and (aq) denote the crystalline and aqueous phase, respectively. Ruetschi also pointed out that a special case exists when Mn^{2+} is present in an electrolyte, since Mn^{2+} from the electrolyte can comproportionate with Mn^{4+} in the crystalline phase (Eq. (2.23)) and thus resulting in an overall decrease in the oxidation state of the deposit.

$$\mathrm{Mn}^{4+}(\mathrm{c}) + \mathrm{Mn}^{2+}(\mathrm{aq}) + 2\,\mathrm{H_2O}(\mathrm{aq}) \longrightarrow 2\,\mathrm{Mn}^{3+}(\mathrm{c}) + 2\,\mathrm{OH}^{-}(\mathrm{c}) + 2\,\mathrm{H}^{+}(\mathrm{aq}) \tag{2.23}$$

However, at room temperature this is only expected to occur at the surface of the deposit since diffusion of cations (and cation vacancies) within the deposit is extremely slow.

Bodoardo et al. [62] suggested that a thin, poorly conducting layer is formed at the MnO_2 surface during the first reduction peak. The oxidation state of the surface layer corresponds to MnOOH. After the first reduction peak, the reduction proceeds at a limiting current until a potential is reached where the surface layer is reduced. Similarly, Nijjer et al. [56] also suggested that an insulating layer is formed during the first reduction peak. However, they suggested that it forms at the substrate/deposit interface rather than at the surface of the deposit.

In addition, several other possible reactions have been suggested for the reduction of MnO_2 in acid, either in parallel with or following the reaction (2.19) [70, 76, 83]:

$$MnOOH + 3\,H^+ + e^- \longrightarrow Mn^{2+} + 2\,H_2O \tag{2.24}$$

$$MnOOH + 3\,H^+ \longrightarrow Mn^{3+} + 2\,H_2O \tag{2.25}$$

$$\frac{1}{2}\,MnO_2 + \frac{1}{2}\,Mn^{2+} + 2\,H^+ \longrightarrow Mn^{3+} + H_2O \tag{2.26}$$

$$Mn^{3+} + e^- \longrightarrow Mn^{2+} \tag{2.27}$$

2.3.4 Raman Spectroscopy

An introduction to Raman spectroscopy is presented in section 3.2, whereas this section only concerns Raman spectroscopy of manganese oxides.

The study of manganese dioxides by Raman spectroscopy can be challenging. Manganese dioxides are less Raman active than expected [48, 84] and there are some discrepancies regarding their Raman spectra in the literature. Some authors found MnO_2 not to be Raman active [85, 86], whereas others found distinct spectra [46, 84, 87–89]. As mentioned above, MnO_2 exists in a range of crystal structures potentially containing a significant amount of defects. The different polymorphs exhibit different Raman spectra, and even within a singel crystal structure impurities or structural disorders may give rise to different Raman spectra. This was illustrated by Gao et al. who compared Raman spectra of β-MnO_2 obtained by different authors [84]. Another issue when examining manganese oxides by Raman spectroscopy is their thermal instability at the point of laser impact. Manganese dioxides are reduced to Mn_2O_3 and eventually to Mn_3O_4 with increasing laser power [46, 87, 88, 90]. Hence, the applicable laser power is quite limited and consequently the signal-to-noise ratio can be relatively poor. In the following, Raman spectra of some of the MnO_2 polymorphs most relevant for this work will be presented, as well as spectra of Mn_2O_3, Mn_3O_4 and MnOOH.

The Raman spectra of pyrolusite and ramsdellite are shown in Figure 2.8 [46]. The authors investigated the Raman spectra of periodic MnO_2 structures and found that the position of the peaks depends mainly on the number of

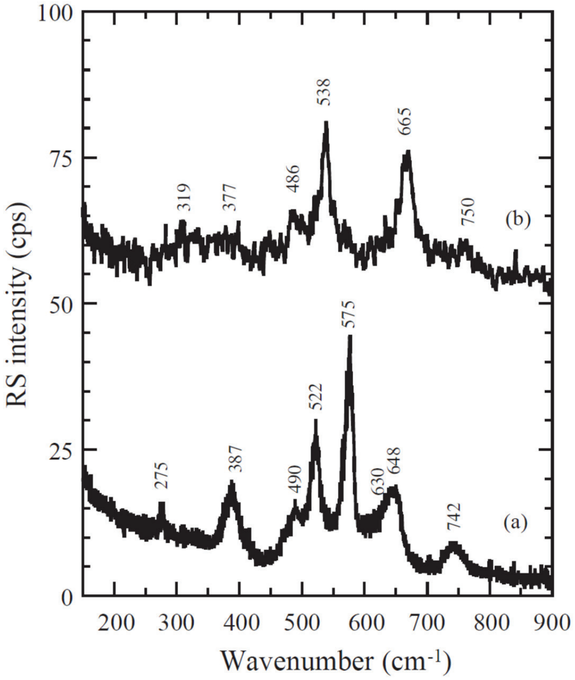

Figure 2.8: "Raman scattering spectra of: (a) ramsdellite R–MnO_2 and (b) pyrolusite β-MnO_2 samples." Reproduced from [46] with permission from Elsevier.

edges shared between the [MnO_6] octahedra as well as the degree of distortion of the octahedra. The oxidation state of Mn was found to be of less importance. In ramsdellite the octahedra share four edges and in pyrolusite they share two edges (Fig. 2.6). Accordingly, the most intense Raman peaks of pyrolusite occur at higher wavenumbers than those of ramsdellite.

As described previously, γ-MnO_2 is considered as a ramsdellite matrix with a certain degree of pyrolusite intergrowth, which can be stated as a percentage (Pr%). The Raman spectra of two γ-MnO_2 samples with different Pr values are shown in Figure 2.9 [48]. Similar Raman spectra of γ-MnO_2 have also been obtained more recently by different authors [91, 92]. Julien et al. found that the peak positions vary with the amount of pyrolusite intergrowth into the ramsdellite matrix, see Figure 2.10 [48]. The middle peak at approximately 575 cm^{-1} was found to be independent of Pr, whereas the peaks to each of its sides showed a dependence on the amount of pyrolusite intergrowth. Thus, Raman spectroscopy can be used to determine the amount of pyrolusite present. As described above, the same authors later found that the wavenumbers depend on the number of edges shared for periodic manganese dioxides [46]. While γ-MnO_2 is not a periodic structure, the average number of shared edges decreases as the amount of pyrolusite increases. Thus, the shift in peak position is in accordance with the number of shared edges between the [MnO_6] octahedra also for γ-MnO_2.

Several different Raman spectra of Mn_2O_3 are reported in the literature [46,85,87,88,93]. Julien et al. [46] reported Raman spectra of a commercial α-Mn_2O_3 sample and γ-Mn_2O_3 obtained by partial thermal decomposition of MnO_2, see Fig. 2.11 (a) and (b) respectively. The Raman spectra of a mineralogical α-Mn_2O_3 sample obtained by Bernard et al. [87] (Figure 2.12) do not resemble that of Julien et al., but interestingly resembles those of γ-MnO_2 (Fig. 2.9). Bernard et al. also observed a peak forming at 633 cm^{-1} when a high laser power was used to investigate MnO_2. They suggested that it was due to the formation of a new phase, such as γ-Mn_2O_3, because of the thermal instability of the manganese oxides. This is in accordance with the γ-Mn_2O_3 Raman spectrum obtained by Julien et al. [46]. Buciuman et al. [88] reported a Raman spectrum of α-Mn_2O_3 resembling that of Mn_3O_4 and also attributed it to the formation of Mn_3O_4 during the acquisition of the spectra. Kapteijn et al. [85] reported a Raman spectrum of Mn_2O_3 quite similar to that acquired for α-Mn_2O_3 by Julien et al. [46], whereas White and Keramidas [93] reported a spectrum not resembling any of the other reported spectra. In conclusion, there are quite large discrepancies regarding the Raman spectra of Mn_2O_3.

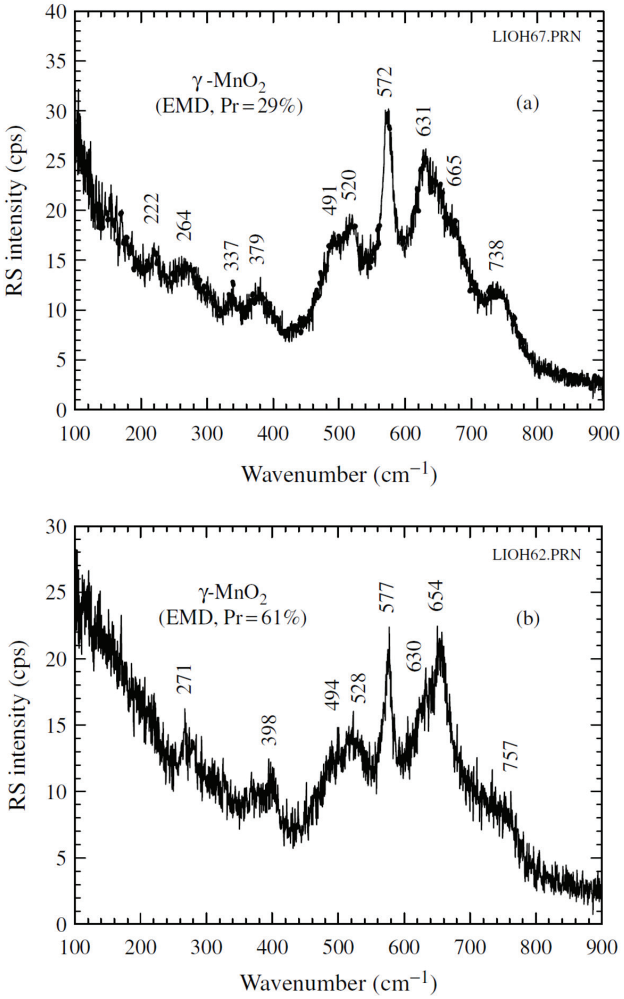

Figure 2.9: "Raman scattering (RS) spectra of γ-MnO_2 with various Pr values of the pyrolusite intergrowth in the ramsdellite matrix: (a) $Pr = 29$ %; (b) $Pr = 61$ %." Reproduced from [48] with permission from Wiley.

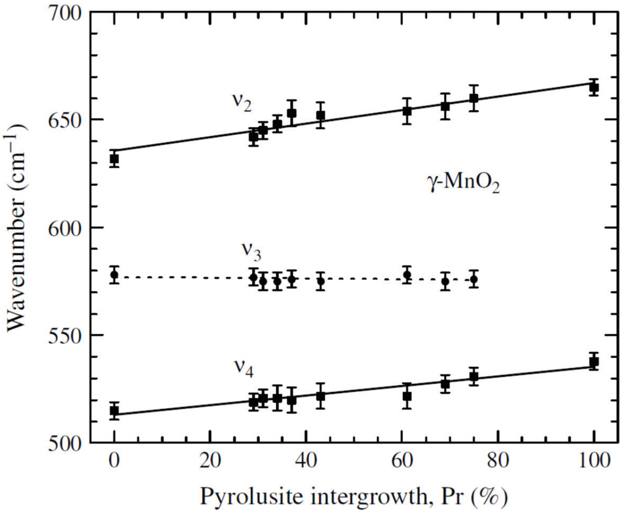

Figure 2.10: "Variation of the Raman band wavenumbers as a function of the value of the structural parameter *Pr* for the pyrolusite intergrowth in γ-MnO_2." Reproduced from [48] with permission from Wiley.

The Raman spectra of MnOOH are displayed in Fig 2.13 (b) and (c) for the α and γ modifications respectively [87]. These are in agreement with the Raman spectra obtained by different authors [46, 94]. The spectrum of Mn_3O_4 is also included in Fig. 2.13 (a) and it is consistent with the Raman spectrum of Mn_3O_4 obtained by other authors [46, 88], see also Fig 2.11 (d). The impact of using a too high laser power is illustrated in Figure 2.13 (d), where γ-MnOOH has been partially transformed to Mn_3O_4 by the heat created by the laser.

Species in the electrolyte can also contribute to the measured Raman spectra. Aqueous sulphate ions are characterized by an intense peak slightly positive of 980 cm^{-1}, in addition to some less intense modes at approximately 450, 620 and 1100 cm^{-1} [95]. Mn^{2+} in solution is present as a hexaaqua complex (i.e. $[Mn(H_2O)_6]^{2+}$). This complex displays a weak band slightly positive of 350 cm^{-1} [95].

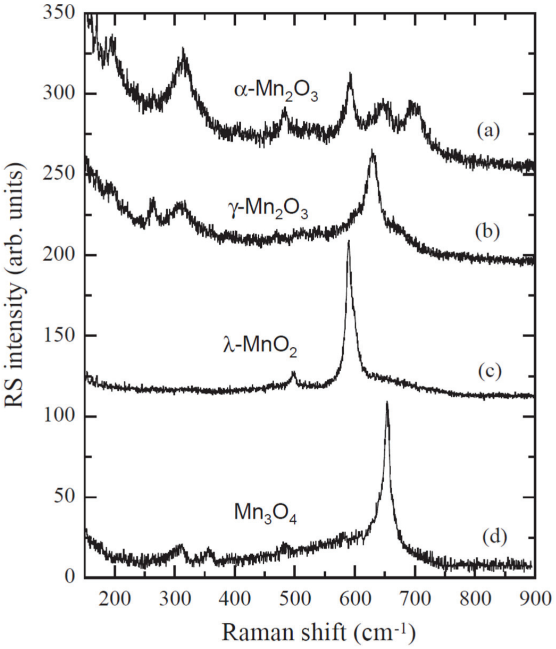

Figure 2.11: "Raman scattering spectra of manganese oxides: (a) bixbyite α-Mn_2O_3, (b) γ-Mn_2O_3, (c) spinel λ-MnO_2, and (d) hausmannite Mn_3O_4." Reproduced from [46] with permission from Elsevier.

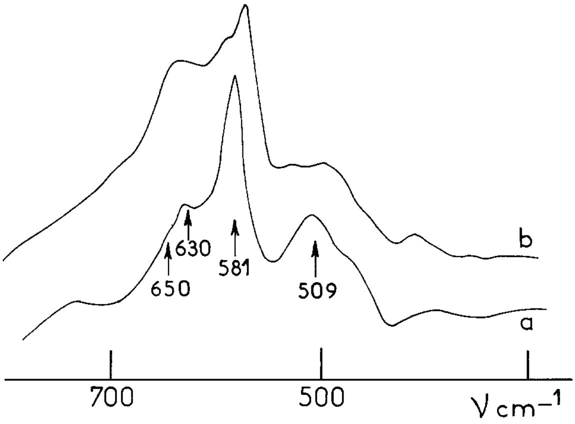

Figure 2.12: "Raman spectra of (a) bixbyite Mn_2O_3, 12.5 mW; (b) id, under water, 20 mW." Reproduced from [87] with permission from The Electrochemical Society.

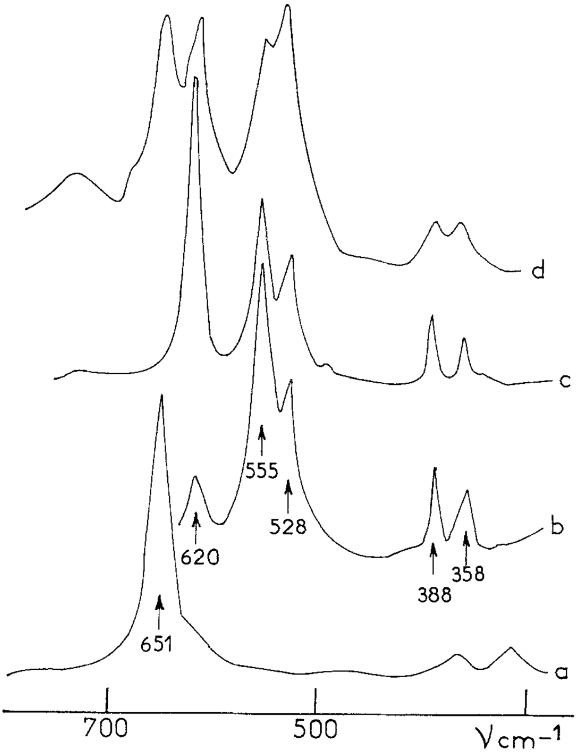

Figure 2.13: "Raman spectra of (a) haussmanite Mn_3O_4; (b) groutite α-MnOOH, 20 mW; (c) manganite γ-MnOOH, 20 mW; and (d) id, 200 mW." Reproduced from [87] with permission from The Electrochemical Society.

Mechanism of manganese oxide deposition/reduction with in-situ Raman spectroscopy

In situ Raman spectroscopy has been employed to study the reduction of MnO_2 in borate medium (pH = 9.2) [87, 96] and in $1\,\mathrm{mol\,L^{-1}}$ KOH [89]. However, in situ Raman spectroscopy has not been employed to investigate the reduction nor the deposition of MnO_2 in acidic medium. The MnO_2 studied in borate medium was electrodeposited at conditions expected to produce γ-MnO_2 (EMD-production, see sec. 2.3.2). Furthermore, the MnO_2 investigated in KOH was electrodeposited from a $MnNO_3$ solution. In borate medium, De Mishma et al. [96] observed no changes to the Raman spectra acquired during reduction up to a point where all MnO_2-related peaks disappeared, whereas Bernard et al. [87] observed some changes in the intensity of the peaks during reduction. Peaks related to MnOOH (Fig. 2.13) was not observed during reduction by either group, nor by Gostola and Weaver [89] during reduction in KOH. However, the latter authors claimed that the appearance of a band at $415\,\mathrm{cm^{-1}}$ was related to MnOOH formation as an intermediate before further reduction to $Mn(OH)_2$.

2.4 Dimensionally Stable Anodes

Dimensionally stable anodes (DSAs, also named mixed metal oxide anodes) were invented by Beer in the 1960's [97, 98]. The invention came to be when Beer discovered that titanium metal did not dissolve anodically, but rather a passivating layer of TiO_2 was formed at the surface. Thus, titanium is ideal as an inert base metal for anodes as it is protected from corrosion during operation by the passive layer. Later, other valve metals have also been considered (Ta, Zr and Nb [99]). The base metal is coated with a metal oxide providing electrical conductivity and electrocatalytic activity towards the desired anodic reaction. Since its discovery, DSAs have gained widespread use in the chlor-alkali industry with a coating consisting of RuO_2 and TiO_2. However, such a coating is not particularly suitable for oxygen evolution in acidic electrolytes, such as in zinc electrowinning, due to the instability of RuO_2 under these conditions [100, 101]. Under the latter conditions, a coating comprised of around 70 % IrO_2 and 30 % Ta_2O_5 is generally regarded to display an optimum in performance and lifetime [1, 102].

DSA electrodes are usually prepared by thermal decomposition. The substrate is first pretreated: degreased, etched and potentially sandblasted. The pretreatment ensures that any preexisting layer of (poorly conducting) TiO_2 is removed. Moreover, it improves the adhesion of the coating by increasing the surface roughness. Subsequently, a precursor solution is applied either by brushing, dipping or spraying. The precursor solution contains salts of the desired metal oxides dissolved in a suitable solvent and is applied in several layers to reach the desired loading. Between each layer and at the end, the electrode is dried (to remove the solvent) and subsequently calcined (to obtain the metal oxides).

The coating composition is important for the lifetime and performance (i.e. electrocatalytic activity and electrochemically active surface area) of DSA anodes. It is frequently comprised of an active component (often IrO_2 or RuO_2) that promotes the electrocatalytic activity and one or more stabilizing components (e.g. Ta_2O_5, TiO_2, SnO_2, ZrO_2 and others) that improves the lifetime of the anode, can promote the dispersion of the active component (i.e. increase the active surface area), and reduces the cost of the coating [1]. As mentioned above, RuO_2 is unstable under the conditions required for OER in acidic electrolytes. Hence, the coatings used in such applications are frequently based on IrO_2 as the active component [103]. It is worth mentioning that the price of iridium has soared in recent years due to an increase in consumption in combination with the very limited amount of iridium produced annually since it is one of the least abundant elements in the earth's crust. Accordingly, the use of iridium should be minimized or even eliminated in future coatings in order for DSA electrodes to be an economically viable alternative to the lead anodes that are typically used for OER in acidic electrolytes today.

The lifetime and performance of the DSA electrodes are affected not only by the choice of coating composition, but also by the various steps in the preparation of the anode [1]. The substrate pretreatment, including the choice of etchant, can have a marked influence on lifetime and electrochemically active surface area of the anodes [99, 104–106]. Furthermore, the quality of the anode is influenced by the choice of solvent, the type of precursor salts (often chloride salts) and their concentration in the solvent, the application technique, the number of layers and the thickness of each layer. Finally, the calcination temperature (and time) is of vital importance both to the performance and lifetime of the anodes. At low calcination temperatures, an amorphous coating of IrO_2-Ta_2O_5 can be obtained that has a larger electrochemically active surface area compared to at higher calcination temperatures [107]. Furthermore, studies have shown that anodic deposition of PbO_2 and MnO_2 from electrolyte species can be suppressed with amorphous IrO_2-Ta_2O_5 electrodes [13,14]. However, a major drawback of employing a low calcination temperature is the decreased lifetime of the resulting anodes [15]. In addition, too low calcination temperatures can result in residual chloride in the coating, thus increasing the resistivity of the coating and resulting in a higher operational voltage. A method for circumventing residual chloride in the coating even at low calcination temperatures has been proposed [108]. On the other hand, at higher calcination temperatures crystal growth and sintering occurs, resulting in a reduction in the electrochemically active surface area [107, 109]. Hence, a compromise between electrocatalytic activity, electrochemically active surface area and lifetime is achieved at intermediate calcination temperatures [110].

The lifetime of DSA electrodes is very important from an industrial perspective, particularly due to the high cost of DSA electrodes compared to lead electrodes that are typically used for OER in acidic solutions today. Consequently, it is important to understand the failure mechanisms of DSA electrodes so that both the coating composition and the preparation procedure can be optimized for improved lifetime of the electrodes. Martelli et al. [111] suggested the following possible failure mechanisms for Ti/IrO_2-Ta_2O_5 electrodes for OER in acidic sulphate-based electrolytes: (a) passivation of the substrate, (b) coating consumption, (c) coating detachment, (d) mechanical damages, and (e) a mixed mechanism. Passivation of the substrate (a) is related to build up of a poorly conducting layer of TiO_2 at the interface between the substrate and the coating, resulting in a sudden increase of the electrode potential. This is strongly related to the employed current density [111]. Passivation of the substrate can to some extent be limited by applying an interlayer between the substrate and the electrocatalytic coating [112, 113]. Coating consumption (b) is caused by steady state corrosion of the active component in the coating. The rate of coating consumption may be accelerated if additives or impurities in the electrolyte (particularly organic compounds) form stable complexes with coating species. Coating consumption is the reason why RuO_2 is rarely used in coatings for OER. Although RuO_2 is more active towards OER than IrO_2 (cf. Fig. 2.3), RuO_2 corrodes more quickly due to formation of RuO_4 that dissolves in the electrolyte [114, 115]. IrO_2 also corrodes, but at a much slower rate than RuO_2 [100, 116]. The corrosion rate of IrO_2 during OER depends on the preparation route and is much higher for amorphous than crystalline IrO_2. The increased dissolution rate of amorphous compared to crystalline (rutile) IrO_2 has been attributed to a difference in OER mechanism where lattice oxygen is involved for amorphous IrO_2 [23, 24], as described in section 2.1.1. Coating detachment (c) can be accelerated by gas evolution that may cause loosely adhering particles at the surface to detach. Pressure from gas bubbles inside coating pores may also cause damages to the coating if OER cannot occur at the surface (covered by impurities/precipitates). Another cause of coating detachment is dissolution of the substrate. The presence of even very low amounts of F^- in the electrolyte (in combination with a cracked or porous coating) greatly increases the risk of this failure mechanism, since Ti forms strong complexes with F^- [117]. Furthermore, studies have shown that recurring current reversals where a metal (e.g. Zn, Sn) is repeatedly deposited at the DSA can have a severe effect on the lifetime of the coating [111, 118]. Overall, the failure mechanisms of DSAs can be complex, but when understood the coating composition and preparation procedure of the electrodes can be tailored for improved lifetime.

Chapter 3

Methods

3.1 Electrochemical Quartz Crystal Microbalance (EQCM)

Electrochemical Quartz Crystal Microbalance (EQCM) is an in-situ gravimetric technique where the change in resonance frequency of a quartz crystal is measured simultaneously with electrochemical signals. The technique derives from quartz crystal microbalance (QCM) technology where mass changes are commonly measured in air or vacuum. The working electrode consists of a quartz disc with an electrode at each side, see Figure 3.1. An alternating voltage is applied between the two electrodes causing thickness shear deformation of the (AT-cut) quartz crystal due to the converse piezoelectric effect. When the crystal is oscillating at its resonance frequency a standing shear acoustic wave is generated as illustrated in the upper part of Fig. 3.1b. The wavelength of the acoustic wave increases when mass is deposited at the electrode as illustrated in the lower part of Fig. 3.1b. Hence, a decrease in frequency is observed when mass is deposited at the electrode, and conversely the frequency increases when the mass decreases.

Under ideal conditions, the change in frequency of a QCM can be related to the mass change of the electrode through the Sauerbrey equation (3.1):

$$\Delta f = \frac{-2f_0^2\Delta m}{A\left(\mu_q\rho_q\right)^{1/2}} = -\mathrm{C_f}\frac{\Delta m}{A} \tag{3.1}$$

where Δf is the measured change in frequency, f_0 the frequency of the

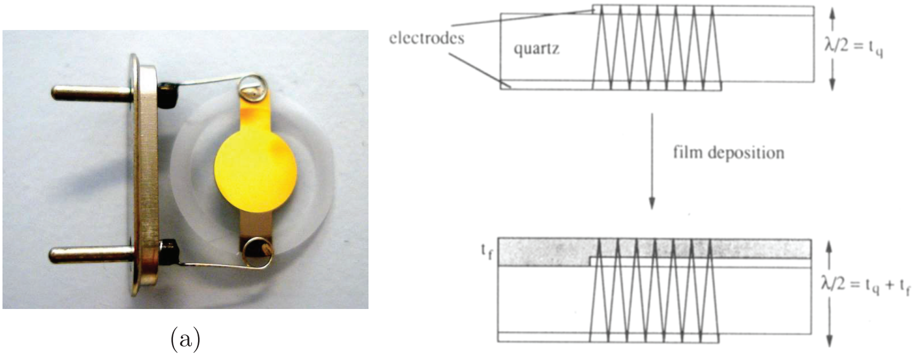

(a)

(b)

Figure 3.1: (a) Picture of a gold EQCM electrode (b) "Schematic representation of the transverse shear wave in a quartz crystal and a composite resonator comprising the quartz crystal and a layer of a foreign material. The acoustic wavelength is longer in the composite resonator due to the greater thickness, resulting in a low resonant frequency compared to the quartz crystal." Reprinted with permission from [119]. Copyright 1992 American Chemical Society.

quartz crystal prior to mass change, Δm the mass change, A the piezoelectric active area, C_f the sensitivity factor (Sauerbrey coefficient), ρ_q the density and μ_q the shear modulus of quartz. For the Sauerbrey equation to be valid several conditions have to be met; the deposited mass must be rigid, uniformly distributed and not too large compared to the mass of the crystal (within 2 % of the crystal mass is considered to be accurate [119]). Furthermore, there should be no slip between the quartz and the foreign material. Moreover, the Sauerbrey equation does not take into account the interaction with liquid in contact with the crystal, which is a prerequisite for EQCM. Hence, it is common practice to calibrate the EQCM with a well defined deposition reaction such as copper metal deposition to find a more suitable value for the sensitivity factor (C_f).

Even after calibrating the crystal there are several factors (other than the mass of the deposit) that may influence the measured frequency signal [119]. Some fraction of the liquid at the interface is expected to contribute to the measured frequency. Consequently, liquid trapped in pores or at the surface of a film with high roughness may give rise to a larger frequency shift than expected. Additionally, adsorption and desorption of electrolyte species at the surface may be observed with EQCM. Furthermore, too high mass loadings causes the sensitivity to decrease resulting in less frequency change than expected. Also, if the mass distribution is not uniform this may lead to erroneous interpretation of the results as the sensitivity of the crystal varies radially. In addition, there are even more factors that may influence the frequency signal, such as viscoelastic effects, internal stresses in the crystal due to the column of liquid, temperature variations and others. Hence, it is important to keep in mind that other factors than the deposited mass may contribute to the measured frequency shift.

The mass change obtained from EQCM can be compared with the measured current when considering Faraday's law as shown in Eq. (3.2):

$$\frac{\mathrm{d}\Delta m_{\mathrm{EQCM}}}{\mathrm{d}t} = \frac{\mathrm{d}}{\mathrm{d}t}\left(\frac{\int I\mathrm{d}t}{nF}M\right) = \frac{M}{nF}I \tag{3.2}$$

Thus, the time derivative of the mass change ($\mathrm{d}\Delta m/\mathrm{d}t$) is proportional to the measured current (I) assuming a constant number of electrons transferred (n), a constant molar mass of the deposit (M) and that the measured frequency change is governed solely by the electrodeposited species.

3.2 Raman Spectroscopy

Raman spectroscopy is a type of vibrational spectroscopy that relies on inelastic scattering of photons. It is frequently used to determine the structure of a sample by a "fingerprint" method based on reference spectra, but can also provide more detailed information about the sample (e.g. about chemical bonds and the coordination of atoms). It probes the local rather than long range structure. Raman spectroscopy is quite suitable for in-situ measurements as gas phases usually have negligible scattering, and the scattering of glass and water is relatively weak (compared to Infrared spectroscopy) [120]. This section will give a brief introduction to the working principle and instrumentation of Raman spectroscopy and also present some limitations of the technique.

Monochromatic light is used to illuminate the sample during Raman spectroscopy. Vibrations in the sample are excited by the incident light to virtual and unstable energy states dependent on the energy of the incident light. When the vibration relaxes a scattered photon is emitted with either lower, equal or higher energy than the incident photon, see Figure 3.2. This is termed Stokes, Rayleigh and anti-Stokes scattering, respectively. Rayleigh

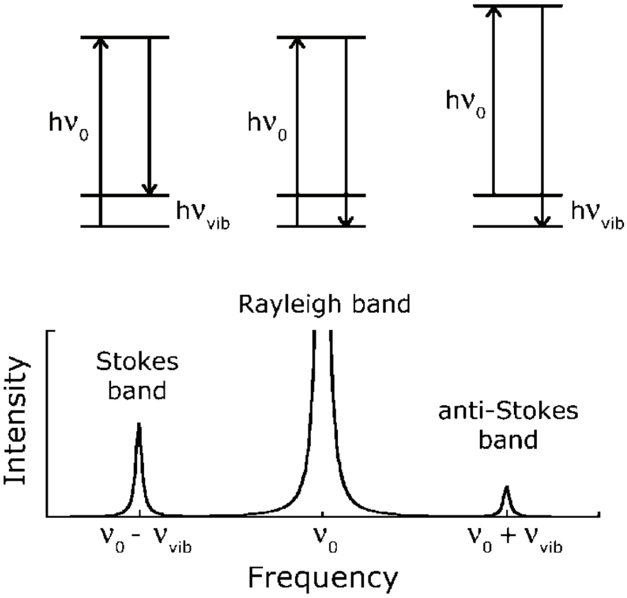

Figure 3.2: Illustration of the different scattering processes that can occur when a sample is illuminated by monochromatic light of frequency ν_0. Energy level diagrams are illustrated at the top and intensity of the affiliated scattering processes at the bottom. Reproduced from [121] with permission from Wiley. The caption is modified and fitted to this thesis.

scattering is elastic (the energy is preserved) and far more frequent than the inelastic Stokes and anti-Stokes scattering events. Furthermore, Anti-Stokes scattering is less frequent than Stokes scattering as it requires that the incident photon excites a vibration that is already excited, and there are less excited vibrations than vibrations at ground state. As mentioned above, Raman spectroscopy depends on inelastic (Stokes and anti-Stokes) scattering where the energy and hence frequency, wavelength and color of the scattered light is different from that of the incident light. Hence, it is necessary to have a good filter that removes the elastically scattered photons that will otherwise dwarf the inelastic scattered photons that are of interest in Raman spectroscopy.

A schematic illustration of a (confocal) Raman spectroscopy set-up is shown in Figure 3.3. The laser emits monochromatic light somewhere in the range of UV to near IR. After being scattered by the sample, the light with the

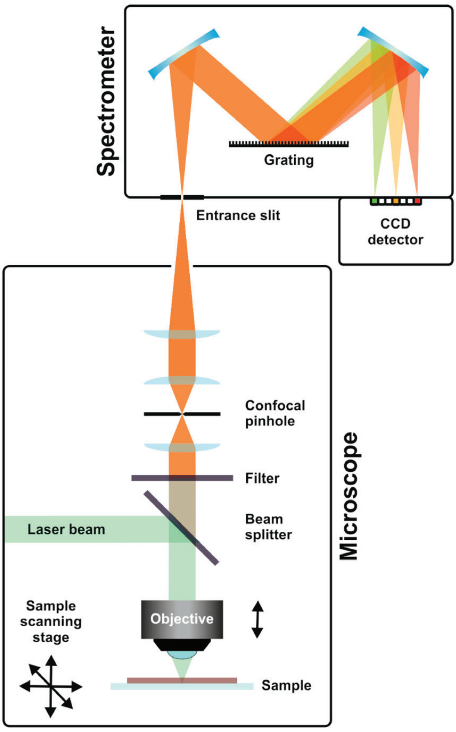

Figure 3.3: Instrumentation of a Raman Microscope. Reprinted from [122] under CC BY 4.0 licence.

same wavelength as the laser beam is removed by a filter (e.g. a notch filter). In confocal Raman microscopes a pinhole limits the depth of field so that the light that passes through to the spectrometer mainly originates from the part of the sample that is in focus. In the spectrometer a grating splits the light in different directions depending on the wavelength before the light is detected by for instance a charge coupled device (CCD).

A vibration can only be detected by Raman spectroscopy if there is a change in the polarizability of the molecule during the vibration. Furthermore, some bands may have too weak intensity to be discernible from the spectral background even though they are Raman active. Hence, it is not possible to observe all substances (or vibrations) nor to definitely exclude the presence of a (Raman active) substance. For instance, metals are either Raman inactive or hard to detect depending on their crystal structure. It is also important to note that a change in the intensity of a Raman peak is not necessarily proportional to a change in the concentration of the corresponding species, but may be affected by material properties. Thus, most attention is usually paid to the position of a band (its frequency) rather than its intensity. Vibrations between metal and oxygen atoms within a lattice are typically found in the range of a few hundred to 1000 cm^{-1} [121].

As mentioned above, the intensity of Raman scattered photons is quite low. Increasing the laser power can increase the intensity of the signal, but it also creates heat. Thermally unstable samples may change their structure during acquisition of a spectrum because of reduction, decomposition, phase transition or other processes. Another issue is that some samples exhibit fluorescence that may cause Raman peaks to be indiscernible from the spectral background.

3.3 Determination of nucleation mechanism

During the initial stages of electrochemical phase formation small nuclei form at the surface. The formation rate of these nuclei is dependent on the overpotential and two limiting cases exist: instantaneous and progressive nucleation. When the nucleation is instantaneous, nuclei immediately form at all available sites at the start of nucleation. On the other hand, the number of nuclei increases with time when the nucleation is progressive. Both cases are illustrated in Figure 3.4.

In a potential step involving the formation of a new (electroactive) phase,

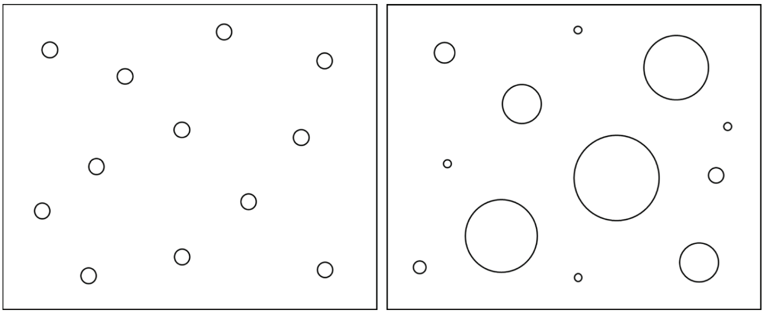

(a) Instantaneous nucleation. (b) Progressive nucleation.

Figure 3.4: Illustrations of instantaneous and progressive nucleation.

the current will initially increase due to the increase in available surface area. Since the number of nuclei at a certain time depends on the type of nucleation (progressive or instantaneous), so does the shape of the current transient. The current expected at short times from instantaneous and progressive nucleation of hemispherical nuclei under diffusion control is given by Eqs. (3.3) and (3.4), respectively [123]:

$$i = \frac{NnF\pi(2Dc)^{3/2}M^{1/2}}{\rho^{1/2}}t^{1/2} \tag{3.3}$$

$$i = \frac{2ANnF\pi(2Dc)^{3/2}M^{1/2}}{3\rho^{1/2}}t^{3/2} \tag{3.4}$$

where A is the first order nucleation rate constant, N the number density of active sites, D the diffusion coefficient, c the bulk concentration, M is the molar mass and ρ the density of the deposited material.

As explained above, the current in a potential step initially increases due to the increase in surface area. However, as the nuclei grow their diffusion zones start to overlap. The current will then pass through a maximum before approaching that expected from linear diffusion to a planar surface (given by the Cottrell equation), assuming that the reaction is diffusion controlled. Dimensionless equations have been derived based on the maximum in the current transient expected for hemispherical nuclei formed under diffusion control [123]. These are given in Eqs. (3.5) and (3.6) for instantaneous and progressive nucleation, respectively:

$$\frac{i^2}{i_m^2} = \frac{1.9542}{t/t_m}\Big\{1 - \exp\big[-1.2564(t/t_m)\big]\Big\}^2 \tag{3.5}$$

$$\frac{i^2}{i_m^2} = \frac{1.2254}{t/t_m}\Big\{1 - \exp\big[-2.3367(t/t_m)^2\big]\Big\}^2 \tag{3.6}$$

where i_m and t_m are the current and time corresponding to the maximum in the current transient, respectively. These equation are plotted in a dimensionless plot in Figure 3.5. Experimental data can be compared to these curves in order to evaluate the nucleation mechanism.

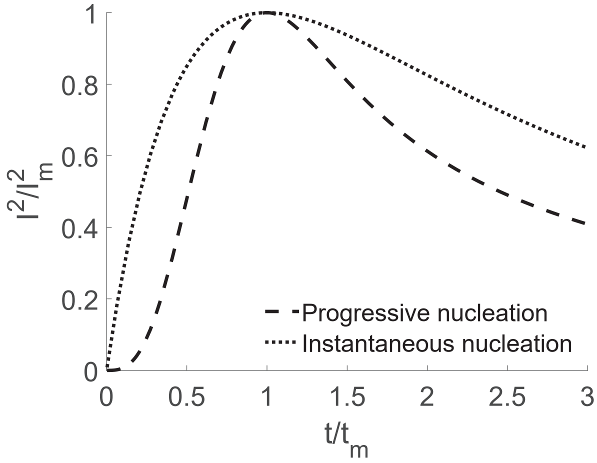

Figure 3.5: Theoretical dimensionless plots for instantaneous and progressive nucleation.

3.4 Charge normalisation of IrO_2 electrodes

Cyclic voltammograms of IrO_2 electrodes (Fig. 3.6) display quite broad peaks in the potential range between oxygen evolution and hydrogen evolution. These peaks are related to a change in the oxidation state of iridium with an associated intercalation of H^+, as illustrated by Eq. (3.7). Similar behavior is also observed in RuO_2 electrodes.

$$\mathrm{IrO_x(OH)_y} + \delta\,\mathrm{H}^+ + \delta\,\mathrm{e}^- \rightleftharpoons \mathrm{IrO_{x-\delta}(OH)_{y+\delta}} \tag{3.7}$$

A method for monitoring the electrochemically active surface area based on the peaks in the voltammogram has been developed for RuO_2 electrodes [124], and has also been applied to IrO_2 electrodes [109, 125]. The method is based on obtaining the voltammetric charge (q^*) in the oxide region (e.g. between 0.4 V and 1.4 V) in CVs obtained at different sweep rates. At very fast sweep rates only the more accessible parts of the surface is thought to contribute to reaction (3.7). In contrast, at slow sweep rates also less accessible parts of the surface (pores, cracks, etc) contribute to the voltammetric charge. The voltammetric charge (q^*) obtained at different sweep rates is used to find the outer or surface charge (q_s^*) related to the more accessible surface regions, the inner charge (q_i^*) related to the less

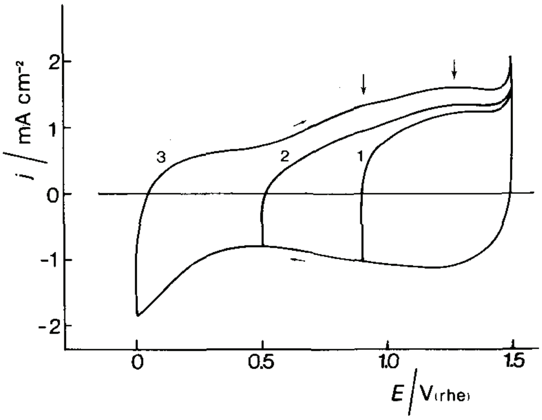

Figure 3.6: "Typical voltammogram of an IrO_2 electrode, prepared at 400 °C, in 0.5 mol dm^{-3} H_2SO_4 solution. Effect of the cathodic scan limit: (1) 0.9 V; (2) 0.5 V; (3) 0.0 V (RHE). Anodic scan limit, 1.5 V (RHE). 25 °C, 20 mV s^{-1}." Reproduced from [109] with permission from Elsevier.

accessible surface regions and the total charge (q^*_{tot}) being the sum of the inner and outer charge:

$$q^*_{tot} = q^*_s + q^*_i \tag{3.8}$$

The total charge is found when extrapolating to zero sweep rate (ν) in a plot of $1/q^*$ vs $\nu^{0.5}$, whereas the outer surface (q^*_s) and is found by extrapolating to infinite sweep rate (ν) in a plot of q^* vs $\nu^{-0.5}$.

In order to make comparisons between different electrodes, it is possible to normalise the current by the outer charge (q^*_s). This allows for comparisons between the activity of electrodes prepared in different ways or between electrodes with different active surface areas or catalyst loadings.

Chapter 4

Experimental

4.1 Synthesis of electrode materials

4.1.1 Dimensionally Stable Anodes (DSA)

Dimensionally stable IrO_2-Ta_2O_5/Ti anodes were prepared by thermal decomposition as outlined in Figure 4.1.

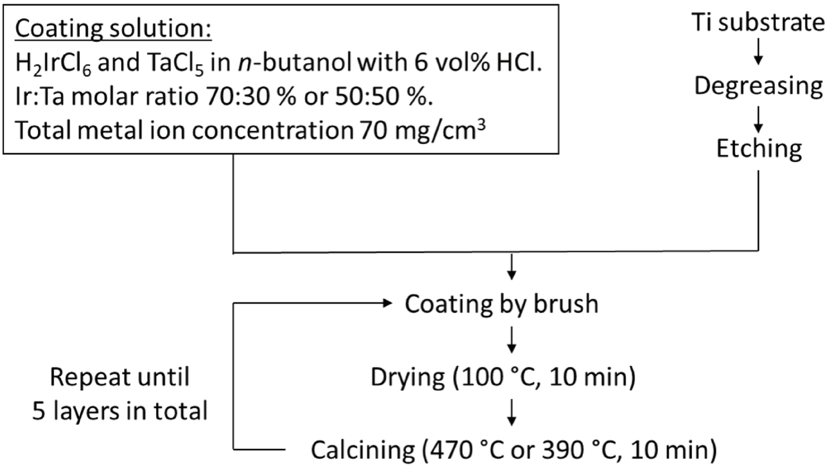

Figure 4.1: Procedure for preparing DSA electrodes.

The titanium substrate (10 cm x 10 cm) was degreased by applying detergent and rinsing with copious amounts of water, before rinsing with acetone and finally isopropanol. The substrate was then etched by boiling for 20 minutes in a solution of 50:50 vol% deionized water and concentrated HCl (37 %).

The precursor solutions were prepared by weighing appropriate amounts of $H_2IrCl_6 \cdot xH_2O$ (Alfa Aesar, 99 %)) and $TaCl_5$ (Alfa Aesar, Puratronic, 99.99 %)) before adding *n*-butanol (Alfa Aesar, 99 %) and 6 vol% HCl (Honeywell Fluka, puriss pa., fuming $\geq$ 37 %). Two different compositions were prepared: one with a molar ratio of 70:30 % Ir:Ta and the other with 50:50 % Ir:Ta. The total metal ion concentration was kept at $70\,\mathrm{mg\,cm^{-3}}$ for both solutions. The precursor solutions were stirred overnight.

The precursor solution was applied to the surface by hand brushing. To control the amount deposited in each layer, 150 µL of the precursor solution was pipetted onto the pretreated titanium substrate before brushing. This was followed by drying for 10 min at 100 °C in a drying cabinet and calcination for 10 min at 470 °C or 390 °C in a Heraeus furnace for the compositions 70:30 mol% and 50:50 mol% Ir:Ta respectively. The latter calcination temperature (390 °C) was chosen based on TGA measurements (Netzsch STA 449C) to ensure that the temperature was set above the phase transition from precursor to oxide. These steps were repeated so that the total number of layers were five for each electrode, giving a theoretical loading of $0.6\,\mathrm{mg\,cm^{-2}}$. The electrodes were calcined at low temperature (390 °C, 50:50 mol% Ir:Ta) and high temperature (470 °C, 70:30 mol% Ir:Ta) will be referred to as amorphous and crystalline DSAs, respectively.

Electrodes for testing the impact of chloride

Some experiments were performed with an early version of the crystalline DSA electrode. These were only used in the experiments where the effect of chloride on manganese oxide deposition was investigated (see the end of section 4.3.1). The preparation procedure for these electrodes differed slightly from that described above. The substrate was a titanium disc of diameter 1.48 cm. Two layers of coating were applied without controlling the amount of precursor solution in each layer. The measured weight gain of the electrode corresponded to a mass change of $0.4\,\mathrm{mg\,cm^{-2}}$. Like for the crystalline DSAs described above, the electrode was dried for 10 min at 100 °C and calcination for 10 min at 470 °C. However, the calcination was performed in a tubular furnace with a flow of synthetic air. Otherwise the synthesis was as described above.

4.1.2 IrO_2 powder preparation

The hydrolysis synthesis route was used to prepare iridium oxide powder. A 0.25 mol L^{-1} solution of NaOH (Merck, EMSURE) was prepared in a conical flask (polypropylene) and heated to 80 °C under continuous stirring. The metal precursor, $H_2IrCl_6 \cdot xH_2O$ (Alfa Aesar, 99 %)), was dissolved in Milli-Q water (Millipore, $\rho > 18\,\mathrm{M\Omega\,cm}$, TOC $< 10\,\mathrm{ppb}$) and added to the hot NaOH solution so that the final metal ion concentration was 0.01 mol L^{-1} and the final NaOH concentration 0.2 mol L^{-1}. This solution was heated at 80 °C for 1 h during which it was continuously stirred. After cooling to room temperature, the pH of the solution was adjusted to 8.0 by addition of 1 mol L^{-1} HNO_3 (Sigma-Aldrich, puriss p.a., ACS reagent). The solution was subsequently reheated and held at 80 °C for 30 min under continuous stirring. The precipitate was separated by centrifugation and washed in Milli-Q water four times. The powder was dried in a heating cabinet at 80 °C and then ground with a mortar an pestle. Finally, the powder was calcined at 600 °C for 30 min in a tubular furnace with a gas flow of synthetic air, cooled and ground again. The iridium oxide powder prepared by the hydrolysis method will be referred to as h-IrO_2 to distinguish it from the iridium oxide on the DSA electrodes.

4.2 Physicochemical Characterization

4.2.1 Scanning Electron Microscopy (SEM) and Energy Dispersive X-Ray Spectroscopy (EDS)

Scanning electron microscopy (SEM) and energy dispersive X-Ray spectroscopy (EDS) was performed with a Hitachi S-3400N SEM equipped with an Oxford Instruments EDS system. The technique was mainly used to study MnO_2 deposited at different conditions on DSAs and Pt. The deposition conditions are described in section 4.3.1. SEM and EDS were also employed to characterize the synthesized electrode materials (DSA electrodes and IrO_2 powder) prepared as described in section 4.1.

SEM images were recorded mainly with an accelerating voltage of 15 kV, whereas EDS spectra were mainly acquired with 25 kV accelerating voltage. The EDS spectra were acquired from the entire area corresponding to 1000x magnification.

Some samples were also studied with a scanning transmission electron microscope (STEM). The instrument was a Hitachi SU9000 equipped with an Oxford Ultim Extreme EDS-system. STEM was used to study an as-prepared crystalline DSA electrode as well as MnO_2 deposits at platinum and crystalline DSA electrodes. The deposition conditions for these samples are given in Table 4.10.

4.2.2 X-Ray Diffraction (XRD)

X-ray diffraction (XRD) was performed with a Bruker D8 A25 DaVinci instrument using Cu K_α radiation. XRD was used to study the synthesised IrO_2 powder as well as the crystalline DSA electrodes (70:30 mol% Ir:Ta calcined at 470 °C) prepared as described in section 4.1.

4.3 Electrochemical Characterization

Four different set-ups were used for electrochemical characterization: a conventional three-electrode cell, an electrochemical quartz crystal microbalance (EQCM) set-up, a rotating disc electrode (RDE) set-up and an in-situ Raman spectroscopy set-up. Each set-up will be described in more detail in the following sections. An Autolab PGSTAT302N potensiostat was used for all the electrochemical measurements in all set-ups. The potensiostat was equipped with an analogue scan generator (SCAN250) that provided true linear scans for sweep rates $10\,\mathrm{mV\,s^{-1}}$ and higher. In addition, the potentsiostat was equipped with the following modules: EQCM, BA, ADC164, DAC164 and FRA2. All measurements were performed at room temperature ($22 \pm 1\,^\circ\mathrm{C}$). An overview of the different electrode materials studied with the different set-ups is given in Table 4.1. A reversible hydrogen electrode (RHE) was used as a reference electrode in all the set-ups, and all potentials are reported versus this electrode. The RHE was a platinum mesh or wire placed inside a glass tube that was sealed in the top. This glass tube was then placed in a glass chamber containing "blank" elec-

Table 4.1: Electrode materials investigated in the different electrochemical set-ups.

Electrode material	**Conventional cell**	**EQCM**	**RDE**	**In-situ Raman S**
Pt	✓	✓	✓	✓
DSA - Crystalline	✓		✓	✓
DSA - Amorphous	✓			
Au		✓		
Ti		✓		
Ti w/IrO_2		✓		

Table 4.2: Electrochemical techniques used in the different set-ups.

Technique	**Conv. cell**	**EQCM**	**RDE**	**In-situ Raman S**
Chronoamperometry	✓	✓	✓	✓
Cyclic voltammetry	✓	✓	✓	
Linear sweep voltammetry	✓			
MnO_2 reduction (LSV)		✓		✓
Combination of techniques	✓	✓		

trolyte of the same concentration as in the the electrolyte in the working electrode compartment (either $0.1\,\mathrm{mol\,L^{-1}}$ or $2\,\mathrm{mol\,L^{-1}}$ H_2SO_4). H_2 gas was produced inside the tube with the Pt mesh providing a stable reference potential. Furthermore, the glass chamber was separated from the working electrode compartment with a ground glass joint, allowing for ionic contact.

Table 4.2 provides an overview of the electrochemical techniques employed with the different set-ups. All techniques were not necessarily performed for all working electrode materials. More details will be provided in the section of each set-up.

Electrolyte

All experiments were conducted in a sulphuric acid electrolyte with a concentration of either $0.10\,\mathrm{mol\,L^{-1}}$ or $2.0\,\mathrm{mol\,L^{-1}}$. The electrolyted was prepared by mixing H_2SO_4 (VWR Chemicals, AnalaR Normapur) with Milli-Q water (Millipore, $\rho > 18\,\mathrm{M\Omega\,cm}$, TOC $< 10\,\mathrm{ppb}$). Na_2SO_4 (Merck, EMSURE, $1.9\,\mathrm{mol\,L^{-1}}$) was in some experiments added to the low concentration sulphuric acid ($0.10\,\mathrm{mol\,L^{-1}}$) to decrease the electrolyte resistance. Manganese ions were added to the electrolyte as $MnSO_4 \cdot H_2O$ (Merck, pro analysi). The concentration of Mn^{2+} was either $5.0 \times 10^{-3}\,\mathrm{mol\,L^{-1}}$ (in combination with $0.10\,\mathrm{mol\,L^{-1}}$ H_2SO_4) or $0.15\,\mathrm{mol\,L^{-1}}$ (mainly in combination with $2.0\,\mathrm{mol\,L^{-1}}$ H_2SO_4). One experiment was also conducted with 100 ppm Cl^- in $0.10\,\mathrm{mol\,L^{-1}}$ H_2SO_4 with $5.0 \times 10^{-3}\,\mathrm{mol\,L^{-1}}$ Mn^{2+}. The chloride was added as NaCl (Merck, EMSURE).

The "high concentration" electrolyte ($2.0\,\mathrm{mol\,L^{-1}}$ H_2SO_4 with or without $0.15\,\mathrm{mol\,L^{-1}}$ Mn^{2+}) was chosen because it resembles the concentrations of the same species in the zinc electrowinning process. The "low concentration" electrolyte ($0.10\,\mathrm{mol\,L^{-1}}$ H_2SO_4 with or without $5.0 \times 10^{-3}\,\mathrm{mol\,L^{-1}}$ Mn^{2+}) was chosen based on existing literature investigating the deposition of MnO_2 by EQCM [61,65]. Both the in-situ Raman and EQCM measurements were conducted in this electrolyte. Higher concentration of Mn^{2+} and sulphuric acid were not attempted because of the sensitivity limitation of the EQCM and the danger of corrosion of crucial materials in the Raman instrument, respectively.

4.3.1 Conventional electrochemical techniques

A large three electrode cell containing approximately one litre electrolyte was used for conventional electrochemical measurements, see Figure 4.2. The working electrode was either a platinum or DSA disc inserted in a sample holder (PEEK). The exposed area was $0.28\,\mathrm{cm^2}$ for the DSA electrodes (final version) and $0.79\,\mathrm{cm^2}$ for the platinum and early version DSA electrodes. The reference electrode was a reversible hydrogen electrode and the counter electrode a gold mesh electrode. Experiments were conducted in both low concentration electrolyte and high concentration electrolyte. The electrolyte used with each working electrode material is indicated in Table 4.3. In order to decrease the electrolyte resistance, saturated Na_2SO_4 was added in the experiments with DSA electrodes in low concentration electrolyte.

The electrochemical cell and other glass parts were cleaned prior to experiments by immersion in sulphuric acid and subsequently heating for more than two hours before rinsing with copious amounts of Milli-Q water. The

Figure 4.2: The cell used for conventional electrochemical measurements, containing a gold mesh CE, a reversible hydrogen reference electrode and a working electrode in a PEEK holder.

Table 4.3: Electrolytes used with the different working electrode materials in the large three electrode cell.

Electrode material	**$0.1\,\mathrm{mol\,L^{-1}}$ H_2SO_4** ($+ 0.005\,\mathrm{mol\,L^{-1}} Mn^{2+}$)	**$2\,\mathrm{mol\,L^{-1}}$ H_2SO_4** ($+ 0.15\,\mathrm{mol\,L^{-1}}$ Mn^{2+})
Pt	✓	
DSA - Crystalline	✓*	✓
DSA - Amorphous		✓

* Including saturated Na_2SO_4

counter electrode, reference electrode and sample holder were cleaned by immersion in a hot hydrogen peroxide bath (10 wt% H_2O_2, 1 vol% H_2SO_4) for approximately one minute and also rinsed with Milli-Q water.

The procedures for preconditioning and iR-compensation varied with the different WE materials used. For the DSA electrodes the resistance was compensated during acquisition by 85 % of the resistance found when running current interrupt at 1.55 V. The measured resistance for the DSA-electrodes in the conventional cell was typically $2\,\Omega$ in high concentration electrolyte and $10\,\Omega$ in low concentration electrolyte. The DSA electrodes were preconditioned by running 200 cycles between 0 V and 1.4 V at scan rate $200\,\mathrm{mV\,s^{-1}}$. The platinum electrodes were preconditioned by running 100 cycles at $100\,\mathrm{mV\,s^{-1}}$ between 0.05 V and 1.6 V. No iR-correction was performed on the Pt electrodes.

Cyclic Voltammetry (CV)

The cyclic voltammograms acquired with the different WE materials in the conventional cell are listed in Table 4.4. The fast voltammograms were acquired at sweep rate $100\,\mathrm{mV\,s^{-1}}$, whereas the slow voltammograms were acquired at $5\,\mathrm{mV\,s^{-1}}$. The CVs were acquired in chronological order from the lowest to the highest upper reversal potential. For the CVs acquired at slow scan rate, a reference CV ($100\,\mathrm{mV\,s^{-1}}$, 0 to 1.4 V, 3 cycles) was acquired between each experiment on the DSA electrode to monitor any changes to the electrode during the series. CVs were also obtained in the EQCM set-up, but those measurements will be described in the next section.

Table 4.4: Cyclic voltammetry performed on the different electrode materials in the conventional electrochemical cell. Electrolyte and upper reversal potential is given.

Material	**Electrolyte**		$\mathbf{E_{upper}}$**/ CV slow**	$\mathbf{E_{upper}}$**/ CV fast**
			Pot. range (# meas.)	Pot. range (# meas.)
DSA$_{\mathrm{cryst.}}$	$2\,\mathrm{mol\,L^{-1}}$ H_2SO_4	Blank	1.38 ... 1.7 V (9)	1.2 ... 1.7 V (6)
		$0.15\,\mathrm{mol\,L^{-1}}$ Mn^{2+}	1.35 ... 1.7 V (21)	1.2 ... 1.7 V (6)
	$0.1\,\mathrm{mol\,L^{-1}}$ H_2SO_4	Blank	1.38 ... 1.7 V (9)	1.2 ... 1.7 V (6)
		$0.005\,\mathrm{mol\,L^{-1}}$ Mn^{2+}	1.35 ... 1.7 V (21)	1.2 ... 1.7 V (6)
DSA$_{\mathrm{amorp.}}$	$2\,\mathrm{mol\,L^{-1}}$ H_2SO_4	Blank	1.38 ... 1.7 V (9)	1.2 ... 1.7 V (6)
		$0.15\,\mathrm{mol\,L^{-1}}$ Mn^{2+}	1.35 ... 1.7 V (21)	1.2 ... 1.7 V (6)
Pt	$0.1\,\mathrm{mol\,L^{-1}}$ H_2SO_4	Blank	1.6 V	1.2 ... 1.7 V (6)
		$0.005\,\mathrm{mol\,L^{-1}}$ Mn^{2+}	1.35 ... 1.7 V (11)	1.2 ... 1.7 V (6)
		$0.15\,\mathrm{mol\,L^{-1}}$ Mn^{2+}	1.6 V	1.2 ... 1.7 V (6)

Cyclic voltammograms were also recorded at a number of sweep rates on the DSA electrodes in order to estimate the surface area as described in section 3.4. The voltammograms were recorded between 0 V and 1.4 V at the following sweep rates: 10, 20, 50, 100, 200, 300 and 500 $\mathrm{mVs^{-1}}$. The charge was found by integrating the current between 0.4 V and 1.2 V with respect to time in the positive-going sweep. The upper integration limit was set to ensure that MnO_2 deposition did not contribute to the charge so that electrodes in both Mn-free and Mn-containing electrolytes can be easily compared.

Linear Sweep Voltammetry (LSV)

Linear sweep voltammetry was performed only at the DSA electrodes from 1.35 V to 1.65 V at sweep rate 5 $\mathrm{mV\,min^{-1}}$. The experiments were conducted both in blank and Mn-containing electrolytes, though the amorphous electrodes were only tested in ”high” concentration electrolyte, as stated above (see Table 4.3).

The performance of a MnO_2 covered crystalline DSA electrode was also tested by running LSV in 2 $\mathrm{mol\,L^{-1}}$ H_2SO_4 at 5 $\mathrm{mV\,min^{-1}}$. The MnO_2 layer was produced by holding the crystalline DSA electrode at 1.45 V for 10 000 s in 2 $\mathrm{mol\,L^{-1}}$ $H_2SO_4 + 0.15\,\mathrm{mol\,L^{-1}}\,Mn^{2+}$. The electrode was carefully rinsed and transferred to the Mn free electrolyte. The linear sweep was initiated from the deposition potential (1.45 V) and stopped at 1.7 V. The MnO_2 deposit was investigated by SEM and EDS after the linear sweep in acid.

Chronoamperometry and SEM

The electrodes were stepped to different potentials for varying duration in order to study the effect on the MnO_2 deposit, see Table 4.5. The deposit was studied with SEM and EDS after each potential step. The current transients and the results from SEM/EDS are presented in sections 5.3.3 and 5.2, respectively. Before each step the electrodes were preconditioned by running CVs as described above. The procedure for estimating the surface area was also performed on the DSA electrodes before the potential step. Before starting a new experiment on a platinum electrode, the surface was wiped with lint free paper and the electrode was polished with alumina paste. For the potential steps on DSA electrodes a fresh electrode was

Table 4.5: Potential steps performed at the different electrode materials.

Material	**1.45 V**			**1.55 V**			**1.65 V**
	100 s	1000 s	10000 s	100 s	1000 s	10000 s	10000 s
$\mathrm{DSA}_{\mathrm{cryst.}}$	✓	✓	✓	✓	✓	✓	✓[a]
$\mathrm{DSA}_{\mathrm{amorp.}}$ [a]	✓	✓	✓	✓	✓	✓	✓
Pt [b]	✓	✓[c]	✓	✓	✓[c]	✓	

[a] Only in high concentration electrolyte

[b] In low concentration electrolyte

[c] Also in low concentration acid ($0.1\,\mathrm{mol\,L^{-1}}$) + high concentration $\mathrm{Mn^{2+}}$ ($0.15\,\mathrm{mol\,L^{-1}}$)

usually employed in each experiment. In some cases (only short deposition time) the $\mathrm{MnO_2}$ on the DSA was removed electrochemically before starting a new experiment. Regardless, the electrode was preconditioned as described above and the procedure to find the inner and outer charge was performed.

Potential steps were also performed on crystalline DSA electrodes with electrodeposited $\mathrm{MnO_2}$ (1.45 V, 10 000 s, $2\,\mathrm{mol\,L^{-1}}$ $\mathrm{H_2SO_4}$ + $0.15\,\mathrm{mol\,L^{-1}}$ $\mathrm{Mn^{2+}}$), as illustrated in Figure 4.3 (including the deposition step). The experiments were performed in high concentration electrolyte, both blank and with $\mathrm{Mn^{2+}}$ ions. The same electrode was used throughout the entire sequence for each electrolyte.

Electrochemical procedure for removal of $\mathrm{MnO_2}$

A sequence of potential steps was performed to try to remove $\mathrm{MnO_2}$ deposited at crystalline DSA electrodes at conditions resembling those in the zinc electrowinning process. An illustration of such a sequence is given in Figure 4.4. The experiments were performed in $2\,\mathrm{mol\,L^{-1}}$ $\mathrm{H_2SO_4}$ + $0.15\,\mathrm{mol\,L^{-1}}$ $\mathrm{Mn^{2+}}$. An initial layer of $\mathrm{MnO_2}$ covering the electrode surface was created at 1.45 V before the potential was stepped to 1.75 V where the current density was comparable to that in the zinc electrowinning process. The electrode was held at 1.75 V for either 3 or 15 hours. A reduction step followed at 0.4 V where the electrode was held for either 100 s or 10 s and $\mathrm{MnO_2}$ was reduced. The potential was then stepped up to 1.75 V again where the convection caused by OER can remove loose flakes of $\mathrm{MnO_2}$. An

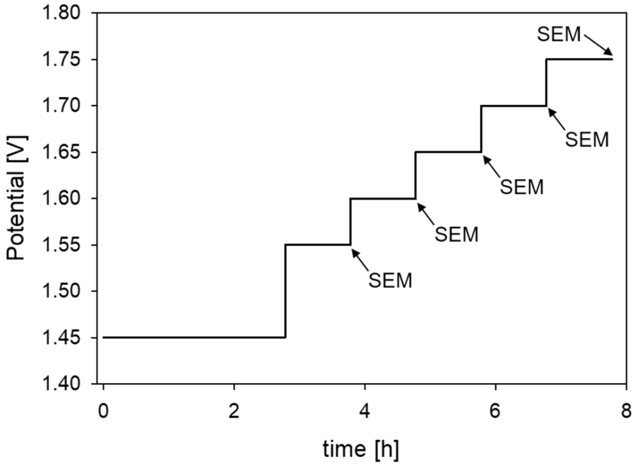

Figure 4.3: Potential steps on crystalline DSA electrodes with MnO_2 deposited at 1.45 V for 10 000 s.

additional reduction step was added to reduce MnO_2 nuclei formed at the high potential in the previous step. Some experiments were performed without forming the initial layer of MnO_2 at 1.45 V. The same current range (100 mA) was used throughout the entire sequence.

The electrode surface was examined by SEM and EDS after each experiment and the sequence was also stopped at different stages in order to study the MnO_2 deposit by SEM and EDS. The conducted experiments are given in Table 4.6. SEM and EDS were used to examine the electrode surface after most of the listed experiments. The current transients and the results from SEM/EDS are presented in section 5.3.4 and at the end of section 5.2.1, respectively. In addition to the listed experiments, the sequence in Figure 4.4 was repeated six consecutive times with a three hour hold at 1.75 V.

In addition to the potential step sequence described above, an attempt was made to electrochemically reduce MnO_2 deposited for 10 000 s at 1.55 V in $2\,\mathrm{mol\,L^{-1}}$ H_2SO_4 + $0.15\,\mathrm{mol\,L^{-1}}$ Mn^{2+}. The electrode was initially cycled between 0 and 1.4 V at $100\,\mathrm{mV\,s^{-1}}$ for 12 cycles with a negative-going sweep starting at OCP in the same electrolyte. Subsequently, the electrode was held at 0.4 V for 5 min before the surface was examined with SEM and EDS. Afterwards, oxygen gas was evolved on the electrode (5 min at 1.75 V) to try to remove loose flakes, before the surface again was examined with SEM

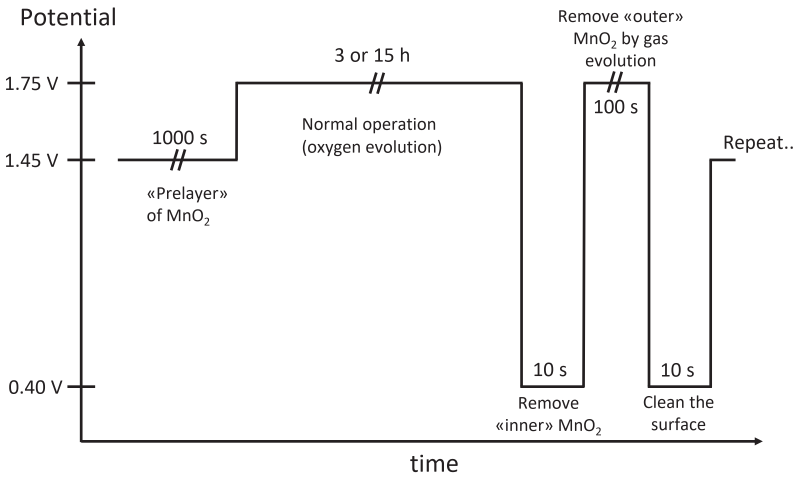

Figure 4.4: Potential step sequence for electrochemical removal of MnO_2.

Table 4.6: Potential step sequences performed with crystalline DSA electrodes in $2\,\mathrm{mol\,L^{-1}}$ H_2SO_4 + $0.15\,\mathrm{mol\,L^{-1}}$ Mn^{2+} followed by SEM and EDS.

1.45 V	**1.75 V**		**0.4 V**		**1.75 V**	**0.4 V**	
1000 s	3 h	15 h	100 s	10 s	100 s	100 s	10 s
✓	✓	✓					
✓	✓	✓	✓				
✓	✓	✓	✓		✓	✓	
No	✓	✓	✓		✓	✓	
✓	✓	✓		✓	✓		✓
No	✓			✓	✓		✓

and EDS.

Effect of chloride on MnO_2 deposition

The effect of chloride in the electrolyte was investigated by running LSV in $0.1\,\mathrm{mol\,L^{-1}}$ H_2SO_4 + $0.005\,\mathrm{mol\,L^{-1}}$ Mn^{2+} with and without 100 ppm Cl^-. No Na_2SO_4 was added in these experiments. An early version of the crystalline DSA was used for these experiments. The linear sweeps were acquired at sweep rate $5\,\mathrm{mV min^{-1}}$ from 1.3 V to 1.7 V.

4.3.2 Electrochemical Quartz Crystal Microbalance (EQCM)

The EQCM measurements were performed with Metrohm Autolab's EQCM module and cell (polypropylene). The reference electrode was a reversible hydrogen electrode and the counter electrode a gold wire. Both electrodes were made to fit the EQCM as well as the Raman cells. The working electrode crystals are described in detail below. The electrolyte consisted of $0.1\,\mathrm{mol\,L^{-1}}$ H_2SO_4 with or without $5 \times 10^{-3}\,\mathrm{mol\,L^{-1}}$ Mn^{2+}. The cell contained approximately 3 mL electrolyte.

The EQCM crystals were 6 MHz AT-cut crystals with 13.6 mm crystal diameter and 6.7 mm electrode diameter. Three different electrode materials were used: titanium with or without IrO_2 powder, platinum and gold. The platinum and gold electrodes consisted of a 100 nm thick layer of the active electrode material on top of a 10 nm TiO_2 adhesion layer and were supplied by International Crystal Manufacturing (part number 151717-6 and 151527-6 respectively). The titanium electrodes consisted of a 100 nm layer of titanium and were supplied by Renlux Crystals Ltd.

The h-IrO_2 powder was prepared as described in section 4.1.2 and applied to the Ti-crystals by an airbrush spray (Biltema, part number 17-372). The ink was prepared by mixing isopropanol (VWR Chemicals, technical) with h-IrO_2 to a concentration of 2.5 wt% h-IrO_2. The ink was dispersed by immersing it in an ultrasonic bath just prior to spraying. The Ti electrode was covered by a mask during spraying so that only a 3 mm diameter area in the center of the electrode was covered with IrO_2. The spraying was stopped when a frequency change of 2000 Hz was reached, corresponding to a loading of approximately $0.1\,\mathrm{mg\,cm^{-2}}$ in the coated area. This loading was chosen as a compromise between the frequency and current signals.

A few experiments were conducted with platinized platinum electrodes to investigate the effect of increased roughness. Those were prepared by depositing platinum for 2 s at −2 V vs. RHE from a solution of Milli-Q water containing 0.1 mol L^{-1} HCl (Merck, p.a.) and 0.02 mol L^{-1} H_2PtCl_6 (J.T.Baker, BAKER ANALYZED A.C.S. Reagent) onto the platinum electrodes described above.

The uncoated crystals were cleaned prior to electrochemical measurements by immersion in a heated hydrogen peroxide bath (10 wt% H_2O_2, 1 vol% H_2SO_4) for a brief time (less than 1 minute). After the immersion, the crystals were rinsed with copious amounts of Milli-Q water and dried under nitrogen atmosphere. The cell parts (polypropylene) were immersed in the heated hydrogen peroxide bath for one hour and rinsed thoroughly with Milli-Q water. The counter and reference electrodes were also cleaned in the same manner, but with one minute immersion in the hot hydrogen peroxide bath.

The electrolyte was deaerated prior to the experiments by purging with Argas (AGA, 5.0). During the experiments the argon outlet was placed directly above the electrolyte surface. The working electrodes were preconditioned by repeatedly cycling them at 100 mV s^{-1} in 0.1 mol L^{-1} H_2SO_4 for 100 cycles prior to the electrochemical measurements. No iR-correction was performed in these experiments.

Cyclic Voltammetry (CV)

The cyclic voltammograms obtained with the EQCM set-up are listed in Table 4.7. The upper reversal potential was 1.6 V in the experiments where the sweep rate was varied.

Chronoamperometry

The potential step experiments conducted with the EQCM set-up are listed in Table 4.8. The initial potential was 1.1 V on the platinum electrodes to ensure that a metal oxide layer had already formed and did not contribute significantly to the measured current after the step. In the case of the gold

Table 4.7: Cyclic voltammetry performed with the different electrode materials in the EQCM cell. Electrolyte, upper reversal potential for sweep rates 5 and $100\,\mathrm{mV\,s^{-1}}$ as well as additional sweep rates are given.

Material	**Electrolyte**	**E_{upper}/ 5 mV/s** Pot. range (# meas.)	**E_{upper}/ 100 mV/s** Pot. range (# meas.)	**Add. sweep r.** mV/s
Pt	Blank	1.6 V and 1.7 V	1.2 ... 1.7 V (6)	-
	Blank with Mn^{2+}	1.39 ... 1.7 V (16)	1.2 ... 1.7 V (6)	10, 50
Platinized Pt	Blank	1.7 V	1.2 ... 1.7 V (6)	-
	$5\,\mathrm{mmol\,L^{-1}}$ Mn^{2+}	1.5 ... 1.7 V (3)	1.7 V	-
Au	Blank	1.6 V and 1.7 V	1.2 ... 1.7 V (6)	-
	$5\,\mathrm{mmol\,L^{-1}}$ Mn^{2+}	1.39 ... 1.7 V (16)	1.2 ... 1.7 V (6)	10, 20, 50
Ti	Blank	2.5 V	2.5 V	-
	$5\,\mathrm{mmol\,L^{-1}}$ Mn^{2+}	2.5 V	2.5 V	-
IrO_2/Ti	Blank	1.6 V	1.6 V	-
	$5\,\mathrm{mmol\,L^{-1}}$ Mn^{2+}	1.39 V ... 1.6 V (13)	1.6 V	-

Table 4.8: Potential steps for 100 s in 0.1 mol L^{-1} H_2SO_4 + 0.005 mol L^{-1} Mn^{2+} with EQCM.

Electrode material	**1.45 V**	**1.50 V**	**1.55 V**
Pt	✓		✓
Au	✓	✓	✓
Ti w/IrO_2	✓	✓	✓

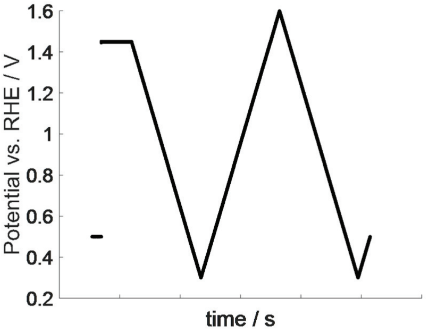

Figure 4.5: Illustration of potential development with time during a step-hold-CV.

electrode, the initial potential was set to 0.5 V as the onset of gold oxide formation overlaps with that of manganese oxide formation. The initial potential was also 0.5 V for the IrO_2-coated Ti-electrode.

Combined techniques

A combination of step, hold and sweep techniques were performed as illustrated in Figure 4.5. This sequence was performed at a Pt, Au and IrO_2-coated Ti-electrode with a 100 s hold at 1.45 V, 1.50 V or 1.55 V.

Calibration of the crystals

Calibration of the crystals was performed with copper deposition. Copper was deposited for 30 s at 0.16 V vs. RHE in 1 mol L^{-1} H_2SO_4 + 0.01 mol L^{-1} $CuSO_4$. Calibration was only performed for one crystal and the same value was assumed for the other crystals. For the IrO_2 coated crystal the calibration was performed at the end of the series of experiments. The calibration was performed slightly differently; copper was deposited for 30 s at 0.18 V vs. RHE in $0.1\,\mathrm{mol\,L^{-1}}$ H_2SO_4 + $0.01\,\mathrm{mol\,L^{-1}}$ $CuSO_4$. The same procedure was performed on a bare titanium electrode to verify that deposition of copper on titanium did not contribute to a mass change at that potential. For all calibrations, regression was performed from a frequency change of 40 Hz was observed (after approximately 1 s) and until the end of the step in order to avoid the double layer charging region.

4.3.3 Rotating disc electrode (RDE)

A glass cell of conventional design was used for the rotating disc electrode measurements. A Pine Instruments rotator was employed. Two different working electrodes were employed: a platinum disc in a PTFE shroud (Pine, AFE3T050PT) or a crystalline DSA electrode (IrO_2-Ta_2O_5/Ti) in a PEEK shroud. The crystalline DSA electrode was prepared as described in section 4.1.1. Both working electrodes had a 5 mm disc of the electroactive material in a 12 mm diameter shroud. The reference electrode was a reversible hydrogen electrode (RHE) and the counter electrode a gold mesh. The experiments were performed in $0.1\,\mathrm{mol\,L^{-1}}$ H_2SO_4 with $5 \times 10^{-3}\,\mathrm{mol\,L^{-1}}$ Mn^{2+} or in $2\,\mathrm{mol\,L^{-1}}$ H_2SO_4 with $0.15\,\mathrm{mol\,L^{-1}}$ Mn^{2+}. The performed experiments were rotation speed was varied are listed in Table 4.9. The electrodes were cleaned in an acidified hydrogen peroxide solution (10 wt% H_2O_2, 1 vol% H_2SO_4) and rinsed thoroughly with Milli-Q water before and between each experiment.

In addition to testing the effect of rotation rate, the effect of electrode post-treatment on subsequent experiments were tested in the RDE set-up (see section 5.6). The different post-treatment procedures involved electrochemical reduction, resting time at open circuit potential, chemical cleaning in an acidified hydrogen peroxide solution (10 wt% H_2O_2, 1 vol% H_2SO_4), or a combination of those. The electrode was either stationary or rotated at 1600 rpm. Furthermore, the development of voltammograms over time were investigated by running multiple cycles on a platinum electrode that was chemically cleaned (in the hydrogen peroxide solution) prior to the experiments. The voltammograms were recorded at sweep rate $20\,\mathrm{mV\,s^{-1}}$ in $0.1\,\mathrm{mol\,L^{-1}}$ H_2SO_4 with $5 \times 10^{-3}\,\mathrm{mol\,L^{-1}}$ Mn^{2+} (300 cycles) and in $2\,\mathrm{mol\,L^{-1}}$ H_2SO_4 with $0.15\,\mathrm{mol\,L^{-1}}$ Mn^{2+} (50 cycles) with an upper

Table 4.9: Experiments performed with rotating disc electrode. In all potential steps the hold potential was 1.45 V.

Electrode material	**Exp.**	**Electrolyte** $mol\,L^{-1}$		**Duration/ sweep rate**	**Rotation rate**
		H_2SO_4	Mn^{2+}	$s\ /\ mV\,s^{-1}$	rpm
Pt	CV	0.1	0.005	20	0, 100, 400, 900, 1600, 2500
	Pot. step	0.1	0.005	100	0, 100, 400, 900, 1600, 2500
				10000	0 with pulses at 1600
		2	0.15	200	0, 100, 400, 900, 1600, 2500
$DSA_{cryst.}$	Pot. step	0.1	0.005	200	0 with pulses at 1600
		2	0.15	200	0 with pulses at 1600

Table 4.10: Deposition conditions for MnO_2 deposits studied with STEM.

Electrode material	**Potential**	**Time**	**Electrolyte** $\mathrm{mol\,L^{-1}}$		**Activated**
	V	s	H_2SO_4	Mn^{2+}	
$DSA_{cryst.}$	1.45	100	0.1	0.005	-
	1.45	1000	2	0.15	✓
	1.45	10 000	2	0.15	✓
Pt	1.45	10	0.1	0.005	✓

limit of 1.6 V and without rotation.

Samples to be studied by STEM were prepared in the RDE set-up and the deposition conditions are listed in Table 4.10. The activated electrodes had experienced MnO_2 deposition prior to formation of the deposit to be studied with STEM. For these electrodes, the previous MnO_2 deposits were removed by electrochemical reduction, but no chemical cleaning was performed. The deposition conditions corresponded to the peak observed in the current transient for all samples except the last DSA entry (10 000 s).

4.3.4 In-situ Raman Spectroscopy

The instrument used for all Raman measurements was a WITec alpha300 R confocal Raman microscope equipped with a 10x magnification objective (Zeiss EC Epiplan 10x/0.25). The light source was a green laser (532 nm Nd:YAG) from WITec GmbH. A low laser power was applied, in the range of 0.5 mW to 3 mW, in order to minimize structural changes in the deposited manganese oxide caused by local heating from the laser beam. The spectrometer was a CCD camera (DR32400_FI) from WITec GmbH. The stability of the instrument was found to be satisfactory when checked against a reference sample (Si) before and after a series of experiments.

A custom-made three electrode PTFE-cell was used for the in-situ Raman measurements, see Figure 4.6. The working electrode was inserted through the bottom of the cell. Two different working electrodes were employed: a platinum disc in a PTFE holder (Pine, AFE3T050PT) or a DSA electrode in a PEEK holder. The DSA electrode was a crystalline IrO_2-Ta_2O_5/Ti electrode (calcined at 470 °C) with a molar ratio of 70:30 % Ir:Ta, prepared

Figure 4.6: The electrochemical cell used for Raman spectroscopy as seen from above.

as described in section 4.1.1. Both working electrodes had a 5 mm disc of the electroactive material in a 12 mm diameter holder. The reference electrode was a reversible hydrogen electrode (RHE) and the counter electrode was a gold wire, both fixed inside the cell. The cell was covered by a glass lid. All experiments were performed in $0.1\,\mathrm{mol\,L^{-1}}$ H_2SO_4 with $5 \times 10^{-3}\,\mathrm{mol\,L^{-1}}$ Mn^{2+}.

Prior to the experiments, the various parts were cleaned by different procedures. The cell was cleaned by immersion into concentrated sulphuric acid at room temperature for one hour and subsequently immersed in Milli-Q water for several hours. The counter and reference electrodes as well as the glass lid were cleaned by immersion into a hot hydrogen peroxide bath (10 wt% H_2O_2, 1 vol% H_2SO_4) for approximately one minute and then rinsed thoroughly with Milli-Q water. The platinum working electrode was polished with alumina paste, rinsed and briefly dipped in an ultrasonic bath (1 min) to remove residual alumina particles. Both working electrodes were dipped in the hydrogen peroxide bath at room temperature for approximately one minute and rinsed with Milli-Q water.

The uncompensated resistance in the system was found from EIS at 1.35 V, and all measurements were compensated by 85 % of this value during measurements. The working electrode was conditioned before each deposition experiment by running minimum 20 cycles from 0.05 V to 1.4 V at

Table 4.11: Experimental conditions for Raman spectroscopy time series performed during MnO_2 deposition.

Electrode	**Potential**		**Duration**	**Int. time**	**Accum.**
	1.45 V	1.55 V	s	s	
Pt	✓	✓	100	10	2
Pt	✓	✓	1000	15	2
Pt	✓	✓	10000	15	3
DSA	✓		1000	15	1
DSA	✓		10000	15	3

$100\,\mathrm{mV\,s^{-1}}$ until a stable and expected voltammogram was obtained.

Time series of Raman spectra were recorded during deposition of manganese oxide at a constant potential (1.45 V or 1.55 V). The different experiments are listed in Table 4.11, also including the settings for integration time and number of accumulations. During deposition, the laser power was kept at 0.5 mW to limit the effect of local heating on the forming manganese oxide film. The stage was also occasionally moved for the same reason.

After deposition, in-situ Raman spectra were acquired with the electrode at OCP. Ex-situ Raman spectroscopy was also performed for the films deposited for longer times (1000 s or more) and where the manganese oxide film did not detach from the electrode surface upon drying. The laser power was kept at 0.5 mW in the ex-situ measurements, whereas it was varied from 0.5 mW to 3 mW in the in-situ measurements. The integration time was 15 s in all measurements. The number of accumulations was varied from one to ten depending on the laser power to improve the signal-to-noise ratio (low laser power), but also to limit exposure time in case of heating (high laser power). A picture of the electrode surface was recorded in bright field mode both before and after a single spectrum was acquired in order to assess any damage caused by local heating.

Two different procedures were employed to remove the manganese oxide between each experiment. For the MnO_2 deposited for short times (100 s), the deposit was reduced electrochemically by keeping the working electrode at 0.5 V for up to 1000 s until the working electrode appeared as before deposition (microscope in bright field mode). The working electrode was subsequently cycled minimum 20 times before performing a new measurement, as described above. For the MnO_2 deposited for longer times, the

Table 4.12: Experimental conditions for Raman spectroscopy time series performed during reduction of MnO_2 electrodeposited at 1.45 V. The reduction was applied as a linear sweep starting from the deposition potential.

Electrode	**Deposition time** s	**Sweep rate** $mV\,min^{-1}$	**Int. time** s	**Accum.**
Pt, DSA	1000	60	15	1
Pt, DSA	10000	5	15	3

electrode surface was carefully wiped with lint free paper and dipped in the hydrogen peroxide bath as described above. The bath held room temperature. The electrode was held for approximately one minute and then rinsed with Milli-Q water.

In addition to investigating the deposition of MnO_2, some experiments were conducted in order to investigate the reduction of the electrodeposited MnO_2. Only the MnO_2 deposited at 1.45 V was investigated. The reduction was performed as a negative-going linear potential sweep from the deposition potential and down to 0.5 V or 0.4 V, well below the reversible potential for MnO_2 reduction. A time series of Raman spectra were recorded during the linear sweep. The conducted experiments are listed in Table 4.12. As in the deposition experiments, the laser power was kept low (0.5 mW) and the stage was occasionally moved. By the end of the linear sweep, any remaining deposit was investigated by single Raman spectra in-situ at OCP with the same settings as described above for the investigation of the as-deposited MnO_2.

Videos (1 or 25 FPS) were also acquired using the Raman microscope in bright field mode during deposition up to 1000 s at both potentials (1.45 V and 1.55 V) and for both working electrodes.

Chapter 5

Results

5.1 Characterization of as-prepared electrode materials

Scanning electron microscopy (SEM) images, scanning transmission electron microscopy (STEM) images and energy dispersive X-Ray spectroscopy (EDS) data of the as-prepared dimensionally stable anodes (DSA) and IrO_2 hydrolysis powder (h-IrO_2) are presented in this section. X-Ray diffraction (XRD) spectra were obtained for the crystalline DSA electrode and the IrO_2 powder and those are presented in Appendix A.

5.1.1 DSA electrodes

SEM images of as-prepared crystalline and amorphous DSA electrodes are presented in Figures 5.1 and 5.2, respectively. In addition, a STEM image is displayed in Figure 5.1c corresponding to an area that appeared flat in Figure 5.1b. The elemental composition determined by EDS is given in Table 5.1 for the DSA electrodes. The elemental composition of an earlier attempt to produce a crystalline DSA is also included. The EDS spectra were acquired at 15 kV acceleration voltage for all the electrodes listed in Table 5.1. In contrast, the EDS data presented in section 5.2 were acquired at 25 kV acceleration voltage. It is worth pointing out that a higher accelerating voltage gives a larger emission volume and hence a greater signal

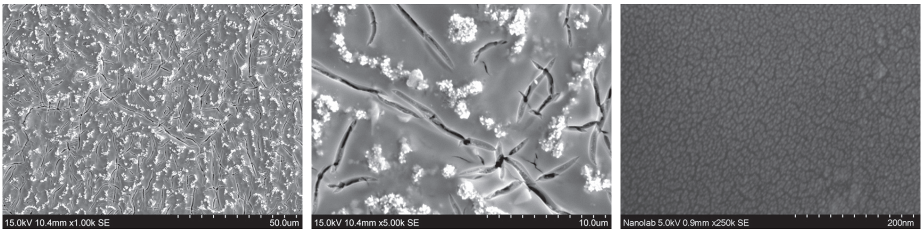

(a) SEM (b) SEM (c) STEM

Figure 5.1: SEM and STEM images of an as-prepared crystalline DSA electrode at different magnifications. The STEM image in (c) shows a magnification of a flat area as observed in (b) (darker area without cracks).

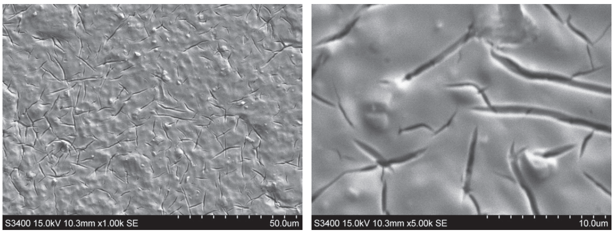

(a) SEM (b) SEM

Figure 5.2: SEM images of an as-prepared amorphous DSA electrode at different magnifications.

from the substrate (Ti). Elemental maps from EDS are shown in Figures 5.3 and 5.4 for the areas displayed in Figures 5.1a and 5.2a, respectively.

Both the crystalline and amorphous electrodes had a mud-cracked structure. The STEM image in Fig. 5.1c revealed that the area that appeared flat in Fig. 5.1b in reality consists of small spheres. Crystallites were present at the crystalline DSA, but not at the amorphous DSA. The iridium map (Fig. 5.3b) overlaps quite well with the observed crystallites. The chlorine map of the crystalline DSA electrode (Fig. 5.3e) overlaps with the most intense spots in the tantalum map (as indicated by the red circles in the elemental maps of tantalum and chlorine in Fig. 5.3). This indicates some residual precursor salt ($TaCl_5$) in the electrocatalytic coating. The titanium map of the crystalline DSA displayed least intensity in the areas with the most mud-cracks. This correlation was not observed with the amorphous DSA. For these electrodes, the titanium map (Fig. 5.4d) seemed to follow the substrate topography in that elevations in the SEM image appeared

Table 5.1: EDS analysis of as-prepared DSA electrodes.

Sample	**Concentration at%**				
	O	Ir	Ti	Ta	Cl
DSA - crystalline	62	15	12	10	1
DSA - early version crystalline	41	6	52	0.7	0.9
DSA - amorphous	61	13	7	15	4

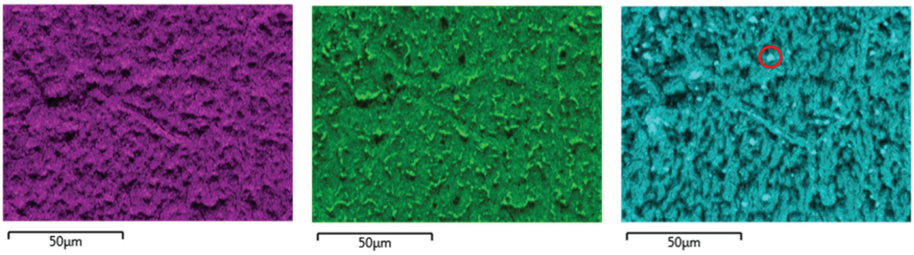

(a) O (b) Ir (c) Ta

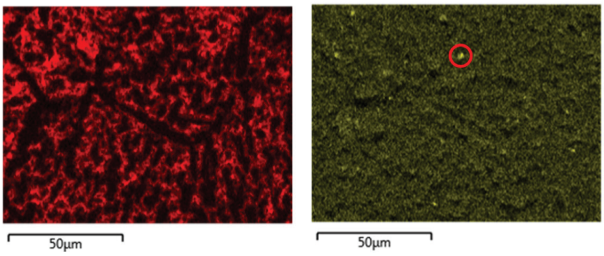

(d) Ti (e) Cl

Figure 5.3: EDS maps of an as-prepared crystalline DSA electrode.

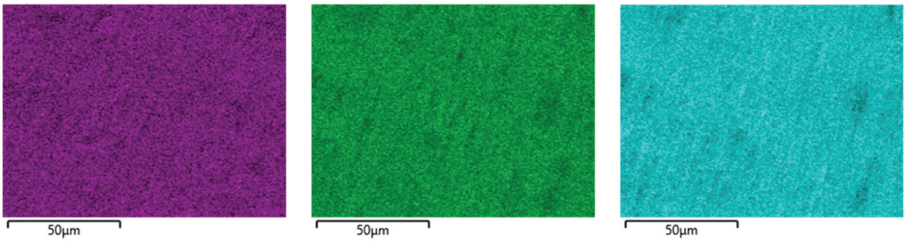

(a) O (b) Ir (c) Ta

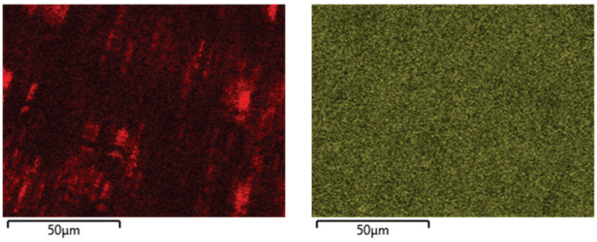

(d) Ti (e) Cl

Figure 5.4: EDS maps of an as-prepared amorphous DSA electrode.

more intense in the Ti-map. Apart from the titanium map, all maps of the amorphous DSA electrode had a rather featureless distribution in intensity.

The amount of detected chlorine was larger for amorphous than for crystalline DSAs. This is as expected since the precursor salts were chlorides and the calcination temperature was lower for the amorphous electrodes. The amount of chlorine in the early version of the crystalline DSA was quite large taking into account the small amounts of Ir and Ta observed. The early version of the crystalline DSA also had a quite large titanium concentration, indicating a thin layer of electrocatalytic coating compared to the other electrodes.

5.1.2 IrO_2 powder

SEM images of IrO_2 powder prepared by hydrolysis are presented in Figure 5.5. Most particles were in the submicron range, but larger aggregates were also observed. EDS analysis gave the following composition: 57 at% O, 35 at% Ir and 7 at% Na. All elements were uniformly distributed.

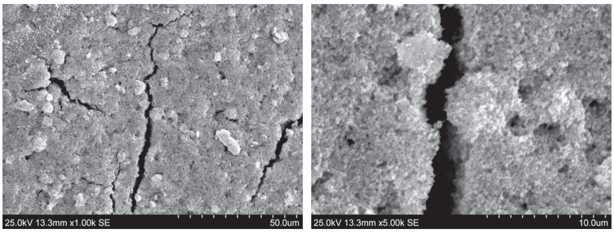

(a) (b)

Figure 5.5: SEM images of the as-prepared IrO_2 hydrolysis powder at different magnifications.

5.2 Morphology and composition of MnO_2

SEM and STEM images as well as EDS analysis of MnO_2 deposits are presented in this section. The current transients of the experiments leading to the obtained deposits are not presented in this section, but rather along with other electrochemical results (mainly in sections 5.3.3 and 5.3.4).

5.2.1 Crystalline DSA electrodes

STEM images of MnO_2 deposited at a crystalline DSA electrode after 100 s at 1.45 V in low concentration electrolyte ($0.1\,\mathrm{mol\,L^{-1}}$ H_2SO_4 + $5\,\mathrm{mmol\,L^{-1}}$ Mn^{2+}) are presented in Figure 5.6. No electrochemical measurements were performed with the electrode prior to deposition. In certain areas, hemispherical structures of MnO_2 were observed (Fig. 5.6a). Their distribution appeared to be random. On closer examination, these consisted of thread-like features that in turn were made up from spheres (Figs. 5.6b and 5.6c).

SEM images of MnO_2 deposited on crystalline DSA electrodes for different times at 1.45 V and 1.55 V in low concentration electrolyte are displayed in Figures 5.7 and 5.8, respectively. The electrodes were pretreated before deposition as described in section 4.3.1. The features observed in Fig. 5.6 were not observed in Fig. 5.7a although the deposition conditions were the same, demonstrating the effect of electrode pretreatment on the obtained deposits.

Manganese oxide covered the entire electrode surface after 1000 s at 1.55 V. A careful examination of the deposit formed after 1000 s at 1.45 V showed

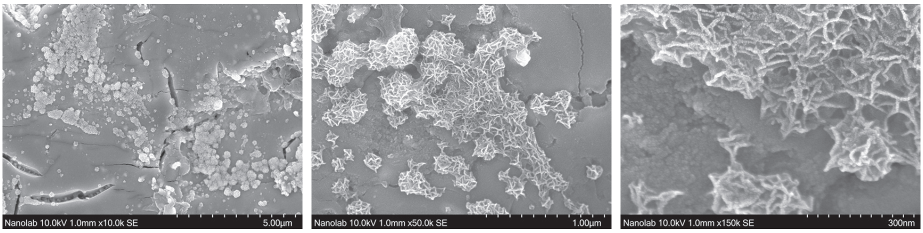

(a) (b) (c)

Figure 5.6: STEM images of MnO_2 deposited for 100 s at 1.45 V on a previously unused crystalline DSA electrode in 0.1 mol L^{-1} H_2SO_4 + 5 mmol L^{-1} Mn^{2+}.

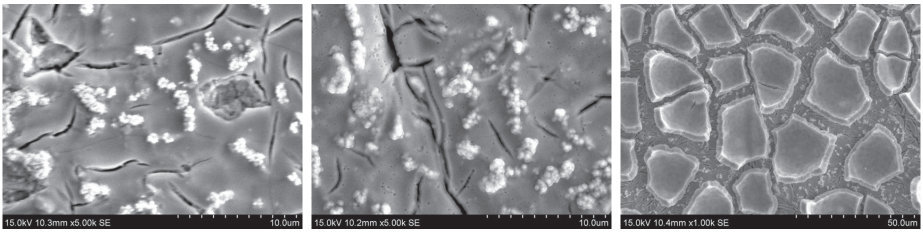

(a) 100 s. (b) 1000 s. (c) 10000 s.

Figure 5.7: SEM images of MnO_2 deposited for different times at 1.45 V on crystalline DSA electrodes in 0.1 mol L^{-1} H_2SO_4 + 5 mmol L^{-1} Mn^{2+}.

that a thin film of manganese oxide covered the entire surface also at this potential. The manganese oxide obtained after deposition for 10 000 s seemed smooth and continuous immediately after removing the electrode from the electrolyte, but cracked and partially detached upon drying as seen in Figures 5.7c and 5.8c. Images were acquired of the edges of some resulting MnO_2 flakes pointing approximately perpendicular to the electrode surface, see Figure 5.9. The thickness of the deposits were estimated from these images. The deposit formed at 1.55 V was thicker and appeared to be more porous than the deposit formed at 1.45 V. Dendrites were only observed after deposition for 10 000 s at 1.55 V (Fig. 5.8c), and only in small amounts.

MnO_2 was deposited by the same procedures, i.e. potentials and time, in high concentration electrolyte (2 mol L^{-1} H_2SO_4 + 0.15 mol L^{-1} Mn^{2+}) as in low concentration electrolyte, see Figures 5.10 and 5.13. The deposits obtained after 1000 s and 10 000 s at 1.45 V was investigated in more detail in a STEM, see Figures 5.11 and 5.12, respectively. MnO_2 was also deposited

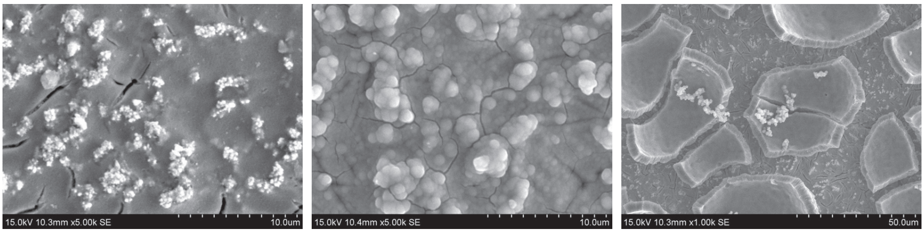

(a) 100 s. (b) 1000 s. (c) 10000 s.

Figure 5.8: SEM images of MnO_2 deposited for different times at 1.55 V on crystalline DSA electrodes in $0.1\,\text{mol L}^{-1}$ H_2SO_4 + $5\,\text{mmol L}^{-1}$ Mn^{2+}.

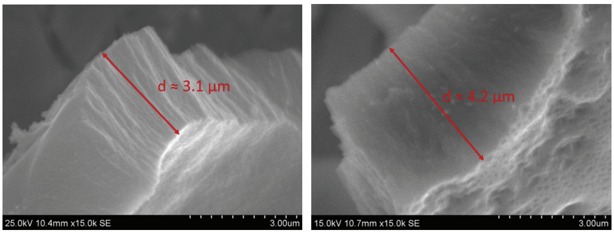

(a) 1.45 V. (b) 1.55 V.

Figure 5.9: SEM images of the edges of MnO_2 flakes observed after deposition for 10 000 s in $0.1\,\text{mol L}^{-1}$ H_2SO_4 + $5\,\text{mmol L}^{-1}$ Mn^{2+} at the specified potentials. An estimate of the thickness of the deposits is indicated.

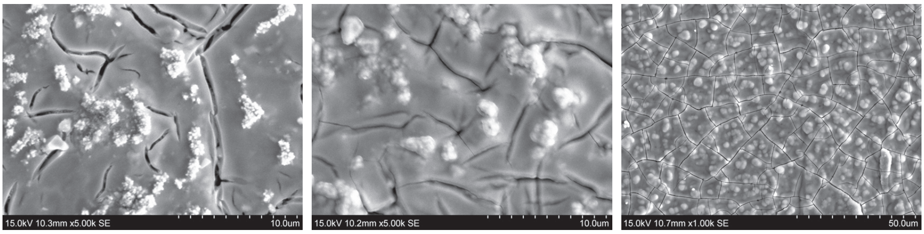

(a) 100 s. (b) 1000 s. (c) 10000 s.

Figure 5.10: SEM images of MnO_2 deposited for different times at 1.45 V on crystalline DSA electrodes in $2\,\text{mol L}^{-1}$ H_2SO_4 + $0.15\,\text{mol L}^{-1}$ Mn^{2+}.

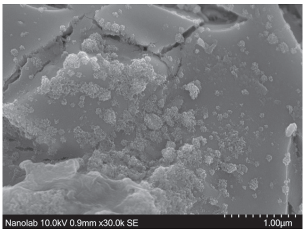

Figure 5.11: STEM image of MnO_2 deposited for 1000 s at 1.45 V on a crystalline DSA electrode in 2 mol L^{-1} H_2SO_4 + 0.15 mol L^{-1} Mn^{2+}.

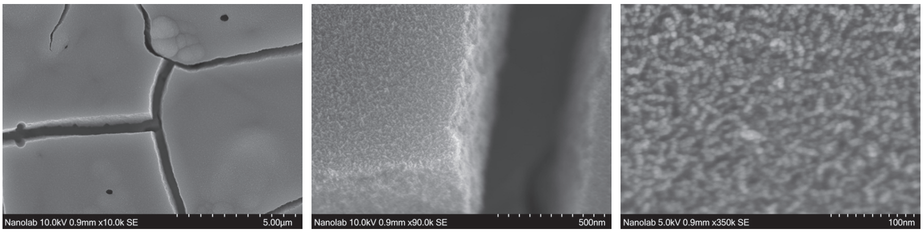

(a) (b) (c)

Figure 5.12: STEM images of MnO_2 deposited for 10 000 s at 1.45 V on a crystalline DSA electrode in 2 mol L^{-1} H_2SO_4 + 0.15 mol L^{-1} Mn^{2+}.

for 10 000 s at 1.65 V in the high concentration electrolyte, see Figure 5.14. In contrast to the deposit formed in the low concentration electrolyte, the manganese oxide did not partially detach upon drying after deposition in the high concentration electrolyte.

The deposit obtained after 10 000 s at 1.45 V was a relatively smooth deposit covering the electrode surface with small cracks (Figs. 5.10c and 5.12a). Upon closer examination with STEM, it became apparent that the deposit consisted of small spherical features, less than 10 nm in diameter (Fig. 5.12c). A thinner, smooth layer of manganese oxide also covered the electrode surface after 1000 s at 1.45 V as observed in the SEM image in Fig. 5.10b. However, a smooth layer was not observed in the STEM image of a deposit obtained at the same conditions (Fig. 5.11). Here, nuclei were observed that appeared similar to those in Figure 5.6. Apparently, less MnO_2 deposition occurred at this electrode compared to at the electrode seen in Figure 5.10b as also indicated by the later peak in the current transient (1000 s vs. 200 s), perhaps due to different activation of the electrodes prior to deposition.

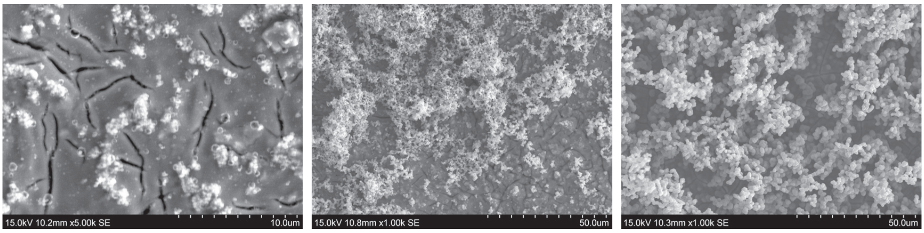

(a) 100 s. (b) 1000 s. (c) 10000 s.

Figure 5.13: SEM images of MnO_2 deposited for different times at 1.55 V on crystalline DSA electrodes in $2\,\mathrm{mol\,L^{-1}}$ H_2SO_4 + $0.15\,\mathrm{mol\,L^{-1}}$ Mn^{2+}.

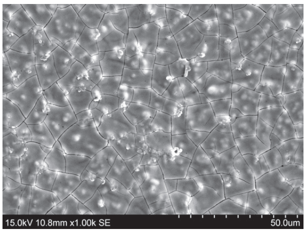

Figure 5.14: SEM image of MnO_2 deposited for 10 000 s at 1.65 V on a crystalline DSA electrode in $2\,\mathrm{mol\,L^{-1}}$ H_2SO_4 + $0.15\,\mathrm{mol\,L^{-1}}$ Mn^{2+}.

At 1.55 V, dendrites of MnO_2 was formed on top of a smooth deposit similar to that observed at 1.45 V. The dendrite formation was rather extensive already after 1000 s deposition, covering most of the electrode surface (Fig. 5.13b). Nuclei were observed after 100 s at 1.55 V. The amount of dendrites was much higher in the high concentration than in the low concentration electrolyte, though a small amount was observed after 10 000 s at 1.55 V in the low concentration electrolyte (Fig. 5.8c). Interestingly, only small amounts of dendrites were observed for the deposit obtained after 10 000 s at 1.65 V (Fig. 5.14), which rather appeared quite similar to the deposit obtained at 1.45 V (Fig. 5.10c).

EDS results of each deposit are presented in Table 5.2. As expected, the manganese content increased with deposition time. The amount of dendrites clearly has a large impact on the EDS results as it affects the emission volume. For instance, the manganese concentration was only 17 at% in a different area with less dendrites on the electrode with manganese oxide deposited for 10 000 s at 1.55 V. Thus, care must be taken when comparing those numbers with more planar surfaces. Similarly, the EDS results in the low concentration electrolyte are affected by how much of the substrate

Table 5.2: EDS analysis of MnO_2 deposits on crystalline DSA electrodes.

Deposition conditions			**Concentration**[a] **at%**				
Electrolyte	Potential	Time	O	**Mn**	Ti	Ir	Ta
Low conc.	1.45 V	100 s	56	**0.9**	33	7	4
		1000 s	65	**3**	22	7	4
		10000 s	70	**15**	8	3	1
	1.55 V	100 s	58	**1**	28	8	4
		1000 s	72	**5**	15	5	3
		10000 s	69	**17**	7	2	1
High conc.	1.45 V	100 s	55	**0.3**	32	8	4
		1000 s	70	**5**	16	5	3
		10000 s	77	**12**	6	3	2
	1.55 V	100 s	61	**2**	27	6	3
		1000 s	76	**10**	8	4	2
		10000 s	63	**32**	3	1	0.6
	1.65 V	10000 s	78	**9**	8	3	2

[a] Small amounts of Cl, S and sometimes Na were detected, but disregarded.

is exposed by partial detachment of MnO_2 flakes. This makes it difficult to compare the two potentials in low concentration electrolyte, as well as to make comparisons between the electrolytes for the 10 000 s experiments. Taking this into account, the EDS results are quite similar regardless of the employed potential and the concentration of the electrolyte, with the exception of deposition for 10 000 s at 1.65 V. The manganese content was in that case lower than expected even though the deposit was planar, indicating a thinner deposit.

An example the of elemental maps obtained by EDS are shown in Figure 5.15. Overall, each element was distributed quite evenly over the entire surface. The small differences in intensity observed in the manganese map matched well with the iridium map as well as the mud-cracks in the SEM image, and was opposite to the titanium map. As for the pristine crystalline

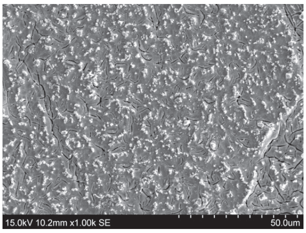

(a) SEM image

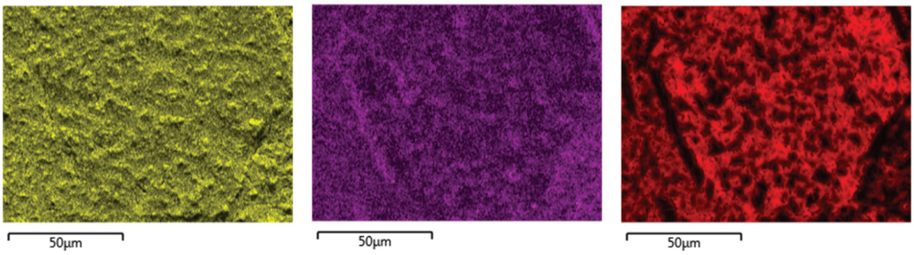

(b) O (c) Mn (d) Ti

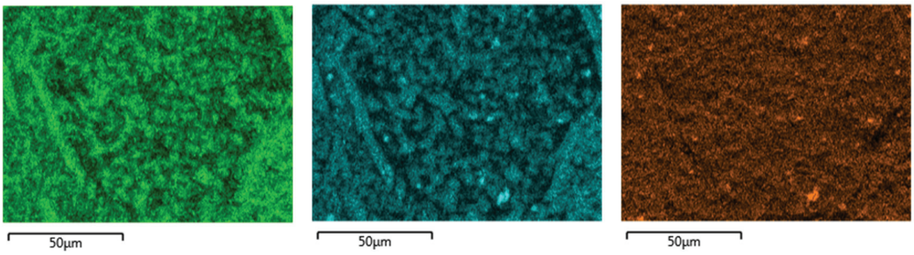

(e) Ir (f) Ta (g) Cl

Figure 5.15: EDS maps and SEM image of MnO_2 deposited on a crystalline DSA electrode for 100 s at 1.55 V in 2 mol L^{-1} H_2SO_4 + 0.15 mol L^{-1} Mn^{2+}.

electrode (Fig. 5.3), the chlorine map matched the most intense spots in the tantalum map (residual $TaCl_5$).

Use of MnO_2 covered electrodes

The performance of a MnO_2 covered crystalline DSA electrode was investigated by performing different experiments on the smooth MnO_2 deposit obtained after 10 000 s at 1.45 V in high concentration electrolyte (see Fig. 5.10c). Images of the surface before and after a linear sweep in 2 mol L^{-1} H_2SO_4 are displayed in Figure 5.16. Potential steps were also performed on

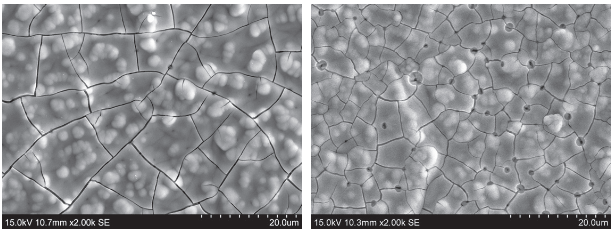

(a) (b)

Figure 5.16: SEM images of a MnO_2 covered crystalline DSA electrode (10 000 s at 1.45 V) before (a) and after (b) a linear sweep (1.45 V to 1.7 V, 5 mV min^{-1}) in 2 mol L^{-1} H_2SO_4.

MnO_2 deposit produced in the same manner, as described in Fig. 4.3. The resulting surfaces are displayed in Figures 5.17 and 5.18 for the potential steps in blank and Mn^{2+}-containing electrolytes, respectively.

Small cavities (around 1 μm diameter) were observed after the experiments in blank electrolyte (2 mol L^{-1} H_2SO_4), both for potential steps (Fig. 5.17) and LSV (Fig. 5.16b). There were also more cracks in the deposit after these experiments, and the cracks widened as the potential was increased in the potential step experiments. In contrast, there were fewer cracks in the deposit after potential steps in Mn^{2+}-containing electrolyte and no cavities were observed. Small amounts of dendrites were observed after each potential step in Mn^{2+}-containing electrolyte. Interestingly, the amount of dendrites formed at 1.55 V (Fig. 5.18a) was significantly lower than for the uncovered electrode (Fig. 5.13).

EDS analysis of the deposits obtained after performing experiments with MnO_2 covered crystalline DSAs are listed in Table 5.3. For the experiments conducted in blank electrolyte the manganese concentration decreased slightly during use, indicating some loss of MnO_2. However, in Mn^{2+}-containing electrolyte the manganese concentration increased up to 1.65 V before stabilizing. This indicates that the thickness of the MnO_2 deposit increased up to that potential, but remained relatively constant above 1.65 V for the short times used in this experiment (1 h).

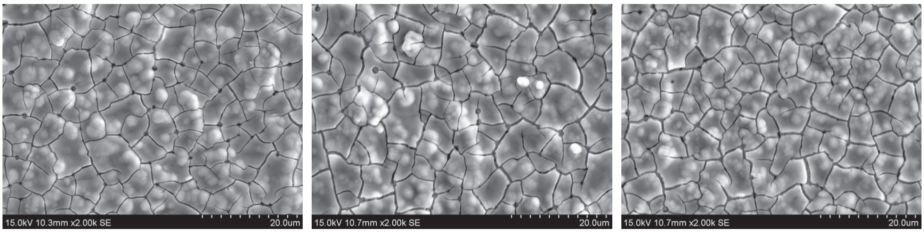

(a) 1.55 V. (b) 1.60 V. (c) 1.65 V.

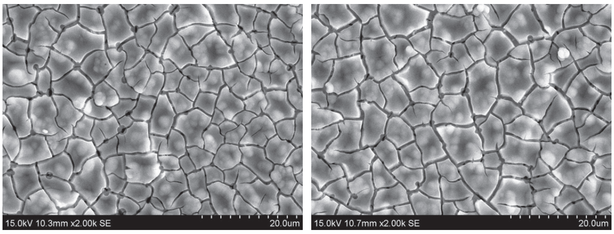

(d) 1.70 V. (e) 1.75 V.

Figure 5.17: SEM images of a MnO_2 covered crystalline DSA electrode (10 000 s at 1.45 V) after 1 hour at the specified potentials in $2\,\mathrm{mol\,L^{-1}}$ H_2SO_4.

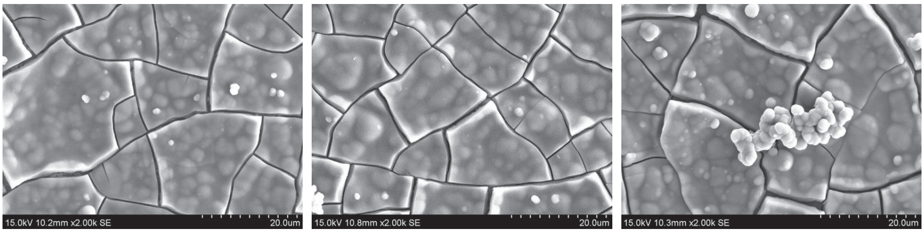

(a) 1.55 V. (b) 1.60 V. (c) 1.65 V.

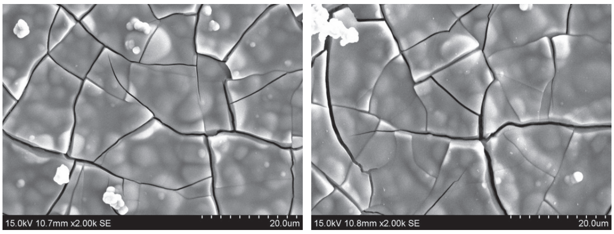

(d) 1.70 V. (e) 1.75 V.

Figure 5.18: SEM images of a MnO_2 covered crystalline DSA electrode (10 000 s at 1.45 V) after 1 hour at the specified potentials in $2\,\mathrm{mol\,L^{-1}}$ $H_2SO_4 + 0.15\,\mathrm{mol\,L^{-1}}\ Mn^{2+}$.

Table 5.3: EDS analysis of the surface after various procedures were performed on MnO_2 covered crystalline DSA electrodes.

Procedure		**Concentration**[a] **at%**				
		O	**Mn**	Ti	Ir	Ta
LSV in acid	1.70 V	77	**9**	8	3	2
Potential step in acid	1.55 V	77	**10**	8	3	2
	1.60 V	77	**9**	9	3	2
	1.65 V	78	**8**	9	3	2
	1.70 V	77	**8**	9	4	2
	1.75 V	77	**7**	10	4	2
Potential step in acid + Mn	1.55 V	75	**17**	5	2	1
	1.60 V	74	**20**	4	1	0.7
	1.65 V	69	**27**	2	0.7	0.4
	1.70 V	70	**26**	2	0.8	0.5
	1.75 V	69	**27**	2	0.7	0.4

[a] Small amounts of Cl and S were detected, but disregarded.

Electrochemical procedure for removal of MnO_2

A sequence of electrode potentials was applied in order to electrochemically remove MnO_2 formed under conditions resembling those in the zinc electrowinning process (see Fig. 4.4 and Tab. 4.6). Formation of MnO_2 on the electrode surface was hard to observe visually during the measurements because of the similar colours of the deposit and the pristine electrode surface. No visual changes to the deposit were observed during the first reduction step and the MnO_2 deposit was still present at the electrode surface at the end of the step. However, most of the deposit readily detached from the electrode surface when the working electrode was lifted out of the electrolyte after the first reduction step. The remaining deposit detached when even gently rinsing the surface with Milli-Q water. In contrast, no deposit detached if the sequence was interrupted before the first reduction step. If the sequence was continued after the first reduction step, gas evolution at 1.75 V caused most of the MnO_2 to detach. The time spent before most of the MnO_2 detached during oxygen evolution ranged from approximately 30 s to 60 s and seemed independent on the deposition conditions, i.e. deposition time and prelayer. After another reduction step the electrode was removed from the electrolyte and the remaining MnO_2 detached when rinsing with Milli-Q water.

As described in Table 4.6, the sequence was interrupted at different stages to acquire SEM images. The resulting images are displayed in Figures 5.19 and 5.20 for sequences with a prelayer of MnO_2 (1000 s at 1.45 V) and a hold time of 3 and 15 hours, respectively. When the sequence was interrupted after the hold at 3 or 15 hours, the surface was covered by a smooth MnO_2 deposit with some cracks, similar to those obtained previously at 1.45 V. No dendrites were observed. The EDS results indicated a thicker deposit after 15 hours (16 at% Mn) than after 3 hours (9 at% Mn). The surface appeared as the pristine electrode surface (Fig. 5.1a) after both the first and second reduction and for both hold times. This was supported by the EDS analysis, which showed no more than 0.2 at% Mn concentration in any of the displayed areas. When the sequence was performed without a prelayer, the surface was also devoid of MnO_2 after the second reduction (and presumably also after the first). This was also the result when the sequence was repeated 6 consecutive times with a 3 hours potential hold at 1.75 V.

Figure 5.21 shows a SEM image of the electrode surface after one full sequence followed by rinsing where loose flakes of MnO_2 were intentionally

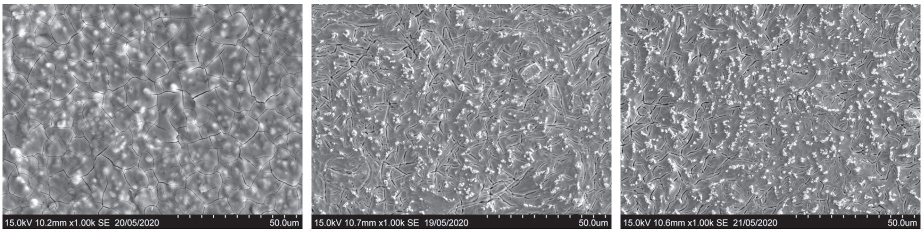

(a) After 3h at 1.75 V. (b) After 1. red. (c) After 2. red.

Figure 5.19: SEM images of the electrode surface at different stages during the procedure for electrochemical removal of MnO_2. A prelayer was formed prior to the 3 h at 1.75 V and the reduction steps lasted for 100 s.

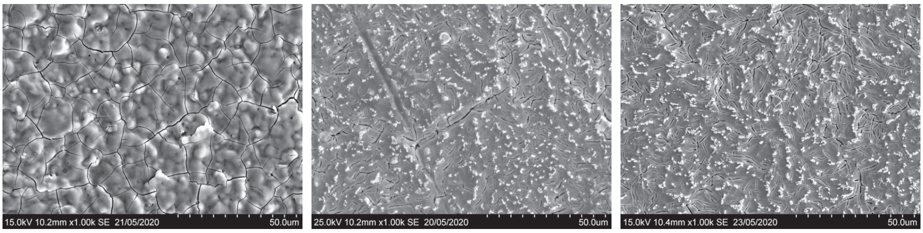

(a) After 15h at 1.75 V. (b) After 1. red. (c) After 2. red.

Figure 5.20: SEM images of the electrode surface at different stages during the procedure for electrochemical removal of MnO_2. A prelayer was formed prior to the 15 h at 1.75 V and the reduction steps lasted for 100 s.

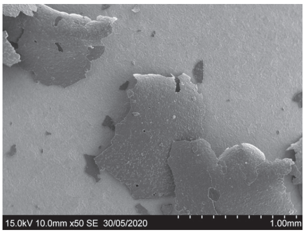

Figure 5.21: SEM image of the electrode surface after the sequence for electrochemical removal of MnO_2. Some of the detached deposit was intentionally left on the surface.

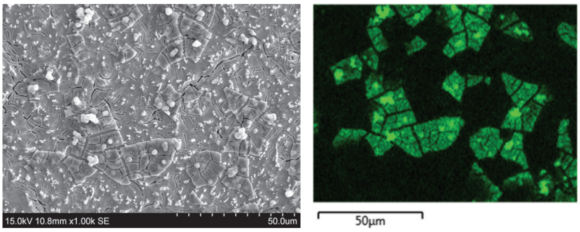

(a) SEM image. (b) Mn map.

Figure 5.22: SEM image and manganese elemental map of a 1.55 V MnO_2 deposit (10 000 s in 2 mol L^{-1} H_2SO_4 + 0.15 mol L^{-1} Mn^{2+}) after partial reduction (5 min at 0.4 V).

left on the surface. Clearly, not all of the deposit was reduced during the reduction steps, but the adhesion to the electrode surface was affected by the reduction.

Reduction of a deposit made at 1.55 V was also attempted, see Fig. 5.22. Some flakes of MnO_2 still adhered to the surface after the reduction step, whereas in other locations they had detached. Subsequently, an attempt was made to remove the flakes by gas evolution (5 min at 1.75 V), but the MnO_2 flakes did not seem affected by the gas evolution.

5.2.2 Amorphous DSA electrodes

MnO_2 was deposited on amorphous DSA electrodes from high concentration electrolyte (2 mol L^{-1} H_2SO_4 + 0.15 mol L^{-1} Mn^{2+}). The resulting deposits are displayed in Figures 5.23, 5.24 and 5.25 for the deposits obtained at 1.45 V, 1.55 V and 1.65 V, respectively. The corresponding elemental compositions found with EDS are given in Table 5.4.

The morphology of the deposits obtained after 10 000 s seem to be independent on the potential applied for the amorphous DSAs. Moreover, the EDS analysis gave only small differences in the manganese concentration for these deposits, indicating that their thickness was relatively similar. A smooth deposit with cracks was obtained, resembling the deposit obtained after 10 000 s at 1.45 V on the crystalline DSAs (Fig. 5.10c). However, there were fewer cracks in the deposit and less elevations were observed with the amorphous DSA electrodes. The latter can probably be attributed to the

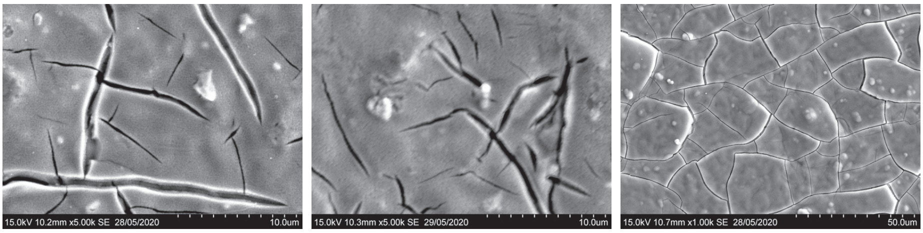

(a) 100 s. (b) 1000 s. (c) 10000 s.

Figure 5.23: SEM images of MnO_2 deposited for different times at 1.45 V on amorphous DSA electrodes in 2 mol L^{-1} H_2SO_4 + 0.15 mol L^{-1} Mn^{2+}.

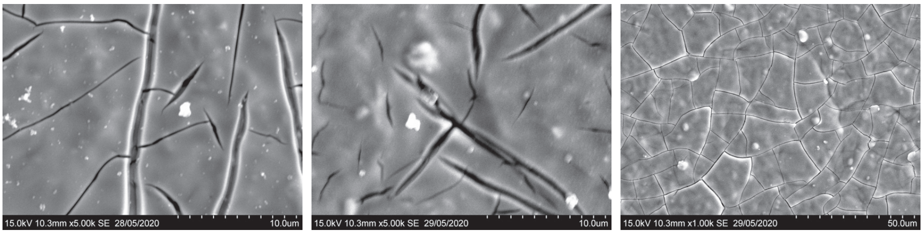

(a) 100 s. (b) 1000 s. (c) 10000 s.

Figure 5.24: SEM images of MnO_2 deposited for different times at 1.55 V on amorphous DSA electrodes in 2 mol L^{-1} H_2SO_4 + 0.15 mol L^{-1} Mn^{2+}.

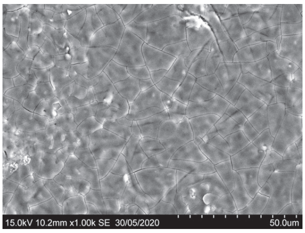

Figure 5.25: SEM image of MnO_2 deposited for 10 000 s at 1.65 V on an amorphous DSA electrode in 2 mol L^{-1} H_2SO_4 + 0.15 mol L^{-1} Mn^{2+}.

Table 5.4: EDS analysis of MnO_2 deposits obtained in $2\,mol\,L^{-1}$ H_2SO_4 + $0.15\,mol\,L^{-1}$ Mn^{2+} on amorphous DSA electrodes.

Deposition conditions		**Concentration**[a] **at%**				
Potential	Time	O	**Mn**	Ti	Ir	Ta
1.45 V	100 s	60	**0.8**	25	6	6
	1000 s	65	**2**	20	6	6
	10000 s	78	**10**	5	2	3
1.55 V	100 s	62	**1**	21	6	7
	1000 s	71	**3**	16	4	5
	10000 s	78	**9**	6	2	3
1.65 V	10000 s	78	**7**	8	3	3

[a] Small amounts of Cl and S were detected, but disregarded.

difference in surface topography between the pristine amorphous and crystalline electrodes (see Figs. 5.1 and 5.2). No dendrites were observed on any of the deposits formed on the amorphous electrodes after 10 000 s. In contrast, extensive dendrite formation was observed at 1.55 V for the crystalline DSA (Fig. 5.13c).

After deposition for shorter times (100 s and 1000 s), the surface looked much like the pristine electrode surface (Fig. 5.2b). Small nuclei (around 100 nm) were observed on the surface after deposition for 100 s at 1.55 V. Some had aggregated in clusters with diameter around 1 µm. These aggregates were also observed on the surface after 1000 s at 1.55 V.

5.2.3 Platinum

MnO_2 was deposited at platinum electrodes in low concentration electrolyte at 1.45 V and 1.55 V, see Figs. 5.26, 5.27 and 5.28. Aggregates of MnO_2 were observed after deposition for 100 s at both potentials (Figs. 5.26a and 5.28a). The STEM images (Fig. 5.27) showed that in addition to the aggregates, the platinum surface was covered by more than one layer of small MnO_2 spheres (less than 10 nm diameter) already after 10 s at 1.45 V,

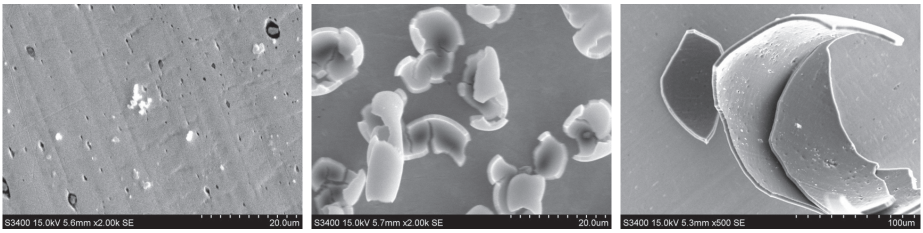

(a) 100 s. (b) 1000 s. (c) 10000 s.

Figure 5.26: SEM images of MnO_2 deposited for different times at 1.45 V on platinum electrodes in 0.1 mol L^{-1} H_2SO_4 + 5 mmol L^{-1} Mn^{2+}.

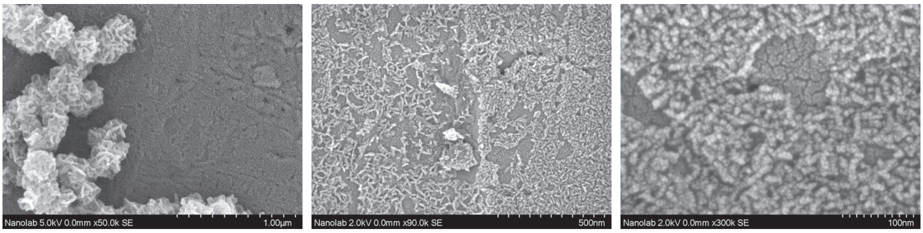

(a) (b) (c)

Figure 5.27: STEM images of MnO_2 deposited for 10 s at 1.45 V on a platinum electrode in 0.1 mol L^{-1} H_2SO_4 + 5 mmol L^{-1} Mn^{2+}.

corresponding to the peak in the current transient. The MnO_2 deposited for longer times (1000 s and 10 000 s) at both potentials seemed smooth and covered the electrode surface straight after removal from the electrolyte, but cracked and partially detached when drying. This also occurred for the deposit made on crystalline DSAs in low concentration electrolyte after 10 000 s (Figs. 5.7c and 5.8c). Some dendrites were observed after deposition for 1000 s at 1.55 V and also in smaller amounts after 10 000 s as indicated by the red circles in Figures 5.28b and 5.28c. Interestingly, the thickness of the deposit obtained after 10 000 s at 1.45 V was less than that obtained after 10 000 s at 1.55 V (see Figs. 5.26c and 5.28c). Moreover, the porosity of the 1.55 V deposit seemed higher than that of the 1.45 V deposit.

The effect of increasing the Mn^{2+}-concentration was investigated for a deposition time of 1000 s at both potentials, see Figure 5.29. A smooth, cracked deposit was obtained. Dendrites were observed on top of the smooth deposit at both potentials, but to a larger extent after deposition at 1.55 V. Other than this, the morphology appeared independent on the applied potential.

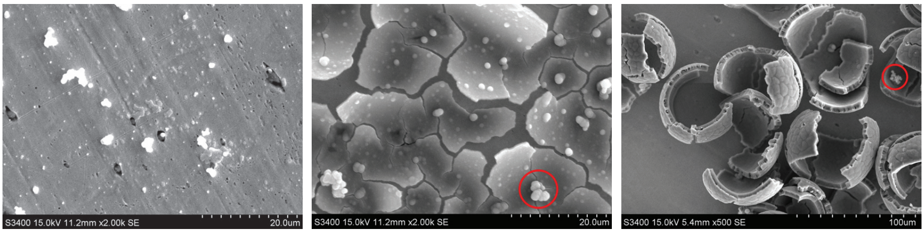

(a) 100 s. (b) 1000 s. (c) 10000 s.

Figure 5.28: SEM images of MnO_2 deposited for different times at 1.55 V on platinum electrodes in 0.1 mol L^{-1} H_2SO_4 + 5 mmol L^{-1} Mn^{2+}.

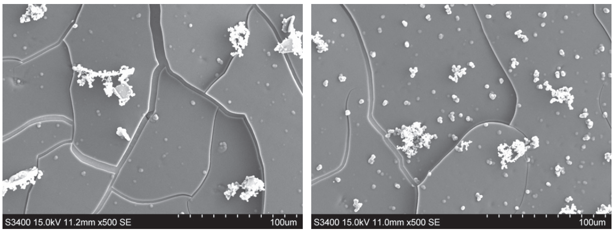

(a) 1.45 V. (b) 1.55 V.

Figure 5.29: SEM images of MnO_2 deposited for 1000 s on platinum electrodes in 0.1 mol L^{-1} H_2SO_4 + 0.15 mol L^{-1} Mn^{2+}.

The MnO_2 flakes had partially detached from the platinum surface. This was even more pronounced in other locations than shown here. Curling of the flakes was not observed in contrast to the deposit obtained at lower concentration of Mn^{2+} (Fig. 5.26b).

5.3 Electrochemical Characterization in Conventional Set-up

The experiments presented in this section was performed with a conventional three electrode set-up in 1 L cell as described in section 4.3.1. A procedure to determine the inner and outer charge of the DSA electrodes (see section 3.4) was performed after the initial preconditioning and at various stages during the series of experiments. The values of inner and outer charge obtained prior to potential step measurements (sec. 5.3.3) as well as prior to performing the procedure for removal of MnO_2 (sec. 5.3.4) are presented in Appendix B, along with the Matlab code used to find the values. The outer charge of the crystalline DSAs was typically around 10 mC after the initial preconditioning and increased to around 15 mC after some use. For amorphous DSA electrodes, the outer charge was typically between 10-20 mC after the initial preconditioning, but increased to around 40 mC after some use.

5.3.1 Cyclic Voltammetry

In this section the cyclic voltammograms obtained at high sweep rate ($100\,\mathrm{mV\,s^{-1}}$) are presented first, followed by CVs obtained at slow sweep rate ($5\,\mathrm{mV\,s^{-1}}$). Where relevant, the CVs acquired in low concentration electrolyte ($0.1\,\mathrm{mol\,L^{-1}}$ H_2SO_4 with or without $5\,\mathrm{mmol\,L^{-1}}$ Mn^{2+}) are presented before those acquired in high concentration electrolyte ($2\,\mathrm{mol\,L^{-1}}$ H_2SO_4 with or without $0.15\,\mathrm{mol\,L^{-1}}$ Mn^{2+}).

Crystalline DSA electrodes

Cyclic voltammograms obtained with crystalline DSAs in low concentration electrolyte at scan rate $100\,\mathrm{mV\,s^{-1}}$ are presented in Figure 5.30. The voltammograms in blank electrolyte were similar and resembles the same features as the ones in Mn^{2+}-containing electrolyte, but the magnitude of the current was slightly higher in blank electrolyte. A comparison between the two electrolytes is given in Figure 5.31. The onset potential for oxygen evolution differed slightly between the two electrolytes, with the blank electrolyte being more favorable for OER. In addition, a small reduction peak was observed around 1.35 V in the negative-going sweep when Mn^{2+} was present in the electrolyte.

Manganese oxide deposition and reduction were further studied by running CVs with sweep rate $5\,\mathrm{mV\,s^{-1}}$ for a number of upper reversal potentials (Figure 5.32). The same CVs are also presented in Figure 5.33 were they are compared with the CVs obtained in blank electrolyte. The onset of manganese oxide deposition occurred around 1.2 V (e.g. Fig 5.33b). A small oxidation shoulder was observed around 1.45 V in the positive-going sweep. This shoulder increased in size as the upper reversal potential increased, as indicated by an arrow in Figure 5.32b. Interestingly, an oxidation peak was observed in the negative-going scan slightly negative of 1.45 V (most

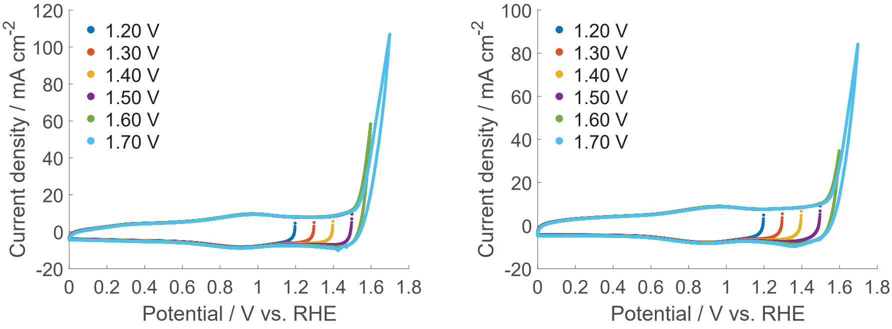

(a)

(b)

Figure 5.30: Cyclic voltammograms of a crystalline DSA electrode in (a) 0.1 mol L^{-1} H_2SO_4 and in (b) 0.1 mol L^{-1} H_2SO_4 + 5 mmol L^{-1} Mn^{2+} at sweep rate 100 mV s^{-1}.

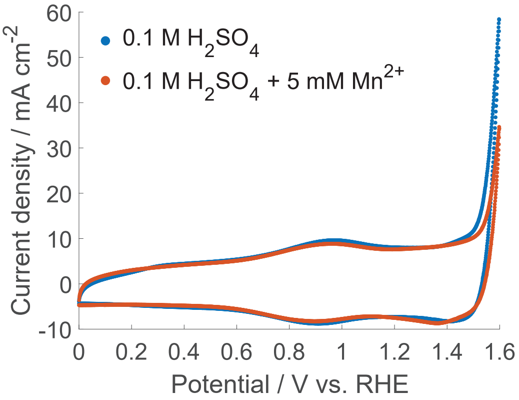

Figure 5.31: Cyclic voltammograms of a crystalline DSA electrode in 0.1 mol L^{-1} H_2SO_4 (blue) and in 0.1 mol L^{-1} H_2SO_4 + 5 mmol L^{-1} Mn^{2+} (red) at sweep rate 100 mV s^{-1} with upper limit 1.6 V.

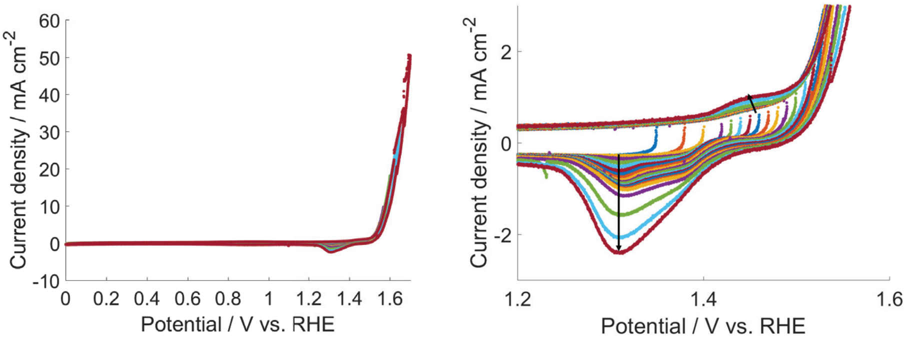

(a) (b)

Figure 5.32: Cyclic voltammograms of a crystalline DSA electrode with varying upper limits in 0.1 mol L^{-1} H_2SO_4 + 5 mmol L^{-1} Mn^{2+} at sweep rate 5 mV s^{-1}. An enlargement of the manganese oxide deposition and reduction region is shown in (b) with arrows indicating increasing upper limit.

apparent in Figs. 5.33d, 5.33e and 5.33f). This was also seen on platinum. A reduction peak was observed slightly positive of 1.3 V, with a shoulder extending to more positive potentials (approximately to 1.4 V). The reduction peak (and shoulder) increased in height as the upper limit increased as indicated by an arrow in Fig 5.32b.

The crystalline DSAs were also employed in high concentration electrolyte. Cyclic voltammograms obtained at sweep rate 100 mV s^{-1} in high concentration electrolyte are displayed in Figure 5.34. A comparison between blank and Mn^{2+}-containing high concentration electrolyte is shown in Figure 5.35. Manganese oxide deposition started around 1.3 V and gave a significant current prior to OER. At 1.6 V the current density was still higher in Mn^{2+}-containing electrolyte, whereas at 1.7 V the current densities were almost equal in the two electrolytes. A reduction peak was observed around 1.4 V in Mn^{2+}-containing electrolyte, with a broad shoulder extending towards more negative potentials.

When comparing with the low concentration electrolyte, the current density at 1.7 V was unexpectedly higher in 2 mol L^{-1} than in 0.1 mol L^{-1} H_2SO_4. This may be due to uncompensated resistance since there were differences in the resistances of the electrolytes. Even though iR-compensation was employed, it seems that it was not sufficient to compensate the voltage drop at such high currents. Another difference between the high and low con-

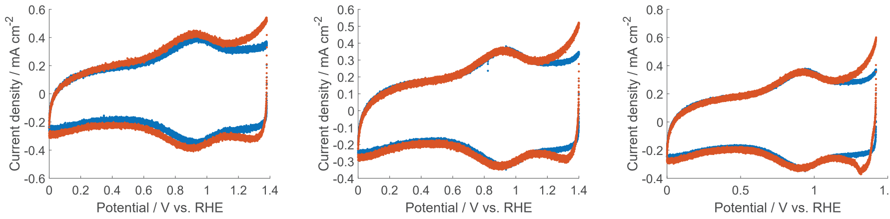

(a) 1.38 V (b) 1.40 V (c) 1.42 V

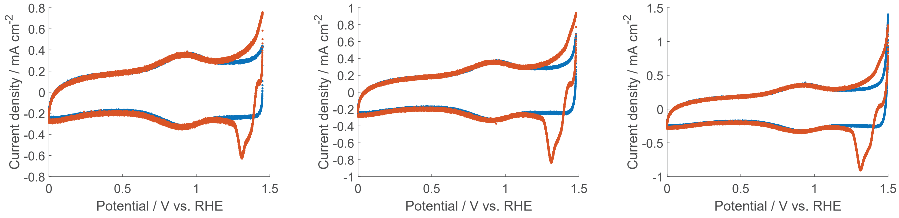

(d) 1.45 V (e) 1.48 V (f) 1.50 V

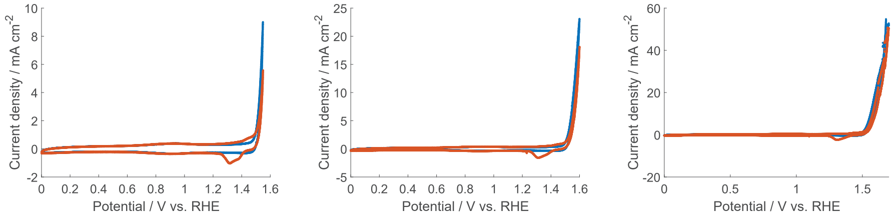

(g) 1.55 V (h) 1.60 V (i) 1.70 V

Figure 5.33: Cyclic voltammograms of crystalline DSA electrodes with varying upper limits recorded at sweep rate 5 mV s^{-1} in 0.1 mol L^{-1} H_2SO_4 (blue) and 0.1 mol L^{-1} H_2SO_4 + 5 mmol L^{-1} Mn^{2+} (red).

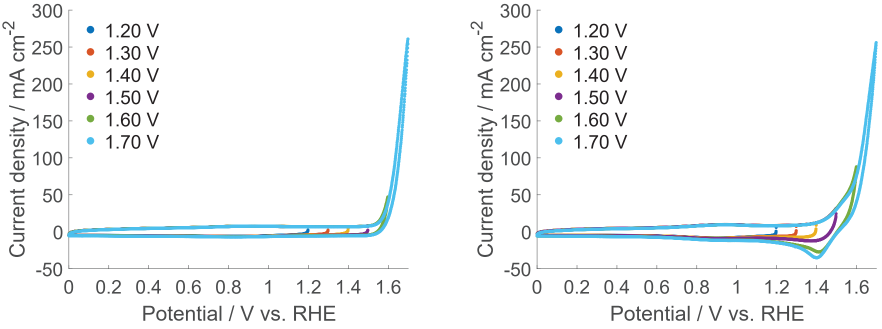

(a)

(b)

Figure 5.34: Cyclic voltammograms of a crystalline DSA electrode with varying upper limits in 2 mol L^{-1} H_2SO_4 (a) and in 2 mol L^{-1} H_2SO_4 + 0.15 mol L^{-1} Mn^{2+} (b) at sweep rate 100 mV s^{-1}.

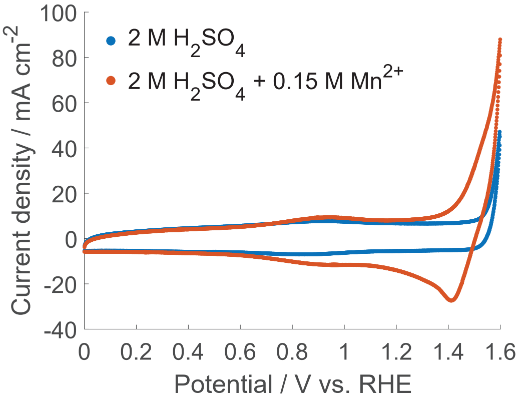

Figure 5.35: Cyclic voltammograms of a crystalline DSA electrode in 2 mol L^{-1} H_2SO_4 (blue) and in 2 mol L^{-1} H_2SO_4 + 0.15 mol L^{-1} Mn^{2+} (red) at sweep rate 100 mV s^{-1} with upper limit 1.6 V.

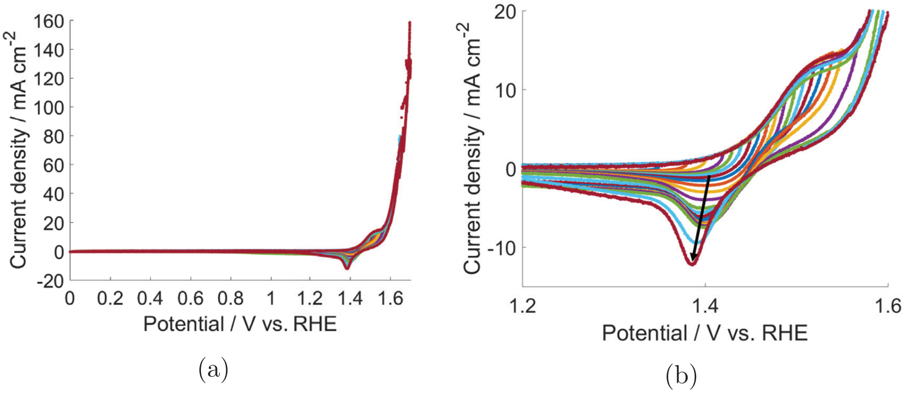

(a)

(b)

Figure 5.36: Cyclic voltammograms of a crystalline DSA electrode with varying upper limits in 2 mol L^{-1} H_2SO_4 + 0.15 mol L^{-1} Mn^{2+} at sweep rate 5 mV s^{-1}. An enlargement of the manganese oxide deposition and reduction region is shown in (b) with an arrow indicating increasing upper limit.

centration electrolytes was the broad shoulder that was observed after the reduction peak in the high concentration electrolyte. A higher overpotential is required to reduce the manganese oxide formed in the high concentration electrolyte.

CVs of the crystalline DSAs obtained at 5 mV s^{-1} in high concentration electrolyte are presented in Figures 5.36 and 5.37. Oxidation of Mn^{2+} started around 1.3 V and an oxidation peak was observed at approximately 1.5 V in the positive-going scan. The oxidation peak observed in the negative-going scan in the low concentration electrolyte was not as apparent in the high concentration electrolyte, but a change of slope was observed around 1.5 V in scans with upper reversal potential 1.55 V and higher (see Figs. 5.37g and 5.37h). A reduction peak was observed slightly negative of 1.4 V. As the upper reversal potential increased, a shoulder extending to more negative potentials appeared. For high upper reversal potentials, the shoulder extended all the way to 0.7 V (Figs. 5.37g and 5.37h). The shoulder was also seen for higher sweep rate (Fig. 5.35).

The position of the reduction peak in high concentration electrolyte was slightly shifted compared to the low concentration electrolyte. In the latter, a peak was observed around 1.3 V with a shoulder extending to more positive potentials (1.4 V).

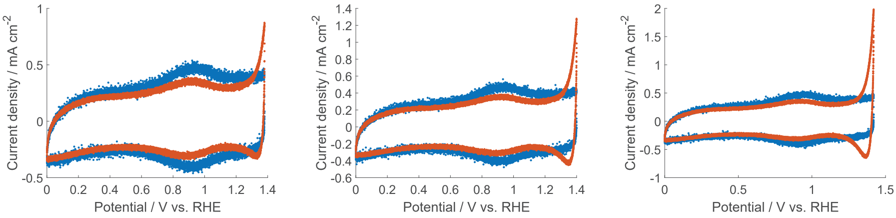

(a) 1.38 V (b) 1.40 V (c) 1.42 V

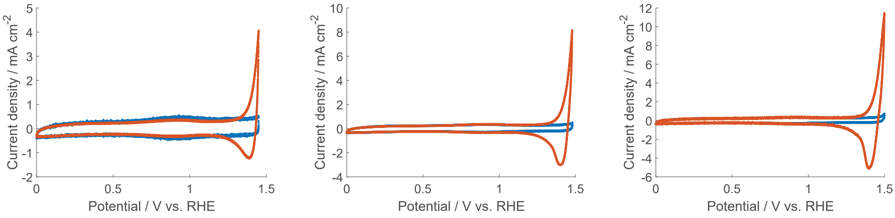

(d) 1.45 V (e) 1.48 V (f) 1.50 V

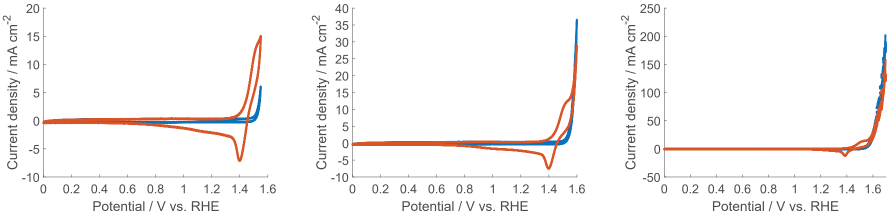

(g) 1.55 V (h) 1.60 V (i) 1.70 V

Figure 5.37: Cyclic voltammograms of crystalline DSA electrodes with varying upper limits recorded at sweep rate $5\,\mathrm{mV\,s^{-1}}$ in $2\,\mathrm{mol\ L^{-1}}$ H_2SO_4 (blue) and $2\,\mathrm{mol\ L^{-1}}$ H_2SO_4 + $0.15\,\mathrm{mol\ L^{-1}}$ Mn^{2+} (red).

Amorphous DSA electrodes

Cyclic voltammograms were acquired with amorphous DSAs in high concentration electrolyte, both at 100 mV s^{-1} (Fig. 5.38 and 5.39) and 5 mV s^{-1} (Fig. 5.40 and 5.41). The onset of Mn^{2+} oxidation occurred around 1.3 V. A slight change of slope was observed around 1.45 V in the negative-going scan for slow CVs with upper reversal potential 1.5 V or higher. A reduction peak was observed around 1.4 V with a small shoulder extending to more negative potentials, most pronounced in Fig. 5.41f.

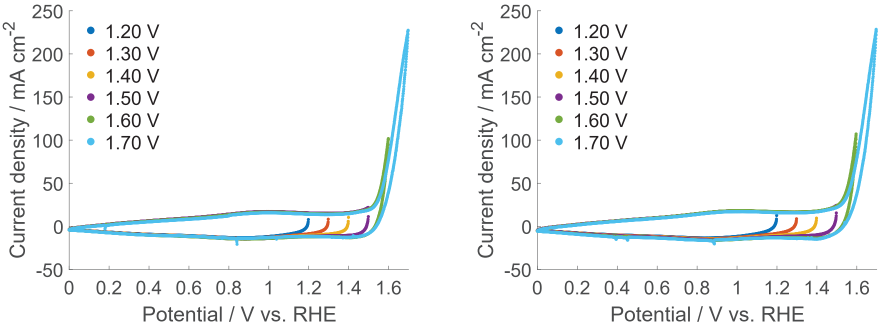

(a)

(b)

Figure 5.38: Cyclic voltammograms of an amorphous DSA electrode with varying upper limits in (a) 2 mol L^{-1} H_2SO_4 and in (b) 2 mol L^{-1} H_2SO_4 + 0.15 mol L^{-1} Mn^{2+} at sweep rate 100 mV s^{-1}.

The voltammograms recorded in blank and Mn^{2+}-containing electrolyte were quite similar despite the high concentration of Mn^{2+}. This indicates a suppression of MnO_2 deposition on amorphous DSAs (Fig. 5.41) compared to crystalline DSAs (Fig. 5.37). The voltammograms obtained with amorphous DSAs in blank electrolyte (Fig. 5.38a) resembled the same features as the crystalline DSAs (Fig. 5.34a), though higher current densities were obtained with the amorphous electrodes. The differences between the crystalline and amorphous DSAs will be further investigated in the section on linear sweep voltammetry (section 5.3.2).

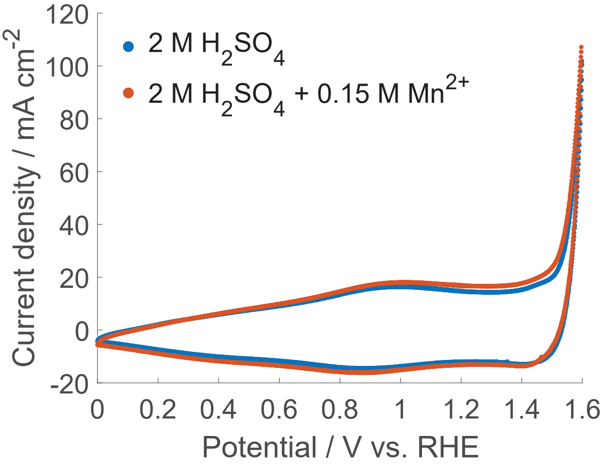

Figure 5.39: Cyclic voltammograms of an amorphous DSA electrode in $2\,\mathrm{mol\,L^{-1}}$ H_2SO_4 (blue) and in $2\,\mathrm{mol\,L^{-1}}$ H_2SO_4 + $0.15\,\mathrm{mol\,L^{-1}}$ Mn^{2+} (red) at sweep rate $100\,\mathrm{mV\,s^{-1}}$ with upper limit 1.6 V.

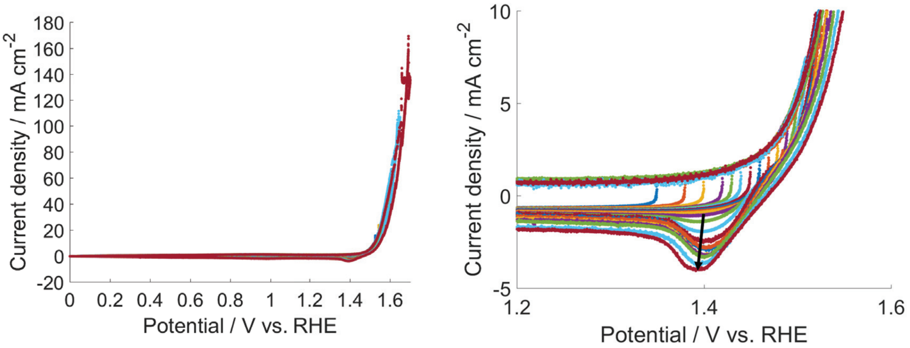

(a)

(b)

Figure 5.40: Cyclic voltammograms of an amorphous DSA electrode with varying upper limits in $2\,\mathrm{mol\,L^{-1}}$ H_2SO_4 + $0.15\,\mathrm{mol\,L^{-1}}$ Mn^{2+} at sweep rate $5\,\mathrm{mV\,s^{-1}}$. An enlargement of the manganese oxide deposition and reduction region is shown in (b) with an arrow indicating increasing upper limit.

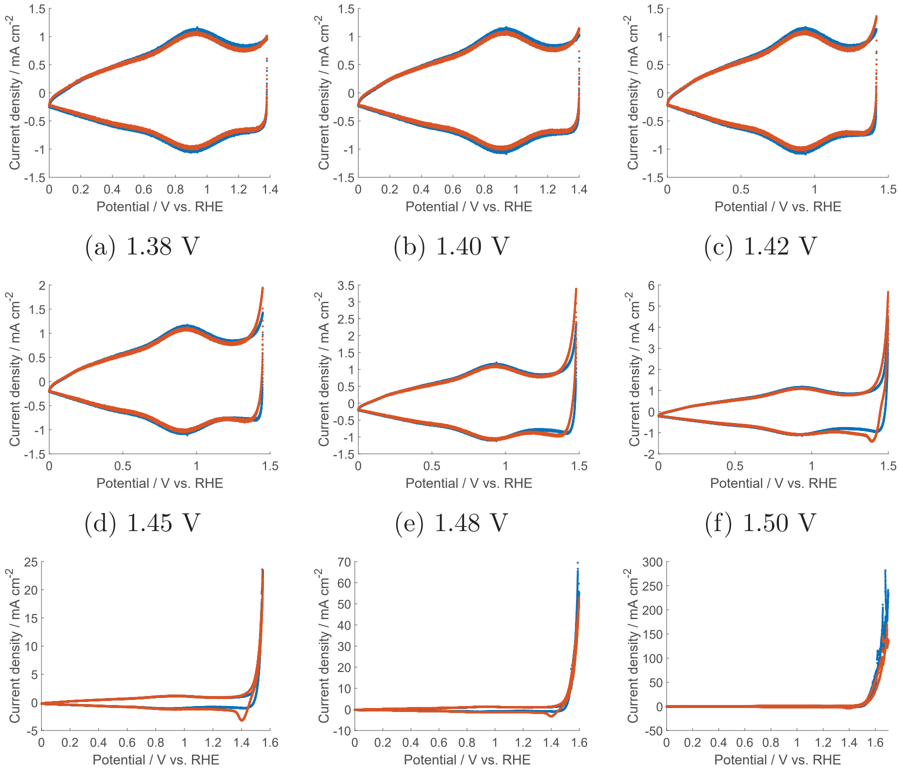

(a) 1.38 V

(b) 1.40 V

(c) 1.42 V

(d) 1.45 V

(e) 1.48 V

(f) 1.50 V

(g) 1.55 V

(h) 1.60 V

(i) 1.70 V

Figure 5.41: Cyclic voltammograms of amorphous DSA electrodes with varying upper limits recorded at sweep rate $5\,\mathrm{mV\,s^{-1}}$ in $2\,\mathrm{mol\,L^{-1}}$ H_2SO_4 (blue) and $2\,\mathrm{mol\,L^{-1}}$ H_2SO_4 + $0.15\,\mathrm{mol\,L^{-1}}$ Mn^{2+} (red).

Platinum

Cyclic voltammograms of platinum electrodes in the conventional three-electrode set-up are presented in this section. CVs of platinum were also obtained with the EQCM set-up and those will be presented in section 5.4. The voltammograms obtained at sweep rate $100\,\mathrm{mV\,s^{-1}}$ in low concentration electrolyte are presented in Figures 5.42 and 5.43. The onset of $\mathrm{Mn^{2+}}$ oxidation occurred around 1.35 V. A shoulder was observed around 1.6 V in the positive-going sweep. A reduction peak for manganese oxide appeared positive of 1.35 V, whereas the platinum oxide reduction peak was positive of 0.7 V. The platinum oxide reduction peak was smaller in $\mathrm{Mn^{2+}}$-containing electrolyte, probably because formation of $\mathrm{MnO_2}$ resulted in less PtO formation. As expected, the hydrogen adsorption and desorption region was not affected by the presence of $\mathrm{Mn^{2+}}$.

Voltammograms obtained at slow scan rate ($5\,\mathrm{mV\,s^{-1}}$) in low concentration electrolyte are presented in Figure 5.44 and 5.45. These show an onset of $\mathrm{Mn^{2+}}$ oxidation before 1.4 V. A distinct oxidation peak was observed slightly above 1.45 V. When the potential was reversed in the rising part of the oxidation peak (1.42 V to 1.45 V) the current continued to increase after change of scan direction (Fig. 5.44b). A second oxidation peak was observed around 1.47 V in the negative-going scan for voltammograms with sufficiently positive upper reversal potentials. This oxidation peak in the negative-going scan was also observed with the crystalline DSAs in the same electrolyte (e.g. Fig. 5.33e). Two reduction peaks were observed in the slow CVs with high upper reversal potentials (1.6 and 1.7 V); the first reduction peak positive of 1.3 V and the second at 1.2 V. The reduction peak around 1.3 V was observed for all upper reversal potentials with shoulders extending in both directions.

The platinum electrodes were also tested in an electrolyte with low concentration of $\mathrm{H_2SO_4}$ ($0.1\,\mathrm{mol\,L^{-1}}$), but with high concentration of $\mathrm{Mn^{2+}}$ ($0.15\,\mathrm{mol\,L^{-1}}$). Cyclic voltammograms obtained at scan rate $100\,\mathrm{mV\,s^{-1}}$ are presented in Figure 5.46. In Figure 5.47, a voltammogram obtained with sweep rate $5\,\mathrm{mV\,s^{-1}}$ in this electrolyte is compared to a CV with low concentrations of both acid and $\mathrm{Mn^{2+}}$. The onset of $\mathrm{Mn^{2+}}$ oxidation occurred around 1.25 V for both sweep rates, and an oxidation peak was observed positive of 1.50 V. For voltammograms with sufficiently positive upper reversal potential, an oxidation shoulder was observed in the negative-going sweep around 1.4-1.5 V (position dependent on the upper reversal potential).

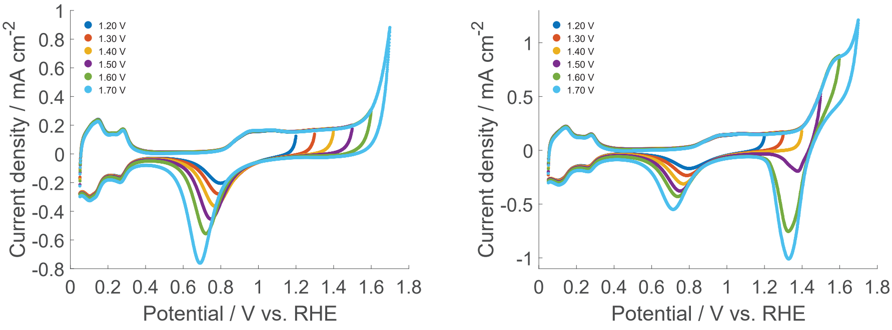

(a) (b)

Figure 5.42: Cyclic voltammograms of a platinum electrode with varying upper limits in (a) 0.1 mol L^{-1} H_2SO_4 and in (b) 0.1 mol L^{-1} H_2SO_4 + 5 mmol L^{-1} Mn^{2+} at sweep rate 100 mV s^{-1}.

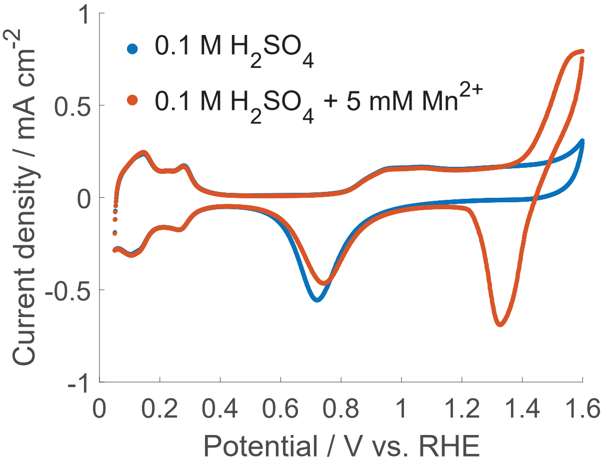

Figure 5.43: Cyclic voltammograms of a platinum electrode in 0.1 mol L^{-1} H_2SO_4 (blue) and in 0.1 mol L^{-1} H_2SO_4 + 5 mmol L^{-1} Mn^{2+} (red) at sweep rate 100 mV s^{-1} with upper limit 1.6 V.

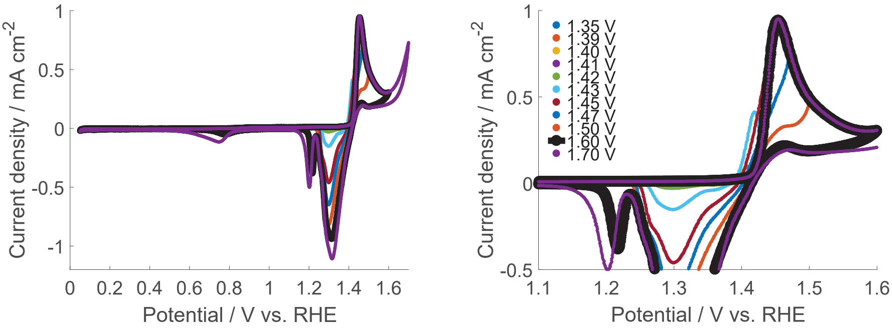

(a) (b)

Figure 5.44: Cyclic voltammograms of a platinum electrode with varying upper limits in 0.1 mol L^{-1} H_2SO_4 + 5 mmol L^{-1} Mn^{2+} at sweep rate 5 mV s^{-1}. An enlargement of the manganese oxide deposition region is shown in (b). The black bold line represent the CV with upper reversal potential 1.6 V.

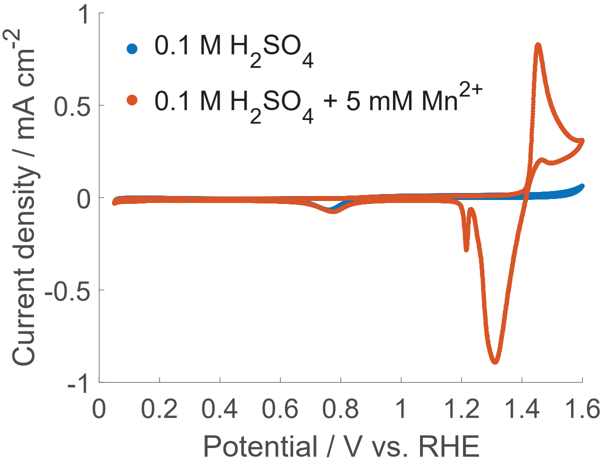

Figure 5.45: Cyclic voltammograms of a platinum electrode in 0.1 mol L^{-1} H_2SO_4 (blue) and in 0.1 mol L^{-1} H_2SO_4 + 5 mmol L^{-1} Mn^{2+} (red) at sweep rate 5 mV s^{-1} with upper limit 1.6 V.

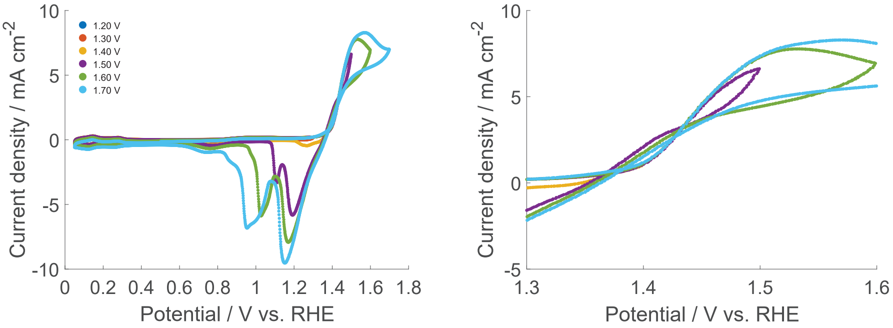

(a)

(b)

Figure 5.46: Cyclic voltammograms of a platinum electrode with varying upper limits in 0.1 mol L^{-1} H_2SO_4 + 0.15 mol L^{-1} Mn^{2+} at sweep rate 100 mV s^{-1}. An enlargement of the manganese oxide deposition region is shown in (b).

The manganese oxide was significantly harder to remove in the electrolyte with high manganese concentration. In the slow CVs, a reduction peak was observed at 1.18 V followed by a slowly diminishing negative plateau current. In fact, the current stayed negative all the way until Mn^{2+} oxidation started again in the positive going sweep of the next cycle (around 1.25 V), indicating that not all of the MnO_2 had been reduced during the cycle. In the fast CVs, two reduction peaks were observed for the highest upper reversal potentials. The first reduction peak was located slightly below 1.2 V and displayed a small shift towards more negative potentials as the upper reversal potential increased. However, the second reduction peak (1.1-0.9 V) shifted significantly and also changed shape (gained shoulders on both sides) as the upper reversal potential increased.

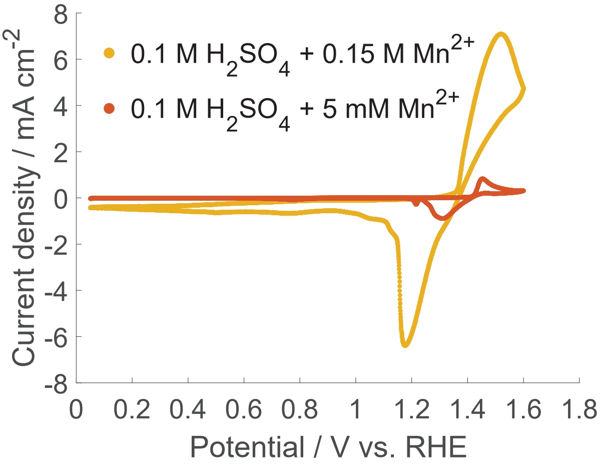

Figure 5.47: Cyclic voltammograms of a platinum electrode with varying upper limits in 0.1 mol L^{-1} H_2SO_4 + 5 mmol L^{-1} Mn^{2+} and in 0.1 mol L^{-1} H_2SO_4 + 0.15 mol L^{-1} at sweep rate 5 mV s^{-1}.

5.3.2 Linear Sweep Voltammetry

Linear sweep voltammograms of crystalline DSA electrodes in low and high concentration electrolytes are shown in Figures 5.48 and 5.49, respectively. In the lower potential region the current density is higher in Mn^{2+}-containing electrolyte than in the blank electrolyte, since oxidation of Mn^{2+} has a lower overpotential than OER. However, at higher potentials the current densities were quite similar in blank and Mn^{2+}-containing electrolyte though slightly higher in acid. The DSA electrodes are expected to display a higher electrocatalytic activity towards OER in blank electrolyte than in Mn^{2+}-containing electrolyte. This is because the electrode surface is covered by MnO_2 by the end of a LSV in Mn^{2+}-containing electrolyte which is expected to have a poorer electrocatalytic activity towards OER than IrO_2. In Mn^{2+}-containing electrolyte, the oxidation of Mn^{2+} will also contribute to the measured current. The difference in activity towards OER was investigated by performing LSV in 2 mol L^{-1} H_2SO_4 on a MnO_2-covered crystalline DSA (Figure 5.50).

The current density in blank electrolyte was higher in 2 mol L^{-1} H_2SO_4 than in 0.1 mol L^{-1} H_2SO_4 at potentials above 1.55 V. It seems that the electrolyte resistance was not properly compensated in the low concentration

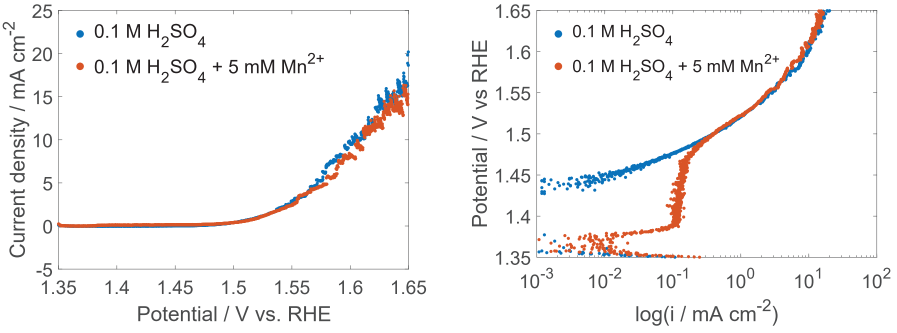

(a)

(b)

Figure 5.48: Linear sweep voltammetry of crystalline DSA electrodes in 0.1 mol L^{-1} H_2SO_4 (blue) and 0.1 mol L^{-1} H_2SO_4 + 5 mmol L^{-1} Mn^{2+} (red) at sweep rate 5 mV min^{-1}, (a) linear and (b) logarithmic current. Saturated Na_2SO_4 present in both experiments.

electrolyte, which had a higher electrolyte resistance even though saturated Na_2SO_4 was added. A more pronounced deviation from a linear curve in the logarithmic presentation of the current density (non-Tafel behavior) was observed with the low concentration electrolyte (Fig. 5.48b) than in high concentration electrolyte (Fig. 5.49b). Signs of uncompensated resistance was also found in the cyclic voltammograms (section 5.3.1).

When Mn^{2+} was present, a plateau current (0.1 mA cm^{-2}) was observed between 1.39 V and 1.47 V in the low concentration electrolyte (Fig. 5.48b). However, in 2 mol L^{-1} H_2SO_4 + 0.15 mol L^{-1} Mn^{2+} (Fig. 5.49b) an oxidation peak was observed at 1.45 V and higher current densities were observed.

Linear sweep voltammograms of amorphous DSA electrodes are shown in Figure 5.51. The outer charge of the two electrodes was equal prior to the linear sweep (24 mC). The shapes of the curves were quite similar to the crystalline DSA electrode, though there was a difference in the magnitude of the current (Figure 5.49).

The performance of the amorphous and crystalline DSA electrodes are compared in Figures 5.52 and 5.53 for blank (2 mol L^{-1} H_2SO_4) and Mn^{2+}-containing electrolyte (2 mol L^{-1} H_2SO_4 + 0.15 mol L^{-1} Mn^{2+}), respectively. The amorphous electrode is more active (per geometric area) than the crystalline electrode in both electrolytes. However, the Mn^{2+} oxidation peak was shifted to more positive potentials by more than 10 mV for the

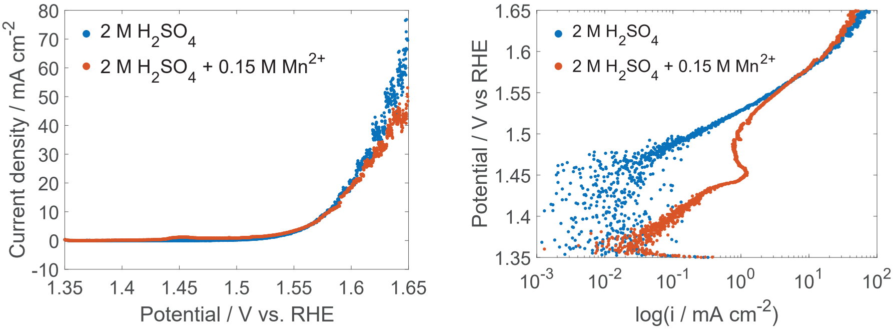

(a) (b)

Figure 5.49: Linear sweep voltammetry of crystalline DSA electrodes in 2 mol L^{-1} H_2SO_4 (blue) and 2 mol L^{-1} H_2SO_4 + 0.15 mol L^{-1} Mn^{2+} (red) at sweep rate 5 mV min^{-1}, (a) linear and (b) logarithmic current.

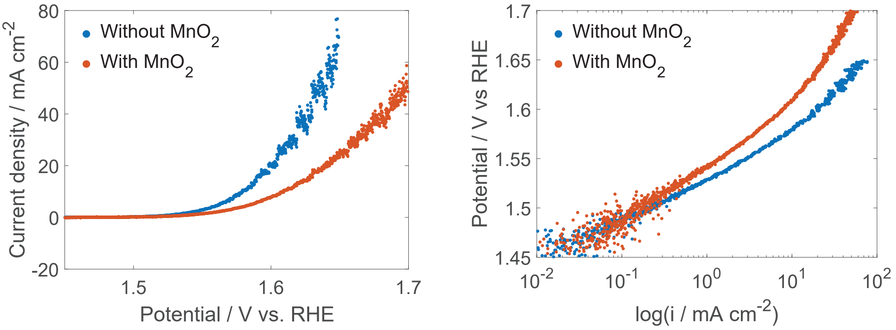

(a) (b)

Figure 5.50: Linear sweep voltammetry of crystalline DSA electrodes (blue) and a crystalline DSA with a MnO_2 layer (1.45 V, 10 000 s) (red) in 2 mol L^{-1} H_2SO_4 at sweep rate 5 mV min^{-1}, (a) linear and (b) logarithmic current.

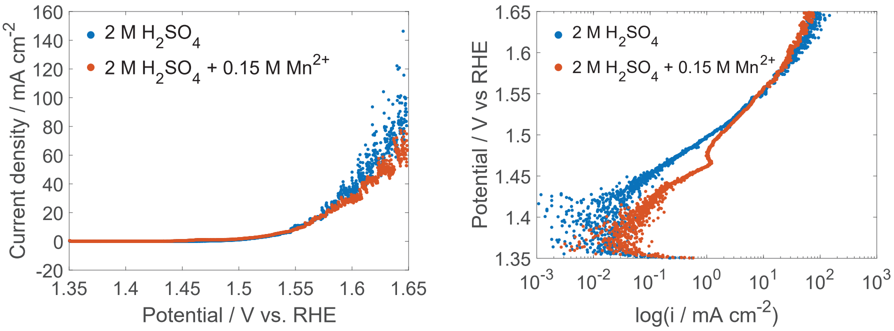

(a) (b)

Figure 5.51: Linear sweep voltammetry of amorphous DSA electrodes in 2 mol L^{-1} H_2SO_4 (blue) and 2 mol L^{-1} H_2SO_4 + 0.15 mol L^{-1} Mn^{2+} (red) at sweep rate 5 mV min^{-1}, (a) linear and (b) logarithmic current.

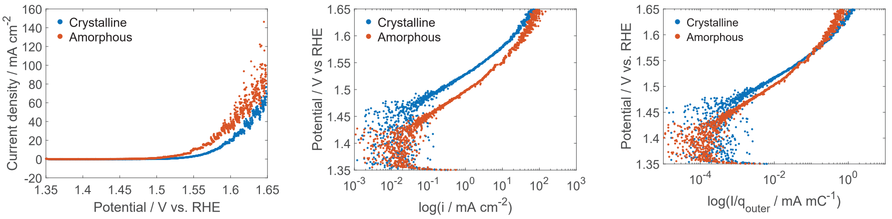

(a) (b) (c)

Figure 5.52: Linear sweep voltammetry of crystalline (blue) and amorphous (red) DSA electrodes in 2 mol L^{-1} H_2SO_4 at sweep rate 5 mV min^{-1}, (a) linear current, (b) logarithmic current and (c) outer charge normalized logarithmic current.

amorphous electrodes (Fig. 5.53b). This demonstrates that the amorphous DSA is less active towards oxidation of Mn^{2+} than the crystalline DSA, as was also observed in the cyclic voltammograms (cf. Figs. 5.41 and 5.37).

The outer charge measured after the end of the linear sweep in blank electrolyte was more than double for the amorphous electrode than for the crystalline electrode (38 mC and 15 mC, respectively). Nevertheless, the amorphous electrodes were more active in 2 mol L^{-1} H_2SO_4 up to about 1.57 V where the activity of the crystalline electrode surpassed that of the amorphous electrode (Fig. 5.52c).

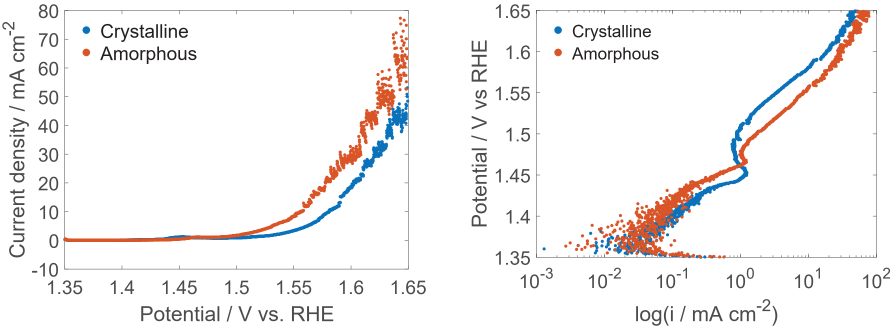

(a) (b)

Figure 5.53: Linear sweep voltammetry of crystalline (blue) and amorphous (red) DSA electrodes in 2 mol L^{-1} H_2SO_4 + 0.15 mol L^{-1} Mn^{2+} at sweep rate 5 mV min^{-1}, (a) linear and (b) logarithmic current.

5.3.3 Chronoamperometry

In this section current transients are presented from the potential steps that lead to the MnO_2 deposits investigated with SEM and EDS in section 5.2. The deposits investigated with SEM and EDS were obtained after different hold times (100, 1000 and 10 000 s). However, in this section the current transients are mainly presented on a 1000 s time scale as the relevant features are in most cases displayed on this time scale. The nucleation mechanism is not considered in this section, but is rather evaluated in section 5.8 together with result from the EQCM measurements.

Crystalline DSA electrodes

The current transients obtained with crystalline DSA electrodes in low and high concentration electrolytes are displayed in Figures 5.54 and 5.55, respectively. As expected, the current density in blank electrolyte at 1.45 V was small in both 0.1 mol L^{-1} and 2 mol L^{-1} H_2SO_4. At 1.55 V, the current density in the low concentration electrolyte was significantly higher in blank than in the corresponding Mn^{2+}-containing electrolyte (Fig. 5.54b), demonstrating that the MnO_2 formed on the surface was less active towards OER than the pristine crystalline DSA. However, in high concentration electrolyte the current densities were of similar magnitude in blank and Mn^{2+}-containing electrolyte both at 1.55 V and at 1.65 V (Figs. 5.55b and

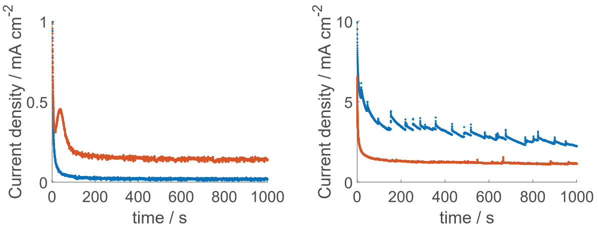

(a) 1.45 V. (b) 1.55 V.

Figure 5.54: Current transients during potential steps to different potentials on crystalline DSA electrodes in 0.1 mol L^{-1} H_2SO_4 (blue) and in 0.1 mol L^{-1} H_2SO_4 + 5 mmol L^{-1} Mn^{2+} (red).

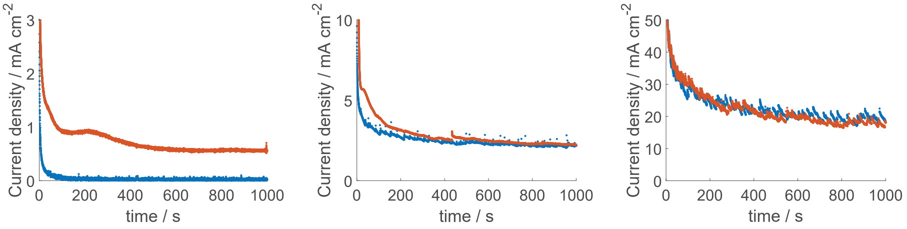

(a) 1.45 V. (b) 1.55 V. (c) 1.65 V.

Figure 5.55: Current transients during potential steps to different potentials on crystalline DSA electrodes in 2 mol L^{-1} H_2SO_4 (blue) and in 2 mol L^{-1} H_2SO_4 + 0.15 mol L^{-1} Mn^{2+} (red).

5.55c).

An oxidation peak was observed after 35 s at 1.45 V in 0.1 mol L^{-1} H_2SO_4 + 5 mmol L^{-1} Mn^{2+} (Fig. 5.54a). In 2 mol L^{-1} H_2SO_4 + 0.15 mol L^{-1} Mn^{2+}, a less distinct oxidation peak appeared after approximately 200 s at 1.45 V in addition to a shoulder around 40 s (Fig. 5.55a). At 1.55 V in 2 mol L^{-1} H_2SO_4 + 0.15 mol L^{-1} Mn^{2+}, a shoulder appeared around 30 s (Fig. 5.55b). However, no oxidation peaks or shoulders were observed during the potential step to 1.65 V in 2 mol L^{-1} H_2SO_4 + 0.15 mol L^{-1} Mn^{2+} (Fig. 5.55c) nor during the step to 1.55 V in 0.1 mol L^{-1} H_2SO_4 + 5 mmol L^{-1} Mn^{2+} (Fig. 5.54b).

Potential steps were also performed on crystalline DSA electrodes covered with MnO_2 as described in Figure 4.3. The current transients from these experiments are displayed in Figure 5.56. Initially, the current density on

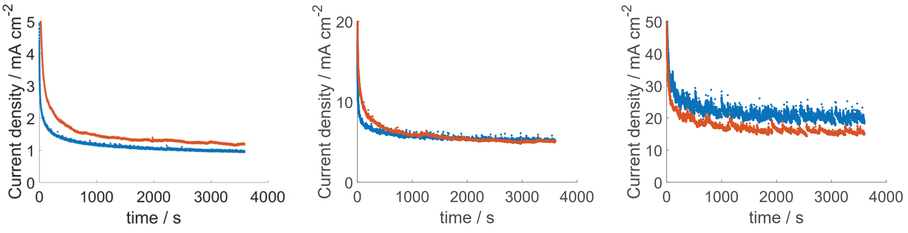

(a) 1.55 V. (b) 1.60 V. (c) 1.65 V.

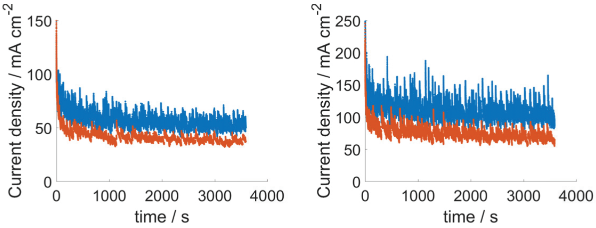

(d) 1.70 V. (e) 1.75 V.

Figure 5.56: Current transients during potential steps to increasingly positive potentials on MnO_2-covered (10 000 s at 1.45 V) crystalline DSA electrodes in 2 mol L^{-1} H_2SO_4 (blue) and in 2 mol L^{-1} H_2SO_4 + 0.15 mol L^{-1} Mn^{2+} (red).

the MnO_2-covered electrodes was slightly lower in blank electrolyte than in Mn^{2+}-containing electrolyte (Fig. 5.56a), but as the potential was increased the current density in blank electrolyte exceeded that in the Mn^{2+}-containing electrolyte. The current density on the MnO_2-covered electrodes was lower than the current densities observed on the pristine electrode surface at 1.55 V (Figs. 5.55b and 5.56a). However, at 1.65 V no large difference was observed between the pristine and the MnO_2-covered electrodes (Figs. 5.55c and 5.56c).

Amorphous DSA electrodes

The current transients from potential steps performed with amorphous DSAs in high concentration electrolyte are presented in Figure 5.57. At 1.45 V, the current density in blank electrolyte was low. When Mn^{2+} was present in the electrolyte a very broad peak was observed around 500 s (Fig. 5.57a). The steady state current in 2 mol L^{-1} H_2SO_4 + 0.15 mol L^{-1} Mn^{2+} was similar in magnitude on the crystalline and amorphous electrodes (Figs.

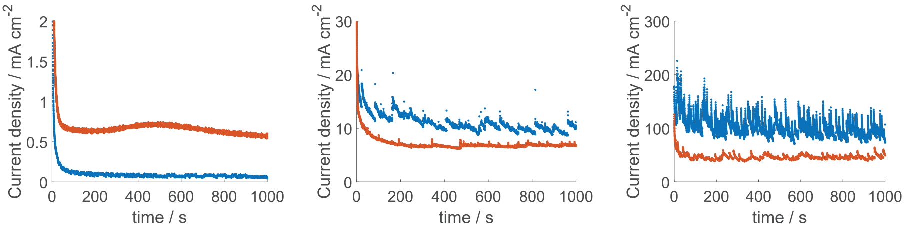

(a) 1.45 V.

(b) 1.55 V.

(c) 1.65 V.

Figure 5.57: Current transients during potential steps to different potentials on amorphous DSA electrodes in 2 mol L^{-1} H_2SO_4 (blue) and in 2 mol L^{-1} H_2SO_4 + 0.15 mol L^{-1} Mn^{2+} (red).

5.55a and 5.57a), but the shape of the current transients were different.

At higher potentials, the amorphous electrodes had a higher current density in blank electrolyte than in Mn^{2+}-containing electrolyte. In contrast, crystalline DSAs showed quite similar current densities in the same electrolytes (Figs. 5.55b and 5.55c). The outer charge of the amorphous electrodes prior to the potential steps was less than half for the electrodes employed in Mn^{2+}-containing compared to in blank electrolyte, see Appendix B. Thus, it is possible that the difference in current density between Mn^{2+}-containing and blank electrolyte in Figures 5.57b and 5.57c arise from a difference in the activation of the electrodes. Overall, the current densities at 1.55 V and 1.65 V were higher on the amorphous than the crystalline electrodes, regardless of the presence (or absence) of Mn^{2+}. This is in accordance with the results from LSV that showed higher current densities on the amorphous DSAs than on the crystalline DSAs (Figs. 5.52 and 5.53).

Platinum

Potential steps were performed on platinum electrodes in 0.1 mol L^{-1} H_2SO_4 with 5 mmol L^{-1} Mn^{2+} or 0.15 mol L^{-1} Mn^{2+}, see Figures 5.58a and 5.58b respectively. For each electrolyte, the steady state current was the same at 1.45 V and 1.55 V. However, the shape of the current transient at short times varied with both the concentration of Mn^{2+} and the electrode potential. An oxidation peak or shoulder was observed in the start of the potential step. In the potential step to 1.45 V in the electrolyte with low concentration of Mn^{2+}, the current initially declined before an oxidation peak appeared

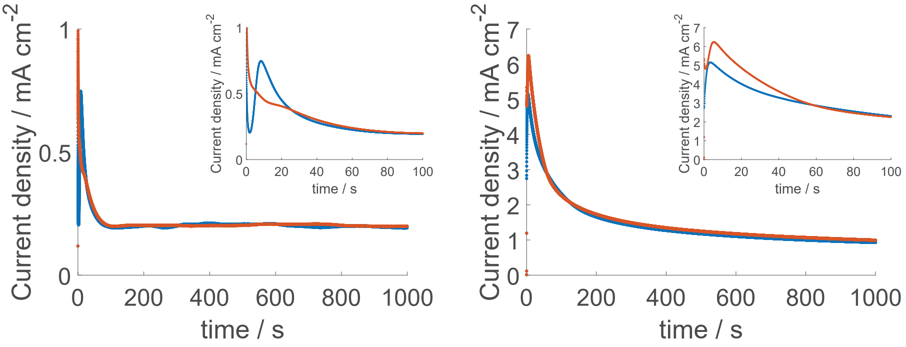

(a) 0.1 mol L^{-1} H_2SO_4 + 5 mmol L^{-1} Mn^{2+}

(b) 0.1 mol L^{-1} H_2SO_4 + 0.15 mol L^{-1} Mn^{2+}

Figure 5.58: Current transients during potential steps to 1.45 V (blue) and 1.55 V (red) on platinum electrodes in 0.1 mol L^{-1} H_2SO_4 with low and high concentration of Mn^{2+}. The inserts show the current transients at shorter times (100 s).

around 8 s. At 1.55 V, two small shoulders were observed around 5 and 20 s. In the electrolyte with higher manganese concentration, an oxidation peak was observed at each potential: around 3 s and 5 s for the potential steps to 1.45 V and 1.55 V, respectively.

5.3.4 Electrochemical procedure for removal of MnO_2

A procedure was suggested in an attempt to remove MnO_2 deposited under condition resembling those in zinc electrowinning, see Figure 4.4. The current transients and related properties are presented here, whereas an account of visual observations during the sequence as well as SEM images and EDS data are presented in section 5.2.1. An example of the observed current transients is given in Figure 5.59, both with and without a prelayer. The current transient for formation of the prelayer (1000 s at 1.45 V) is presented in Figure 5.55a. The charge passed during each step of each experiment is listed in Table 5.5. Note that the same current range was used throughout the entire sequence. Consequently, there is a higher uncertainty for low current densities, especially the hold at 1.45 V.

The charge passed at 1.75 V (3 h or 15 h) did not seem related to whether or not a prelayer was present. The differences in charge were better explained

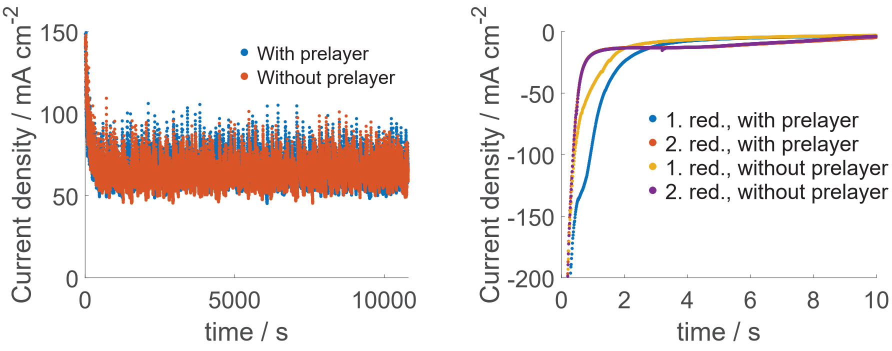

(a) Operation at 1.75 V.

(b) 1. and 2. reduction.

Figure 5.59: Current transients on crystalline DSA electrodes in 2 mol L^{-1} H_2SO_4 + 0.15 mol L^{-1} Mn^{2+} at different stages during the sequence for electrochemical removal of MnO_2.

by the difference in activation of the electrodes as indicated by the outer charge, see for example samples C, J & K with high outer charge. Similarly, the shape of the current transient seemed independent on the presence of a prelayer (Fig. 5.59a). On the other hand, the shape of the current transient during first reduction step was influenced by the presence of a prelayer (Fig. 5.59b). Correspondingly, the charge passed in the first reduction step was slightly higher when a prelayer was present. In the second step to 1.75 V, no clear trends were observed for the passed charge. As mentioned in section 5.2.1, the time required at 1.75 V before most of the MnO_2 detached from the electrode surface appeared to be random. This could influence the available area for OER on the uncovered DSA which in turn could influence the charge. The second reduction did not seem to be affected by the presence of the prelayer (Fig. 5.59b). This was as expected since the layer was removed in the previous step (at 1.75 V) and replaced by a thin layer of MnO_2 formed at high potential. Hence, MnO_2 present after the second step to 1.75 V should ideally be independent of the preceding steps and show the same reduction behaviour.

The sequence to remove MnO_2 was also performed six consecutive times with a three hours potential hold at 1.75 V. The charge from each step is listed in Table 5.6. Overall, a small decline in the charge was observed for all steps, but with quite large variations between each sequence. The most important step to monitor is the 3 h hold at 1.75 V as this corresponds to normal operation of the cell. During the six sequences the charge passed

Table 5.5: Charge passed at the different electrode potentials in the sequence for MnO_2 removal. The outer charge determined prior to each sequence is also included.

Sample	**Charge / C**								**Outer charge / mC**
	1.45 V	1.75 V		0.4 V		1.75 V	0.4 V		
	1000 s	3h	15 h	100 s	10 s	100 s	100 s	10 s	
Blank	0.005	280		-0.031		4.55	-0.028		10.9
A	0.179	211							11.8
B	0.161		934						9.3
C	0.186	283		-0.141					13.8
D	0.166		990	-0.121					11.9
E	0.202	200		-0.122		3.36	-0.097		11.4
F	0.178		976	-0.121		3.74	-0.101		11.6
G	-	195		-0.115		3.38	-0.097		12.0
H	-		961	-0.109		3.94			11.0
I	0.185	200			-0.070	3.20		-0.067	11.5
J	0.180		1049		-0.074	3.80		-0.065	12.7
K	-	283			-0.064	4.06		-0.067	13.6

Table 5.6: Charge passed during each step when the sequence to remove MnO_2 was repeated 6 consecutive times.

Seq. #	**Charge / C**				
	1.45 V 1000 s	1.75 V 3h	0.4 V 10 s	1.75 V 100 s	0.4 V 10 s
1	0.205	299	-0.090	4.05	-0.068
2	0.163	292	-0.084	3.46	-0.069
3	0.166	288	-0.082	3.79	-0.066
4	0.169	292	-0.082	4.02	-0.065
5	0.192	293	-0.078	3.82	-0.064
6	0.137	288	-0.079	3.70	-0.064

at this step stayed quite high which is beneficial with regards to a possible implementation of the sequence in the zinc electrowinning process.

5.3.5 Effect of chloride on MnO_2 deposition

The effect of chloride in the electrolyte was investigated on an early version of the crystalline DSA. The early version of the crystalline DSA electrode had a higher residual chloride content in the catalytic coating, relative to the amount of Ir and Ta, than the final version (see Table 5.1). Linear sweep voltammograms are presented in Figure 5.60. Chloride in the electrolyte did not seem to have an effect on the performance of the electrode.

The linear sweep voltammograms of the early version were quite similar to those of the final version crystalline DSA (Fig. 5.48). A slightly higher (geometric) current density was observed with the early version crystalline DSA.

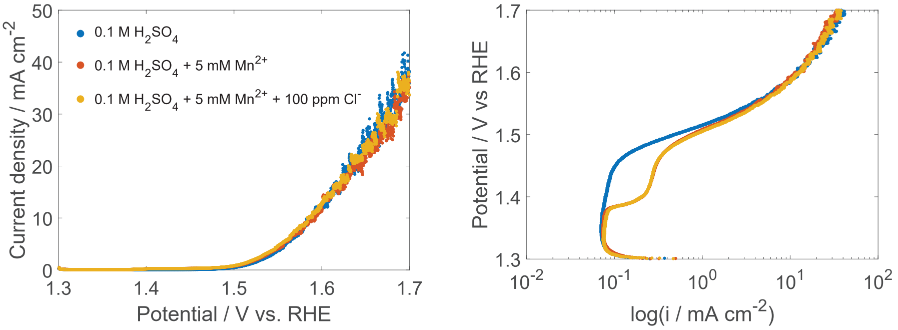

(a) (b)

Figure 5.60: Linear sweep voltammetry of an early version crystalline DSA electrode at sweep rate 5 mV min^{-1}, (a) linear and (b) logarithmic current.

5.4 EQCM

5.4.1 Cyclic Voltammetry

Cyclic voltammograms and their corresponding massograms obtained in the EQCM set-up are presented in this section. Cyclic voltammograms of platinum were also recorded in other set-ups (see Tab. 4.1 and sections 5.3.1, 5.5 and 5.6).

Platinum

The cyclic voltammograms and massograms of platinum obtained at sweep rate 100 mV s^{-1} in both blank and Mn^{2+}-containing electrolyte are presented in Figure 5.61. Platinum oxide formation commenced around 0.8 V. The platinum oxide was completely reduced in the negative-going sweep in a reduction wave peaking at around 0.7 V. The massograms showed a weight increase during platinum oxide formation and a corresponding weight loss during the platinum oxide reduction peak (Fig. 5.61b). The voltammograms and massograms of platinum in 0.1 mol L^{-1} H_2SO_4 are similar to those reported in the literature [126].

In Mn^{2+}-containing electrolyte (Figs. 5.61c and 5.61d), the oxidation of Mn^{2+} started prior to 1.4 V and coincided with a larger increase in mass

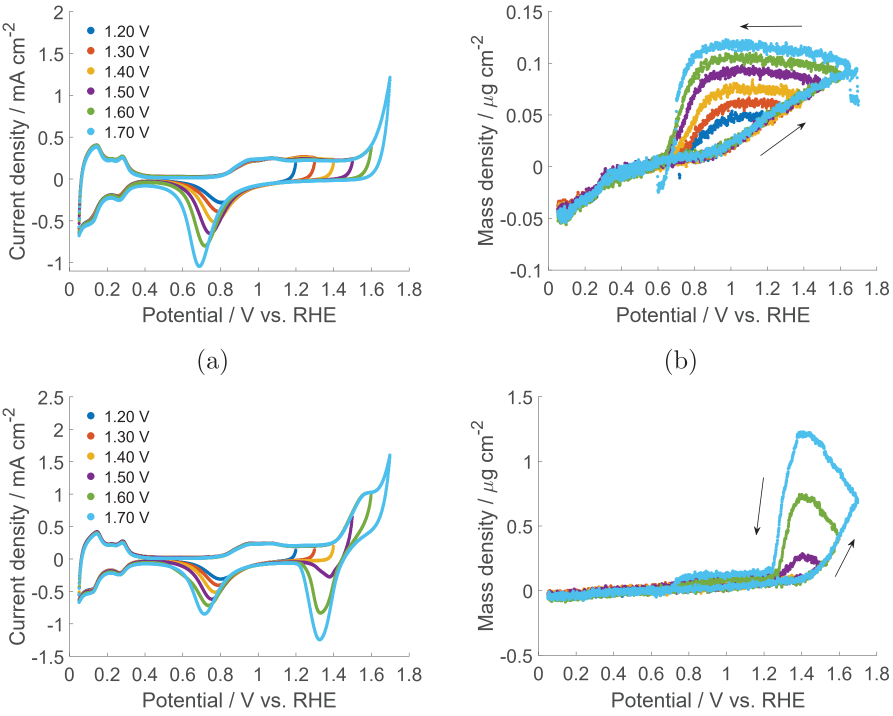

(a) (b)

(c) (d)

Figure 5.61: Cyclic voltammograms and massograms of a platinum electrode in 0.1 mol L^{-1} H_2SO_4 (a and b) and in 0.1 mol L^{-1} H_2SO_4 + 5 mmol L^{-1} Mn^{2+} (c and d) at sweep rate 100 mV s^{-1}.

than observed for platinum oxide formation. A shoulder caused by oxidation of manganous species was observed at 1.55 V. As expected, the mass continued to increase after potential reversal and peaked as the current became negative. A reduction peak was observed negative of 1.4 V during which most of the mass added during the cycle disappeared. The rest disappeared during the platinum oxide reduction peak.

The effect of upper reversal potential was also studied at sweep rate 5 mV s^{-1} (Fig. 5.62). At this sweep rate, a distinct oxidation peak appeared with an apex around 1.46 V ($p_{ox,1}$). When the upper reversal potential was prior to the apex of the oxidation peak the current continued to increase after potential reversal (see Fig. 5.62c). Interestingly, a second oxidation peak ($p_{ox,2}$) appeared on the negative-going scan at the same potential as the first oxidation peak (around 1.45 V) when the potential was reversed positive of the apex of the first oxidation peak (i.e. for upper reversal potentials 1.48 V and higher).

A reduction peak located around 1.3 V ($p_{red,1}$) was observed for all upper reversal potentials with shoulders extending in both directions. The shoulders were more pronounced at low upper reversal potentials. A second reduction peak ($p_{red,2}$) appeared around 1.2 V only when the upper reversal potentials was sufficiently positive (1.55 V and above). This peak moved towards more negative potentials as the upper reversal potential increased. When the upper reversal potential was 1.6 V or higher yet another reduction peak (with a shoulder) appeared around 0.9 V partially overlapping with the PtO reduction peak.

The time derivative of the massograms was compared to the current density and are presented in Figure 5.63 for selected upper reversal potentials. As explained in section 3.1 this comparison can give information on the relative rate of electrochemical reactions to other events that can cause a mass change, such as chemical reactions.

Both oxidation peaks showed a good correlation between the current and the time derivative of mass. The difference between the current and time derivative of mass at the most positive potentials is probably due to some oxygen evolution at these potentials, which contributes to the measured current, but not to the mass. Also, the mass is seen to increase slightly prior to the onset of the first oxidation peak, perhaps indicating an adsorption process prior to the oxidation and formation of manganese deposit.

For the main part of the first reduction peak, more charge was passed than the mass signal indicated if assuming a two electron reduction of MnO_2 to Mn^{2+}. However, towards the end of the peak (around 1.27 V) a shoulder was observed in the current signal that coincided with a considerable mass loss (e.g. Fig. 5.63c). This feature appeared for all upper reversal potentials. For cases in which the second reduction peak was present (i.e. upper reversal potential 1.55 V and higher), a higher mass loss than predicted was observed also during this reduction.

Voltammograms were also recorded at different sweep rates with upper limit 1.6 V, see Figure 5.64. The peak current in the forward oxidation peak does not show a clear dependence on the sweep rate. The small oxidation peak observed in the reverse scan is clearly visible for the slower sweep rates, but

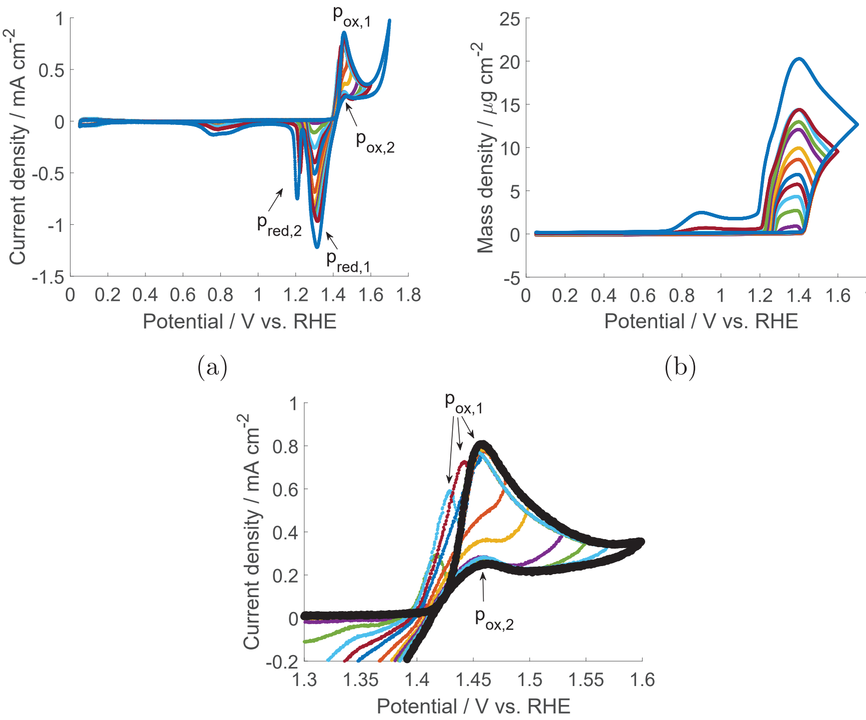

(a)

(b)

(c)

Figure 5.62: Cyclic voltammograms (a) and massograms (b) of a platinum electrode in 0.1 mol L^{-1} H_2SO_4 + 5 mmol L^{-1} Mn^{2+} with varying upper reversal potentials at sweep rate 5 mV s^{-1}. An enlargement of the manganese oxidation region in (a) is shown in (c), with upper reversal potential 1.6 V in black bold.

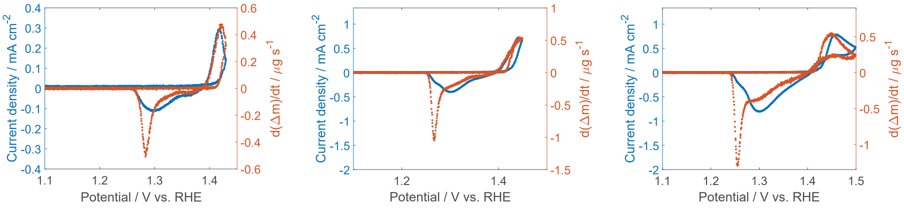

(a) 1.43 V (b) 1.45 V (c) 1.50 V

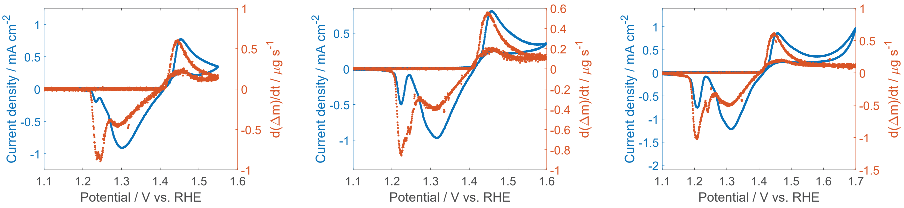

(d) 1.55 V (e) 1.60 V (f) 1.70 V

Figure 5.63: Cyclic voltammograms (blue, left y-axis) and time derivative of massograms (red, right y-axis) of a platinum electrodes with varying upper limits recorded at sweep rate $5\,\mathrm{mV\,s^{-1}}$ in $0.1\,\mathrm{mol\,L^{-1}}$ H_2SO_4 + $5\,\mathrm{mmol\,L^{-1}}$ Mn^{2+}.

exists only as a change in slope for the faster sweep rates.

A second reduction peak was only observed at slow sweep rates ($20\,\mathrm{mV\,s^{-1}}$ and below). This peak shifted negatively with decreasing sweep rate, i.e. with increasing time in the positive current region, as was also observed when increasing the upper limit while keeping the sweep rate at $5\,\mathrm{mV\,s^{-1}}$ (Fig. 5.62a).

Platinized platinum

The effect of increased surface roughness was investigated by running CVs on platinized platinum (not shown here). As expected, the magnitude of the peaks related to the substrate itself, i.e. platinum oxide formation and reduction as well as hydrogen adsorption and desorption, increased as the available surface area increased. However, an effect on the peaks related to manganese oxide formation and reduction was only observed at fast sweep rate ($100\,\mathrm{mV\,s^{-1}}$) with a slight increase in peak current densities. At slow sweep rate ($5\,\mathrm{mV\,s^{-1}}$) the current density in features related to manganese

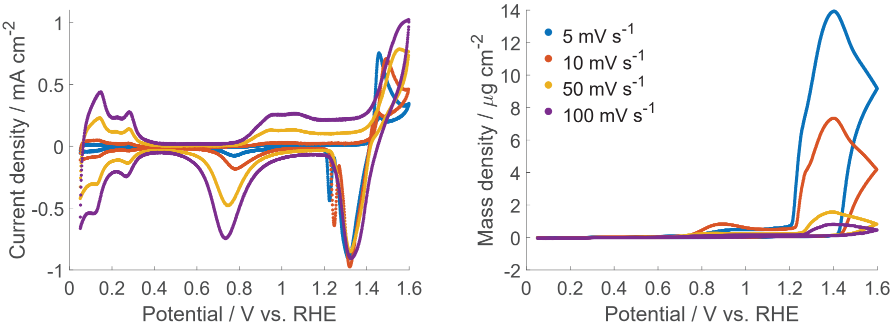

(a) (b)

Figure 5.64: Cyclic voltammograms (a) and massograms (b) of a platinum electrode in 0.1 mol L^{-1} H_2SO_4 + 5 mmol L^{-1} Mn^{2+} with different sweep rates.

oxide formation and reduction was identical on platinum and on platinized platinum. This indicates that the surface area becomes independent of the initial roughness when the manganese oxide deposit reaches a certain thickness.

Gold

Cyclic voltammograms acquired with gold EQCM electrodes at sweep rate 100 mV s^{-1} and 5 mV s^{-1} are presented in Figures 5.65 and 5.66, respectively. Gold oxide started forming at approximately 1.4 V as seen both in the the voltammograms and massograms (Figs. 5.65a and 5.65b, respectively). The reduction of the gold oxide occurred in a wave peaking slightly negative of 1.2 V, coinciding with loss of the mass that was gained in the gold oxide formation region. The voltammograms and massograms obtained in blank electrolyte are similar to those reported in the literature [127].

In Mn^{2+}-containing electrolyte the onset of gold oxide and manganese oxide formation overlapped to a large degree. An oxidation peak caused by manganese oxide deposition was observed for both sweep rates: located at 1.55 V for sweep rate 100 mV s^{-1} and positive of 1.46 V for sweep rate 5 mV s^{-1}. The current continued to increase after reversing the potential when the potential was reversed prior to the apex of the oxidation peak ((Fig. 5.66c)). A second oxidation peak was observed around 1.46 V in the negative-going

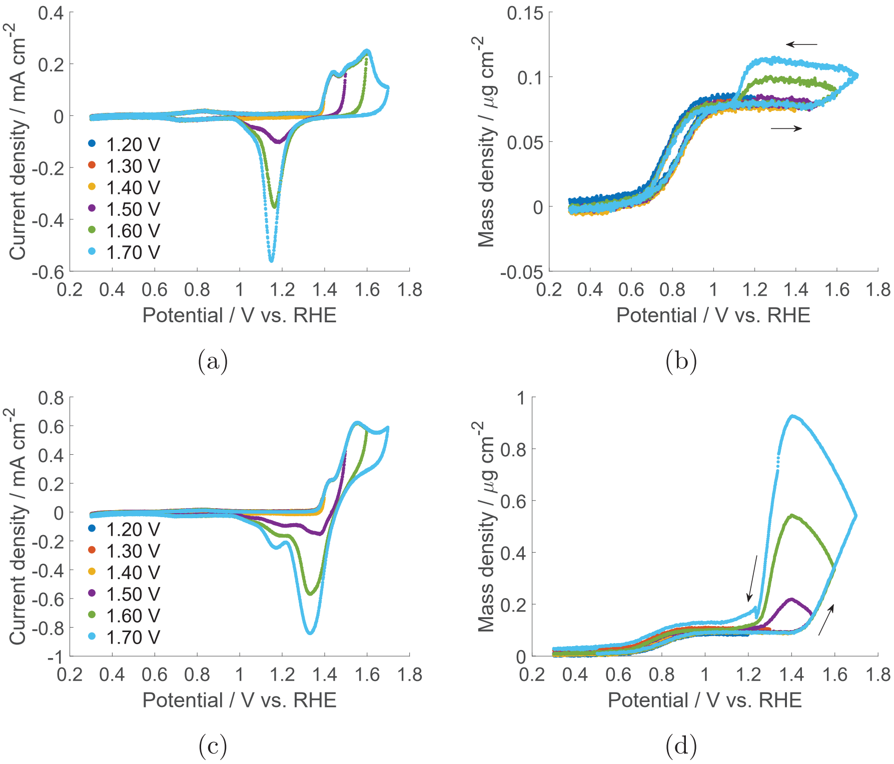

(a)

(b)

(c)

(d)

Figure 5.65: Cyclic voltammograms and massograms of a gold electrode in 0.1 mol L^{-1} H_2SO_4 (a and b) and in 0.1 mol L^{-1} H_2SO_4 + 5 mmol L^{-1} Mn^{2+} (c and d) at sweep rate 100 mV s^{-1}.

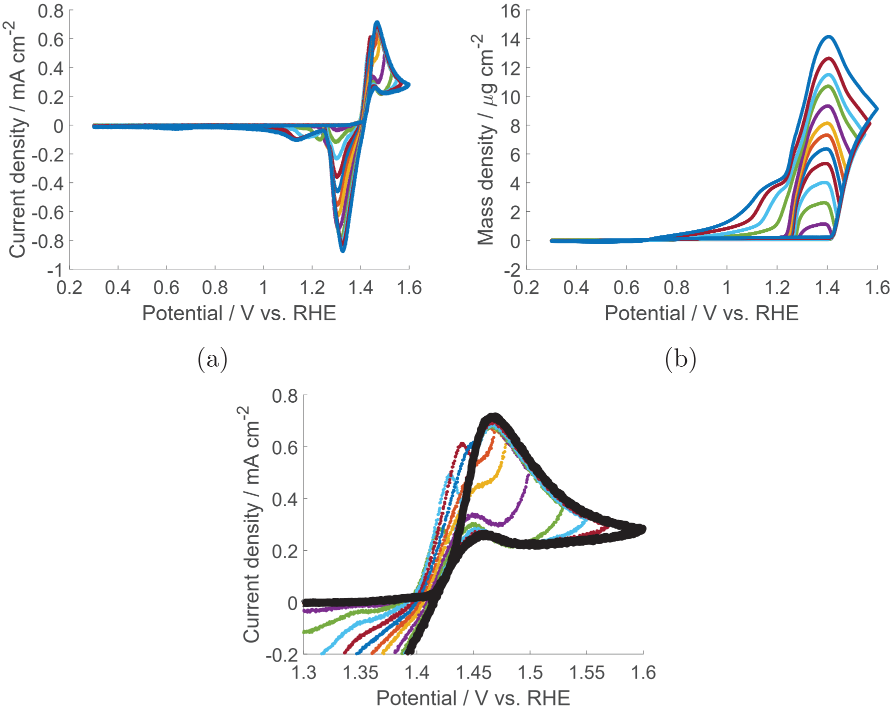

(a) (b)

(c)

Figure 5.66: Cyclic voltammograms (a) and massograms (b) of a gold electrode in 0.1 mol L^{-1} H_2SO_4 + 5 mmol L^{-1} Mn^{2+} with varying upper reversal potentials at sweep rate 5 mV s^{-1}. An enlargement of the manganese oxidation region in (a) is shown in (c), with upper reversal potential 1.6 V in black bold.

sweep. Overall, the gold and platinum electrodes displayed the same features related to Mn^{2+}-oxidation at the employed conditions (see Figs. 5.61 and 5.62).

The reduction behaviour at fast sweep rate were dominated by two peaks: the first at approximately 1.35 V and the second slightly negative of 1.2 V (Fig. 5.65c). The first peak is related to the reduction of manganese oxide, as it was not present in blank electrolyte and since the mass gained during manganese oxide deposition was removed during the peak (Fig. 5.65d). No significant mass change was observed in the second reduction peak and it appears to be solely due to the gold oxide reduction reaction. Less gold oxide was formed in Mn^{2+}-containing electrolyte, as evident when comparing the charge passed during the second reduction peak in the two electrolytes (Figs. 5.65a and 5.65c).

At slow sweep rate a manganese oxide reduction peak was observed around 1.3 V for all upper reversal potentials (Fig. 5.66a). This peak had shoulders extending in both directions. A second reduction peak was observed for upper reversal potentials of 1.53 V and higher, starting at 1.25 V and moving more negative as the upper reversal potential increased. This peak partially overlapped with the gold oxide reduction peak located at 1.20 V (not shown here), but was much larger in magnitude. Hence, the second reduction peak is both related to manganese oxide reduction and to gold oxide reduction.

The manganese oxide reduction features were very similar to those on the platinum electrode for the fast scan rate and the first reduction peak at slow scan rate (Figs. 5.61 and 5.62). However, the second reduction peak (and the corresponding mass loss) occurred at more negative potentials on the gold electrode and was less pronounced. These results are in accordance with the findings of Lee et al. and Maskell [68–70] who found that the first reduction peak of electrodeposited MnO_2 was independent on the substrate, whereas the second peak was not.

The voltammograms obtained with the gold electrode at $5\,\mathrm{mV\,s^{-1}}$ are compared to the time derivative of the mass signal for selected upper reversal potentials in Figure 5.67. The signals overlapped quite well in the oxidation region. The mass increase started slightly before the current, perhaps indicating an adsorption process prior to the charge transfer. The mass change was less than expected in the main part of the first reduction peak. However, in the shoulder negative to the first reduction peak (ca. 1.25 V) the mass change was much larger than expected from the current, especially

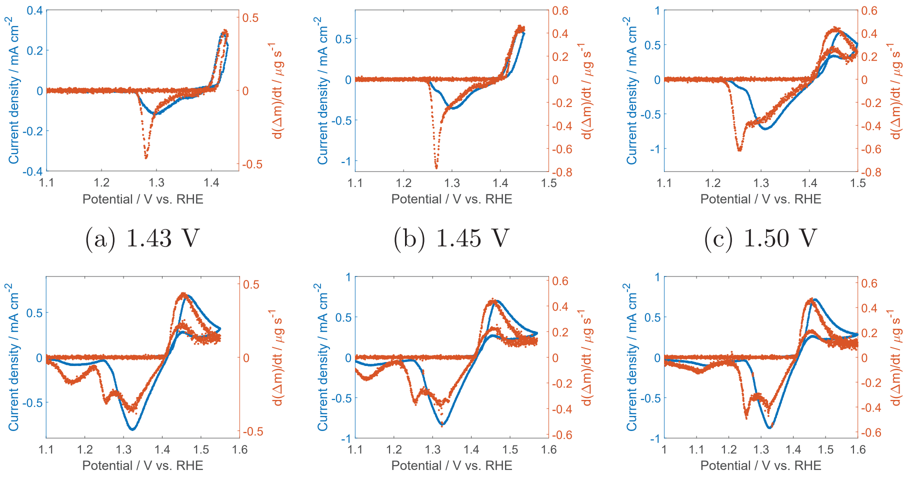

(a) 1.43 V

(b) 1.45 V

(c) 1.50 V

(d) 1.55 V

(e) 1.57 V

(f) 1.60 V

Figure 5.67: Cyclic voltammograms (blue, left y-axis) and time derivative of massograms (red, right y-axis) of a gold electrodes with varying upper limits recorded at sweep rate 5 mV s^{-1} in 0.1 mol L^{-1} H_2SO_4 + 5 mmol L^{-1} Mn^{2+}.

for low upper reversal potentials (Figs. 5.67b and 5.67c). Similarly, the mass change was also larger than expected from the current in the second reduction peak, when present (Figs. 5.67d, 5.67e and 5.67f). The same observations were also made with the platinum electrode (Fig. 5.63).

Cyclic voltammograms acquired with different sweep rates on gold are presented in Figure 5.68. Many of the observations made with the platinum electrode are also valid for the gold electrode. The peak current of the oxidation peak in the positive-going sweep does not seem to be dependent on the sweep rate. The peak potential moves to more positive potentials with increasing sweep rate. The second oxidation peak in the negative-going sweep was only observed for sweep rates up to and including 20 mV s^{-1}.

The second manganese oxide reduction peak on gold is harder to evaluate than that on platinum due to the overlap with the gold oxide reduction peak. As argued above, the second reduction peak observed at 100 mV s^{-1} is mainly due to gold oxide reduction (see Figs. 5.65c and 5.65d). The shape and position of the second reduction peak at 50 mV s^{-1} (and small mass loss) suggests that it is also governed by the gold oxide reduction reaction. However, at sweep rate 20 mV s^{-1} a more distinct reduction appeared

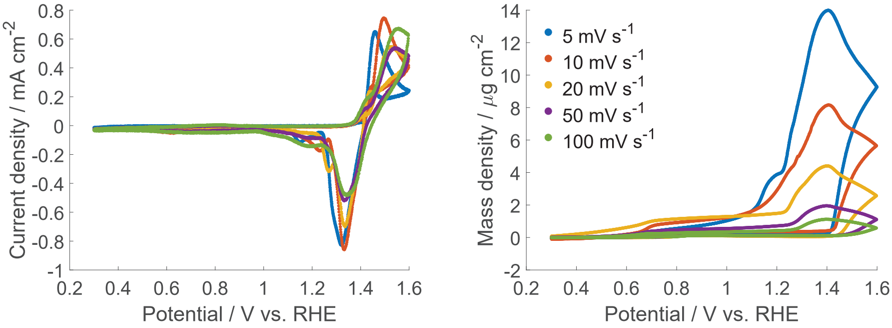

(a) (b)

Figure 5.68: Cyclic voltammograms (a) and massograms (b) of a gold electrode in 0.1 mol L^{-1} H_2SO_4 + 5 mmol L^{-1} Mn^{2+} with different sweep rates.

at more positive potentials than the gold oxide reduction peak, which is probably related to the manganese oxide reduction reaction. The shoulder observed negative of this peak can probably be attributed to gold oxide reduction. The distinct manganese oxide reduction peak moved towards more negative potentials as the scan rate decreased, making it completely overlap with the gold oxide reduction peak. However, both the charge and the mass loss was greater than expected for gold oxide reduction.

Titanium

The performance of a bare titanium EQCM electrode is displayed in Figure 5.69. As expected, titanium was not particularly active towards OER [128]. During the first cycle (not shown here) an oxidation wave was observed that probably corresponded to the irreversible formation of titanium oxide. The oxidation peak observed at approximately 2.3 V in both electrolytes (Fig. 5.69a) is probably also related to oxidation of the substrate.

Deposition of MnO_2 only started close to the reversal potential (2.5 V) for sweep rate 100 mV s^{-1} and slightly before 1.8 V for sweep rate 5 mV s^{-1}. Multiple reduction waves were observed in the voltammograms at both sweep rates. The mass started decreasing around 1 V at both sweep rates. However, the time required for the mass to return to its initial value depended on the amount of MnO_2 deposited (i.e. the sweep rate). Hence, the mass returned to its initial value around 0.2 V on the negative-going sweep

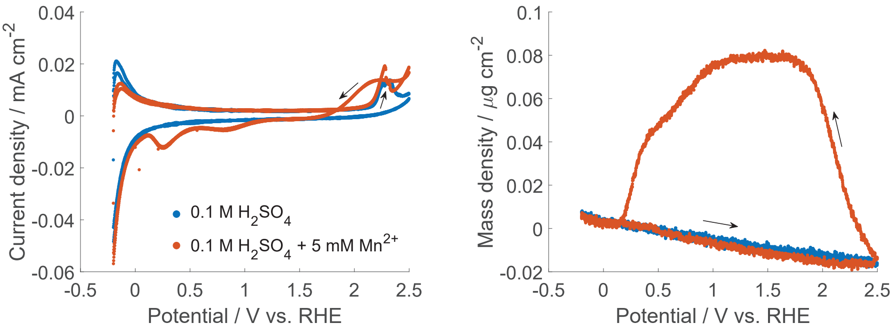

(a) $100\,\mathrm{mV\,s^{-1}}$ (b) $100\,\mathrm{mV\,s^{-1}}$

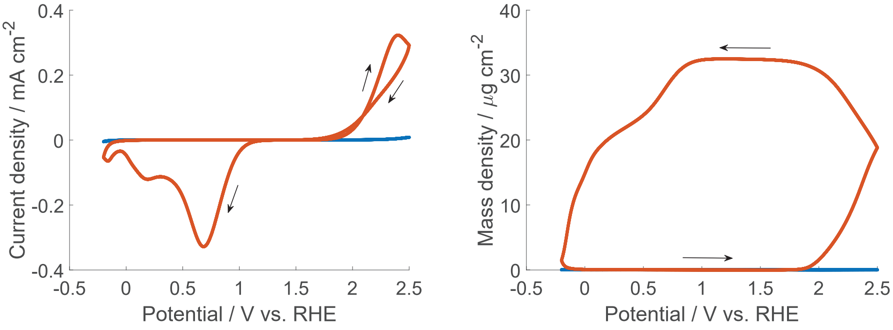

(c) $5\,\mathrm{mV\,s^{-1}}$ (d) $5\,\mathrm{mV\,s^{-1}}$

Figure 5.69: Cyclic voltammograms and massograms of a titanium electrode in $0.1\,\mathrm{mol\,L^{-1}}$ H_2SO_4 + $5\,\mathrm{mmol\,L^{-1}}$ Mn^{2+} at sweep rate $100\,\mathrm{mV\,s^{-1}}$ (a and b) and $5\,\mathrm{mV\,s^{-1}}$ (c and d).

at fast sweep rate, but only around 0 V on the positive-going sweep at slow sweep rates.

When comparing with gold and platinum, it is apparent that the deposition and reduction of MnO_2 requires much higher overpotential on titanium. More mass was deposited at the Ti electrode at slow scan rate than on Au and Pt (Figs. 5.66b and 5.62b), but the deposition time was longer for Ti.

IrO_2/Ti

The cyclic voltammograms and massograms obtained with a h-IrO_2-covered titanium electrode in blank and Mn^{2+}-containing electrolyte with upper limit 1.6 V are presented in Figure 5.70. In addition, the effect of varying the upper reversal potential at sweep rate $5\,mV\,s^{-1}$ was investigated, see Figure 5.71. The h-IrO_2-powder was sprayed on the titanium EQCM-electrodes as described in section 4.3.2. This may result in differences in the frequency measurements between this and the other (smooth) electrode materials. The current and mass are not normalized by the geometric area for this electrode because of the difference in available surface area and since only a fraction of the titanium disc was covered. Some noise in the current was experienced with this electrode, probably because of the low loading of IrO_2. However, a higher loading resulted in significant instability of the frequency measurements.

A mass loss was observed at positive potentials in the blank experiments for both sweep rates. The mass was recovered during the reverse scan. The magnitude of the mass loss was similar for both sweep rates. The massogram obtained at sweep rate $5\,mV\,s^{-1}$ was similar to that reported by Birss et al. [129] at the same sweep rate in $0.3\,mol\,L^{-1}$ H_2SO_4. They explained the observed mass loss by that iridium(III)oxide loses SO_4^{2-} and H_3O^+, but gains H_2O as it is oxidized. This can be described by the following equation in acidic environments [130]:

$$\begin{aligned}&\mathrm{Ir(IV)oxide}\cdot n\mathrm{H_2O} + x\mathrm{H_3O^+} + y\mathrm{A^-} + \mathrm{e^-} \rightleftharpoons \\ &\qquad \mathrm{Ir(III)oxide}\cdot m\mathrm{H_2O(H_3O^+)}_x\mathrm{A}_y^- + (n-m)\mathrm{H_2O} \qquad (5.1)\end{aligned}$$

where A^- represents the electrolyte anion, and *x, y, n* and *m* are coefficients depending on the reaction conditions. If subtracting the mass change observed in blank electrolyte, the massograms obtained in $0.1\,mol\,L^{-1}$ H_2SO_4

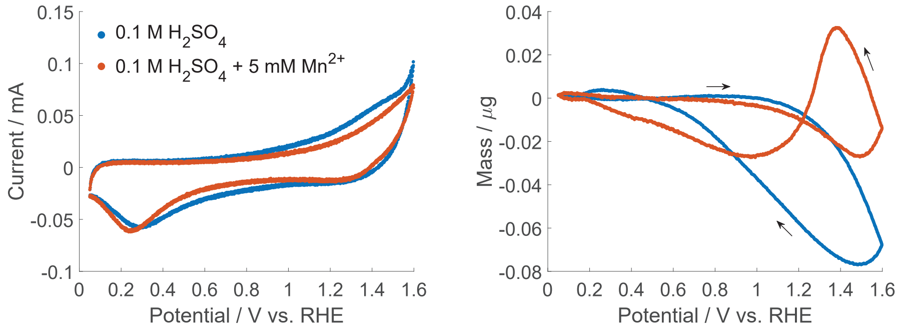

(a) $100\,\mathrm{mV\,s^{-1}}$ (b) $100\,\mathrm{mV\,s^{-1}}$

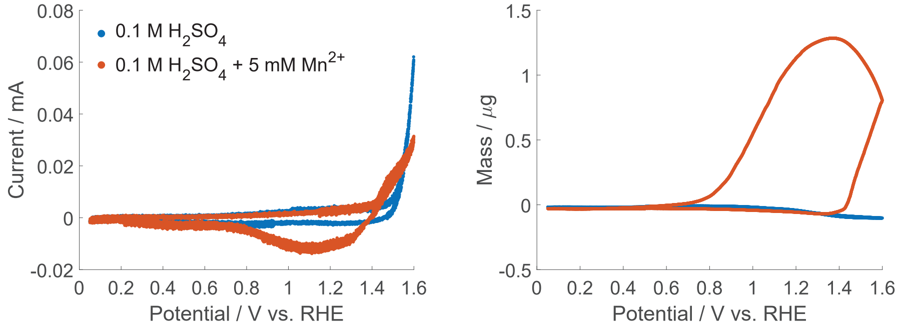

(c) $5\,\mathrm{mV\,s^{-1}}$ (d) $5\,\mathrm{mV\,s^{-1}}$

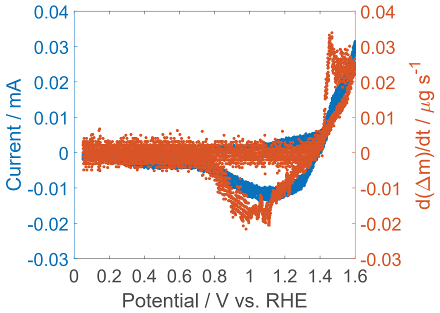

(e)

Figure 5.70: Cyclic voltammograms and massograms of a h-IrO$_2$-coated titanium electrode in $0.1\,\mathrm{mol\,L^{-1}}$ H$_2$SO$_4$ (blue) and in $0.1\,\mathrm{mol\,L^{-1}}$ H$_2$SO$_4$ + $5\,\mathrm{mmol\,L^{-1}}$ Mn^{2+} (red) at sweep rate $100\,\mathrm{mV\,s^{-1}}$ (a and b) and $5\,\mathrm{mV\,s^{-1}}$ (c and d). A different representation of the CV recorded at sweep rate $5\,\mathrm{mV\,s^{-1}}$ in $0.1\,\mathrm{mol\,L^{-1}}$ H$_2$SO$_4$ + $5\,\mathrm{mmol\,L^{-1}}$ Mn^{2+} is shown in (e) where the cyclic voltammogram (blue, left y-axis) is compared to the time derivative of the massogram (red, right y-axis).

+ 5 mmol L^{-1} Mn^{2+} at 100 mV s^{-1} (Fig. 5.70b) resembled those obtained on platinum and gold (Figs. 5.61d and 5.65d).

The shape of the voltammograms obtained at sweep rate 100 mV s^{-1} appeared distorted, with a reduction peak at 0.3 V (Fig. 5.70a). This indicate the presence of a resistance in the electrode. The voltammograms obtained at sweep rate 5 mV s^{-1} were less distorted (Fig. 5.70c).

The onset of oxygen evolution occurred around 1.5 V in blank electrolyte at sweep rate 5 mV s^{-1}. In Mn^{2+}-containing electrolyte the onset of Mn^{2+}-oxidation was visible around 1.3 V in the massogram and around 1.4 V in the voltammogram obtained at sweep rate 5 mV s^{-1}. Note that this is caused by deposition on IrO_2 and not on the titanium substrate. Manganese oxide deposition on titanium did not occur until approximately 1.8 V as described in the previous section (see Fig. 5.69). A shoulder caused by Mn^{2+}-oxidation appeared around 1.5 V in the voltammogram at sweep rate 5 mV s^{-1} (Fig. 5.70c). Interestingly, a peak was observed in the time derivative of the massogram at approximately 1.46 V (Fig. 5.70e), although no peak was observed in the current signal. This is the same potential at which an oxidation peak was observed with the gold and platinum electrodes (Figs. 5.63 and 5.67).

The manganese oxide reduction occurred in a very broad reduction peak with an apex around 1.1 V (Fig. 5.70c). The reduction peak was in reasonable agreement with the time derivative of mass in the same region (Fig. 5.70e). The reduction was slow compared to that on gold and platinum (Figs. 5.62 and 5.66), both in terms of the voltammograms and the massograms. Furthermore, no change to the reduction mechanism (i.e. transition from one to two reduction waves) was observed at the IrO_2-covered electrode as the upper reversal potential was increased.

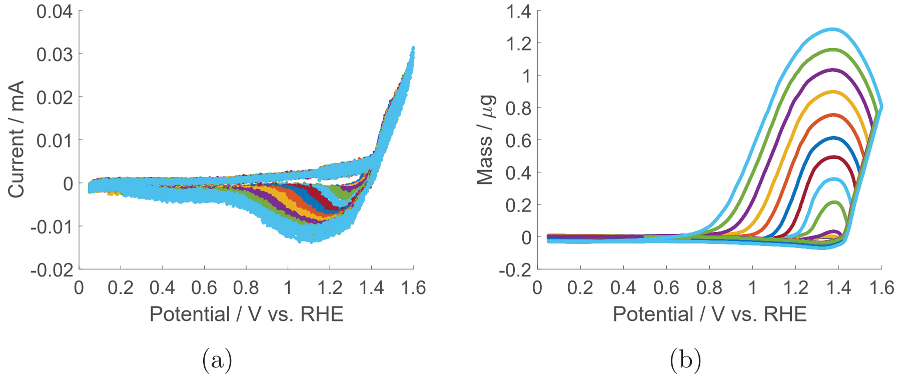

(a) (b)

Figure 5.71: Cyclic voltammograms (a) and massograms (b) of a h-IrO_2-coated titanium electrode in 0.1 mol L^{-1} H_2SO_4 + 5 mmol L^{-1} Mn^{2+} with varying upper reversal potentials at sweep rate 5 mV s^{-1}.

5.4.2 Chronoamperometry

Chronoamperometric data were collected at potentials on each side of the apex (1.46 V) of the oxidation peak observed in the cyclic voltammograms of platinum and gold (Figs. 5.62c and 5.66c). Initial experiments showed that the charge passed during chronoamperometric experiments first increased during the oxidation peak, but experienced a minimum at even more positive potentials (around 1.5 V) before increasing once more. Based on this, three potentials were selected (1.45 V, 1.50 V and 1.55 V) and the measured current and mass responses are presented in Figure 5.72. The potentials 1.45 V and 1.55 V were selected since they possess similar steady state currents while representing potentials at both sides of the apex.

The current transients were similar at all potentials with the exception of the nucleation and growth signature at shorter times at 1.45 V on both platinum and gold (Fig. 5.72a). The nucleation mechanism for these and other experiments is evaluated in section 5.8 (Fig. 5.85). For the potential steps to 1.45 V, diffusion characteristics ($I \propto t^{-1/2}$, Cottrell behaviour) was observed from approximately 20 s to 60 s, in agreement to that observed by Dupont and Donne [61].

Interestingly, although the overall charge passed was found to be similar, the accumulated mass observed at the lower potential (1.45 V) was found to be significantly higher than that at the more positive potentials (1.50 V

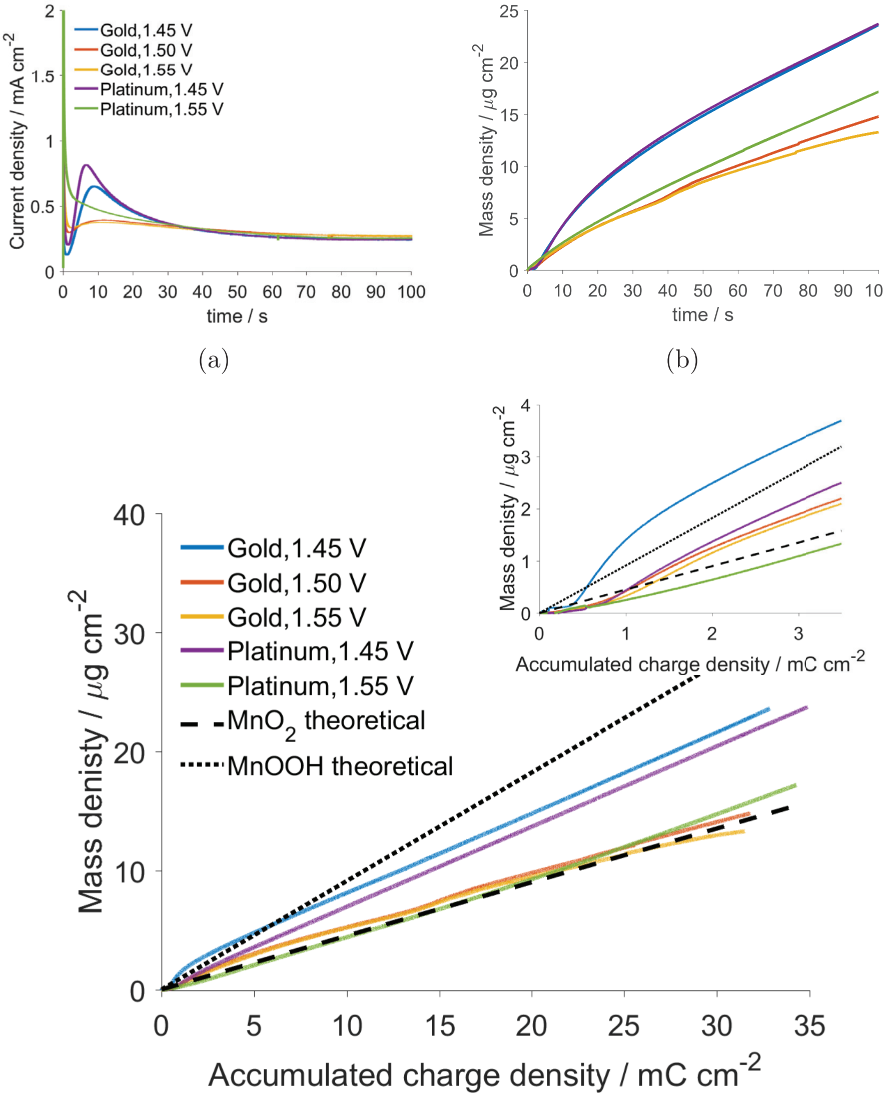

(a)

(b)

(c)

Figure 5.72: Current transients (a) and mass transients (b) for potential steps on platinum and gold electrodes in 0.1 mol L^{-1} H_2SO_4 + 5 mmol L^{-1} Mn^{2+}. A different representation of the same experiments are shown in (c) where the mass density calculated from the frequency is plotted versus the accumulated charge calculated from the current. The theoretical development for MnO_2 and MnOOH formation are also included.

and 1.55 V) (Fig. 5.72b). This demonstrates that the contribution to the oxidation current is different at either side of the apex. Figure 5.72c compares the deposited mass as a function of charge with the theoretical mass increase of MnOOH (n = 1) and MnO_2 (n = 2) for the recorded current and mass transients. From this figure it is apparent that more charge is needed to produce a given amount of mass at higher potentials. In fact, the mass density vs accumulated charge density matches the theoretical line of MnO_2 formation at 1.55 V. Conversely, at 1.45 V the slope lies in between those of MnO_2 and MnOOH indicating an incomplete oxidation to MnO_2. A slope in between that of MnOOH and MnO_2 was also observed by Dupont and Donne during at 1.3 V vs. SCE with higher manganese concentration [61].

The insert in Figure 5.72c shows the mass change vs charge up to the time where a maximum was observed in the current transients in the 1.45 V potential steps, i.e. ca 7 s (Fig. 5.72a). Initially, almost no mass was deposited although charge was passed. After this induction time, the mass increased more rapidly particularly for the potential steps to 1.45 V. For a while, the slope of the 1.45 V potential steps was steeper than that expected for MnOOH formation before gradually decaying.

Chronoamperometric experiments were also conducted on h-IrO_2-coated titanium electrodes, see Figure 5.73. The current density is based on the geometric area that was coated. The current density and deposited mass increased as the potential increased (Figs. 5.73a and 5.73b). The initial decline in mass can probably be attributed to the oxidation of Ir(III)oxide to Ir(IV)oxide through reaction (5.1). Unlike on Pt and Au (Fig. 5.72a), there was no peak in the current transient at short times. Rather, the current was still slightly rising at the end of the hold.

Interestingly, the development of the mass deposited with respect to the passed charge was almost identical for all three potentials (Fig. 5.73c), in contrast to what was observed with the gold and platinum electrodes (Fig. 5.72c). If disregarding the initial mass loss, the slope of the curve was in fact higher than predicted for MnOOH deposition.

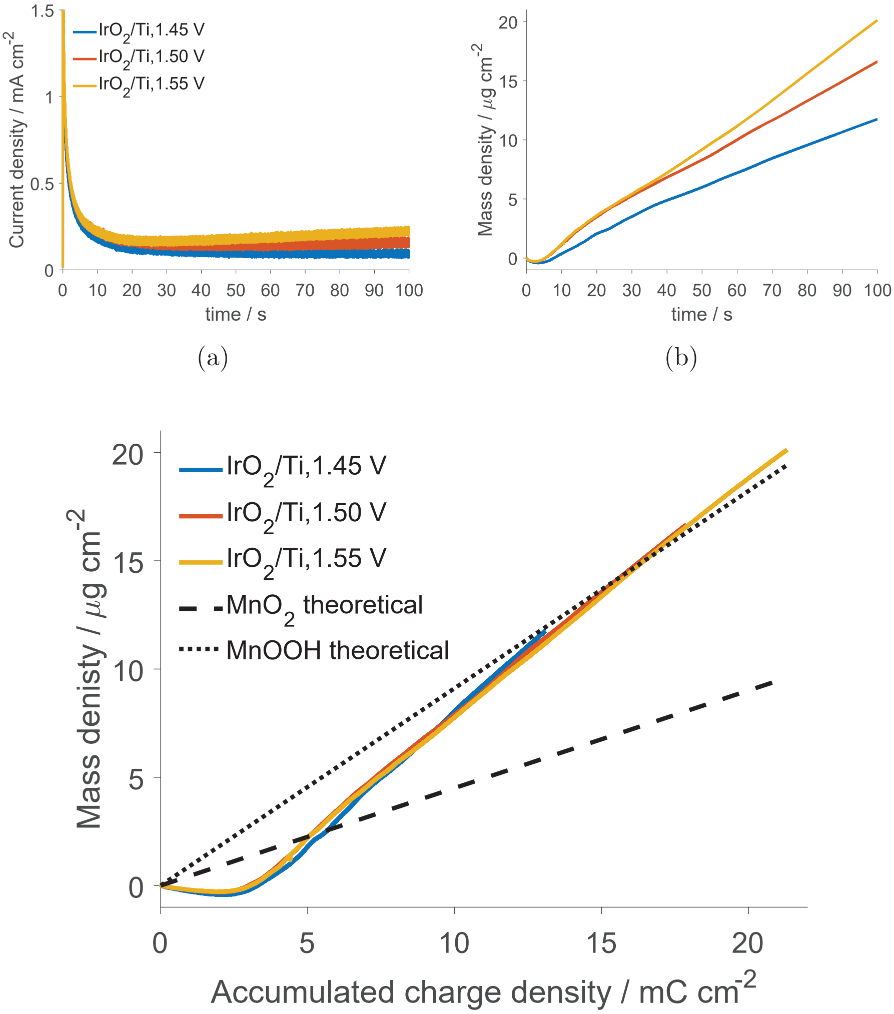

(a) (b)

(c)

Figure 5.73: Current transients (a) and mass transients (b) for potential steps on a h-IrO_2-coated titanium electrode in 0.1 mol L^{-1} H_2SO_4 + 5 mmol L^{-1} Mn^{2+}. A different representation of the same experiments are shown in (c) where the mass calculated from the frequency is plotted versus the accumulated charge calculated from the current. The theoretical development for MnO_2 and MnOOH formation are also included.

5.4.3 Step-Hold-CV

The reduction behavior of manganese oxide was further investigated by performing a combination of step, hold and sweep techniques as described in Figure 4.5. Negative-going linear sweeps initiated immediately after the potential steps presented in the previous section (Figs. 5.72 and 5.73) are displayed in Figure 5.74.

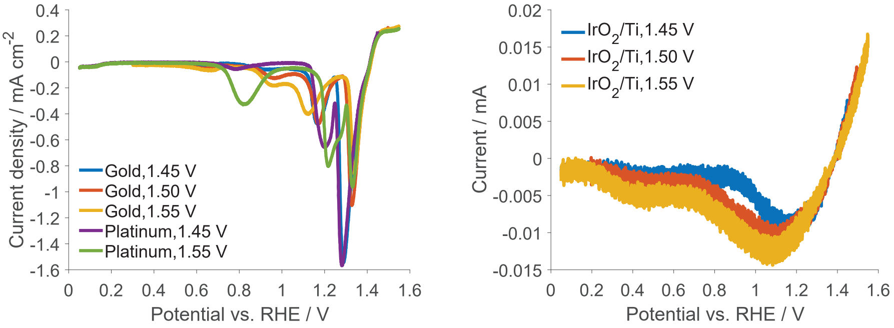

(a) Pt and Au

(b) h-IrO_2/Ti

Figure 5.74: Negative-going linear sweep voltammograms at sweep rate 5 mV s^{-1} following potential steps to various potentials for 100 s on Au and Pt (a) and h-IrO_2/Ti (b) in 0.1 mol L^{-1} H_2SO_4 + 5 mmol L^{-1} Mn^{2+}.

On platinum and gold (Fig. 5.74a) a number of reduction peaks occurred in the first negative-going sweep where shape, size and position depended on the hold potential and substrate, analogous to what was observed when varying the upper reversal potential (Figs. 5.62a and 5.66a). An additional reduction peak appeared when a sweep preceded the hold and even more reduction peaks appeared when a positive-going sweep was initiated after the hold (not shown here). Clearly, more charge was passed during the first reduction peak (1.3 V, Fig. 5.74a) in the negative-going sweep from 1.45 V than from higher potentials. Correspondingly, the peak potential shifted to more negative potentials.

On the other hand, the negative-going sweeps on the IrO_2/Ti electrode did not seem significantly influenced by the hold potential (Fig. 5.74b). Once more, this is analogous to what was observed when the upper reversal potential was varied (Fig. 5.71).

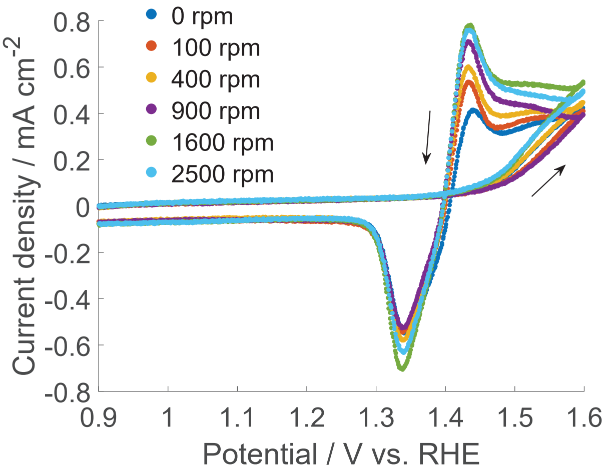

Figure 5.75: Cyclic voltammograms showing the first cycle of a platinum RDE at different rotation speed in $0.1\,\mathrm{mol\,L^{-1}}$ H_2SO_4 + $5\,\mathrm{mmol\,L^{-1}}$ Mn^{2+} at sweep rate $20\,\mathrm{mV\,s^{-1}}$. Arrows indicate sweep direction. The electrode was chemically cleaned between each experiment.

5.5 Rotating Disc Electrode

The effect of rotation speed on a chemically cleaned platinum electrode was investigated with cyclic voltammetry (Fig. 5.75) and potential steps (Fig. 5.76). The anodic portion of the voltammogram was influenced by the rotation rate, most pronounced after potential reversal. The current densities were in expected order with respect to rotation rate around the oxidation peak on the negative-going sweep, but not on the positive-going sweep. The effect of rotation was less on the reduction peak than on the anodic part of the voltammogram, displaying only a slight variation in current density as the rotation rate changed.

As in the CV, the effect of rotation rate was small at short times (few seconds) in the potential steps (Fig. 5.76). However, the effect progressively increased as the peak in the current transient was approached. Similar dependency on rotation rate was observed with crystalline DSA electrodes (not shown here). At a point after the peak in the current transients, diffusion limitations were observed in both electrolytes, i.e. linear relation between $1/I$ vs $\omega^{-1/2}$ (Figs. 5.76c and 5.76d).

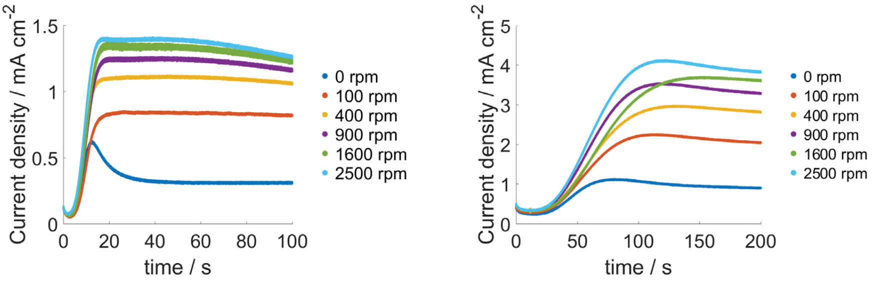

(a) 0.1 M H_2SO_4 + 5 mM Mn^{2+} (b) 2 M H_2SO_4 + 0.15 M Mn^{2+}

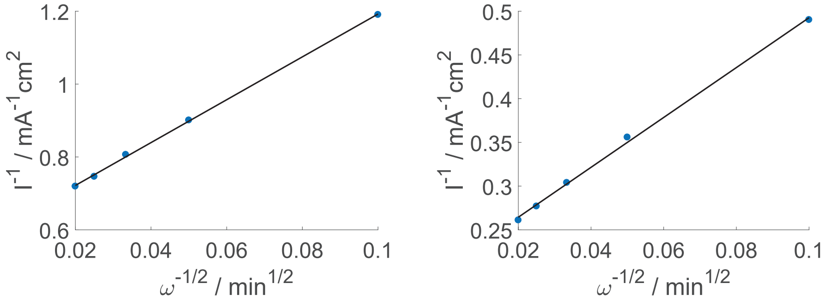

(c) 0.1 M H_2SO_4 + 5 mM Mn^{2+} (d) 2 M H_2SO_4 + 0.15 M Mn^{2+}

Figure 5.76: (a) and (b): Current transients at various rotation rates of a chemically cleaned platinum electrode stepped to 1.45 V. The electrode was cleaned between each step. Figures (c) and (d) show plots of $1/I$ vs $\omega^{-1/2}$ for the current densities at 50 s and 200 s in figures (a) and (b), respectively.

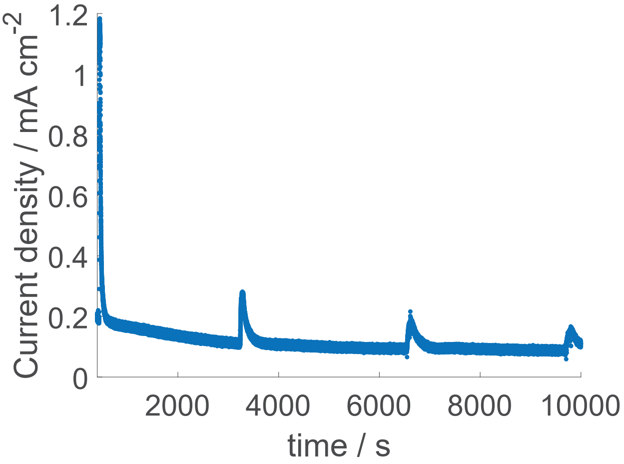

Figure 5.77: Potential step to 1.45 V for 10 000 s at a chemically cleaned platinum RDE in 0.1 mol L^{-1} H_2SO_4 + 5 mmol L^{-1} Mn^{2+}. The electrode was mainly stationary, but rotation spikes (1600 rpm) were applied at approximately 450 s, 3250 s, 6550 s and 9700 s.

The effect of mass transport on longer times scales were investigated by performing a potential step to 1.45 V for 10 000 s at a chemically cleaned platinum RDE in 0.1 mol L^{-1} H_2SO_4 + 5 mmol L^{-1} Mn^{2+}, see Figure 5.77. The electrode was mainly maintained at 0 rpm, but spikes at 1600 rpm were applied at regular intervals. The effect of increased rotation rate diminished significantly as the deposition time increased.

5.6 Remaining MnO_x-deposits

The effect of residual manganese oxide at the surface was studied in an RDE set-up. Selected cycles of the anodic portion of voltammograms obtained between 0 and 1.6 V at sweep rate 20 mV s^{-1} in 0.1 mol L^{-1} H_2SO_4 + 5 mmol L^{-1} Mn^{2+} and in 2 mol L^{-1} H_2SO_4 + 0.15 mol L^{-1} at a platinum electrode are presented in Figure 5.78. The electrode was cleaned by immersion in a H_2O_2-solution before the first cycle. The voltammograms changed considerably during cycling. The effect was most pronounced in 0.1 mol L^{-1} H_2SO_4 + 5 mmol L^{-1} Mn^{2+} where at first only an oxidation shoulder was observed during the forward sweep (positive of 1.5 V) that developed to a peak

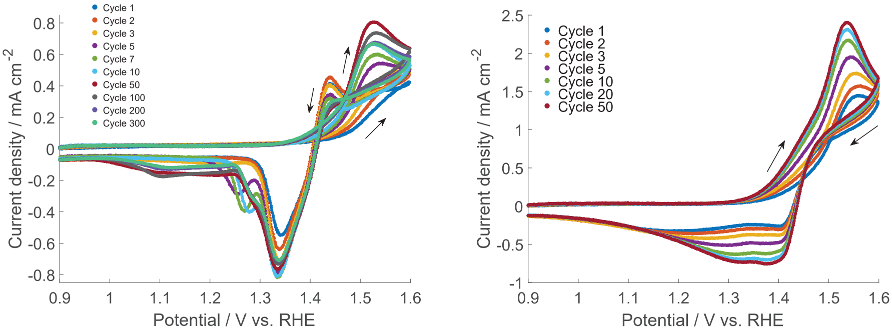

(a) 0.1 mol L^{-1} H_2SO_4 + 5 mmol L^{-1} Mn^{2+} (b) 2 mol L^{-1} H_2SO_4 + 0.15 mol L^{-1} Mn^{2+}

Figure 5.78: Cyclic voltammograms of a chemically cleaned platinum electrode at sweep rate 20 mV s^{-1}. No rotation. Arrows indicate sweep direction.

with repeated cycling (Fig. 5.78a). The peak reached its maximum value around 50 cycles before the height again reduced. On the reverse sweep, a second oxidation peak was observed around 1.45 V in the first few cycles. However, this peak rapidly diminished as the number of cycles increased. The onset of Mn^{2+} oxidation shifts to lower potentials as the number of cycles decreased in both electrolytes showing that the residual manganese oxide facilitates deposition in subsequent cycles. In 2 mol L^{-1} H_2SO_4 + 0.15 mol L^{-1} Mn^{2+} (Fig. 5.78b), the oxidation peak on the forward sweep (positive of 1.5 V) was present already from the first cycle and its height increased as the number of cycles increased. No noticeable oxidation peak on the reverse sweep was detected in this electrolyte.

The reduction behavior also changed considerably in the low concentration electrolyte (Fig. 5.78a), starting with only one reduction peak (1.34 V) during the first cycles. The charge passed during this peak did not change considerably as more manganese oxide was deposited, rather a second oxidation peak appeared from cycle 5. The size of this second peak first increased for a few cycles, before diminishing to a shoulder. Simultaneous to the diminishing of the second reduction peak, a third reduction feature started to emerge. This third feature was a plateau current rather than a peak, starting from ca. 1.2 V. The magnitude of the plateau current decreased from cycle 100 to cycle 200, simultaneous to a decrease in the amount of manganese oxide deposited in the anodic portion of the voltammogram. The size

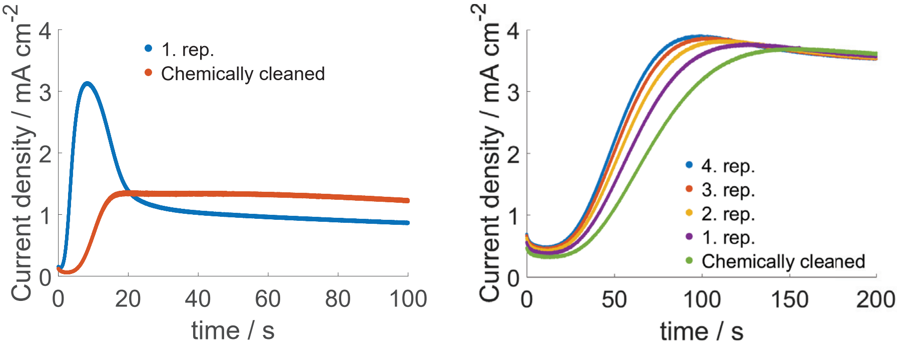

(a) 0.1 mol L^{-1} H_2SO_4 + 5 mmol L^{-1} Mn^{2+}

(b) 2 mol L^{-1} H_2SO_4 + 0.15 mol L^{-1} Mn^{2+}

Figure 5.79: Current transients of the first and subsequent steps to 1.45 V of a chemically cleaned platinum electrode at rotation rate 1600 rpm. The electrode was not chemically cleaned between each step, but held for 10 s at 0.5 V.

of the reduction in the high concentration electrolyte (Fig. 5.78b) increased as more manganese oxide was deposited with increasing cycle number. However, the position and number of the peaks did not change as they did in the low concentration electrolyte.

The effect of remaining MnO_x deposits were also investigated in potential steps with and without rotation, see Figures 5.79 and 5.80. The peak in the current transient shifted to shorter times and higher current densities as the number of repetitions (without chemical cleaning in between) increased. The effect was more pronounced in low concentration electrolyte (0.1 mol L^{-1} H_2SO_4 + 5 mmol L^{-1} Mn^{2+}, Fig. 5.79a) than in high concentration electrolyte (2 mol L^{-1} H_2SO_4 + 0.15 mol L^{-1} Mn^{2+}, Fig. 5.79b). Furthermore, the increase in current was more pronounced at a platinum electrode (Fig. 5.79a) than at a crystalline DSA electrode (5.80a). The time at OCP following a reduction step clearly reduced the effect (blue and yellow curves in Fig. 5.80b), shifting the peak in the current transient to longer times.

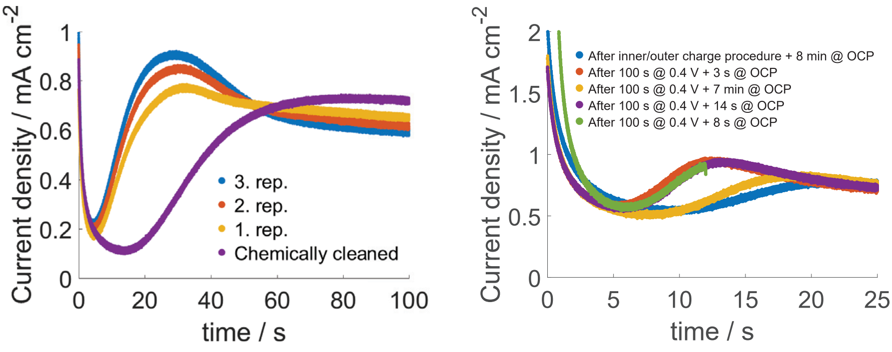

(a) (b)

Figure 5.80: Current transients for a crystalline DSA electrode held at 1.45 V in 0.1 mol L^{-1} H_2SO_4 + 5 mmol L^{-1} Mn^{2+}. (a) The electrode was chemically cleaned before the first experiment, but only held for 10 s at 0.5 V between each subsequent repetition. Rotation rate 1600 rpm. (b) The electrode was treated differently between each potential step as specified in the legend. No rotation.

5.7 In-situ Raman Spectroscopy

Representative Raman spectra are given in Figure 5.81 for the deposits obtained after 10 000 s on the different electrode materials. The most prominent peak appeared at approximately 575 cm^{-1} with one broad peak to each of its sides: slightly above 510 cm^{-1} and slightly below 650 cm^{-1}. The spectra resembles those obtained by Julien et al. [48] for γ-MnO_2 (Figs. 2.9 and 2.10). This is as expected as the deposition conditions resembles those of electrolytic manganese dioxide (EMD) which forms γ-MnO_2.

The Raman spectra were independent on the applied potential as well as the working electrode material. Furthermore, the spectra were independent on the deposition time. Time series were acquired during deposition (Tab. 4.11). The time series acquired for 100 s deposition time only displayed noise and the single spectra acquired immediately after deposition had quite low intensities. Time series acquired at longer deposition times had better signal - especially after moving the stage slightly and refocusing. The intensities often diminished slightly over time. Single value decomposition was performed on all time series to search for any changes in the Raman spectra during deposition, but peaks were only found at the same positions as in

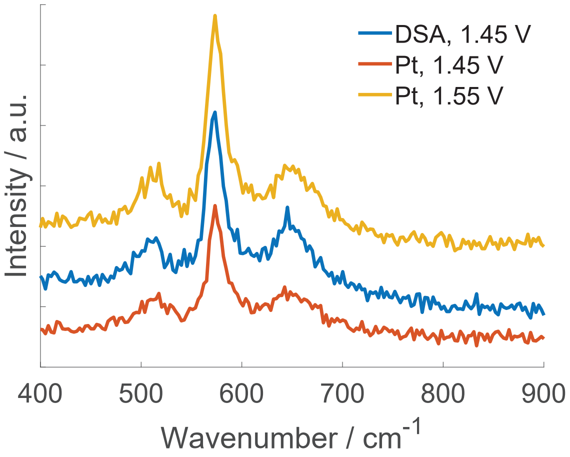

Figure 5.81: Raman spectra acquired after MnO_2 was deposited for 10 000 s in 0.1 mol L^{-1} H_2SO_4 + 5 mmol L^{-1} Mn^{2+} at the specified electrodes and potentials.

Figure 5.81. The obtained ex-situ spectra also displayed the same peak positions.

Images of the MnO_2 deposits were acquired with the Raman microscope in bright field mode, see Figure 5.82. These images were acquired immediately after a time series deposition (laser power 0.5 mW). A small hole in the deposit was observed in the center of the images where the laser beam had hit, perhaps most pronounced in Figure 5.82b. Holes were also observed in other spots depending on the movement of the stage during deposition. This demonstrates the thermal instability of the deposit.

The images in Figure 5.82 clearly show that the dendrite formation (small darker spots) was greater at 1.55 V than at 1.45 V, as was also observed to a less extent for the deposits examined with SEM (Figs. 5.26 and 5.28). Furthermore, the images show a change in color of the deposit depending on the deposition time. At first a brown deposit was obtained as seen in Figs. 5.82a and 5.82d. However, after some time the deposits appeared multicolored, best illustrated in Fig. 5.82e. This was probably due to thin-film interference. Videos showed that the same spot at the surface displayed several different colours during deposition. Identical Raman spectra were acquired for areas displaying different colors.

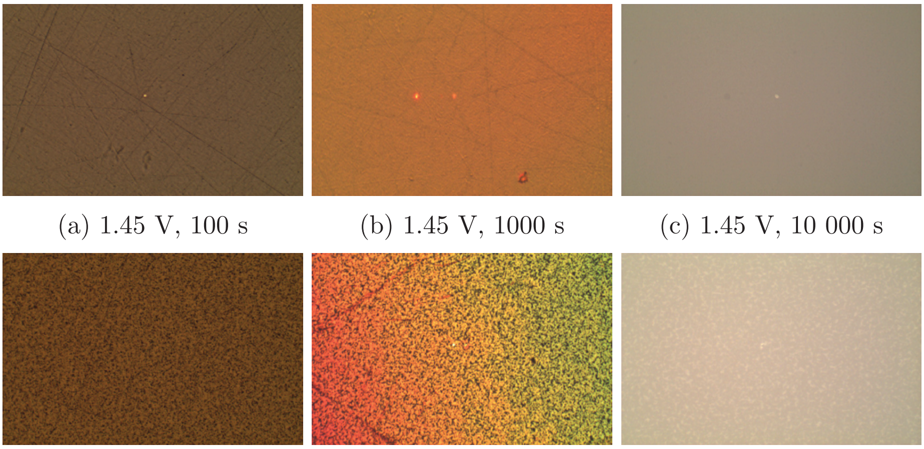

(a) 1.45 V, 100 s (b) 1.45 V, 1000 s (c) 1.45 V, 10 000 s

(d) 1.55 V, 100 s (e) 1.55 V, 1000 s (f) 1.55 V, 10 000 s

Figure 5.82: In situ bright field images acquired with the Raman microscope of the MnO_2 deposits obtained on a platinum electrode in 0.1 mol L^{-1} H_2SO_4 + 5 mmol L^{-1} Mn^{2+}.

Time series of Raman spectra were also acquired during reduction of deposits obtained at 1.45 V (Tab. 4.12). For the thinner deposits (1000 s) the intensity of the Raman peaks gradually decreased and eventually disappeared during the reduction. No changes in peak position was observed. However, for the thicker deposits (10 000 s) no changes to the Raman spectra were observed during the reduction , meaning that manganese oxide was still present at the surface at the end of the sweep, both at the DSA and platinum electrodes. Moreover, the in situ images acquired after reduction at the platinum electrode showed that parts of the surface was still covered with manganese oxide (brown/black color), whereas it had disappeared in other locations (Fig. 5.83). This could not be evaluated for the DSA electrodes since the color of the DSA surface is similar to that of the manganese oxide deposit.

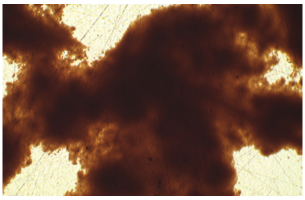

Figure 5.83: In situ bright field image acquired at the end of the reduction of a MnO_2 deposit (10 000 s at 1.45 V in 0.1 mol L^{-1} H_2SO_4 + 5 mmol L^{-1} Mn^{2+}) at a platinum electrode.

5.8 MnO_x deposition - Effect of substrate

The cyclic voltammograms obtained of all the different electrode materials in 0.1 mol L^{-1} H_2SO_4 + 5 mmol L^{-1} Mn^{2+} are compared in Figure 5.84. The Ti, Pt, Au and Ti/IrO_2 voltammograms were acquired in the EQCM set-up, whereas the crystalline DSA voltammogram was acquired in the conventional cell. The y-axis is limited for the crystalline DSA (cf. Fig. 5.33h) in order to maintain focus on the features related to manganese oxide deposition and reduction.

The manganese oxide formation features were similar on gold, platinum and crystalline DSA electrodes in 0.1 mol L^{-1} H_2SO_4 + 5 mmol L^{-1} Mn^{2+} with an oxidation peak or shoulder at approximately 1.45 V. The manganese oxide formation overlapped with OER on the crystalline DSA, but not on the gold and platinum electrodes. The overpotential for Mn^{2+} oxidation was low on the crystalline DSA commencing as early as at 1.2 V at sweep rate 5 mV s^{-1} (cf. Fig. 5.33). In contrast, oxidation only started at potentials closer to 1.4 V on platinum and gold electrodes. Similarities between gold, platinum and crystalline DSA electrodes were also observed in the reduction features with a reduction wave at approximately 1.3 V at all three substrates. A second reduction peak was observed at more negative potentials on the gold and platinum electrodes (cf. Figs. 5.62a and 5.66a), but not on the crystalline DSA where only one reduction peak was observed (cf. Fig. 5.33).

Similar to the electrodes mentioned above, the Ti-electrode covered with h-IrO_2 powder also displayed an oxidation shoulder in the positive-going sweep, but at a slightly more positive potential (closer to 1.5 V). Based on the massograms, the onset of Mn^{2+} oxidation occurred around 1.3 V on

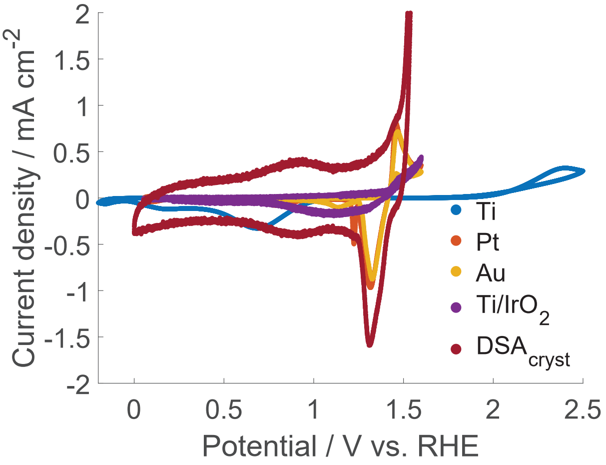

Figure 5.84: Cyclic voltammograms recorded at the different electrode materials in 0.1 mol L^{-1} H_2SO_4 + 5 mmol L^{-1} Mn^{2+} at sweep rate 5 mV s^{-1}.

the h-IrO_2 covered electrode (Fig. 5.70d), which is intermediate between the crystalline DSA and gold/platinum. However, the reduction occurred in a very broad wave peaking around 1.1 V. As mentioned previously (end of section 5.4), the loading of the electrocatalyst was limited in order to prevent a failure of the EQCM frequency signal. This resulted in poor quality of the measured current signal.

In contrast to the electrode materials mentioned so far, Ti-electrodes require a high overpotential both for reduction and deposition of manganese oxide. Similarly, the overpotential on lead electrodes is also quite high with deposition only occurring above 2 V in 2 mol L^{-1} H_2SO_4 + 0.15 mol L^{-1} Mn^{2+} at sweep rate 10 mV s^{-1} [131].

The amorphous DSA electrodes were only tested in 2 mol L^{-1} H_2SO_4 with or without 0.15 mol L^{-1} Mn^{2+}, see Tab. 4.3. Comparisons between the amorphous and crystalline DSA electrodes in this electrolyte are presented at the end of the LSV section (5.3.2).

The nucleation behavior on the different electrode materials were compared with those expected from instantaneous and progressive nucleation [123], see Figure 5.85. In order to be evaluated according to this method a peak needs to be present in the current transient. This was not always the case, particularly not at high potential (1.55 V). Accordingly, not all the performed

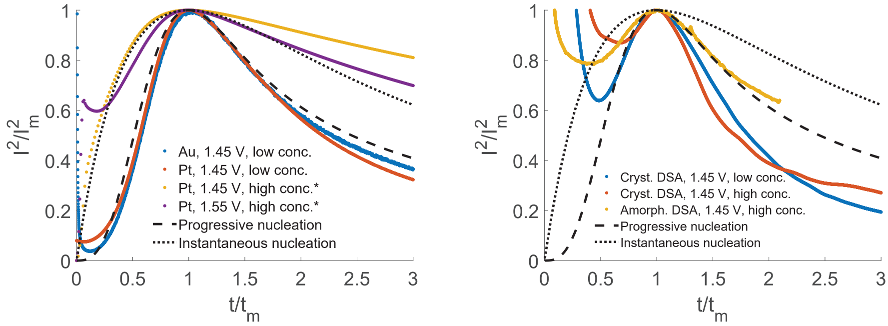

(a) Pt and Au.

(b) DSA.

Figure 5.85: Dimensionless plots for nucleation on different electrode materials. The theoretical curves for instantaneous and progressive nucleation are also displayed. The experiments were performed at the given potentials in an electrolyte consisting of either 0.1 mol L^{-1} H_2SO_4 + 5 mmol L^{-1} Mn^{2+} (denoted low conc. for all materials), 0.1 mol L^{-1} H_2SO_4 + 0.15 mol L^{-1} Mn^{2+} (only on Pt, denoted high conc.*) or 2 mol L^{-1} H_2SO_4 + 0.15 mol L^{-1} Mn^{2+} (only on DSA electrodes, denoted high conc.).

chronoamperometric experiments are included in the figure.

Platinum and gold electrodes displayed a progressive nucleation mechanism when deposition occurred at 1.45 V in 0.1 mol L^{-1} H_2SO_4 + 5 mmol L^{-1} Mn^{2+} (Fig. 5.85a). However, when the Mn^{2+}-concentration increased an instantaneous nucleation mechanism was observed at the platinum electrode. The DSAs displayed a progressive nucleation mechanism at the examined deposition conditions (Fig. 5.85b), though the fit was poorer than for the platinum and gold electrodes.

Chapter 6

Discussion

Manganese oxide formation on oxygen evolving electrodes represents an industrially important limitation to introducing active anodes in manganese rich sulphate electrolytes, such as in the zinc, manganese and nickel electrowinning. Due to the possible oxidation states that manganese can possess, as seen in the Pourbaix diagram (Fig. 2.5), the reaction mechanisms for its oxidation and reduction are known to be complicated, involving various chemical and electrochemical steps with partially stable reaction intermediates depending on the reaction conditions, i.e. potential, acid strength, mass transport, manganese concentration and temperature [72]. The following reactions will be considered as a framework for the discussion of manganese oxide deposition below:

$$Mn^{2+} \longrightarrow Mn^{3+} + e^- \tag{6.1}$$

$$Mn^{3+} + 2\,H_2O \longrightarrow MnOOH + 3\,H^+ \tag{6.2}$$

$$MnOOH \longrightarrow MnO_2 + H^+ + e^- \tag{6.3}$$

$$2\,Mn^{3+} \longrightarrow Mn^{2+} + Mn^{4+} \tag{6.4}$$

$$Mn^{4+} + 2\,H_2O \longrightarrow MnO_2 + 4\,H^+ \tag{6.5}$$

It is generally accepted that the first step in manganese oxide deposition is the oxidation of Mn^{2+} to Mn^{3+} (Eq. (6.1)). Based on results obtained in this work as well as in the literature [58], the second reaction is a chemical step, either forming a Mn(III) intermediate represented by MnOOH in Eq. (6.2) or combining with an adjacent Mn^{3+} in a disproportionation reaction, forming Mn^{2+} and Mn^{4+} (Eq. (6.4)). Mn^{4+} is very unstable at the conditions used in this work and will immediately form MnO_2 at the surface (Eq. (6.5)). The Mn(III) intermediate can be further oxidized to MnO_2 at higher potentials (Eq. (6.3)). The first mechanism is referred to as the ECE mechanism (Eqs. (6.1), (6.2) and (6.3)), while the second is referred to as the disproportionation reaction (Eqs. (6.1), (6.4) and (6.5)). Both mechanisms are thought to occur simultaneously, but their relative rates depend highly on the pH as it is directly linked to the stability of the Mn^{3+}-ion which decreases with decreasing acid strength [57]. Clarke et al. found that the ECE mechanism is favoured in slightly acidic electrolytes and the disproportionation mechanism is promoted at higher acid strengths (lower pH), due to the difference in stability of the Mn^{3+}-ion [58].

The presence of an Mn(III) intermediate, such as MnOOH, was confirmed from the accumulated charge density versus mass density during potential steps with EQCM (Figs. 5.72c and 5.73c). A mixture between MnO_2 and the Mn(III) intermediate is produced at lower potentials (1.45 V) at platinum and gold electrodes (Fig. 5.72c), in accordance with Dupont and Donne for a Pt electrode [61]. However, the oxidation product is only MnO_2 at higher potentials (1.55 V) at platinum and gold electrodes. These results are in accordance with the ECE mechanism, where MnOOH is formed at lower potentials (Eqs. (6.1) and (6.2)) and is further oxidized to MnO_2 at higher potentials (Eq. (6.3)). MnO_2 is expected to be formed at lower potentials as well, but the kinetics of reaction (6.3) might not be sufficient to convert all the formed MnOOH to MnO_2. Alternatively, the MnO_2 formed at the lower potential might originate from the disproportionation mechanism given by Equations (6.1), (6.4) and (6.5). It is worth pointing out that since H^+ is produced in the overall reaction, the disproportionation mechanism might become more prevalent with increasing deposition time due to a local reduction of pH at the surface.

At higher potentials formation of permanganate ions is expected (cf. 2.5), according to the total reaction (2.10). A colour change of the electrolyte towards red was observed when the potential was sufficiently positive, i.e. above at least 1.60 V.

Manganese oxide deposition is a complex process that varies with time and potential. The discussion is divided into what happens at short times (section 6.1) and longer times (section 6.2). The first section (6.1) concerns nucleation and initial growth phase, i.e. up to approximately one minute, and the second section (6.2) concerns deposition for up to several hours. In the subsequent sections, reduction (section 6.3) and removal (section 6.4) of manganese oxide are discussed.

6.1 Initial stages of deposition

The first step in oxidation of manganese ions must involve interaction with the electrode followed by an electrochemical reaction. This step must be the oxidation of Mn^{2+} to Mn^{3+} at the electrode surface, in accordance with both the ECE and disproportionation mechanisms. First of all, there was no observation of any formed solid manganese oxides nor any color changes in the bulk of the electrolyte at any of the bath compositions as long as there was no current flowing through the cell. Furthermore, EQCM measurements show no mass change in the first few seconds during potential step measurements, although charge was passed, both on gold and platinum electrodes (cf. insert in Fig. 5.72c) as well as on h-IrO_2 (Fig. 5.73). A delay in mass increase versus charge during potential step measurements was also observed by Dupont and Donne at 1.3 V vs. SCE at a platinum electrode in $0.1\,\mathrm{mol\,L^{-1}}$ sulphuric acid with $10\,\mathrm{mmol\,L^{-1}}$ Mn^{2+} [61]. This is in accordance with an electrochemical reaction without an associated mass change as the initial step (6.1), where desorption of Mn^{3+} is faster than a subsequent reaction involving an increase in mass (6.2).

6.1.1 Nucleation and growth

Based on an evaluation of the shape of current transients, nucleation occurs by a progressive mechanism at 1.45 V in $0.1\,\mathrm{mol\,L^{-1}}$ H_2SO_4 + $5\,\mathrm{mmol\,L^{-1}}$ Mn^{2+} for all substrates (Fig. 5.85). The method for determining the nucleation mechanism assumes that the nucleation is diffusion controlled and that the nuclei form hemispheres [123] (cf. sec. 3.3). Deposition of manganese oxide was found to be diffusion controlled after some nucleation had occurred, as will be further elaborated below. Hemispherical growth on platinum electrodes was observed both in STEM images in this work (Fig. 5.27) and in SEM images obtained by Fleischmann et al. [66]. In Figure 5.27, deposition was stopped at the peak observed in the current transient at 1.45 V and a large number of nuclei was observed. In contrast, the nuclei observed in the SEM images obtained by Fleischmann et al. were produced at low overpotentials and short times, likely well before any peak in the current transient. Hence, the nuclei number density was lower in their work. Development of morphology on longer time scales will be discussed in section 6.2.1.

The rate of nucleation must be affected by the electrolyte pH. Nucleation occurred faster in low concentration ($0.1\,\mathrm{mol\,L^{-1}}$ H_2SO_4 + $5\,\mathrm{mmol\,L^{-1}}$ Mn^{2+}) than in high concentration electrolyte ($2\,\mathrm{mol\,L^{-1}}$ H_2SO_4 + $0.15\,\mathrm{mol\,L^{-1}}$ Mn^{2+}), as indicated by the earlier peak in the current transient (Figs. 5.54a vs 5.55a). This was also evident from STEM images where comparable amounts of nuclei had formed when deposition was stopped at the peak observed in the current transient in the two electrolytes (Figs. 5.6 and 5.11). Even though more Mn^{3+} ions were formed in high concentration electrolyte (higher charge passed), their stability is greater at low pH and consequently nucleation is slower. This is in agreement with the works of Petitpierre et al. [55] and Nijjer [72] who found that the cathodic charge in cyclic voltammograms decreased significantly with increasing H^+ concentration (although the anodic charge was less affected), indicating that less MnO_x was formed in more acidic electrolytes.

Effect of mass transport. Based on measurements with a rotating disc electrode, mass transport is not a limiting factor initially, but diffusion limitations arise after some nucleation has occurred. Initially, i.e. before nucleation occurred, the effect of rotation rate was limited both on Pt (Fig. 5.76) and on crystalline DSA electrodes. This means that the rate of reaction (6.1) on those substrates is unaffected by mass transport, but rather controlled by other factors such as adsorption/desorption or charge transfer. However, as nucleation of MnO_x commences and proceeds, the effect of rotation rate becomes apparent. This implies that reaction (6.1) on the growing MnO_x deposit is controlled by diffusion of Mn^{2+}-ions in the electrolyte, as was also indicated by the linear relation between I^{-1} vs $\omega^{-1/2}$. Correspondingly, Cottrell behavior ($I \propto t^{-1/2}$) was observed from 20 s to 60 s in the current transients without rotation of potential steps to 1.45 V on Pt (Fig. 5.76) and Pt and Au (Fig. 5.72a). Dupont et al. [132] also observed Cottrell behavior on a similar time scale during deposition of MnO_2 on a platinum electrode at 1.35 V vs. SCE in $0.1\,\mathrm{mol\,L^{-1}}$ H_2SO_4 + $0.01\,\mathrm{mol\,L^{-1}}$ $MnSO_4$. In contrast to what was observed in this work, they also observed Cottrell behavior initially, i.e. prior to the peak in the current transient. However, they applied a more positive potential (1.35 V vs. SCE) so mass transport limitations are expected to arise earlier due to faster MnO_x nucleation.

The effect of mass transport at short deposition times has been studied by several authors [58–60, 72, 75]. While some have seen an effect indicating that mass transport influences the overall reaction rate, others have observed little or no effect of rotation or stirring, particularly at low temperatures. However, the deposition conditions in the literature vary, as illustrated in Table 2.1. Hence, the onset of mass transport limitations at short deposition times is affected not only by electrode potential and potential ramp, but also by other deposition conditions such as concentration of Mn^{2+}, acid strength, substrate and temperature. In agreement with the results in this work, Paul and Cartwright [52] found that the deposition of manganese dioxide at a graphite electrode was controlled by diffusion of Mn^{2+}-ions in the electrolyte at short times, i.e. less than 100 s, as long as the concentration of Mn^{2+}-ions was low, i.e. less than around $0.02\,\mathrm{mol\,L^{-1}}$ in combination with $0.16\,\mathrm{mol\,L^{-1}}$ H_2SO_4.

Effect of remaining MnO_x. Deposited MnO_x cannot be completely removed by electrochemical reduction alone. Chemically cleaned Pt or DSA electrodes behave differently than activated Pt or DSA electrodes that have experienced MnO_x deposition - even after electrochemical reduction of the deposited MnO_x. This is clearly illustrated by the earlier onset of Mn^{2+} oxidation in the continuous voltammetry experiments in Figure 5.78 and in the potential step experiments in Figures 5.79 and 5.80. This decrease in overpotential is caused by incomplete removal of the MnO_x deposited in the previous cycle/potential step. The time spent at potentials where MnO_x reduction is expected is not sufficient to remove all the deposited MnO_x, although the current and mass appear to return to their initial values prior to manganese oxide deposition (e.g. Fig. 5.63). As a result, the amount of remaining MnO_x increases with each cycle/potential step. In addition to the time for electrochemical reduction, the time held at OCP after electrochemical reduction also had an effect on the amount of residual MnO_x (yellow curve in Fig. 5.80b), indicating that a chemical reaction is involved in removal of MnO_x. The effect of remaining MnO_x was less pronounced in high concentration electrolyte ($2\,\mathrm{mol\,L^{-1}}$ H_2SO_4 + $0.15\,\mathrm{mol\,L^{-1}}$ Mn^{2+}) than in low concentration electrolyte ($0.1\,\mathrm{mol\,L^{-1}}$ H_2SO_4 + $5\,\mathrm{mmol\,L^{-1}}$ Mn^{2+}) (Figs. 5.78 and 5.79), indicating that the amount of remaining deposit af-

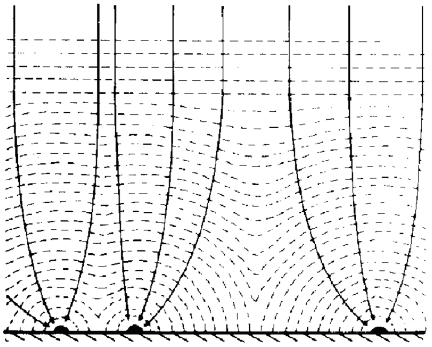

Figure 6.1: "Schematic representation of the growth of diffusion zones and their eventual overlap." Reproduced from [123] with permission from Elsevier.

ter reduction was less in the high concentration electrolyte. This can be explained in terms of (i) slower deposition of MnO_x in more acidic electrolytes, with correspondingly less remaining MnO_x after reduction or (ii) more complete electrochemical reduction of the deposit formed in high concentration electrolyte. The reason for the incomplete electrochemical removal of deposited MnO_x will be further discussed in section 6.3, whereas in the following the effect of remaining MnO_x on subsequent measurements is discussed.

The remaining MnO_x must increase the rate of oxidation of Mn^{2+} and is also proposed to increase the rate of further nucleation. As discussed in the section on effect of mass transport, reaction (6.1) occurs faster on deposited MnO_x than on chemically cleaned Pt and crystalline DSA electrodes. This can explain the earlier rise in current when remaining MnO_x is present. In addition, further nucleation and deposition may occur faster when remaining MnO_x is present, as was also observed at a composite Pb-MnO_2 electrode [133]. This can be explained either by the increased availability of Mn^{3+} ions or because of more energetically favorable sites for nucleation. An increased deposition rate would lead to a more rapid increase in available surface area and result in a further increase in current as long as the diffusion layer thickness is on a smaller scale than the surface roughness (see Fig. 6.1), and could potentially explain the considerable increase in peak height observed in Figure 5.79a.

Oxidation peak on reverse scan ($p_{ox,2}$). A small oxidation peak or shoulder is often observed during the negative-going scan at potentials about 1.40-1.45 V that appears to be governed by several factors; change in local pH, stability of Mn^{3+}, change in surface area and development of diffusion layer thickness. In the following, any feature related to current or mass occurring in this potential region is assigned as $p_{ox,2}$ (see Fig. 5.62). An explanation for the governing processes in this potential region must satisfy the following experimental observations:

i) $p_{ox,2}$ correlates with a mass increase (e.g. Fig 5.63).

ii) $p_{ox,2}$ occurs at about the same potential for DSA, Pt and Au electrodes in $0.1\,mol\,L^{-1}$ H_2SO_4 + $5\,mmol\,L^{-1}$ Mn^{2+} (Figs. 5.33, 5.63 and 5.67).

iii) $p_{ox,2}$ increases with increasing rotation rate, i.e. mass transport (Fig. 5.75).

iv) The height of the current peak in $p_{ox,2}$ decreases with increasing upper reversal potential and disappears if the potential is reversed at potentials above about 1.7 V (Fig. 5.63f), or has a preformed layer of MnO_2 (see Fig. 8 in [134]). However, a mass increase is still observed.

v) $p_{ox,2}$ is clearly apparent in the continuous voltammetry experiment in $0.1\,mol\,L^{-1}$ H_2SO_4 + $5\,mmol\,L^{-1}$ Mn^{2+} (Fig. 5.78a) increasing slightly from the first to the second cycle before it rapidly declines to a shoulder with increasing cycle number.

vi) $p_{ox,2}$ is not as visible in $2\,mol\,L^{-1}$ H_2SO_4 + $0.15\,mol\,L^{-1}$ Mn^{2+}, but might be present as a shoulder (Figs. 5.37 and 5.78b). However, it is hard to distinguish between such a shoulder and the onset of MnO_x reduction.

It may be proposed that upon reversing and approaching $p_{ox,2}$ the second electrochemical reaction in the ECE mechanism (MnOOH to MnO_2, Eq. (6.3)) diminishes and may disappear. That means that the ECE mechanism would mainly lead to formation of MnOOH, which is not electrochemically converted to MnO_2 at this potential. This leads to a decrease in the rate of H^+ formation, since $3H^+$ are formed instead of $4H^+$, and a relatively higher pH within the deposit. A higher pH will destabilize any Mn^{3+} formed within the deposit and a more rapid formation of MnOOH is to be expected, accompanied with a mass increase (i).

The current peak in $p_{ox,2}$ is proposed to depend on a change in electroactive surface area in combination with development of diffusion layer thickness. As long as the amount of MnO_x deposit is limited, i.e. short deposition times, a simultaneous increase in both current and mass was observed. While it may seem counter-intuitive that the current increases when an electrochemical reaction (Eq. (6.3)) is no longer occurring, it is expected that the more rapid formation of MnOOH contributes to a larger available surface area for Mn^{2+} oxidation to Mn^{3+} (Eq. (6.1)). Since the reaction takes place at the deposit, the current in $p_{ox,2}$ is not expected to be influenced by the substrate (ii). As discussed above, deposition of manganese oxide is at short times controlled by diffusion of Mn^{2+} in the electrolyte, as also evident from the dependency of $p_{ox,2}$ on rotation rate (iii). As long as the diffusion layer thickness is on a smaller scale than the increase in surface roughness, an increase in available surface area will lead to an increase in current. However, for longer deposition times, the diffusion layer thickness may develop to a larger scale than the surface roughness so that an increase in surface area no longer leads to an increase in current, as illustrated in Figure 6.1. This explains why the current in $p_{ox,2}$ decreases with increasing deposition time, i.e. with increasing upper reversal potential, even though a mass increase is still observed (iv). Although the electrical conductivity of the deposit is expected to decrease with an increasing amount of Mn(III) oxide in the deposit [51], it is assumed here that the thickness of the deposit is small so that the potential drop through the deposit does not significantly influence the rate of reaction (6.1).

The change of diffusion layer thickness can also explain the development of $p_{ox,2}$ in the continuous voltammetry experiments (v). In those experiments, the amount of remaining MnO_x after each complete cycle increases with increasing cycle number as discussed above in the section concerning incomplete electrochemical removal of deposited MnO_x. Reaction (6.1) is expected to be faster on MnO_x than on the substrate (see: Effect of mass transport). Consequently, there is an increasing demand on mass transport of Mn^{2+} with increasing cycle number due to more MnO_x being present at the surface. This leads to a more rapid development of the diffusion layer thickness with increasing cycle number so that the increase in available surface area experienced during $p_{ox,2}$ does not contribute significantly to the current.

$p_{ox,2}$ must decrease in magnitude at lower pH since deposition primarily occurs by the disproportionation mechanism (Eqs. (6.1), (6.4) and (6.5)). The magnitude of $p_{ox,2}$ is related to the ECE mechanism that is more prevalent in less acidic electrolytes. In more acidic electrolytes the Mn^{3+} ion is expected to be more stable and deposition of MnOOH (Eq. (6.2)) is not expected to occur to a large extent. Reaction (6.3) is limited by the amount of MnOOH produced through reaction (6.2) and only proceeds to a limited extent. Consequently, the rate of H^+ formation is not expected to change significantly in more acidic electrolytes when the potential becomes insufficient for reaction (6.3) to occur. As a result $p_{ox,2}$ diminishes or disappears, in accordance with the results in this work (vi).

Oxidation peak on forward scan ($p_{ox,1}$). The existence of an oxidation peak on the forward scan ($p_{ox,1}$, see Fig. 5.62) can also be explained by an increase in surface area due to nucleation of a new phase in combination with development of the diffusion layer thickness and mass transport limitations. The peak shifted to higher potentials and became less pronounced with increasing sweep rate, but no clear trend in peak current density was observed (Figs. 5.64a and 5.68a). Similar peak current trends with sweep rates were observed by Nijjer [72]. However, at higher manganese concentration and elevated temperatures Rodrigues et al. [76] found the peak current to be proportional to the square root of sweep rate indicating diffusion limitations at these conditions. For slow sweep rates in low concentration electrolyte ($0.1\,\mathrm{mol\,L^{-1}}$ H_2SO_4 + $5\,\mathrm{mmol\,L^{-1}}$ Mn^{2+}), nucleation through reaction (6.2) has more time to occur, leading to an increase in the active surface area and in extension an increased current. This increase in surface area is particularly evident in CVs at slow sweep rates with upper reversal potential prior to the apex of $p_{ox,1}$ (Figs. 5.62c and 5.66c), and is a signature for nucleation and growth with an electrochemical reaction occurring on the surface of the growing nuclei. As discussed above, reaction (6.1) proceeds faster on MnO_x than on the substrate, further amplifying the increase in current. This puts an increasing demand on mass transport of Mn^{2+} ions and eventually the increase in surface area no longer contributes to an increased current, i.e. the diffusion layer becomes too thick (cf. Fig. 6.1). It is worth mentioning that no oxidation peak was observed during the first cycles of a chemically cleaned Pt electrode in $0.1\,\mathrm{mol\,L^{-1}}$ H_2SO_4 + $5\,\mathrm{mmol\,L^{-1}}$ Mn^{2+} at $20\,\mathrm{mV\,s^{-1}}$ (Fig. 5.78a), but the peak developed with increasing cycle number and increased in size up to cycle 50, demonstrating the influence of mass transport and effect of remaining MnO_x on the peak. At high sweep rates, nucleation have less time to proceed and the effect of increasing surface area is less. Consequently, $p_{ox,1}$ is less distinct. Since the electrode area at the peak is expected to vary with sweep rate, a plot of peak current vs square root of the sweep rate is not expected to be linear.

Cyclic voltammograms of chemically cleaned Pt electrodes (Fig. 5.78b) indicate that nucleation occurs faster during CVs in high concentration electrolyte ($2\,\mathrm{mol\,L^{-1}}$ H_2SO_4 + $0.15\,\mathrm{mol\,L^{-1}}$ Mn^{2+}) than in low concentration electrolyte ($0.1\,\mathrm{mol\,L^{-1}}$ H_2SO_4 + $5\,\mathrm{mmol\,L^{-1}}$ Mn^{2+}). In high concentration electrolyte, $p_{ox,1}$ appeared already during the first cycle on a chemically cleaned Pt electrode, indicating that the surface area increases faster than in low concentration electrolyte. Nucleation is expected to occur through reaction (6.5) rather than reaction (6.2) in this electrolyte. The former reaction is expected to be fast because of the low stability of the Mn^{4+} ion, and the overall reaction rate is rather dependent on two Mn^{3+} ions that meet and disproportionate (6.4). Since the concentration of Mn^{2+} is higher in the high concentration electrolyte it appears that nucleation occurs faster, even though the overall reaction is impeded by the increased H^+ concentration.

Effect of substrate. The difference between substrates at short deposition times, i.e. current density in potential steps, $p_{ox,1}$ and $p_{ox,2}$, can be explained in terms of a different rate of nucleation or different distribution of nuclei. Both oxidation peaks ($p_{ox,1}$ and $p_{ox,2}$) were less pronounced on crystalline DSA electrodes than on Pt and Au (Fig. 5.84) at the same conditions. In fact, the current density per geometric area was less for the crystalline DSA when subtracting the response in blank electrolyte (cf. Figs. 5.33 and 5.45), indicating that the rate of reaction (6.1) is lower at the DSA electrode during the initial stages of deposition even though the onset potential appears to be lower at the DSA (Figs. 5.33a and 5.45). This can be explained in terms of slower nucleation at the DSA electrode or different distribution of nuclei at the surface. From STEM images, the platinum electrode seemed to be completely covered by MnO_x after only 10 s at 1.45 V (Fig. 5.27), whereas only small amounts of MnO_x was observed in certain areas on the surface at the crystalline DSA electrode after deposition for 100 s at 1.45 V (Fig. 5.6) although the charge passed was comparable. As discussed in the section on effect of mass transport, reaction (6.1) occurs faster at the growing deposit of MnO_x than on the substrate (Pt or crystalline DSA). However, when the nuclei gather in specific areas, as seen in Fig. 5.6, their diffusion zones will overlap more quickly and the effect of increased surface area will be less. This will result in lower current densities at the peak in potential steps and in CVs, in agreement with the results in this work.

The fact that Pt and Au electrodes behaved differently from an h-IrO_2 covered titanium electrode in potential step measurements with EQCM, may be associated with the larger surface area of iridium oxide. Due to this larger surface area, the local pH at the h-IrO_2 surface is presumably less affected by the electrodeposition of manganese oxide than Pt and Au for any given deposition rate. At Pt and Au electrodes, the measurements showed that a mixture between Mn(III) oxide and MnO_2 is formed at 1.45 V (Fig. 5.72c). According to the explanation of the oxidation peak on the reverse scan ($p_{ox,2}$) proposed above, reaction (6.3) is not occurring at this potential. Hence, the gradually increasing amount of MnO_2 at 1.45 V is caused either by disproportionation within the solid phase (Eq. (2.20)) or because of an increasing rate of the disproportionation mechanism, specifically reactions (6.4) and (6.5), due to the decrease in local pH caused by manganese oxide deposition. At higher potentials (1.50 V and 1.55 V), reaction (6.3) is able to proceed and hence a full oxidation to MnO_2 is observed. However, for the h-IrO_2 covered titanium electrodes, the oxidation product is only the Mn(III) oxide within the time frame of the potential steps regardless of the deposition potential (Fig. 5.73). The absence of MnO_2 at 1.45 V can be explained by the difference in surface area between the rough h-IrO_2 powder and the smooth Pt and Au electrodes. Since the available surface area is presumably larger for the h-IrO_2 covered electrode, the local pH is not affected as much by MnO_x deposition and an increase in the rate of the disproportionation mechanism is not observed within the time frame of the potential step. The reason for the slow rate of reaction (6.3) at h-IrO_2 at higher potentials (1.50 V and 1.55 V) is not clear.

6.1.2 Nature of Mn(III) intermediate

In this work, Raman spectroscopy was performed to investigate the chemical nature of the Mn(III) intermediate confirmed from EQCM measurements. The chemical nature of this intermediate is debated in the literature and several previous works have suggested that the intermediate is MnOOH [55, 56, 59–61]. Distinct Raman spectra have been obtained for MnOOH and MnO_2 [48, 87] (Figs. 2.9 and 2.13), so it might be possible to distinguish between them with Raman spectroscopy. However, the in-situ Raman spectra obtained at platinum and crystalline DSA electrodes in this work (Fig. 5.81) only showed the presence of γ-MnO_2 and no MnOOH was found. This was regardless of the deposition conditions and substrate. It should be noted that the signal of MnOOH could inherently be less intense than that of γ-MnO_2 and hence be masked by the latter. Additionally, the amount of MnOOH in the deposit could be low since it can be converted to MnO_2 through reaction (2.16) or (2.20), also resulting in low intensities. Furthermore, heat created by the laser can have caused a phase transition of the Mn(III) intermediate before it was possible to detect it, since deposited manganese dioxide is not thermally stable [90]. Based on this it is not possible to exclude the presence of MnOOH.

Another possible Mn(III) intermediate is Mn_2O_3. Multiple Raman spectra of Mn_2O_3 have been reported in the literature (e.g. Fig. 2.12 or 2.11). While the Raman spectrum of α-Mn_2O_3 reported by Bernard et al. [87] (Fig. 2.12) resembles that of γ-MnO_2, multiple dissimilar Raman spectra of Mn_2O_3 have also been reported [46,85,88,93]. Hence, it is difficult to reach a conclusion regarding the presence of Mn_2O_3 because of the discrepancies in the literature spectra. Furthermore, care should be taken when interpreting the Raman spectra for the same reasons as explained above for MnOOH. Thus, as for MnOOH, it is not possible to exclude the presence of Mn_2O_3 based on the Raman spectra.

It may be suggested that the Mn(III) intermediate is not a separate phase, but that Mn^{3+} is accommodated in the crystal structure of γ-MnO_2, resulting in different Raman spectra then expected from e.g. MnOOH or Mn_2O_3. Ruetschi [51] suggested a cation vacancy model for γ-MnO_2, where it is assumed that Mn^{3+} can be accommodated within the crystal structure, compensated by an appropriate amount of OH^- replacing O^{2-} in the lattice. This causes a volume expansion of the lattice, but since the ionic radii are not too dissimilar the crystal structure can be maintained. γ-MnOOH has a crystal structure resembling that of pyrolusite (β-MnO_2), whereas α-MnOOH has a crystal structure resembling that of ramsdellite (R-MnO_2) [31]. If the crystal structure of MnO_x formed in this work is that of γ-MnO_2 (Fig. 2.7) with a fraction of the Mn^{4+} sites occupied by Mn^{3+}, the Raman spectra might not at all resemble the Raman spectra of MnOOH obtained in the literature (Fig. 2.13). Rather, it is possible that the Raman spectrum does not change significantly from that of γ-MnO_2 even though a higher fraction of Mn^{3+} is present in the lattice.

6.2 Later stages of deposition

The effect of mass transport of Mn^{2+} at longer deposition time, for example in Fig. 5.77, can be explained by a layer of poorly conducting manganese oxide forming at the surface of the growing deposit. During the initial stages of deposition after some nucleation has occurred, the overall reaction rate is limited by diffusion of Mn^{2+} ions in the electrolyte, as discussed in section 6.1. However, as the deposited manganese oxide grows in thickness, the effect of mass transport in the free electrolyte adjacent to the surface gradually decreases as observed when applying spikes in rotation rate (Fig. 5.77). This is also evident from the decrease in current with time at constant rotation rate in Figures 5.76a and 5.79a where a constant current would be expected for a process limited by diffusion in the electrolyte, after the initial nucleation and growth. The observed behavior is in accordance with the decrease in oxidation of Mn^{2+} observed in the literature when a composite Pb-MnO_2 anode became covered by a layer of MnO_2 [133]. Based on measurements in this work, it is suggested that the overall reaction rate becomes influenced by diffusion through a porous layer of a poorly conducting intermediate at the outer surface of the growing deposit, as was first proposed by Paul and Cartwright [52–54]. This is in accordance with other experimental observations such as that the current density based on geometric area was independent on substrate (Figs. 5.54a vs 5.58a and Figs. 5.55a vs 5.57a) and potential (Figs. 5.58 and 5.72a) at longer deposition times for measurements not influenced by OER, demonstrating that the deposition is not limited by the kinetics of an electrochemical reaction.

The conductivity of MnO_x is expected to decrease with increasing Mn^{3+} fraction (see Eq. (2.13)) [51], and the poorly conducting outer layer is expected to contain a high fraction of Mn^{3+}. While the Mn(III) intermediate is continuously oxidized to MnO_2 either through reaction (6.3) or (2.20) thereby improving the electrical conductivity of the deposit, these reactions are initially slower than formation of the intermediate causing the poorly conducting layer to grow thicker until a steady state is reached. Reaction (6.3) is dependent on electrode potential and requires a higher overpotential than reaction (6.1). So where the potential is insufficient for reaction (6.1) to occur, the same is true for reaction (6.3). Accordingly, electrochemical oxidation of the intermediate (Eq. (6.3)) occurs first near the substrate and then the reaction zone moves outwards in the deposit as the conductivity improves with formation of MnO_2.

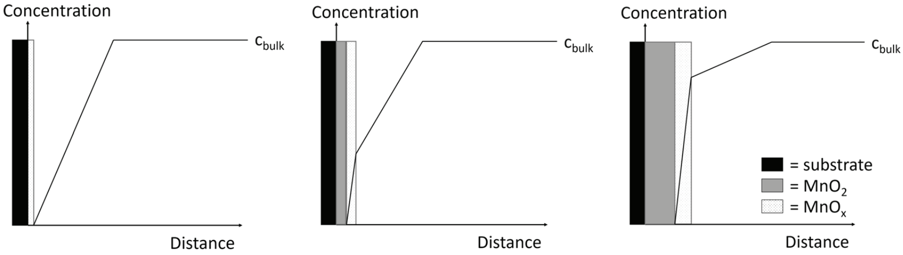

(a) (b) (c)

Figure 6.2: Illustration of a possible development of concentration profile of Mn^{2+} ions with increasing deposition time assuming that the diffusion coefficient for Mn^{2+} is lower in MnO_x than in the electrolyte.

The varying dependence of mass transport on the reaction rate in Figure 5.77 may be explained by a two layer model in which both diffusion in the electrolyte and in a growing oxide layer on the electrode contributes. During the initial stages of growth, reaction (6.1) is able to proceed at the outer surface of the growing deposit since the potential drop through the deposit is not too large. However, as the deposit grows thicker, the potential drop becomes significant and reaction (6.1) is no longer able to proceed at the surface of the growing deposit. Now, Mn^{2+} ions must diffuse a distance into the growing deposit where the potential is sufficiently high for them to be oxidized. Two models for the suggested development of the concentration profile of Mn^{2+} ions with deposition time are illustrated in Figures 6.2 and 6.3, respectively. In both models there is a transition from one to two diffusion layers with increased deposition time; one in the electrolyte and one through the porous, poorly conducting outer layer of the deposit. Both models are in agreement with the decreased effect of rotation rate with deposition time (Fig. 5.77), assuming that rotation rate does not affect mass transport inside the porous oxide layer.

The model presented in Figure 6.2 assumes that the diffusion coefficient of Mn^{2+} ions is lower in the porous oxide layer than in the electrolyte. At the interface between two media with different diffusion coefficients the following relationship exists [135]:

$$D_1 \frac{\delta c_1}{\delta x} = D_2 \frac{\delta c_2}{\delta x} \tag{6.6}$$

Hence, the concentration gradient changes at the interface if the diffusion coefficients for Mn^{2+} ions in the oxide layer and in the electrolyte are dis-

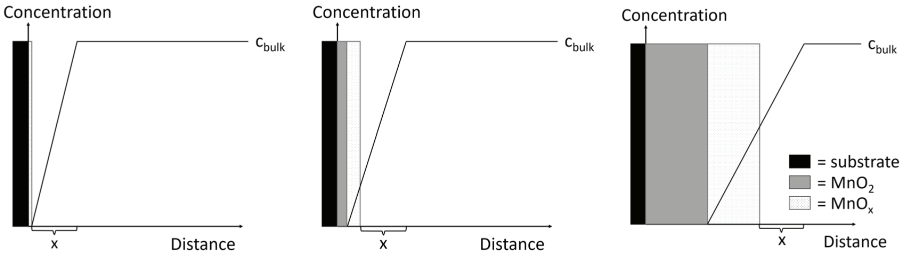

(a) (b) (c)

Figure 6.3: Illustration of a possible development of concentration profile of Mn^{2+} ions with increasing deposition time assuming that the diffusion coefficient for Mn^{2+} is the same in the electrolyte as in MnO_x. The diffusion layer thickness in the electrolyte (denoted x) is assumed to be constant.

similar. Since the concentration gradient in the electrolyte diminishes with deposition time, the effect of rotation rate will gradually diminish.

The model presented in Figure 6.3 assumes that the diffusion coefficient for Mn^{2+} ions is equal in the oxide layer as in the electrolyte. Furthermore, the diffusion layer thickness in the electrolyte (x) is assumed to be constant so that the total diffusion layer thickness, i.e. in the oxide and in the electrolyte, increases with deposition time. Since rotation only affects the thickness of the diffusion layer in the electrolyte, the effect of rotation will gradually diminish as observed in Figure 5.77.

6.2.1 Morphology

A smooth deposit is expected from the model in Figure 6.2 with a gradually decreasing conductivity and consequently lower experienced potential with distance from the substrate-deposit interface. Most deposits appeared relatively smooth and compact at all substrates after longer deposition times independently of potential, electrolyte and substrate (e.g. Figs. 5.7c, 5.26c, 5.10c, 5.8 and 5.23c), as was also observed in the literature [59, 71, 72, 133]. A closer look at the surface of the MnO_x deposit shows that the deposit is in fact built up by small and interconnected nanoparticles of uniform size ($\sim$ 10 nm) and spherical shape, see high resolution images in Figs. 5.12, 5.6 and 5.27. These nanospheres are suggested to form in the chemical step in the ECE mechanism (Eq. (6.2)), and have poor conductivity until the deposit has been transformed to MnO_2. If the spheres are formed from the disproportionation reaction, the higher conductivity of MnO_2 would increase the likeliness of dendrite formation instead of forming a smooth surface. Hence, the spheres are formed by the ECE mechanism.

The poor conductivity in the outer part of the deposit can also explain why the deposit formed at a low overpotential (i.e. 1.45 V) is more compact, i.e. less porous, than the deposit formed at 1.55 V, as seen in Figs. 5.9 and 5.26c vs 5.28c. At 1.55 V, the Mn(III) intermediate can be converted to MnO_2 through reaction (6.3) (cf. Fig. 5.72c), resulting in a reduction of the thickness of the poorly conducting part of the deposit compared to at 1.45 V. Hence, reaction (6.1) and subsequent deposition can to a larger extent take place near the outer surface of the growing deposit instead of in the interior of the deposit. This may lead to a less structured and more porous and thicker deposit. For the DSA electrodes, the porosity at 1.55 V may be influenced by oxygen bubbles since OER is occurring simultaneous to manganese oxide deposition, but at Pt electrodes OER is not expected to occur.

A thin layer of the poorly conducting intermediate may also explain the beginning of dendrite formation observed after 1000 s at 1.55 V at Pt (Fig. 5.28b) and crystalline DSA (5.8b). At longer times the deposit still became smooth (Figs. 5.28c and 5.13c), showing that the thickness of the poorly conducting part of the growing deposit develops with time also at 1.55 V.

Ideal conditions for mass transport, stability and amount produced of Mn^{3+} is suggested to result in the extensive dendrite formation observed at crystalline DSA electrodes at 1.55 V in $2\,\mathrm{mol\,L^{-1}}$ H_2SO_4 + $0.15\,\mathrm{mol\,L^{-1}}$ Mn^{2+} (Fig. 5.13). The pH is expected to be higher at the surface of the deposit than at its interior, due to the production of H^+ from both manganese oxide deposition and OER. When Mn^{3+} ions are transported out of the deposit, nucleation can occur according to Eq. (6.2) at the surface of the deposit due to the lower stability Mn^{3+}. In addition to transport by diffusion, mass transport of Mn^{3+} ions is affected by the rate of OER, since this causes convection of the electrolyte. At 1.55 V in $2\,\mathrm{mol\,L^{-1}}$ H_2SO_4 + $0.15\,\mathrm{mol\,L^{-1}}$ Mn^{2+}, the production, stability and mass transport of Mn^{3+} ions is suggested to be sufficient for them to be transported out of the deposit where nucleation occurs. At electrodes experiencing more extensive oxygen evolution, i.e. higher electrode potentials (Fig. 5.14) or amorphous DSA electrodes (Fig. 5.24), the Mn^{3+} ions may be transported away from the surface of the deposit before reaction (6.2) has time to occur. At electrodes where less amounts of Mn^{3+} ions are produced, i.e. in $0.1\,mol\,L^{-1}$ H_2SO_4 + $5\,mmol\,L^{-1}$ Mn^{2+} (Fig. 5.8c) or at electrodes with a preformed layer of manganese oxide (Fig. 5.18a), most of the Mn^{3+} might be consumed before it can reach the surface. Hence, dendrite formation is only expected to occur when sufficient amounts of Mn^{3+} ions are produced and only for specific mass transport conditions.

A higher porosity of manganese oxide deposits formed in low concentration electrolyte ($0.1\,mol\,L^{-1}$ H_2SO_4 + $5\,mmol\,L^{-1}$ Mn^{2+}) is suggested to be the reason why these deposits detached and contracted upon drying (e.g. Figs. 5.7c and 5.26c). In low concentration electrolyte, the disproportionation mechanism is expected to be slower than in $2\,mol\,L^{-1}$ H_2SO_4 + $0.15\,mol\,L^{-1}$ Mn^{2+}. The disproportionation mechanism is more likely to occur at the interior of the deposit where the local pH is lower than in bulk. A higher rate of the disproportionation mechanism can therefore lead to a higher nucleation rate within the deposit and consequently a denser deposit with less pores. The pores are filled with electrolyte that will evaporate when the electrode is removed from the solution and left to dry. Since the deposits formed in low concentration electrolyte are expected to contain more electrolyte, their structural integrity is more affected by drying and consequently they detach and contract more easily.

6.2.2 Stability of MnO_x and OER activity

Although manganese oxide cover the entire surface, oxygen evolution still occurs predominantly at the substrate, at least at low electrode potentials. This is evident from the lack of oxygen evolution at platinum electrodes covered with manganese oxide at 1.55 V (Fig. 5.58). However, the amount of evolved oxygen is influenced by how much of the active area of the substrate that is blocked by manganese oxide, i.e. how much the deposit interfere with the substrate-electrolyte interface. OER currents are therefore more affected by manganese oxide deposition at conditions where nucleation occurs faster, i.e. low H^+ concentration (cf. Figs. 5.54b vs 5.55b). Furthermore, OER currents are also more affected at higher surface area electrodes, i.e. at amorphous DSAs (cf. Figs. 5.57 vs 5.55). This is proposed to be due to pores and cracks at the substrate being blocked by manganese oxide so that a larger fraction of the surface area becomes inactive towards OER. For crystalline DSA electrodes in $2\,mol\,L^{-1}$ H_2SO_4 + $0.15\,mol\,L^{-1}$ Mn^{2+}, the blocking effect of manganese oxide was reduced as the electrode potential increased (Fig. 5.55). This is most likely an effect of the more porous deposit created at higher potentials, allowing for more easy access to the substrate.

The OER current at electrodes covered by manganese oxide depends on the deposit thickness and the number of cracks in the deposit. A thin prelayer of MnO_2 (1000 s at 1.45 V) did not affect OER currents at a crystalline DSA at 1.75 V in $2\,mol\,L^{-1}$ H_2SO_4 + $0.15\,mol\,L^{-1}$ Mn^{2+} (Fig. 5.59a). However, OER currents in $2\,mol\,L^{-1}$ H_2SO_4 were significantly reduced at an electrode covered by a thick layer of MnO_2 (10 000 s at 1.45 V, Fig 5.50). For thick deposits, the OER current depends on areas of reduced deposit thickness such as cracks, where higher OER current densities are obtained. Cavities caused by oxygen bubbles were observed at the surface of deposited manganese oxide after oxygen gas had been evolved in blank electrolyte on electrodes covered by a thick layer of manganese oxide (Figs. 5.16b and 5.17). The cavities were predominantly observed in cracks and structurally weak locations at the surface, demonstrating that oxygen had formed underneath the deposit and gathered at these presumably weak spots. The number of cracks were also higher in these deposits indicating that the cracks were most likely propagating due to the pressure exerted by oxygen bubbles. The cracks progressively widened with increasing potential, i.e. as an increasing amount of oxygen gas formed (Fig. 5.17). This effect was likely also enhanced from drying of the deposit (for SEM) between each applied potential. When Mn^{2+} ions were present in the electrolyte, the number of observed cracks were significantly reduced (Fig. 5.18) accompanied by a reduction in the oxygen evolution current (Fig. 5.56).

6.3 Reduction

Reduction of deposited manganese oxide is a complex process that depends among other things on the amount of deposit present at the electrode. Based on the results in this work, reduction is suggested to occur according to reactions (6.7) and (6.8), as suggested by Lee et al. and Maskell [68–70]:

$$MnO_2 + H^+ + e^- \longrightarrow MnOOH \tag{6.7}$$

$$2\,MnOOH + 2\,H^+ \longrightarrow MnO_2 + Mn^{2+} + 2\,H_2O \tag{6.8}$$

All reduction processes can be explained in terms of reactions (6.7) and (6.8) and taking into account that the electrical conductivity of manganese oxide decreases with increasing fraction of Mn^{3+}, i.e. MnOOH, in the deposit. In low concentration electrolyte ($0.1\,\mathrm{mol\,L^{-1}}$ H_2SO_4 + $5\,\mathrm{mmol\,L^{-1}}$ Mn^{2+}), a reduction peak around 1.3 V ($p_{red,1}$, see Fig. 5.62) was observed in all experiments. $p_{red,1}$ was the only reduction feature observed in experiments where small amounts of manganese oxide were formed, i.e. at fast sweep rates or low upper reversal potentials (Figs. 5.64 and 5.63, respectively). However, in experiments where more manganese oxide were present at the surface prior to reduction, a second reduction peak ($p_{red,2}$) appeared. For even thicker deposits, more reduction features, i.e. peak or plateau current, were observed at potentials negative of $p_{red,2}$ (Figs. 5.78a and 5.47). The conductivity within the deposit decreases during reduction since the chemical reaction (6.8) is slower than the electrochemical reaction (6.7). A slower chemical reaction is in accordance with the effect of time at OCP on the amount of remaining MnO_x (yellow curve in Fig. 5.80b); during the time spent at OCP, only the chemical step (Eq. (6.8)) can occur, and this can therefore be the only cause for the shift in current maximum in Fig. 5.80b. The results in this work is in accordance with the work of Lee et al. [68], who found a decreased conductivity in the deposit after $p_{red,1}$, along with a reduction in density of the deposit. The electrochemical reduction then takes place at progressively shorter distances from the substrate/deposit interface due to the potential drop through the deposit. Electrical conductivity is partially restored through the chemical reaction that regenerates Mn^{4+} in the lattice. However, two neighbouring Mn^{3+} in the lattice are required for reaction (6.8) to occur.

The processes responsible for each reduction feature are described in more detail below, based on experiments performed in low concentration electrolyte.

The first reduction peak ($p_{red,1}$). This reduction peak can be understood as a net balance between anodic and cathodic processes. In $0.1\,\mathrm{mol\,L^{-1}}$ H_2SO_4 + $5\,\mathrm{mmol\,L^{-1}}$ Mn^{2+}, reaction (6.7) commences positive of 1.40 V as the net current becomes negative at around 1.40 V (e.g. Fig 5.63a). While reaction (6.7) gives a negative contribution to the current, there is still a positive contribution from reaction (6.1). This positive current contribution can be deduced from the progressively more negative onset potential with increasing amount of remaining deposit, i.e. with increasing cycle number, during the positive-going sweep in Fig. 5.78a. Oxidation of Mn^{2+} continues to take place until the potential reaches approximately 1.35 V (see Fig. 5.63a). Consequently, deposition of MnOOH through the chemical reaction (6.2) still takes place in the same potential region (1.40 V to 1.35 V) and beyond, with an accompanying increase in mass. The net mass change is negative in this potential region, implying that reaction (6.8) proceeds at a faster rate than reaction (6.2). The equilibrium in reaction (6.2) is shifted to the right as the local pH increases due to reactions (6.7) and (6.8) and proceeds until all Mn^{3+} ions in the electrolyte are consumed, around 1.30 V in Fig. 5.63a. This potential depends on the specific deposition conditions. Below this potential the net rate of mass loss increases since it is now primarily affected by reaction (6.8), which in turn depends on reaction (6.7) and in-solid diffusion of Mn^{3+}. It should be noted that the sharp mass decrease observed towards the end of $p_{red,1}$ (or $p_{red,2}$) could be influenced by particles detaching from the substrate due to lower adhesion as a result of the progressing reduction processes.

The current in the first reduction peak is due to reaction (6.7) occurring at a limited distance from the substrate/deposit interface where the potential drop through the deposit is small. This is illustrated by the fact that the charge passed in $p_{red,1}$ does not increase significantly after the third cycle in Fig. 5.78a, even though the anodic charge continues to increase. For very thin deposits the entire deposit can be reduced during $p_{red,1}$. The charge passed in the first reduction peak was higher when manganese oxide was produced at low oxidation potentials, i.e. 1.45 V (cf. Fig. 5.74a). This can be explained in terms of the more dense deposit obtained at 1.45 V (cf. Fig. 5.9) so that the potential drop through the deposit was less than for the more porous deposits obtained at 1.55 V.

The second reduction peak ($p_{red,2}$). For thicker deposits, the potential drop through the deposit becomes too large and prevents the complete electrochemical reduction of MnO_2 (Eq. (6.7)) within $p_{red,1}$. However, as the overpotential increases in magnitude during the negative-going sweep, reduction can occur at larger distances away from the substrate resulting in $p_{red,2}$.

Plateau current. At potentials negative of $p_{red,2}$, the rate of reaction (6.7) is entirely dependent on reaction (6.8), partially restoring electrical conductivity through the deposit. As the total amount of deposit decreases,

Mn^{3+} must diffuse over longer distances to recombine with a second Mn^{3+} (Eq. (6.8)), lowering the rate of reaction (6.7) as well.

6.4 Removal

The results and discussion above has significant implications for an optimum procedure for removal of manganese oxide. A prelayer formed at 1.45 V was included in the removal sequence (Fig. 4.4) since experiments showed that the deposit formed at this potential was easier to remove than deposits formed at higher potentials (cf. Figs. 5.74a and 5.22). This may be related to formation of a denser deposit at this potential as discussed above (sec. 6.3). The time at 1.45 V was set to 1000 s to ensure that the entire electrode surface was covered by a dense manganese oxide layer before increasing the potential. The electrode was then stepped to 1.75 V where the current density at the crystalline DSA electrodes was comparable to the current density employed in the industry, i.e. $600\,\mathrm{A\,m^{-2}}$. The reduction was performed at 0.4 V, well below the onset potential for manganese oxide reduction. The time at the reduction potential was successfully reduced from 100 s to 10 s and could potentially be further reduced since most of the reduction charge is passed within the first 3 s (blue curve in Fig. 5.59b). The adhesion of the remaining manganese oxide layer was severely affected by the short reduction step, as was also observed by Lee et al. [68] when a linear sweep was stopped after the first reduction peak. It is believed that the reduced adhesion arises because reduction of deposited manganese oxide occurs preferentially near the substrate/deposit interface due to the potential drop through the deposit as discussed in section 6.3. Consequently, after the short reduction step the outer part of the deposit may easily be removed mechanically either by rinsing or imposing oxygen evolution (the second step to 1.75 V). If the outer layer of manganese oxide is removed by OER, an additional reduction step (0.4 V) was included in the sequence in order to remove MnO_2 nuclei formed at this high potential at the newly exposed substrate surface. These nuclei are expected to be harder to remove and may lead to a more porous deposit and less efficient deposit removal in subsequent sequences.

A similar attempt at removing MnO_2 formed at conditions resembling those in zinc electrowinning was performed at constant current by Nijjer [72], see Fig. 6.4. In her work, most of the MnO_2 formed during a 10 hour electrol-

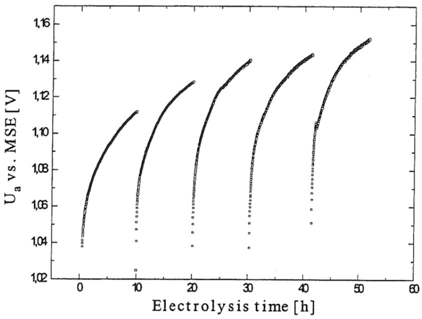

Figure 6.4: Anodic potential of an IrO_2-Ta_2O_5/Ti electrode at 0.05 A cm^{-2} in 2 mol L^{-1} H_2SO_4 + 10 g L^{-1} Mn^{2+} at 35 °C. A CV at 10 mV s^{-1} was performed between each 10 hour electrolysis period. Reproduced from [72].

ysis period was removed during a CV before the next electrolysis period. The potential at the end of each 10 hour period increased slightly during the experiment (1.11-1.15 V vs MSE), indicating that remaining MnO_x was present at the surface after the CV. An effect of remaining MnO_x was also observed in this work when the sequence was run six consecutive times (Tab. 5.6). Although the method described here works without formation of a pre-layer, it is believed that a pre-layer formed at a low potential (1.45 V) will lead to a smaller increase in overpotential of the DSA electrode during operation as this step allows for more efficient deposit removal. The prelayer is believed to be more effective when the the manganese oxide is removed by rinsing rather than by OER, as the latter involves nucleation of MnO_2 at higher electrode potentials that is expected to be harder to remove (c.f. the comment above). However, the optimum way of maintaining a low electrode potential necessary for implementing DSA electrodes in zinc electrowinning is yet to be established.

Chapter 7

Conclusions

The aim of this thesis work has been to understand manganese oxide deposition and removal, ultimately leading to better control of manganese oxide in zinc electrowinning. Manganese oxide deposition occurred at all studied substrates; Pt, Au, Ti and amorphous and crystalline IrO_2-Ta_2O_5/Ti (DSA) electrodes. It is suggested to occur both by a disproportionation mechanism and by an ECE mechanism. The first step in both mechanisms is the oxidation of Mn^{2+} to Mn^{3+}. The overall rate of each mechanism depends highly on the stability of Mn^{3+} ions in the solution that in turn depends on the pH. The ECE mechanism is more prevalent in less acidic solutions, whereas the disproportionation mechanism is more prevalent in more acidic solutions. An Mn(III) intermediate was confirmed from potential steps with EQCM at low potentials, as expected for the ECE mechanism. In situ Raman spectroscopy was performed to determine the chemical nature of this intermediate, but only γ-MnO_2 was observed.

Nucleation was found to occur by a progressive mechanism, consisting of manganese oxide nanoparticles of around 10 nm. Nucleation occurs more rapidly when the H^+ concentration is low, likely due to the lower stability of Mn^{3+} ions in the less acidic electrolyte. Potential step measurements at a rotating disc electrode showed that oxidation of Mn^{2+} ions proceeds faster on deposited manganese oxide than on the studied substrates. When sufficient nucleation has occurred, i.e. from around the peak in the current transients, the overall reaction rate becomes limited by diffusion of Mn^{2+} ions in the electrolyte. The peak in current transients from potential steps as well as the oxidation peaks observed in CVs are explained by a changing electrode area combined with a gradual development of diffusion layer thickness. Eventually, the diffusion layer has developed to a thickness where an increase in surface area no longer leads to an increase in current.

At longer times, i.e. up to several hours, it is suggested that the deposition rate is limited by diffusion through a non-conducting porous layer formed at the outer surface of the growing deposit. The effect of forced convection, i.e. rotation rate, was found to gradually diminish with increasing deposit thickness, as pore diffusion rather than diffusion in the free electrolyte adjacent to the surface becomes rate limiting. Formation of a non-conducting layer at the surface is consistent with the smooth surface of manganese oxide obtained at most deposition conditions.

The oxygen evolution reaction (OER) was found to occur predominantly at the substrate surface, at least at low electrode potentials. A reduction in OER current was observed for IrO_2-Ta_2O_5/Ti (DSA) electrodes depending on how effectively manganese oxide blocked the substrate surface, and was significant for thick and compact deposits with few cracks and cavities. However, a thin and compact layer of MnO_2 (1000 s at 1.45 V) was not found to reduce the OER at these electrodes.

Reduction of deposited manganese oxide is suggested to involve an electrochemical step followed by a slower chemical step. The conductivity of the deposit changes during reduction resulting in different reduction behaviour depending on the thickness of the deposit. A more efficient reduction was observed for manganese oxide formed at low potentials. This is suggested to be due to the lower porosity (thickness) of these deposits leading to a lower potential drop through the deposit. Complete removal of manganese oxide was not achieved with applying a low electrode potential alone. A chemical cleaning step, or allowing sufficient time for the slow chemical step was necessary to remove all the deposit.

A tailored sequence for effectively removing deposited manganese oxide was developed based on the obtained understanding of the mechanism for manganese oxide deposition and removal. The sequence consisted of applying several electrode potentials, most importantly having a thin pre-layer formed at low potentials (1.45 V) before applying a potential close to normal operating current densities. When removal was desired, an electrochemical reduction (0.4 V) was applied that reduced the adhesion of the remaining deposit to the substrate. The remaining deposit could then be removed either by rinsing or by OER. The sequence was validated with crystalline DSA electrodes in a laboratory cell with synthetic electrolyte (2 mol L^{-1} H_2SO_4 + 0.15 mol L^{-1} Mn^{2+}). Even though the removal worked without formation of a prelayer at a low potential, the prelayer is assumed to ensure a more effective removal of deposited manganese oxide with repeated deposition. This is also assumed to be the case when the deposit is removed by rinsing instead of by OER. A more efficient removal of deposited manganese oxide will lead to a slower decrease in anode overpotential during its service life. Further work is required to verify and optimize this sequence to industrial conditions, i.e. electrolyte, temperature, cell geometry and mass transport regime.

Chapter 8

Outlook

Industrial removal of manganese oxide deposits. A method for removing manganese oxide deposits from the anode surface is required in order to convert to more energy efficient and environmentally friendly anodes in zinc electrowinning. The removal sequence suggested in this work worked well in a laboratory cell with synthetic electrolyte, but needs to be further validated and optimized before it can be implemented in an industrial setting. Experiments should be conducted in an industrial electrolyte at industrially relevant temperatures. The effect of additives on the method should be examined. These could alter the substrate surface properties and influence the efficiency of manganese oxide removal. Initially, experiments should be performed in a laboratory cell with geometries that resembles those in the zinc electrowinning process more closely (larger planar electrodes and electrolyte flow), before moving on to larger scales.

In an industrial setting, we picture the reduction step occurring in a separate tank with subsequent removal by rinsing with water or electrolyte. Subsequently, a prelayer can be deposited before the anode is returned to normal operation. We believe that both removing the outer layer by rinsing (in contrast to by OER) as well as applying a prelayer will result in a slower increase in overpotential at the anode during its service life, but this needs to be verified.

An optimization of the time the electrode can perform at normal operation before removal is required. This is important for economic considerations as the anodes must be removed and handled before they can be returned to production. With dimensionally stable anodes this process can be automated since they do not change dimensions due to corrosion. From an economic perspective, implementation of DSAs in zinc electrowinning depends on many factors such as the price and lifetime of new anodes, the gained energy efficiency, the price of electricity and the cost related to removal of manganese oxide at different anode materials (labour costs and downtime).

Mechanism for manganese oxide deposition and reduction. The early stages of nucleation of manganese oxide are not well understood and could be further investigated with deposition on a TEM-grid [136] or with in-situ AFM measurements. The difference in nucleation and overall reaction rate between the two deposition mechanisms (disproportionation and ECE) should be investigated further by performing EQCM measurements in electrolytes with varying concentrations of H^+. Furthermore, an attempt should be made to monitor localized pH changes at the anode during deposition, for instance by implementing a surface plasmon resonance technique [137].

The chemical nature of the Mn(III) intermediate is yet to be determined. A possible way for achieving this is by performing in situ XRD measurements [138]. Even if Mn(III) does not form a separate phase, lattice expansion is expected if Mn^{3+} replaces Mn^{4+} in the lattice [51] and consequently different XRD spectra are expected. In situ XRD should be performed both during deposition and reduction of manganese dioxide. The effect of time at OCP after reduction should also be investigated. Note, however, that there exist a dispute regarding the crystal structure of electrochemical manganese dioxide (EMD) in the literature [45, 50].

In our work we have assumed that soluble Mn^{3+} ions do not form during reduction of manganese oxide deposits. This could perhaps be verified by performing rotating ring disc measurements using a ring electrode and conditions that selectively detect Mn^{3+} ions. This method can also be used to indirectly study the nucleation rate at different acid concentrations.

Dynamic impedance spectroscopy (DEIS) could provide more information about the manganese oxide deposition and reduction mechanism at different time scales. DEIS allows for impedance spectra to be recorded at electrodes where the surface conditions changes with time, such as growing oxides [139].

Bibliography

[1] C. Comninellis and G. Vercesi. Characterization of DSA®-type oxygen evolving electrodes: Choice of a coating. *J. Appl. Electrochem.*, 21(4):335–345, 1991.

[2] M. S. Moats. Will lead-based anodes ever be replaced in aqueous electrowinning? *JOM*, 60(10):46–49, 2008.

[3] T. Parada and E. Asselin. Reducing power consumption in zinc electrowinning. *JOM*, 61(10):54–58, 2009.

[4] J. Thonstad. *Fag 53541 Elektrolyseprosesser*. Institutt for teknisk elektrokjemi, Norges teknisk-naturvitenskapelige universitet, Trondheim, 1998.

[5] S. Trasatti. Progress in the understanding of the mechanism of chlorine evolution at oxide electrodes. *Electrochim. Acta*, 32(3):369 – 382, 1987.

[6] J. E. Bennett. Electrodes for generation of hydrogen and oxygen from seawater. *Int. J. Hydrogen Energy*, 5(4):401–408, 1980.

[7] N. N. Greenwood. *Chemistry of the elements*. Elsevier Butterworth-Heinemann, Amsterdam, 2nd edition, 1997.

[8] T. Tekin and M. Bayramoğlu. Kinetics of the reduction of MnO_2 with Fe^{2+} ions in acidic solutions. *Hydrometallurgy*, 32(1):9–20, 1993.

[9] T. Jiang, Y. Yang, Z. Huang, B. Zhang, and G. Qiu. Leaching kinetics of pyrolusite from manganese-silver ores in the presence of hydrogen peroxide. *Hydrometallurgy*, 72(1-2):129–138, 2004.

[10] G. Senanayake. A mixed surface reaction kinetic model for the reductive leaching of manganese dioxide with acidic sulfur dioxide. *Hydrometallurgy*, 73(3):215–224, 2004.

[11] E. Godunov, I. Artamonova, I. Gorichev, and Y. Lainer. Influence of oxalic acid on the dissolution kinetics of manganese oxide. *Russian Metallurgy (Metally)*, 2012(11):935–941, 2012.

[12] J. Y. Welsh. Role og manganic ion in production of electrolytic manganese dioxide. *Electrochemical Technology*, 5(11-1):504–&, 1967.

[13] K. Kawaguchi, G. Haarberg, and M. Morimitsu. Control of amorphization of IrO_2-Ta_2O_5/Ti electrodes to suppress unwanted side reactions. *ECS Trans.*, 16(39):41–47, 2008.

[14] M. Morimitsu and N. Oshiumi. Accelerated Oxygen Evolution and Suppressed MnOOH Deposition on Amorphous IrO_2-Ta_2O_5 Coatings. *Chem. Lett.*, 38(8):822–823, 2009.

[15] W. Xu, G. M. Haarberg, F. Seland, S. Sunde, A. P. Ratvik, S. Holmin, J. Gustavsson, Åsa Afvander, E. Zimmerman, and T. Åkre. The durability of the thermally decomposed IrO_2-Ta_2O_5 coated titanium anode in a sulfate solution. *Corros. Sci.*, 150:76 – 90, 2019.

[16] A. M. Couper, D. Pletcher, and F. C. Walsh. Electrode materials for electrosynthesis. *Chem. Rev.*, 90(5):837–865, 1990.

[17] Y. Feng, L. Yang, J. Liu, and B. E. Logan. Electrochemical technologies for wastewater treatment and resource reclamation. *Environ. Sci.: Water Res. Technol.*, 2:800–831, 2016.

[18] J. O'M. Bockris. Kinetics of activation controlled consecutive electrochemical reactions: Anodic evolution of oxygen. *The Journal of Chemical Physics*, 24(4):817–827, 1956.

[19] J. Rossmeisl, Z.-W. Qu, H. Zhu, G.-J. Kroes, and J. Nørskov. Electrolysis of water on oxide surfaces. *J. Electroanal. Chem.*, 607(1–2):83 – 89, 2007.

[20] L.-P. Wang, Q. Wu, and T. Van Voorhis. Acid-base mechanism for ruthenium water oxidation catalysts. *Inorg. Chem.*, 49(10):4543–4553, 2010.

[21] M. G. Mavros, T. Tsuchimochi, T. Kowalczyk, A. McIsaac, L.-P. Wang, and T. Van Voorhis. What can density functional theory tell us about artificial catalytic water splitting? *Inorg. Chem.*, 53(13):6386–6397, 2014.

[22] M. Wohlfahrt-Mehrens and J. Heitbaum. Oxygen evolution on Ru and RuO_2 electrodes studied using isotope labelling and on-line mass spectrometry. *J. Electroanal. Chem. Interfacial Electrochem.*, 237(2):251–260, 1987.

[23] S. Geiger, O. Kasian, M. Ledendecker, E. Pizzutilo, A. M. Mingers, W. T. Fu, O. Diaz-Morales, Z. Li, T. Oellers, L. Fruchter, A. Ludwig, K. J. J. Mayrhofer, M. T. M. Koper, and S. Cherevko. The stability number as a metric for electrocatalyst stability benchmarking. *Nature Catalysis*, 1(7):508–515, 2018.

[24] T. Binninger, R. Mohamed, K. Waltar, E. Fabbri, P. Levecque, R. Koetz, and T. J. Schmidt. Thermodynamic explanation of the universal correlation between oxygen evolution activity and corrosion of oxide catalysts. *Sci. Rep.*, 5, 2015.

[25] D. Ohms, V. Plzak, S. Trasatti, K. Wiesener, and H. Wendt. Electrode kinetics and electrocatalysis of hydrogen and oxygen electrode reactions. In H. Wendt, editor, *Electrochemical Hydrogen Technologies: Electrochemical Production and Combustion of Hydrogen.* Elsevier, 1990.

[26] S. Trasatti. Electrocatalysis by oxides — attempt at a unifying approach. *J. Electroanal. Chem. Interfacial Electrochem.*, 111(1):125–131, 1980.

[27] L.-E. Owe, M. Tsypkin, K. Wallwork, R. Haverkamp, and S. Sunde. Iridium-ruthenium single phase mixed oxides for oxygen evolution: Composition dependence of electrocatalytic activity. *Electrochim. Acta*, 70:158–164, 2012.

[28] G. Cao. *Nanostructures And Nanomaterials: Synthesis, Properties And Applications.* Imperial College Press, 2004.

[29] J. R. Rumble, editor. *CRC handbook of chemistry and physics.* CRC Press/Taylor & Francis, Boca Raton, Fl, 100th edition, 2019.

[30] M. Tangstad. Chapter 7 - manganese ferroalloys technology. In M. Gasik, editor, *Handbook of Ferroalloys*, pages 221 – 266. Butterworth-Heinemann, Oxford, 2013.

[31] J. E. Post. Manganese oxide minerals: Crystal structures and economic and environmental significance. *Proceedings of the National Academy of Sciences*, 96(7):3447–3454, 1999.

[32] A. H. Reidies. *Ullmann's Encyclopedia of Industrial Chemistry*, chapter Manganese Compounds, pages 223–244. Wiley, 2000.

[33] A. Biswal, B. Chandra Tripathy, K. Sanjay, T. Subbaiah, and M. Minakshi. Electrolytic manganese dioxide (EMD): a perspective on worldwide production, reserves and its role in electrochemistry. *RSC Adv.*, 5:58255–58283, 2015.

[34] R. Frydendal, E. A. Paoli, I. Chorkendorff, J. Rossmeisl, and I. E. L. Stephens. Toward an active and stable catalyst for oxygen evolution in acidic media: Ti-stabilized MnO_2. *Adv. Energy Mater.*, 5(22):1500991, 2015.

[35] G. Elmaci, S. Cerci, and D. Sunar-Cerci. The evaluation of the long-term stability of α-MnO_2 based OER electrocatalyst in neutral medium by using data processing approach. *J. Mol. Struct.*, 1195:632 – 640, 2019.

[36] Z. M. Chan, D. A. Kitchaev, J. N. Weker, C. Schnedermann, K. Lim, G. Ceder, W. Tumas, M. F. Toney, and D. G. Nocera. Electrochemical trapping of metastable Mn^{3+} ions for activation of MnO_2 oxygen evolution catalysts. *Proceedings of the National Academy of Sciences*, 115(23):E5261–E5268, 2018.

[37] Y. Meng, W. Song, H. Huang, Z. Ren, S.-Y. Chen, and S. L. Suib. Structure–property relationship of bifunctional MnO_2 nanostructures: Highly efficient, ultra-stable electrochemical water oxidation and oxygen reduction reaction catalysts identified in alkaline media. *J. Am. Chem. Soc.*, 136(32):11452–11464, 2014.

[38] M. Huynh, D. K. Bediako, and D. G. Nocera. A Functionally Stable Manganese Oxide Oxygen Evolution Catalyst in Acid. *J. Am. Chem. Soc.*, 136(16):6002–6010, 2014.

[39] T. N. Andersen. The manganese dioxide electrode in aqueous solution. In R. E. White, editor, *Modern aspects of electrochemistry: 30*, volume 30, pages 313–413, New York, 1996. Plenum Press.

[40] J. B. Fernandes, B. D. Desai, and V. Dalal. Manganese dioxide — a review of a battery chemical part I. Chemical syntheses and x-ray diffraction studies of manganese dioxides. *J. Power Sources*, 15(4):209 – 237, 1985.

[41] D. D. Macdonald. The thermodynamics and theoretical corrosion behavior of manganese in aqueous systems at elevated temperatures. *Corros. Sci.*, 16(7):461–482, 1976.

[42] S. Luo, H. Guo, Z. Wang, X. Li, J. Wang, and G. Yan. The electrochemical performance and reaction mechanism of coated titanium anodes for manganese electrowinning. *J. Electrochem. Soc.*, 166(14):E502, 2019.

[43] G. H. Aylward and T. J. V. Findlay. *SI Chemical Data.* Wiley, Milton, 6th edition, 2008.

[44] F. A. Cotton, G. Wilkinson, C. A. Murillo, and M. Bochmann. *Advanced inorganic chemistry.* Wiley, New York, 6th ed. edition, 1999.

[45] Y. Chabre and J. Pannetier. Structural and electrochemical properties of the proton / γ-MnO_2 system. *Prog. Solid State Chem.*, 23(1):1 – 130, 1995.

[46] C. Julien, M. Massot, and C. Poinsignon. Lattice vibrations of manganese oxides: Part I. Periodic structures. *Spectrochim. Acta, Part A*, 60(3):689 – 700, 2004.

[47] P. M. de Wolff. Interpretation of some γ-MnO_2 diffraction patterns. *Acta Crystallogr.*, 12(4):341–345, Apr 1959.

[48] C. Julien, M. Massot, S. Rangan, M. Lemal, and D. Guyomard. Study of structural defects in γ-MnO_2 by Raman spectroscopy. *J. Raman Spectrosc.*, 33(4):223–228, 2002.

[49] A. H. Heuer, A. Q. He, P. J. Hughes, and F. H. Feddrix. *ITE Lett.*, 1(6):B50, 2000.

[50] C.-H. Kim, Z. Akase, L. Zhang, A. H. Heuer, A. E. Newman, and P. J. Hughes. The structure and ordering of ε-MnO_2. *J. Solid State Chem.*, 179(3):753 – 774, 2006.

[51] P. Ruetschi. Cation-vacancy model for MnO_2. *J. Electrochem. Soc.*, 131(12):2737–2744, 1984.

[52] R. Paul and A. Cartwright. The mechanism of manganese dioxide deposition. In *MnO_2 symposium*, volume 2, pages 290–304, 1980.

[53] R. Paul and A. Cartwright. The mechanism of the deposition of manganese dioxide: Part II. Electrode impedance studies. *J. Electroanal. Chem. Interfacial Electrochem.*, 201(1):113 – 122, 1986.

[54] R. Paul and A. Cartwright. The mechanism of the deposition of manganese dioxide: Part III. Rotating ring-disc studies. *J. Electroanal. Chem. Interfacial Electrochem.*, 201(1):123 – 131, 1986.

[55] J. P. Petitpierre, C. Comninellis, and E. Plattner. Oxydation du $MnSO_4$ en dioxyde de manganese dans H_2SO_4 30%. *Electrochim. Acta*, 35(1):281–287, 1990.

[56] S. Nijjer, J. Thonstad, and G. M. Haarberg. Oxidation of manganese(II) and reduction of manganese dioxide in sulphuric acid. *Electrochim. Acta*, 46:395–399, 2000.

[57] G. Davies. Some aspects of the chemistry of manganese(III) in aqueous solution. *Coord. Chem. Rev.*, 4(2):199 – 224, 1969.

[58] C. Clarke, G. Browning, and S. Donne. An RDE and RRDE study into the electrodeposition of manganese dioxide. *Electrochim. Acta*, 51(26):5773–5784, 2006.

[59] Z. Rogulski, H. Siwek, I. Paleska, and A. Czerwiński. Electrochemical behavior of manganese dioxide on a gold electrode. *J. Electroanal. Chem.*, 543(2):175 – 185, 2003.

[60] W.-H. Kao and V. Weibel. Electrochemical oxidation of manganese(II) at a platinum electrode. *J. Appl. Electrochem.*, 22(1):21–27, 1992.

[61] M. Dupont and S. Donne. Nucleation and growth of electrodeposited manganese dioxide for electrochemical capacitors. *Electrochim. Acta*, 120:219–225, 2014.

[62] S. Bodoardo, J. Brenet, M. Maja, and P. Spinelli. Electrochemical behaviour of MnO_2 electrodes in sulphuric acid solutions. *Electrochim. Acta*, 39(13):1999 – 2004, 1994.

[63] M. Chotkowski, Z. Rogulski, and A. Czerwiński. Spectroelectrochemical investigation of MnO_2 electro-generation and electro-reduction in acidic media. *J. Electroanal. Chem.*, 651(2):237 – 242, 2011.

[64] A. Cross, A. Morel, M. Drozd, I. Olcomendy, A. Hollenkamp, and S. Donne. Active mass analysis on thin films of electrodeposited manganese dioxide for electrochemical capacitors. *Electrochim. Acta*, 87:133 – 139, 2013.

[65] S. Devaraj and N. Munichandraiah. EQCM investigation of the electrodeposition of MnO_2 and its capacitance behavior. *Electrochem. Solid-State Lett*, 12(9):F21–F25, 2009.

[66] M. Fleischmann, H. Thirsk, and I. Tordesillas. Kinetics of electrodeposition of γ-manganese dioxide. *Trans. Faraday Soc.*, 58:1865–1877, 1962.

[67] A. J. Gibson, B. Johannessen, Y. Beyad, J. Allen, and S. W. Donne. Dynamic electrodeposition of manganese dioxide: Temporal variation in the electrodeposition mechanism. *J. Electrochem. Soc.*, 163(5):H305–H312, 2016.

[68] J. Lee, W. Maskell, and F. Tye. The electrochemical reduction of manganese dioxide in acidic solutions: Part I. Voltammetric peak 1. *J. Electroanal. Chem. Interfacial Electrochem.*, 79(1):79 – 104, 1977.

[69] W. Maskell. The electrochemical reduction of manganese dioxide in acidic solutions: Part II. Voltammetric peak 2. *J. Electroanal. Chem. Interfacial Electrochem.*, 199(1):127 – 137, 1986.

[70] J. Lee, W. Maskell, and F. Tye. The electrochemical reduction of manganese dioxide in acidic solutions: Part III. Voltammetric peak 3. *J. Electroanal. Chem. Interfacial Electrochem.*, 110(1–3):145 – 158, 1980.

[71] M. Moats. MnO_2 deposition on coated titanium anodes in copper electrowinning solutions. *World Metall. ERZMETALL*, 63(6):286–291, 2010.

[72] S. Nijjer. *Deposition and reduction of manganese dioxide on alternative anode materials in zinc electrowinning.* NTH, Trondheim, 2000.

[73] M. Owen, G. Lawrance, and S. Donne. An electrochemical quartz crystal microbalance study into the deposition of manganese dioxide. *Electrochim. Acta*, 52(14):4630–4639, 2007.

[74] L. Pajunen, J. Aromaa, and O. Forsén. The effect of dissolved manganese on anode activity in electrowinning. In C. Young, A. Alfantazi, C. Anderson, and A. James, editors, *Proc. TMS Fall Extract. Process. Conf.*, volume 2, pages 1255–1265, Vancouver, BC, 2003.

[75] A. Pilla, M. M. Duarte, and C. E. Mayer. Manganese dioxide electrodeposition in sulphate electrolytes: the influence of ferrous ions. *J. Electroanal. Chem.*, 569(1):7 – 14, 2004.

[76] S. Rodrigues, N. Munichandraiah, and A. K. Shukla. A cyclic voltammetric study of the kinetics and mechanism of electrodeposition of manganese dioxide. *J. Appl. Electrochem.*, 28(11):1235–1241, 1998.

[77] W. Zhang, M. Robichaud, E. Ghali, and G. Houlachi. Electrochemical behavior of mesh and plate oxide coated anodes during zinc electrowinning. *Trans. Nonferrous Met. Soc. China*, 26(2):589–598, 2016.

[78] P. Yu and T. J. O'Keefe. Evaluation of lead anode reactions in acid sulfate electrolytes: II. Manganese reactions. *J. Electrochem. Soc.*, 149(5):A558–A569, 2002.

[79] A. J. Gibson, R. C. Burns, M. F. Dupont, and S. W. Donne. Mesoscale morphological control of electrodeposited manganese dioxide films. *Electrochim. Acta*, 170:343 – 352, 2015.

[80] C. Zhang, L. Jiang, F. Xu, N. Duan, B. Xin, G. Han, G. Zhang, and Y. Wen. New insight into cleaner control of heavy metal anode slime from aqueous sulfate electrolytes containing Mn(II): Preliminary characterization and mechanism analysis. *J. Cleaner Prod.*, 177:276 – 283, 2018.

[81] A. Dutra and I. Almeida. Electrolytic manganese dioxide nucleation and growth on titanium substrates. *Mater. Sci. Forum*, 570:114–119, 2008.

[82] P. Ruetschi. Influence of cation vacancies on the electrode potential of MnO_2. *J. Electrochem. Soc.*, 135(11):2657–2663, 1988.

[83] S. Nijjer, J. Thonstad, and G. M. Haarberg. Cyclic and linear voltammetry on Ti/IrO_2-Ta_2O_5-MnO_x electrodes in sulfuric acid containing Mn^{2+} ions. *Electrochim. Acta*, 46(23):3503–3508, 2001.

[84] T. Gao, H. Fjellvåg, and P. Norby. A comparison study on Raman scattering properties of α- and β-MnO_2. *Anal. Chim. Acta*, 648(2):235 – 239, 2009.

[85] F. Kapteijn, A. Vanlangeveld, J. Moulijn, A. Andreini, M. Vuurman, A. Turek, J. Jehng, and I. Wachs. Alumina-supported manganese oxide catalysts: I. Characterization: Effect of precursor and loading. *J. Catal.*, 150(1):94 – 104, 1994.

[86] B. R. Strohmeier and D. M. Hercules. Surface spectroscopic characterization of manganese/aluminum oxide catalysts. *The Journal of Physical Chemistry*, 88(21):4922–4929, 1984.

[87] M. Bernard, A. Hugot-Le Goff, B. V. Thi, and S. Cordoba de Torresi. Electrochromic reactions in manganese oxides: I. Raman analysis. *J. Electrochem. Soc.*, 140(11):3065–3070, 1993.

[88] F. Buciuman, F. Patcas, R. Craciun, and D. R. T. Zahn. Vibrational spectroscopy of bulk and supported manganese oxides. *Phys. Chem. Chem. Phys.*, 1:185–190, 1999.

[89] D. Gosztola and M. J. Weaver. Electroinduced structural changes in manganese dioxide + manganese hydroxide films as characterized by real-time surface-enhanced Raman spectroscopy. *J. Electroanal. Chem. Interfacial Electrochem.*, 271(1):141 – 154, 1989.

[90] E. Widjaja and J. T. Sampanthar. The detection of laser-induced structural change of MnO_2 using in situ Raman spectroscopy combined with self-modeling curve resolution technique. *Anal. Chim. Acta*, 585(2):241 – 245, 2007.

[91] A. Li, H. Ooka, N. Bonnet, T. Hayashi, Y. Sun, Q. Jiang, C. Li, H. Han, and R. Nakamura. Stable potential windows for long-term electrocatalysis by manganese oxides under acidic conditions. *Angew. Chem. Int. Ed.*, 58(15):5054–5058, 2019.

[92] G. Mulè, C. Burlet, and Y. Vanbrabant. Automated curve fitting and unsupervised clustering of manganese oxide Raman responses. *J. Raman Spectrosc.*, 48(11):1665–1675, 2017.

[93] W. B. White and V. G. Keramidas. Vibrational spectra of oxides with the C-type rare earth oxide structure. *Spectrochim. Acta A*, 28(3):501 – 509, 1972.

[94] T. Gao, F. Krumeich, R. Nesper, H. Fjellvåg, and P. Norby. Microstructures, surface properties, and topotactic transitions of manganite nanorods. *Inorg. Chem.*, 48(13):6242–6250, 2009.

[95] W. W. Rudolph and G. Irmer. Raman spectroscopic investigation of speciation in $MnSO_4$(aq). *J. Solution Chem.*, 43(3):465–485, 2014.

[96] B. De Mishima, T. Ohtsuka, and N. Sato. In-situ Raman spectroscopy of manganese dioxide during the discharge process. *J. Electroanal. Chem. Interfacial Electrochem.*, 243(1):219 – 223, 1988.

[97] H. B. Beer. Electrode and coating therefor, U.S. Patent 3632498A, Jan. 1972.

[98] H. B. Beer. The invention and industrial development of metal anodes. *J. Electrochem. Soc.*, 127(8):C303–C307, 1980.

[99] G. Vercesi, J. Rolewicz, C. Comninellis, and J. Hinder. Characterization of DSA-type oxygen evolving electrodes. Choice of base metal. *Thermochim. Acta*, 176(C):31–47, 1991.

[100] R. Kötz and S. Stucki. Stabilization of RuO_2 by IrO_2 for anodic oxygen evolution in acid media. *Electrochim. Acta*, 31(10):1311–1316, 1986.

[101] S. Cherevko, S. Geiger, O. Kasian, N. Kulyk, J.-P. Grote, A. Savan, B. R. Shrestha, S. Merzlikin, B. Breitbach, A. Ludwig, and K. J. Mayrhofer. Oxygen and hydrogen evolution reactions on Ru, RuO_2, Ir, and IrO_2 thin film electrodes in acidic and alkaline electrolytes: A comparative study on activity and stability. *Catal. Today*, 262:170 – 180, 2016.

[102] R. Mráz and J. Krýsa. Long service life IrO_2/Ta_2O_5 electrodes for electroflotation. *J. Appl. Electrochem.*, 24(12):1262–1266, 1994.

[103] W. Zhang, E. Ghali, and G. Houlachi. Review of oxide coated catalytic titanium anodes performance for metal electrowinning. *Hydrometallurgy*, 169:456 – 467, 2017.

[104] C. A. Huang, S. W. Yang, C. Z. Chen, and F.-Y. Hsu. Electrochemical behavior of IrO_2-Ta_2O_5/Ti anodes prepared with different surface pretreatments of Ti substrate. *Surf. Coat. Technol.*, 320:270 – 278, 2017.

[105] W. Xu, G. M. Haarberg, S. Sunde, F. Seland, A. P. Ratvik, S. Holmin, J. Gustavsson, Åsa Afvander, E. Zimmerman, and T. Åkre. Sandblasting effect on performance and durability of Ti based IrO_2-Ta_2O_5 anode in acidic solutions. *Electrochim. Acta*, 295:204 – 214, 2019.

[106] K. L. Hardee, L. M. Ernes, R. C. Carlson, and D. E. Thomas. Metal substrate of improved surface morphology, U.S. Patent 5167788A, Dec. 1992.

[107] G. Vercesi, J.-Y. Salamin, and C. Comninellis. Morphological and microstructural the Ti/IrO_2-Ta_2O_5 electrode: effect of the preparation temperature. *Electrochim. Acta*, 36(5-6):991–998, 1991.

[108] S. P. Sandoval, M. D. Waite, and C. J. Clayton. Electrochemically active composition, methods of making, and uses thereof, U.S. Patent 8 124 556, Feb. 2012.

[109] S. Ardizzone, A. Carugati, and S. Trasatti. Properties of thermally prepared iridium dioxide electrodes. *J. Electroanal. Chem. Interfacial Electrochem.*, 126(1):287 – 292, 1981.

[110] W. Xu, G. M. Haarberg, S. Sunde, F. Seland, A. P. Ratvik, E. Zimmerman, T. Shimamune, J. Gustavsson, and T. Åkre. Calcination temperature dependent catalytic activity and stability of IrO_2–Ta_2O_5 anodes for oxygen evolution reaction in aqueous sulfate electrolytes. *J. Electrochem. Soc.*, 164(9):F895–F900, 2017.

[111] G. Martelli, R. Ornelas, and G. Faita. Deactivation mechanisms of oxygen evolving anodes at high current densities. *Electrochim. Acta*, 39(11):1551 – 1558, 1994.

[112] Y. Kamegaya, K. Sasaki, M. Oguri, T. Asaki, H. Kobayashi, and T. Mitamura. Improved durability of iridium oxide coated titanium anode with interlayers for oxygen evolution at high current densities. *Electrochim. Acta*, 40(7):889 – 895, 1995.

[113] B. Correa-Lozano, C. Comninellis, and A. De Battisti. Service life of Ti/SnO_2-Sb_2O_5 anodes. *J. Appl. Electrochem.*, 27(8):970–974, 1997.

[114] R. Kötz, H. J. Lewerenz, and S. Stucki. XPS studies of oxygen evolution on Ru and RuO_2 anodes. *J. Electrochem. Soc.*, 130(4):825–829, apr 1983.

[115] R. Kötz, S. Stucki, D. Scherson, and D. Kolb. In-situ identification of RuO_4 as the corrosion product during oxygen evolution on ruthenium in acid media. *J. Electroanal. Chem. Interfacial Electrochem.*, 172(1):211 – 219, 1984.

[116] R. Kötz, H. Neff, and S. Stucki. Anodic iridium oxide films: XPS-studies of oxidation state changes and O_2-evolution. *J. Electrochem. Soc.*, 131(1):72–77, 1984.

[117] W. J. James. In A. J. Bard, editor, *Encyclopedia of electrochemistry of the elements*, volume 5, page 305, New York, 1976. Marcel Dekker.

[118] M. Morimitsu, R. Otogawa, and M. Matsunaga. Effects of cathodizing on the morphology and composition of IrO_2-Ta_2O_5/Ti anodes. *Electrochim. Acta*, 46:401–406, 2000.

[119] D. A. Buttry and M. D. Ward. Measurement of interfacial processes at electrode surfaces with the electrochemical quartz crystal microbalance. *Chem. Rev.*, 92(6):1355–1379, 1992.

[120] G. Mestl. In situ Raman spectroscopy — a valuable tool to understand operating catalysts. *J. Mol. Catal. A: Chem.*, 158(1):45 – 65, 2000.

[121] J. W. Niemantsverdriet. *Vibrational Spectroscopy*, chapter 8, pages 217–249. John Wiley & Sons, Ltd, 2007.

[122] T. Schmid and P. Dariz. Raman microspectroscopic imaging of binder remnants in historical mortars reveals processing conditions. *Heritage*, 2(2):1662–1683, 2019.

[123] B. Scharifker and G. Hills. Theoretical and experimental studies of multiple nucleation. *Electrochim. Acta*, 28(7):879 – 889, 1983.

[124] S. Ardizzone, G. Fregonara, and S. Trasatti. Inner and outer active surface of RuO_2 electrodes. *Electrochim. Acta*, 35(1):263–267, 1990.

[125] C. D. Pauli and S. Trasatti. Electrochemical surface characterization of $IrO_2 + SnO_2$ mixed oxide electrocatalysts. *J. Electroanal. Chem.*, 396(1):161 – 168, 1995.

[126] V. Birss, M. Chang, and J. Segal. Platinum oxide film formation—reduction: an in-situ mass measurement study. *J. Electroanal. Chem.*, 355(1):181 – 191, 1993.

[127] Z. Jusys, S. Bruckenstein, and A. R. Hillman. New insights into the Belousov-Zhabotinskii reaction derived from EQCM measurements at a gold electrode. *Phys. Chem. Chem. Phys.*, 13:5373–5382, 2011.

[128] R. Saldanha, B. Gomes, G. da Rocha Torres, B. de Lima, J. de Castro, L. da Silva, and E. Ferreira. Inhibition of the oxygen evolution reaction during titanium passivation in aqueous phosphoric acid solution. *J. Solid State Electrochem.*, 24(8):1991–1998, 2020.

[129] V. Birss, H. Elzanowska, and S. Gottesfeld. Quartz crystal microbalance measurements during oxidation/reduction of hydrous Ir oxide electrodes. *J. Electroanal. Chem. Interfacial Electrochem.*, 318(1):327 – 333, 1991.

[130] V. Birss, C. Bock, and H. Elzanowska. Hydrous Ir oxide films: the mechanism of the anodic prepeak reaction. *Can. J. Chem.*, 75(11):1687–1693, 1997.

[131] S. M. Skaftun. Anodeprosesser i elektrokjemisk fremstilling av sink. Master's thesis, NTNU, 2013.

[132] M. Dupont, A. F. Hollenkamp, and S. W. Donne. Electrochemically active surface area effects on the performance of manganese dioxide for electrochemical capacitor applications. *Electrochim. Acta*, 104(Supplement C):140 – 147, 2013.

[133] M. Mohammadi and A. Alfantazi. Evaluation of manganese dioxide deposition on lead-based electrowinning anodes. *Hydrometallurgy*, 159:28–39, 2016.

[134] S. Skaftun, S. Sunde, G. Haarberg, and F. Seland. An electrochemical quartz crystal microbalance investigation of manganese oxide deposition and dissolution in sulfuric acid relevant for zinc electrowinning. *ECS Transactions*, 85(4):103–119, 2018.

[135] J. Crank. *The mathematics of diffusion.* Clarendon Press, Oxford, 2nd edition, 1975.

[136] J. Ustarroz, U. Gupta, A. Hubin, S. Bals, and H. Terryn. Electrodeposition of Ag nanoparticles onto carbon coated TEM grids: A direct approach to study early stages of nucleation. *Electrochem. Commun.*, 12(12):1706–1709, 2010.

[137] S. K. Mishra and B. D. Gupta. Surface plasmon resonance based fiber optic pH sensor utilizing Ag/ITO/Al/hydrogel layers. *Analyst*, 138:2640–2646, 2013.

[138] M. Ndjeri, S. Peulon, M. Schlegel, and A. Chaussé. In situ grazing-incidence X-ray diffraction during electrodeposition of birnessite thin films: Identification of solid precursors. *Electrochem. Commun.*, 13(5):491–494, 2011.

[139] R. L. Sacci, F. Seland, and D. A. Harrington. Dynamic electrochemical impedance spectroscopy, for electrocatalytic reactions. *Electrochim. Acta*, 131:13–19, 2014.

Appendix A

X-Ray Diffraction

X-Ray Diffraction (XRD) spectra obtained for as-prepared crystalline dimensionally stable anodes (DSA) and IrO_2 hydrolysis powder are presented in Figure A.1 and A.2, respectively.

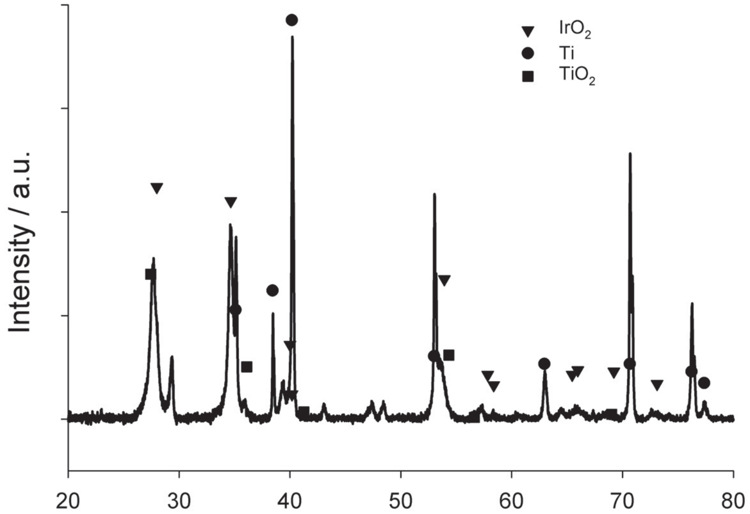

Figure A.1: XRD spectra of the crystalline DSA electrode.

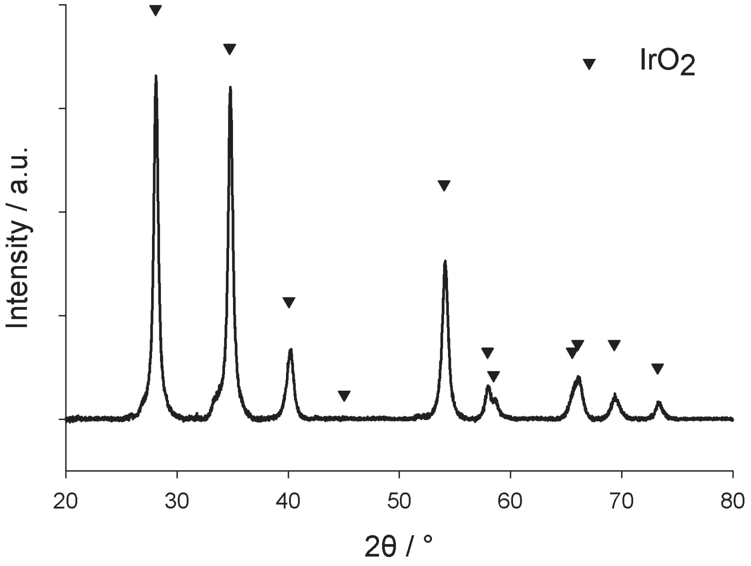

Figure A.2: XRD spectra of the IrO_2 hydrolysis powder.

Appendix B

Inner and outer charge

The values of total, inner and outer charge determined prior to potential steps with crystalline and amorphous DSA electrodes in different electrolytes are listed in Table B.1. Total, inner and outer charge values were also determined prior to potential step sequences for manganese oxide removal and those are listed in Table B.2. The values were determined from a Matlab script using files of CVs with sweep rates between 10 and $500\,\mathrm{mV\,s^{-1}}$. The Matlab code is presented in Listing B.1 and an example of the output graphs from this code is presented in Figure B.1.

Table B.1: Total, inner and outer charge for crystalline DSA electrodes used for potential steps.

WE	**Electrolyte** mol L^{-1}		**Pot.**	**Time**	**Total q**	**Inner q**	**Outer q**
	H_2SO_4	Mn^{2+}	V	s	mC	mC	mC
DSA$_{\text{cryst.}}$	0.1	-	1.45	10 000	18.5	3.9	14.6
			1.55	10 000	18.5	3.9	14.6
	0.1	0.005	1.45	100	16.2	3.4	12.9
				1000	14.8	4.3	10.5
				10 000	10.6	3.4	7.2
			1.55	100	11.2	3.0	8.2
				1000	9.8	2.4	7.4
				10 000	12.4	3.2	9.2
	2	-	1.45	10 000	20.5	5.5	14.9
			1.55	10 000	20.5	5.5	14.9
			1.65	10 000	12.6	3.1	9.4
	2	0.15	1.45	100	9.7	1.9	7.8
				1000	15.3	3.2	12.1
				10 000	15.1	3.6	11.6
			1.55	100	11.9	2.4	9.5
				1000	14.3	2.8	11.5
				10 000	14.6	3.4	11.2
			1.65	10 000	15.0	3.5	11.5
DSA$_{\text{amorp.}}$	2	-	1.45	10 000	49.7	10.7	38.9
			1.55	10 000	50.4	12.3	38.1
			1.65	10 000	52.1	13.9	38.2
	2	0.15	1.45	100	47.2	8.8	38.4
				1000	41.9	28.9	13.0
				10 000	47.9	38.9	9.0
			1.55	100	41.9	20.5	21.4
				1000	50.8	37.6	13.3
				10 000	54.8	43.1	11.7
			1.65	10 000	36.2	18.5	17.8

Table B.2: Total, inner and outer charge for crystalline DSA electrodes used to perform potential step sequences in $2\,\mathrm{mol\,L^{-1}}$ $H_2SO_4 + 0.15\,\mathrm{mol\,L^{-1}}$ Mn^{2+}.

Time at potential					**Total**	**Inner**	**Outer**
1.45 V	1.75 V	0.4 V	1.75 V	0.4 V	**charge**	**charge**	**charge**
s	h	s	s	s	mC	mC	mC
1000	3	-	-	-	13.7	2.0	11.8
1000	15	-	-	-	11.2	1.9	9.3
1000	3	100	-	-	19.0	5.2	13.8
1000	15	100	-	-	15.2	3.3	11.9
1000	3	100	100	100	13.5	2.1	11.4
1000	15	100	100	100	14.3	2.7	11.6
-	3	100	100	100	14.4	2.4	12.0
-	15	100	100	100	14.3	3.2	11.0
1000	3	10	100	10	14.0	2.5	11.5
1000	15	10	100	10	15.5	2.8	12.7
-	3	10	100	10	15.3	1.7	13.6
1000	3 x 6	10	100	10	16.3	2.8	13.4

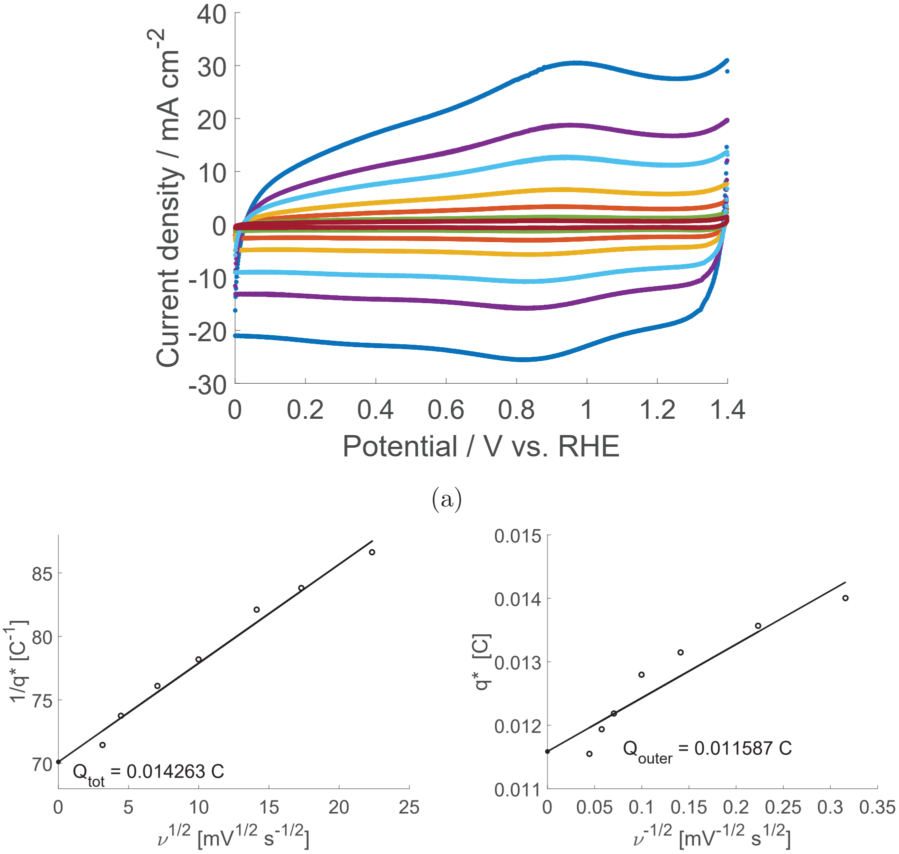

(a)

(b)

(c)

Figure B.1: An example of the determination of total and outer charge. (a) The cyclic voltammograms used to evaluate the total and outer charge. These were obtained at various sweep rates with a crystalline DSA in 2 M H_2SO_4 + 0.15 M Mn^{2+}. (b) Reciprocal of charge against square root of sweep rate. (c) Charge against reciprocal square root of sweep rate.

Listing B.1: Matlab code for determining inner and outer charge.

```matlab
%Sweeprate is collected from the file name, file name e.g.:
%'220520_CV_10mVs_B23_2Msvovelsyre_150mMMn_0til1400mV.txt'
%Files are tab delimited ascii files

clear all
close all

[a, b] = uigetfile('*.txt','MultiSelect','on');
antall_filer = length(a); %number of files

for iterator=1:antall_filer

    ai=char(a(1,iterator));
    path=fullfile(b,ai);

    file_id = fopen(path);
    linje1=fgetl(file_id);
    linje1=fgetl(file_id); %Skips the first row (headings)

    i = 0;
    while linje1 ≠ -1
        i = i + 1;
        matrise1(i,1:5) = str2num(linje1);
        linje1=fgetl(file_id);
    end

    E=matrise1(:,3);        %Potential, 3. column in file
    I=matrise1(:,4);        %Current, 4. column in file
    n=matrise1(:,1);        %Scan number, 1. column in file
    t=matrise1(:,2);        %Time, 2. column in file
    index=matrise1(:,5);    %Row element, 5. column in file

    s = 2; %cycle number, only used for plotting of CVs
    j=1;
    for i=1:length(n)
        if n(i)==s
                    ts(j)=t(i);
                    Es(j)=E(i);
                    Is(j)=I(i);
                    j=j+1;
        end
    end

    Antall_sykler = n(length(n)-10); % Number of cycles in file
    Mindist = length(E)/(Antall_sykler+0.5);

    %Finding upper reversal potentials for all cycles:
    [maxpks,maxlocs] = findpeaks(E,'MinPeakDistance',Mindist);
```

```

    %Finding lower reversal potentials for all cycles:
    invert_E = -E;
    [minpeaks,minlocs] = ...
        findpeaks(invert_E,'MinPeakDistance',Mindist);

    Estart = 0.4;  %Desired start potential for integration
    Eslutt = 1.2;  %Desired end potential for integration

    %defining where to start searching for and stopp searching
    %for intergration limits. The spesific elements are chosen
    %since the files start at approx 0.6 V with a positive-
    %going scan. The integration therfore start towards the
    %end of the first cycle and proceeds into the second.

    Startlete = minlocs(1);
    %Start to search after passing the 1. lower reversal pot.
    Sluttlete = maxlocs(2);
    %Stop to search before reaching the 2. upper reversal pot.

    %new vectors to search for integration limits:
    j=1;
    for i = Startlete:Sluttlete
        tlete(j)= t(i);
        Elete(j) = E(i);
        Ilete(j) = I(i);
        j = j+1;
    end

    %Finding the value closest to the desired start potential,
    %and its row index:
    tempstart = abs(Elete-Estart);
    [¬, startidx] = min(tempstart);
    %New vectors with the value of potential and current for
    %the starting point of integration:
    Startpot(iterator) = Elete(startidx);
    StartI(iterator) = Ilete(startidx);

    %Finding the value closest to the desired stop potential,
    %and its row index:
    tempslutt = abs(Elete-Eslutt);
    [¬, sluttidx] = min(tempslutt);
    Sluttpot(iterator) = Elete(sluttidx);

    area=0;
    % Integrating current with respect to time between
    %the two potentials:
    for i=startidx:sluttidx
        area = area + ...
```

```
            ((Ilete(i)+Ilete(i+1))*(1/2)*(tlete(i+1)-tlete(i)));
    end

    %the voltammetric charge for each file:
    charge(iterator)=area;

    %Working on the filename to extract the sweep rate:
    C = strsplit(ai, {'_', 'mVs', '.txt'});

    sveiphastighet(iterator) = str2double(C(3));  %sweep rate

    %plot cycle 2 from each file:
    figure(1);
    hold on;
    plot(Es,Is,'.', 'MarkerSize', 12);
    xlabel('Potential [V]');
    ylabel('Current [A]');
    set(gca,'fontsize',24);

    %need to clear most vectors in case the files are
    %of different length:
    clear matrise1
    clear I
    clear E
    clear n
    clear t
    clear index
    clear ts
    clear Es
    clear Is
    clear invert_E
    clear Elete
    clear Ilete
    clear tlete
    clear tempstart
    clear tempslutt

end

figure(2)
% Plots 1/q* vs square root of sweep rate
x1=sqrt(sveiphastighet);
y1=1./charge;
hold on
set(gca,'fontsize',24);
%Linear regression:
polyfit1=polyfit(x1,y1,1);
scatter(x1,y1,'k','LineWidth', 2);
%Plots intercept at x = 0:
```

```matlab
scatter(0,polyfit1(2), 'k*', 'Linewidth', 2)
x = [x1 0];
%Plots regression line:
plot(x,polyfit1(1).*x + polyfit1(2),'k','LineWidth', 2)
xlabel('\nu^1^/^2 [mV^1^/^2 s^-^1^/^2]')
ylabel('1/q* [C^-^1]')

qtot = 1/polyfit1(2)  % Total charge
% Adds the value of the intercept to the plot:
xqtot = 0+1;
yqtot = polyfit1(2)-1;
textqtot = ['Q_{tot} = ',num2str(qtot), ' C'];
text(xqtot,yqtot, textqtot,'FontSize',24);

figure(3)
%Plot q vs 1/sqrt(v)
x2=1./(sqrt(sveiphastighet));
y2=charge;
set(gca,'fontsize',24);
hold on
polyfit2 = polyfit(x2,y2,1);        %Linear regression
scatter(x2,y2,'k','LineWidth', 2);
scatter(0,polyfit2(2), 'k*','LineWidth',2);
x = [x2 0];
plot(x,polyfit2(1).*x + polyfit2(2),'k','LineWidth', 2)
xlabel('\nu^-^1^/^2 [mV^-^1^/^2 s^1^/^2]')
ylabel('q*  [C]')

qytre = polyfit2(2)     %Outer charge
qindre = qtot-qytre     %Inner Charge

% writes the value of outer charge in the plot:
xqytre = 0+.08;
yqytre = polyfit2(2);
textqytre = ['Q_{outer} = ',num2str(qytre), ' C'];
text(xqytre,yqytre, textqytre,'FontSize',24);
```

ISBN 978-82-326-6032-2 (printed ver.)
ISBN 978-82-326-6849-6 (electronic ver.)
ISSN 1503-8181 (printed ver.)
ISSN 2703-8084 (online ver.)

NTNU
Norwegian University of
Science and Technology